Dr. Seuss Knows Graduate School

You have brains in your head.
You have feet in your shoes.
You can steer yourself
in any direction you choose.
You're on your own. And you know what you know.
And YOU are the guy who'll decide where to go.

Out there things can happen
and frequently do
to people as brainy
and footsy as you.

I'm sorry to say so
but, sadly, it's true
that bang-ups and hang-ups
can happen to you.

And when you're in a slump,
you're not in for much fun.
Un-slumping yourself
is not easily done.

You'll get mixed up, of course,
as you already know.
You'll get mixed up
with many strange birds as you go.
So be sure when you step.
Step with care and great tact
and remember that life's
a great balancing act.
Just never forget to be dextrous and deft.
And never mix up your right foot with your left.

And will you succeed?
Yes! You will, indeed!
(98 and 3/4 percent guaranteed).

– Dr. Seuss
(1904 - 1991)
Oh the Places You'll Go!

University of Alberta

Terahertz radiation from InAs, GaAs and InP emitters at high excitation fluences and applications

by

Matthew Reid

A thesis submitted to the Faculty of Graduate Studies and Research in partial fulfillment of the requirements for the degree of **Doctor of Philosophy**.

Department of Electrical and Computer Engineering

Edmonton, Alberta

Fall 2005

Library and Archives Canada

Published Heritage Branch

395 Wellington Street
Ottawa ON K1A 0N4
Canada

Bibliothèque et Archives Canada

Direction du Patrimoine de l'édition

395, rue Wellington
Ottawa ON K1A 0N4
Canada

Your file Votre référence
ISBN: 978-0-494-23140-1
Our file Notre référence
ISBN: 978-0-494-23140-1

NOTICE:
The author has granted a non-exclusive license allowing Library and Archives Canada to reproduce, publish, archive, preserve, conserve, communicate to the public by telecommunication or on the Internet, loan, distribute and sell theses worldwide, for commercial or non-commercial purposes, in microform, paper, electronic and/or any other formats.

The author retains copyright ownership and moral rights in this thesis. Neither the thesis nor substantial extracts from it may be printed or otherwise reproduced without the author's permission.

AVIS:
L'auteur a accordé une licence non exclusive permettant à la Bibliothèque et Archives Canada de reproduire, publier, archiver, sauvegarder, conserver, transmettre au public par télécommunication ou par l'Internet, prêter, distribuer et vendre des thèses partout dans le monde, à des fins commerciales ou autres, sur support microforme, papier, électronique et/ou autres formats.

L'auteur conserve la propriété du droit d'auteur et des droits moraux qui protège cette thèse. Ni la thèse ni des extraits substantiels de celle-ci ne doivent être imprimés ou autrement reproduits sans son autorisation.

In compliance with the Canadian Privacy Act some supporting forms may have been removed from this thesis.

While these forms may be included in the document page count, their removal does not represent any loss of content from the thesis.

Conformément à la loi canadienne sur la protection de la vie privée, quelques formulaires secondaires ont été enlevés de cette thèse.

Bien que ces formulaires aient inclus dans la pagination, il n'y aura aucun contenu manquant.

Canada

Abstract

In this thesis, terahertz emission from semiconductor surfaces is studied at high optical excitation fluences in order to investigate the scaling of such sources to high efficiencies. A quantitative comparison of terahertz emission from InAs surfaces, one of the more efficient semiconductor sources, to the most efficient reported pulsed terahertz emitter, a large-aperture GaAs photoconductive switch, is carried out. It is found that at high bias voltages the large-aperture photoconductive switch is more efficient at converting optical to far-infrared energy but that the InAs semiconductor source has a higher frequency bandwidth.

In the high excitation fluence regime, it is found that the dominant emission mechanism from InAs surfaces changes from the previously reported photo-carrier dominated processes at low excitation fluences. A detailed calculation of bulk and surface electric-field induced optical rectification from zinc blende crystals is performed. The calculations are compared to the experimental observation of optical second-harmonic generation and terahertz emission from InAs surfaces for various crystal orientations. The results indicate that the dominant emission mechanism for terahertz radiation from InAs is surface electric-field induced optical rectification.

A comparison of emission of THz radiation from porous crystalline surfaces of InP versus unstructured surfaces was carried out. It was demonstrated, for the first time, that an increased conversion efficiency of terahertz radiation could be achieved with the introduction of porosity and in particular that the optical rectification component

of terahertz emission from InP surfaces could be enhanced with the introduction of porosity. The mechanism for the enhancement is tentatively attributed to local-field enhancement within the porous network.

A terahertz time-domain spectrometer set-up was constructed, employing a semi-large aperture photoconductive switch. This system was characterized and applied to the study of wood and wood products. Specifically, it was demonstrated in a transmission mode that wood samples exhibit both birefringence and diattenuation. These results could lead to potential applications for the determination of fiber orientation in wood products such as the analysis of fiber orientation in paper products.

Acknowledgments

I would like to express my gratitude for the access to expert knowledge and guidance as well as the many opportunities for career advancement that have been provided by my supervisor, Dr. Fedosejevs. I would also like to acknowledge significant support from Dr. Y. Y. Tsui and Dr.Hegmann with some of the finer details of this thesis work.

This project would not have been possible without the expertise provided by Blair Harwood and Rick Conrad with many of the electronics and technological details.

My peers provided me with the support required to reach my goals, as well as much valuable input along the way. For this, I sincerely express my gratitude to Sean Kirkwood, Mike Taschuk, Michael Argument, James Gospodyn, Roman Holenstein and Craig Unick. I am also very grateful to these same people for providing me with the opportunity to learn the game of bridge.

Of all the things I have accomplished during the course of my degree, I am most grateful for being blessed with two wonderful children, Victoria and Dean, and a wonderful wife, Christina. I would also like to thank my friends and family for supporting me in times of need. I would like to thank my mother, Debbie Reid, and brother, Mark Reid for their support along the way. I would also like to thank my grandparents, Ed and Jean Boutilier, for their support. I am very grateful to my wonderful in-laws, Eva and John Werlberger, for helping with our children and making it possible to pursue our family goals. I would also like to thank Mark Shegelski for keeping me on-track and focused, as well as Val Hart, Dave Reid and Luke Reid for their help along the way.

I would also like to acknowledge the financial support provided by NSERC, iCORE and MPB Technologies Inc., without which I would not have been able to do this work.

To my family: Victoria and Dean - the only reason I have maintained my sanity throughout, and the support of my loving wife Christina.

Contents

1 Introduction 1

1.1 Context of terahertz radiation in this thesis 1

1.2 Applications 2

1.3 Generation of terahertz radiation 3

1.3.1 Photo-carrier related emission mechanisms 4

1.3.2 Bulk optical rectification 6

1.3.3 Surface electric-field induced optical rectification 8

1.4 Thesis statement 10

1.5 Layout of the thesis 10

2 Description of the experimental set-up used for the generation and detection of THz radiation 12

2.1 General description and overview 12

2.2 Electronic and Electro-optic Components 14

2.3 Optics 15

2.4 Terahertz detector 15

2.5 Terahertz emitters 16

3 Electro-optic detection of terahertz radiation **17**

3.1 Detection of pulsed terahertz radiation 17

3.1.1 Background 17

3.1.2 Thermal detection 18

3.1.3 photoconductive switch and electro-optic sampling 19

3.2 Calculation of electro-optic response in ZnTe 22

3.2.1 Balanced detection 22

3.2.2 Induced birefringence 28

3.2.3 Polarization dependence of ZnTe electro-optic detection 33

3.2.4 ZnTe electro-optic detection as a polarization analyzer 34

3.3 Examination of the ZnTe electro-optic response 38

3.3.1 Calibration of the electro-optic response of lithium niobate . . . 38

3.3.2 Comparison of ZnTe and $LiNbO_3$ electro-optic responses 42

4 Comparison of large-aperture photoconductive switch and InAs surface emission **46**

4.1 Description of the large-aperture photoconductive switch 46

4.2 Direct comparison 48

5 Terahertz radiation from InAs surfaces at high excitation fluences **59**

5.1 Emission mechanism of terahertz radiation from InAs (100) 60
5.2 Bulk electric-dipole radiation 65
5.2.1 Calculation of bulk electric-dipole radiation 65
5.2.2 Measurements of optical second-harmonic generation from InAs 72
5.3 Electric-field induced nonlinearity 76
5.3.1 Calculation of surface electric-field induced optical rectification . 76
5.3.2 Terahertz emission from InAs 79
5.4 Comparison of second-harmonic generation and terahertz emission from InAs 87

6 Terahertz emission from porous and unstructured InP **92**
6.1 InP (111) 93
6.1.1 Experimental 93
6.2 InP (100) 100

7 Semi-large aperture photoconductive switch **109**
7.1 Description of the SLAPCS 109
7.2 Construction of the SLAPCS 111
7.3 Performance of the SLAPCS 111
7.3.1 Terahertz emission scaling with applied bias field 112
7.3.2 Terahertz emission scaling with optical pump energy 113
7.3.3 Noise scaling with operation frequency 114

7.3.4 Estimate of source efficiency 116

8 Applications **124**

8.1 Birefringence of wood 124

8.2 Waveplates constructed from solid wood 128

8.3 Birefringence of lens paper 131

8.4 A method to image wood in transmission 133

9 Conclusion and future work **150**

9.1 Conclusions 150

9.2 Future Work 151

Bibliography **153**

A Appendix **164**

A.1 Electro-optic detection in ZnTe 164

A.1.1 Derivation of relation 3.26 164

A.1.2 Derivation of Eq. 3.35 165

A.2 Calculation of the bulk electric-dipole contribution to nonlinear susceptibility 166

A.3 Calculation of surface electric-field induced nonlinearity 168

List of Tables

3.1 Zeros of the polarization response function of the ZnTe electro-optic detector (Equations 3.37 and 3.38). 36

3.2 Extrema of the polarization response function of the ZnTe electro-optic detector (Equations 3.37 and 3.38). 36

4.1 Parameters used in estimation of optical to far-infrared conversion efficiency 51

5.1 Rotation matrices to bring crystal coordinates to beam coordinate system 67

5.2 Electric dipole susceptibility tensor, $\chi^{(2)}(\phi)$, in the transformed coordinate systems 69

5.3 THz or SH field strengths for different polarization combinations. Combinations are listed as $E_{in,out}$ 72

5.4 Measured and calculated values for ratios of the coefficients in the fitting functions. The ratios are obtained by using the fitting functions and the functional dependence of the radiation on the angle ϕ from Table. 5.3. Error bars on the measured values are 3 σ errors in this case. 75

5.5 THz field strengths for different polarization combinations. Combinations are listed as $E_{in,out}$. 80

8.1 Table of birefringence measurements. Those listed with a (*) superscript reflect data that was taken only in the time domain due to poor signal-to-noise ratios. 128

List of Figures

1.1 Schematic diagram of THz emission from photo-carrier effects. 5

1.2 Schematic diagram of THz emission from bulk optical rectification. . . 7

1.3 Schematic diagram of THz emission from surface electric-field induced opticalrectification. 9

2.1 Schematic diagram of general THz set-up. 13

3.1 Photo-conductive vs. electro-optic detection of THz radiation. 20

3.2 Probe and THz polarization geometry in ZnTe calculation. 23

3.3 Induced birefringent axes geometry in ZnTe calculation. 24

3.4 Schematic diagram of balanced detection for ZnTe electro-optic detection. 25

3.5 Birefringent axes and THz polarization for ZnTe calculation. 29

3.6 Orientation of the induced birefringent axes in ZnTe. 32

3.7 Polarization orientations for ZnTe as a polarization analyzer. 35

3.8 Experimental and theoretical polarization dependencies for ZnTe as a polarization analyzer. 37

3.9 Experimental set-up for measuring the electro-optic coefficient in $LiNbO_3$. 40

3.10 Phase retardance as a function of applied bias field in $LiNbO_3$. 41

3.11 THz waveforms from a large-aperture photoconductive switch measured in ZnTe and $LiNbO_3$. 43

4.1 Set-up used for comparing InAs and GaAs large-aperture photoconductive emitters. 54

4.2 Saturation measurements for InAs and GaAs. 55

4.3 THz waveforms defining pulsewidth in the time domain. 56

4.4 Conversion efficiencies measured from GaAs and InAs emitters. 57

4.5 Frequency spectra measured for GaAs and InAs emitters. 58

5.1 Crystal orientation dependence of THz emission from InAs (100). . . . 62

5.2 Polarization dependence of THz emission from InAs (100). 63

5.3 Geometry for bulk and surface-field induced optical rectification calculations. 66

5.4 Pump beam polarization definitions for bulk and surface-field induced optical rectification calculations. 70

5.5 Set-up for measuring second-harmonic emission from InAs surfaces. . . 73

5.6 Experimental and theoretical curves for SH emission from InAs surfaces. 74

5.7 Set-up for measuring THz emission from InAs surfaces. 81

5.8 Experimental and theoretical curves for THz emission from InAs surfaces. 82

5.9 THz (s-polarized) emission with theoretical curves for (110) InAs. . . . 85

5.10 THz (p-polarized) emission with theoretical curves for (110) InAs. . . . 86

5.11 Experimental and theoretical curves for THz and SH emission from InAs. 88

6.1 SEM micrograph of porous InP (111). 94

6.2 Set-up for measuring THz emission from bulk and porous InP. 95

6.3 THz signals from bulk and porous InP (111). 96

6.4 Excitation fluence dependence of THz from bulk and porous InP (111). 98

6.5 Crystal orientation dependence of THz from bulk and porous InP (111). 99

6.6 SEM micrograph of porous InP (100). 101

6.7 Crystal orientation dependence of p-polarized THz from bulk and porous InP (100). 102

6.8 Crystal orientation dependence of p- and s-polarized THz from porous InP (100). 103

6.9 Crystal orientation dependence of s-polarized THz from bulk and porous InP (100). 104

6.10 Crystal orientation dependence of p-polarized SH emission from bulk and porous InP (100). 106

6.11 Crystal orientation dependence of s-polarized SH emission from bulk and porous InP (100). 107

7.1 Schematic diagram of the semi-large aperture photoconductive switch. . 112

7.2 Set-up for using the semi-large aperture photoconductive switch. 113

7.3 Dependence of THz emission from the SLAPCS on applied bias field. . 119

7.4 Dependence of THz emission from the SLAPCS on excitation fluence. . 120

7.5 Noise definition for a typical THz waveform measured from the SLAPCS. 121

7.6 Frequency resolved noise measurements made on the SLAPCS. 122

7.7 THz waveform with amplitude in V/cm from the SLAPCS. 123

8.1 Time-domain birefringence of oak. 125

8.2 Frequency resolved index of refraction and absorption measured in the THz range for oak wood. 135

8.3 Time domain THz signals measured in transmission through spruce wood. 136

8.4 Time-domain birefringence observation in THz transmission through spruce. 137

8.5 Frequency resolved index of refraction and absorption measured in the THz range for spruce wood. 138

8.6 Schematic diagram of the grain orientation in spruce. 139

8.7 THz polarization characteristics in transmission through spruce at 320 GHz. 140

8.8 THz polarization characteristics in transmission through spruce at 356 GHz. 141

8.9 THz polarization characteristics in transmission through spruce at 391 GHz. 142

8.10 THz polarization characteristics in transmission through spruce at 711 GHz. 143

8.11 Schematic defining the operating point for time-domain birefringence measurement. 144

8.12 Time-domain measurement of birefringence of lens paper. 145

8.13 Observation of time-delay due to birefringence in lens paper. 146

8.14 Frequency resolved index of refraction measured by THz transmission through lens paper. 147

8.15 Optical image of douglas fir. 148

8.16 Linear THz transmission map of douglas fir. 148

8.17 Optical and THz image of douglas fir. 149

Definitions

Symbols

A	Area
α	Power absorption coefficient
c	Speed of light in vacuum
d_{ij}	Succeptibility tensor element in contracted notation
∂_{ij}	Effective second-order susceptibility tensor element
E	Electric field
e	Electronic charge
ϵ	Dielectric permittivity
F	Fluence, Flux
g	Conductance
Γ	Phase retardance
$H(\omega)$	Frequency-dependent transfer function
h	Planck's constant
I	Current, Optical intensity
k	Imaginary part of the complex index of refraction
L	Thickness

λ_i	Eigenvalues
λ	Wavelength
M_{rot}	Jones matrix for rotation
M_Γ	Jones matrix for phase retardance
μ	Mobility
n_o	Ordinary index of refraction
n_e	Extraordinary index of refraction
n	Index of refraction
$\hat{n}$	Complex index of refraction
$n(t)$	Carrier density
η_{ij}	Impermeability tensor element
η_0	Impedance of free-space
η	Conversion efficiency
P	Power
$\mathbf{P}$	Polarization
ϕ,Ψ,θ	Angle
Q	Charge
q	Charge
R	Power reflectivity

R_{ij}	Rotation transformation matrix element
r_{ij}	Linear electro-optic tensor element
r_{eff}	Effective linear electro-optic coefficient
σ_s	Surface conductivity
T_i	Far-infrared Fresnel transmission coefficient
t_i	Optical Fresnel transmission coefficient
τ_R	Carrier recombination time
ν	Frequency (Hz)
v	Velocity
W	Energy
Ω	Frequency (rad / s)
ω	Frequency (rad / s)
χ	Susceptibility

Abbreviations, Acronyms

THz	Terahertz
LAPCS	Large-aperture photoconductive switch
SLAPCS	Semi-large aperture photoconductive switch
OR	Optical rectification

SH	Second Harmonic
SHG	Second-harmonic generation
lhs	left hand side

Chapter 1

Introduction

The terahertz portion of the electromagnetic spectrum is roughly defined as the frequency range from 100 GHz to 10 THz. At 1 THz (single oscillation period of 1 ps), the free-space wavelength of the radiation is 300 μm, corresponding to a photon energy of 4.1 meV or a temperature of 48^o K. In this chapter, the motivation for studying the generation and detection of pulsed terahertz radiation will be given, and the details of the outline for the thesis presented.

1.1 Context of terahertz radiation in this thesis

The terahertz portion of the electromagnetic spectrum has been accessible for some time by various means including molecular gas lasers, gyrotrons and free-electron lasers [1]. Due to complexity, cost and limited frequencies of operation, these sources have traditionally made it difficult to gain full access to the terahertz frequency range.

Microwave electronics have traditionally been able to access the lower frequency range of the THz spectrum, however, driving electronic emission of electromagnetic radiation beyond 100 GHz is technologically challenging. Similarly, optical methods for generating electromagnetic radiation have generated sources of radiation extending to the mid-infrared, proving more difficult to generate coherent sources in the terahertz range.

It has only been in the last 20 years that a significant breakthrough in the generation technology for terahertz radiation has occurred [2]. Since this time, a number of reviews characterizing systems capable of generating free-space radiation in this frequency range have appeared [3, 4].

As the technology for accessing this portion of the electromagnetic spectrum is so new, there are new application areas appearing frequently in the literature. This is a very good time to be involved with research in this area, as it offers the opportunity to examine unexplored application areas for the technology. The next section examines some of the application areas that exist today.

1.2 Applications

While there are many application areas being explored, the two main areas receiving the greatest attention in the last few years are imaging and spectroscopy.

The generation of pulsed terahertz radiation together with coherent detection allows many different imaging techniques to be applied. Simple absorption of the far-infrared energy can be used to map out materials such as IC's or to use the strong absorption of water to map out water concentration such as in a leaf [5]. The imaging mode employed in Ref. [5] was a point-by-point scanning method, which has been further developed [6]. Since this time, other imaging modalities have been developed, including computed tomography [7], impulse ranging [8] multi-static reflection imaging [9] and two-dimensional electro-optic imaging [10]. Methods for terahertz imaging based on mixing of optical wavelengths in photoconductors to generate terahertz radiation without femtosecond lasers, and subsequent electro-optic detection have also been studied [11].

The interest in imaging with far-infrared radiation stems from the long wavelengths (compared to optical wavelengths) that mitigate scattering in many media, whereas at the same time having short wavelengths (compared to microwave frequencies) allows for reasonable spatial resolution. In addition, many materials are transparent at far-infrared frequencies. For example, regular clothing is transparent at terahertz frequencies [12], opening up many application areas for security. It has also been shown that to some degree sand is transparent, opening up applications to land-mine detection [13].

In addition to security applications, much attention is being paid to possible biomedical applications of terahertz-pulse imaging , with demonstrations of, for example, imaging of basal cell carcinoma [14] and dental tissue analysis [15].

A number of the imaging techniques rely on the absorption of far-infrared radiation by water. In fact, even small amounts of atmospheric water vapor can attenuate far-infrared in the pulsed terahertz experiments [16], which limit potential communications applications of terahertz radiation to short-haul terrestrial communications.

The strong absorption of terahertz radiation by water has successfully been measured in a terahertz time-domain spectroscopy system in reflection mode [17], demonstrating the robust capabilities of terahertz time-domain spectroscopy. One might be tempted to assume that thermal background radiation may be a problem in terahertz time-domain spectroscopy; however, the coherent time-gated nature of the detection virtually removes any thermal background, allowing for such impressive measurements as the water absorption lines in a flame [18].

Such a high sensitivity to water has also been exploited to generate extremely sensitive monitors of water, sensitive to nanometer water layers [19], and even to sub-monolayer water adsorption [20].

Spectroscopy in the far-infrared is of interest to researchers as many molecules have rotational energies in the terahertz frequency range. Examples of applications that use rotational energies of molecules is that of gas sensing using terahertz time-domain spectroscopy [21].

It has also been shown that many biologically important molecules, such as retinal [22] and DNA [23] have activity in the terahertz frequency range. For these larger molecules, the far-infrared activity has been attributed to torsional modes in the molecules [22]. Other examples of spectro-chemical applications of terahertz radiation include illicit-drug detection [24].

Spectroscopy using terahertz radiation is a powerful technique, since it offers access to a large frequency range, and with coherent detection can give access to the full complex dielectric function of the material. This has been used for spectroscopy on semiconductors [25], and more recently, to gain insight into the nature of conductivity by time-resolved measurements in low-temperature GaAs [26], organic semiconductors [27], and solvated electrons [28] using optical pump - terahertz probe techniques.

Aside from the unique spectral properties of terahertz radiation that contribute to the increasing application areas, one important feature is of critical importance. Many materials are transparent to terahertz radiation, offering application areas in quality control [21] and security [29]. For most of these applications, the terahertz technology would be in direct competition with x-ray imaging techniques. The advantage that terahertz systems offer is non-ionizing radiation that is not a significant safety hazard. The electromagnetic levels radiated from the standard terahertz-pulse imaging systems are orders of magnitude below what might be harmful to people [30].

As the application areas for terahertz technology grow, a greater demand for efficient emitters and detectors is being recognized. In the next section, some of the standard techniques for generating pulsed terahertz radiation for terahertz-pulse imaging are discussed.

1.3 Generation of terahertz radiation

The three methods traditionally used to generate pulsed THz radiation are: (i) Transient current generation at semiconductor surfaces [31], (ii) emission from a photoconductive switch [2], and (iii) nonlinear optical interactions [32, 33].

The generation of terahertz radiation from semiconductor surfaces has attracted much attention since initial reports of high conversion efficiencies, using InAs in a magnetic field [34]. Since this time, InAs surface emission has proven to be a relatively bright source of pulsed THz radiation, especially under the influence of an external magnetic field [35, 36, 37, 38]. As one of the more efficient emitters of terahertz radiation, it is of practical interest to examine the limitations of emission from InAs emitters.

Aside from the practical significance of terahertz emission from InAs surfaces, the emission is especially interesting due to the complex nature of the radiation. This results from multiple competing mechanisms that lead to the radiation. Contributions from photo-carrier acceleration in the depletion field [31, 39], photo-carrier diffusion [40], and optical rectification [41, 42, 43] have all been reported. The relative magnitudes of radiation resulting from the various processes is strongly dependent on excitation fluence

[44]. In order to fully understand the limitations on the generation of THz radiation, it is important to clearly differentiate all of the mechanisms leading to the emission, and understand how the emission scales with optical excitation energy.

The main generation mechanisms that have been reported to contribute to terahertz emission from semiconductor surfaces will be briefly reviewed at this point, in order to demonstrate the various dependencies on crystallographic orientation and pump polarization.

1.3.1 Photo-carrier related emission mechanisms

When a femtosecond optical beam strikes a semiconductor surface with photon energies greater than the band-gap, electron-hole pairs are generated on the time-scale of the optical excitation pulse. This situation may then lead to a transient current, $J(t)$, as shown schematically in Fig. 1.1.

The transient current may result from the diffusion of carriers away from the surface after excitation due to differences in mobilities for electrons and holes (photo-Dember effect) as shown in Fig. 1.1 (a) [40]. In addition, a transient current may develop as a result of the photo-generated carriers being accelerated by the surface electric-field as shown in Fig. 1.1 (b) [31]. In either case, the transient current develops in a region given by the optical absorption depth of the incident radiation, which for most materials is on the order of 1 μm or less. The time-varying current will then lead to radiation in the terahertz frequency range as:

$$E_{THz}^{rad} \propto \frac{\partial J(t)}{\partial t} \tag{1.1}$$

where J is the transient current density. The free-space wavelength at 1 THz is 300 μm, and therefore, the emission of electromagnetic radiation in this frequency range, originating from a transient current with dimensions on the order of 1 μm may be considered as dipole radiation.

For dipole radiation, with the dipole oriented perpendicular to a dielectric-air interface (as is the present case), it can be shown that the polarization of the radiation is always in the plane of incidence (p-polarized) [45]. That is, there will be no s-polarized terahertz emission from such a source.

In addition, the transient current only depends on the injection of electron-hole pairs within the optical absorption depth, and therefore does not depend on crystallographic orientation. Moreover, the dependence on pump polarization comes only through Fresnel coupling of the pump beam.

These points can be summarized as follows for the terahertz emission from photo-carrier related effects:

- THz polarization: p-polarized emission only.
- Dependence on crystallographic orientation: None.

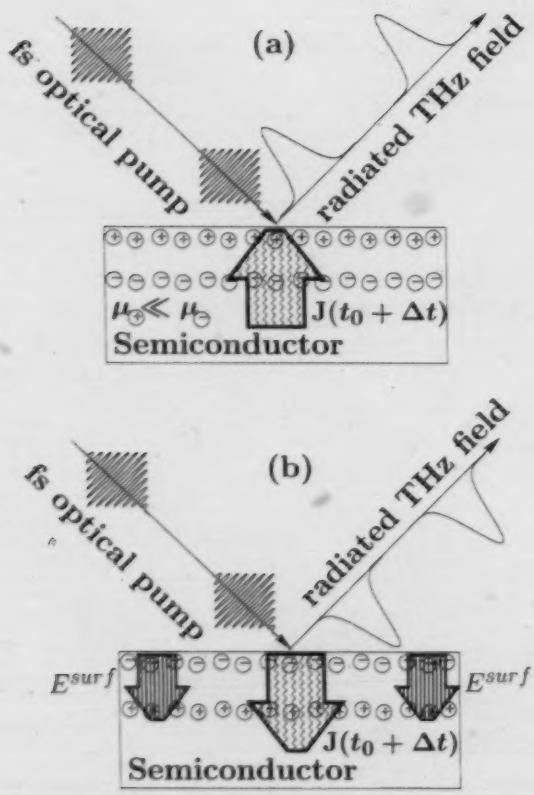

Figure 1.1: When a femtosecond optical beam strikes a semiconductor surface, with photon energies greater than the band-gap, electron-hole pairs are produced. This can lead to a transient current as a consequence of the difference in mobilities of electrons and holes resulting in a diffusion current (a), or by the acceleration of carriers in the surface electric-field (b).

- Dependence on pump polarization: Weak - comes through the varying Fresnel reflection of the pump beam. file:///usr/share/doc/mozilla-browser/localstart.html

These points will be used extensively later in the thesis in order to distinguish the photo-carrier related contributions to the radiated terahertz field from semiconductor surfaces.

1.3.2 Bulk optical rectification

When an intense optical beam interacts with a non-centrosymmetric material, a second-order nonlinear polarization of the material results. In general, this can lead to the second-order processes of optical rectification and optical second-harmonic generation.

It has been known for a long time, that emission of radiation in the far-infrared can result from optical rectification of an optical pulse [46]. In addition to this, optical rectification from crystal surfaces as a result of bulk optical rectification within the optical absorption depth can contribute significantly to the radiated terahertz field from semiconductor surfaces [43].

The process is shown schematically in Fig. 1.2. An optical pump beam excites a time-dependent polarization of the lattice within the optical absorption depth of the pump beam. This time-dependent polarization tracks the intensity profile of the optical excitation beam, and radiates a far-infrared wave with terahertz frequency components:

$$E_{THz}^{rad} \propto \frac{\partial^2 P(t)}{\partial t^2} \tag{1.2}$$

where P(t) is the polarization of the crystal which is given by:

$$P \propto \chi^{(2)}(0; -\omega, \omega) E_{opt}(-\omega) E_{opt}(\omega) \tag{1.3}$$

where E_{opt} is the optical excitation field and $\chi^{(2)}$ is the second-order nonlinear response of the material.

The polarization of the crystal depends on the orientation of the optical pump fields with respect to the crystallographic axes, and the specific symmetry of the nonlinear crystal. Thus, in general, the radiated terahertz field depends strongly on the orientation of the crystal, as well as the polarization of the pump field. In addition, it is possible to generate various output polarizations of the radiated terahertz field.

This can be summarized as follows:

- THz polarization: Both s- and p-polarized emission as well as combinations thereof can be generated.
- Dependence on crystallographic orientation: Strong dependence which is dictated by the symmetry class of the nonlinear medium.

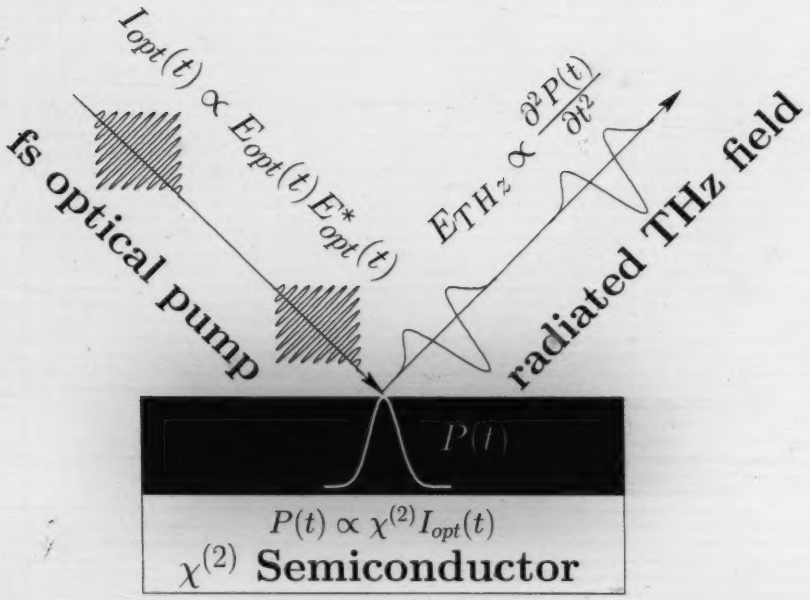

Figure 1.2: When a femtosecond optical beam strikes a semiconductor surface, bulk optical rectification can contribute to the radiated terahertz field. A time-dependent polarization of the lattice results within the optical absorption depth of the optical pump beam, acting as a source term in Maxwell's equations and radiating a terahertz wave.

- Dependence on pump polarization: Strong dependence which is dictated by the symmetry class of the nonlinear medium.

The exact dependencies of the terahertz radiation on crystallographic orientation and on pump polarization are calculated later in the thesis for the case of crystals with $\bar{4}3m$ symmetry, such as InAs. These dependencies will be used to identify contributions to the radiated terahertz field from bulk optical rectification when exciting semiconductor surfaces.

1.3.3 Surface electric-field induced optical rectification

When an intense optical beam interacts with an arbitrary material, a nonlinear polarization of the material results as a result of the third-order nonlinear response.

In a material which has an applied electric field, the third-order nonlinear response, in combination with the applied DC field can result in an effective second-order nonlinear response which can lead to electric-field induced optical rectification or second-harmonic generation [47, 41].

For the case where a semiconductor is excited by an intense optical pulse, and the semiconductor has an intrinsic surface electric-field, then this effective second order polarization of the lattice can be written as:

$$P = \chi^{(3)}(0; -\omega, \omega, 0) E_{opt}(-\omega) E_{opt}(\omega) E_{surf}(0) \tag{1.4}$$

where E_{opt} is the optical excitation field, $\chi^{(3)}$ is the third-order nonlinear response of the medium, and E_{surf} is the surface electric field as shown schematically in Fig. 1.3

The time-dependent polarization, P(t), tracks the intensity profile of the excitation pulse and radiates a far-infrared wave as:

$$E_{THz}^{rad} \propto \frac{\partial^2 P(t)}{\partial t^2} \tag{1.5}$$

The polarization of the crystal depends on the orientation of the optical pump field with respect to the crystallographic axes, and the specific symmetry of the nonlinear crystal. In general, the terahertz field depends strongly on the orientation of the crystal, as well as the polarization of the pump field. In addition, it is possible to generate various output polarizations of the radiated terahertz field.

This can be summarized as follows:

- THz polarization: Both s- and p-polarized emission as well as combinations thereof can be generated.
- Dependence on crystallographic orientation: Strong dependence which is dictated by the symmetry class of the nonlinear medium.

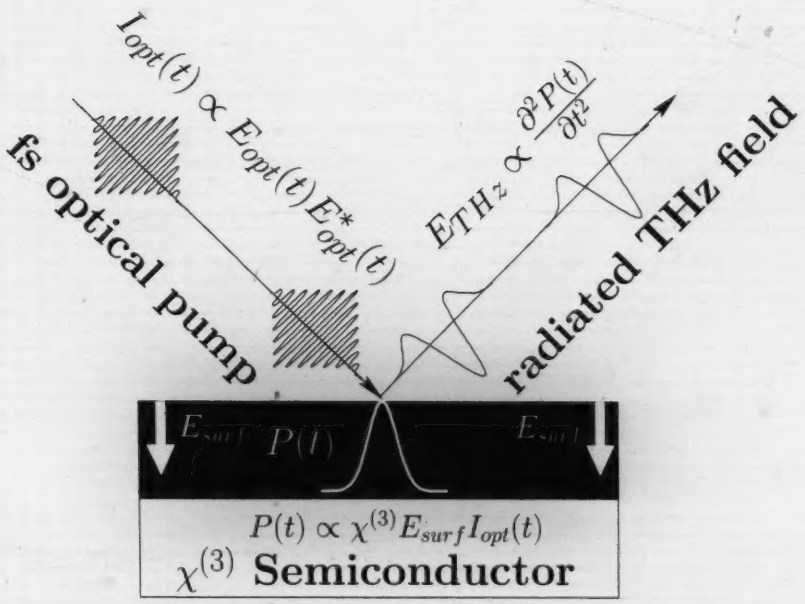

Figure 1.3: When a femtosecond optical beam strikes a semiconductor surface, at which there exists an intrinsic surface electric-field, then an effective second-order polarization of the lattice results from the third-order nonlinear response of the material within the optical absorption depth of the excitation beam.

- Dependence on pump polarization: Strong dependence which is dictated by the symmetry class of the nonlinear medium.

The exact dependencies of the terahertz radiation on crystallographic orientation and on pump polarization are calculated later in the thesis for the case of crystals with $\bar{4}3m$ symmetry, such as InAs. These dependencies will be used to identify contributions to the radiated terahertz field from electric field induced optical rectification.

1.4 Thesis statement

This thesis examines the detailed generation mechanisms and efficiency of terahertz radiation from InAs surfaces at high optical excitation densities in order to find ways of improving the conversion of optical to far-infrared energy. As terahertz technology is in its infancy, there are many potential applications of this portion of the electromagnetic spectrum which have yet to be studied in detail. This thesis will also examine one possible branch of industrial applications for pulsed terahertz radiation which is the use of pulsed terahertz radiation for examining wood and wood-related products. This is an exciting technology for wood-related products, as it provides access to the upper frequency range (below X-rays) for which wood is transparent.

1.5 Layout of the thesis

Chapter 2 examines the experimental set-up used in the generation and detection of pulsed terahertz radiation. In chapter 3, a detailed description of the electro-optic detector is given, where it is found that the electro-optic crystal can be used as a polarization analyzer, which is used extensively throughout the remainder of the thesis.

In chapter 4 the thesis extends the work on terahertz emission from InAs surfaces to high optical excitation fluences. For the first time, a quantitative estimate of the maximum conversion efficiency from InAs surfaces (without an applied magnetic field) will be obtained, and a comparison to the standard high efficiency terahertz pulse energy emitter, the large-aperture photoconductive switch, carried out, resulting in the conclusion that the large-aperture photoconductive switch is a superior emitter of far-infrared energy.

In chapter 5, a detailed analysis of the terahertz emission characteristics from InAs surfaces at high excitation densities is carried out, where the emission is found to be inconsistent with carrier-related effects, which were the previously reported emission mechanisms from InAs surfaces. The emission characteristics are then shown to match both a pure surface nonlinear optical response and that of an electric-field induced nonlinear optical response. Further experiments reveal that the most likely mechanism responsible for the emission of terahertz radiation at high excitation densities is that of surface electric-field induced optical rectification.

In chapter 6, given that a nonlinear optical response dominates the terahertz emission from InAs surfaces at high excitation densities, a method based on structuring the surface is investigated to increase the radiated conversion efficiency from InAs surfaces. The method is demonstrated to generate more terahertz power from InP. Second-harmonic generation and terahertz emission are both investigated from the engineered InP samples, giving evidence that the conversion efficiency from InAs may be enhanced in a similar way.

In chapter 7, the fact that photoconductive terahertz emitters have proven to be the most efficient at converting optical to far-infrared energy is used to construct a system for spectroscopic investigation. The system is characterized and described in detail. This system is then used to investigate potential industrial applications involving wood and wood products as reported in chapter 8. Here it is demonstrated for the first time that wood is birefringent under excitation from freely propagating radiation in the far-infrared. The industrial applications of this phenomenon should be important in quality control of a variety of wood products.

Chapter 2

Description of the experimental set-up used for the generation and detection of THz radiation

In this chapter the details of the experimental set-up used in this thesis will be outlined. The details of the electronics and optics used will be outlined, followed by a brief discussion of the detector used. A brief summary of the various emitters used throughout the thesis will also be given.

2.1 General description and overview

There are two laser sources used as femtosecond optical pump sources in generating terahertz radiation in this thesis. One is a Ti:Sapphire oscillator with an optical pulse width of 80 fs, a repetition rate of 82 MHz, operating at 800 nm with an output power of up to 0.8 W (Spectra Physics MaiTai). The other is a regeneratively amplified Ti:Sapphire laser system with an optical pulse width of 120 fs (Gaussian FWHM), a repetition rate of up to 1 kHz, operating at 800 nm with an output power of up to 0.75 W.

The output from one of these two laser sources, depending on the emitter that was being examined, is taken to the terahertz set-up which is shown schematically in Fig. 2.1.

The pump beam is split into pump (92 %) and probe (4 %) beams using a wedged window. The probe beam is passed through an optical delay line, allowing an absolute time-delay between the probe pulses and the THz pulses at the detector. The probe beam is focused onto the ZnTe crystal after passing through a small hole drilled through the focal axis of the parabolic mirror. The probe beam is linearly polarized (horizontally) at the ZnTe detector, where a birefringence is induced on the probe as a consequence of the application of the THz field. This polarization modulation is then analyzed using

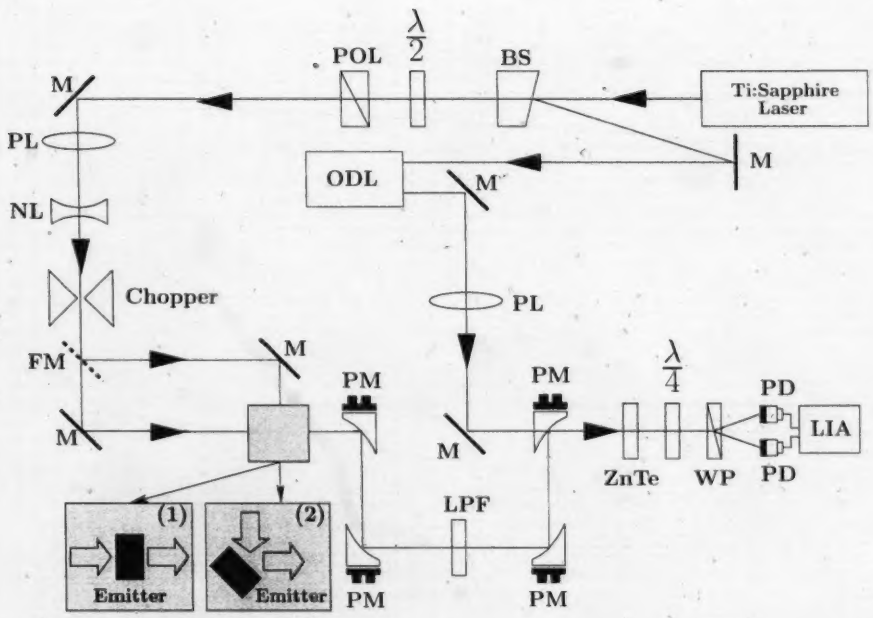

Figure 2.1: Schematic diagram of the set-up used in the thesis. BS is a beam splitter; $\frac{\lambda}{2}$ is a half-wave plate; POL is a polarizer; M is a mirror; FM is a flip-mirror; ODL is an optical delay line; PL is a positive lens; NL is a negative lens; PM is a parabolic mirror; LPF is a low-pass filter blocking the optical leakage and passing the far-infrared radiation; $\frac{\lambda}{4}$ is a quarter-wave plate; WP is Wollaston prism; PD are photo-diodes; LIA is a lock-in-amplifier. The emitters of terahertz radiation are either used in a transmission geometry (1) or a reflection geometry (2). Various emitters are used in the thesis.

a polarization bridge. The linear polarization of the probe beam is converted to a circular polarization using a quarter-wave plate, which is used to balance the detection under no applied THz field. The polarization state is analyzed differentially using a Wollaston prism to separate the two orthogonal polarization components, which are detected by a pair of photodiodes. The photo-diode signal is balanced using the quarter-wave plate. The differential photo-diode signal is detected using a lock-in amplifier, where the reference frequency comes from the optical chopping frequency of the pump beam. For the case when the emitter is a photoconductive switch, no chopping of the optical beam is used, and instead the reference signal is derived from the alternating bias applied to the emitter.

The pump beam is passed through a half-wave plate and polarizer combination, which acts as a variable attenuator, allowing the optical pump fluence at the emitter to be adjusted. The pump beam is then telescoped to an appropriate diameter for the desired fluence range by using a pair of lenses as shown in Fig. 2.1. If a reference frequency is required, the beam is optically chopped using a mechanical chopper wheel. The chopper typically operates at a frequency of approximately 330 Hz when the 1 kHz amplified optical source is being used, and 2 kHz when the oscillator source is being used. Depending on the emitter being used, either a transmission or reflection generation geometry is chosen by use of a flip mirror as shown in Fig. 2.1. The emitted THz radiation is then collected using four off-axis parabolic mirrors, forming an image of the THz radiation at the emitter on the ZnTe crystal.

The THz field is mapped in time by varying the delay between the optical probe beam and the THz field using the optical-delay line. The electro-optic detection used here is a coherent detection scheme, allowing both amplitude and phase of the THz fields to be recorded.

2.2 Electronic and Electro-optic Components

The electronic and electro-optic components used in the THz set-up are a crucial part of the experiments. As such, a brief overview of the electronics and devices used in the set-up described in section 2.1 is given here. There are three main components that will be discussed here. These are the large-area photodiodes used to differentially detect the probe polarization modulation, the computer scanned optical delay line used to map out the THz field, and the lock-in amplifier used to collect the THz waveforms with good signal-to-noise ratios.

The photodiodes that were used were ultra low-noise, large aperture photodiodes (Advanced Photonix). These diodes were chosen for two reasons. First, the dark current and noise-equivalent power ($3.8 \times 10^{-14} W Hz^{-1/2}$) put them well below the noise floor of the detection system, and therefore will not contribute to the noise. Secondly, the large area of the photodiode elements ($20\ mm^2$) removes any significant noise that may result due to pointing instability in the laser source.

The optical delay line was constructed from a high-grade, 1" aperture, gold-coated corner cube retro-reflector (PLX Inc.) mounted on a translation stage (PI stage). The translation stage has a maximum linear displacement of 15 mm, corresponding to 100 ps of probe delay. In addition to this, it has a placement repeatability of better than 0.5 μm (3.3 fs in time).

The lock-in amplifier was a model 7265 DSP lock-in amplifier (Perkin-Elmer), with dual input channels, where the differential photo-diode signal was detected directly in the lock-in amplifier. The lock-in amplifier was operated with an output filter setting of 24 dB / octave, yielding an equivalent noise bandwidth of 6 Hz for a lock-in time constant of 20 ms, and operates at reference frequencies up to 250 kHz.

Data acquisition from the photo-diodes, lock-in amplifier, and digital control of the lock-in amplifier and optical delay line was automated using LabVIEW [1] installed on a lap-top computer. To accommodate multiple serial devices, USB-to-RS-232 adapters along with a USB hub were used.

2.3 Optics

Various optical components were used to guide the optical excitation and optical probe beams. These include mirrors, polarizers, lenses and waveplates. The mirrors used were dielectric mirrors for 45^o or 0^o high reflectivity use. The lenses were BK7 glass optics, some of which were anti-reflection coated for 800 nm (for focal lengths less than or equal to 25 cm). The polarizers used in the optical pump or optical probe beam lines were broadband Glan-Taylor calcite polarizers with a 1 cm aperture (Coherent Inc.). In addition, one Wollaston prism is used to separate orthogonal polarization components on the probe beam, which is a broadband, calcite polarizer with a 15^o angular separation of the orthogonal polarization components (CASIX). The waveplates used were zero-order waveplates (CVI Laser Optics) constructed from quartz. For the terahertz beam, broadband off-axis parabolic mirrors were used to collimate and focus the radiation in order to minimize chromatic aberration. The parabolic mirrors were F/2, with a diameter of 2 inches and coated with gold (Janos Tech. Inc.).

2.4 Terahertz detector

A 1mm thick, (110)-oriented ZnTe crystal (eV Products Inc.) was used as an electro-optic detector for the terahertz radiation [48]. This detection scheme is outlined in detail in chapter 3. Briefly, an optical probe beam is passed co-linearly with a terahertz field inside of the ZnTe crystal. The terahertz field acts as a bias field for the linear electro-optic effect (Pockels effect), which induces a polarization modulation on the

[1] LabVIEW is a commercial data-acquisition software package available through National Instruments Inc.

probe beam. The polarization modulation is measured using a Wollaston prism and a pair of photo-diodes to monitor the differential polarization signal, which is balanced in the absence of a terahertz field. The differential photo-diode signal is measured with a lock-in amplifier, and the terahertz signal is mapped out in time by varying the probe delay with respect to the terahertz pulse.

2.5 Terahertz emitters

In total, 5 different terahertz emitters are examined at various levels of detail in this thesis. These are: surface emission from InAs, InP and porous InP, as well as terahertz emission from a large-aperture photoconductive switch and a semi-large aperture photoconductive switch.

Chapter 3

Electro-optic detection of terahertz radiation

This chapter will discuss electro-optic detection of THz radiation. It will begin with an overview of the detectors that can be used for detecting radiation in the THz frequency range, and the reasons for adopting electro-optic detection using ZnTe will be outlined. A calculation of the electro-optic response of the ZnTe crystal will be given. The results will be shown to agree with those published by Planken et al. [49]. The calculations are repeated here to emphasize the importance of the crystallographic orientation of the ZnTe electro-optic crystal. Specifically, it will be demonstrated that the ZnTe crystal itself can be used as an analyzer, to detect either vertically or horizontally polarized THz radiation. This is used extensively throughout the remainder of the thesis. This is an important point, which has not previously been highlighted. Finally, the calibration procedure implemented to extract the magnitude of the linear electro-optic coefficient of ZnTe will be outlined, and the results compared to literature values.

3.1 Detection of pulsed terahertz radiation

There are a number of methods used to detect far-infrared radiation. Thermal detection as well as coherent detection using electro-optic crystals and photoconductors can be used for detecting pulsed terahertz radiation. The linear electro-optic effect will be discussed in detail in this chapter. The use of ZnTe electro-optic detection will be compared to other possible detectors.

3.1.1 Background

Traditionally, radiation in the near-infrared through the visible wavelength range at higher frequencies can be detected with great sensitivity. In fact, many devices are sensitive to radiation at the photon level in these wavelength regions. Examples of such devices are

photo-multipliers, photoconductors and photodiodes. These devices essentially operate on the same principle: a photon has sufficient energy to generate a free electron or charge-carrier pair which is detected electronically. These methods work sufficiently well when the photon energies of the radiation to be detected are large enough to generate the charge carriers. All of these detectors suffer from a lower cut-off frequency that cannot be avoided, and results from the intrinsic limitation on liberating the charge carriers.

The photon energy at 1 THz is about 4 meV, making it very difficult to employ the standard techniques for photon detection listed above for higher frequencies. At the same time, very sensitive detection of electromagnetic radiation can be achieved for very long wavelengths by electronic means. For example, the detection of radio waves using antennas can be very efficient. However, it becomes more and more difficult to operate antennas, as well as the corresponding electronics, at higher and higher frequencies. It therefore requires somewhat unique technology for detecting radiation in the THz frequency range, lying between the well developed detection technology for the visible and the well developed detection technology for the microwave portion of the electromagnetic spectrum.

There are basically two types of detection that one would consider - direct detection and coherent detection of THz radiation. Direct detection would likely be considered when a coherent source of THz radiation is not available, or when the source is a narrow frequency source at moderate power. Examples of direct detection would be thermal detectors such as pyroelectric or bolometric detectors. For higher sensitivity, a nonlinear detector such as a Schottky barrier diode or hot electron bolometer can be used in a heterodyne configuration. For a comparison of the noise performance of the various devices in heterodyne detection of THz radiation see, for example, Gerecht et. al. [50]. For the case of coherent detection, the two primary methods are photoconduction and electro-optic detection [48].

3.1.2 Thermal detection

Traditionally, spectroscopy in the far-infrared has been accomplished using Fourier-transform infrared spectroscopy (FTIR spectroscopy). A detailed comparison of FTIR and terahertz time-domain spectroscopy using electro-optic detection has been carried out by Han. et al. [51].

The detector used in FTIR applications is usually a thermal detector, either a bolometer or pyroelectric detector. The source used is traditionally an incoherent source using, for example, a mercury arc-lamp.

In contrast to this, time-domain spectroscopy using electro-optic detection employs a pulsed source of coherent far-infrared radiation, and the electro-optic detection is coherent and time-gated. The coherent nature of the source and detection allows exceptional noise performance.

A figure of merit for the detection system is the noise-equivalent power (NEP), which

can be as good as $10^{-16}WHz^{-1/2}$ for the electro-optic detection [51]. Typical values for the NEP of liquid helium cooled bolometers are in the range of $10^{-12}WHz^{-1/2}$, and for pyroelectric detectors, they are in the range of $10^{-8} - 10^{-10}WHz^{-1/2}$. It should be pointed out that, primarily due to group-velocity mismatch in the electro-optic detection, the thermal detectors performance is superior to electro-optic detection above approximately 3THz [51]. However, for the purposes of the present investigations, we are concerned primarily with frequencies in the range of 0.1-2 THz.

It is primarily due to the limitations of the thermal detection that electro-optic detection was employed in the work presented in this thesis. As the terahertz radiation was being generated with a coherent, pulsed optical laser source, the main components required for coherent electro-optic detection were present. Using a thermal detector would lead to a poorer signal-to-noise ratio in the measurements. Moreover, thermal detectors have an essentially flat frequency response in the far-infrared, causing problems with background incoherent radiation at high temperatures.

Another method for detecting pulsed terahertz radiation, in a coherent manner, is by using a photoconductive switch as a detector. Therefore, the choice of coherent THz detectors is between a photoconductive and electro-optic detector.

3.1.3 photoconductive switch and electro-optic sampling

A nice description of free-space electro-optic sampling (FS-EOS) and photoconductive sampling (PCS) is given in the review article by Dragoman [48]. In addition, detailed comparisons of the two methods for coherent detection of THz radiation have been published [52, 53].

PCS and FS-EOS are shown schematically in Fig. 3.1. In photoconductive sampling, the THz field acts as a bias, driving a current which, in turn, is gated by the probe pulse which momentarily reduces the resistivity of the switch. The probe is varied in time with respect to the terahertz pulse and generates a photocurrent that is proportional to the applied THz field.

As the probe strikes the PCS, a total charge, Q, is generated. The charge is dependent on the gating time, τ, and is given by [52]:

$$Q(\tau) = \int dt v(t) g(t - \tau) \tag{3.1}$$

where the induced bias voltage, $v(t)$, generated across the PCS depends on the applied THz field, $E(\omega)$, and the antenna response function, $H(\omega)$, as:

$$v(t) \sim \int d\omega H(\omega) E(\omega) e^{i\omega t} \tag{3.2}$$

and the time-dependent conductance, g(t), depends on the probe intensity profile in time, I(t), and the photo-current rise and recovery times of the substrate, τ_C and τ_R, respectively:

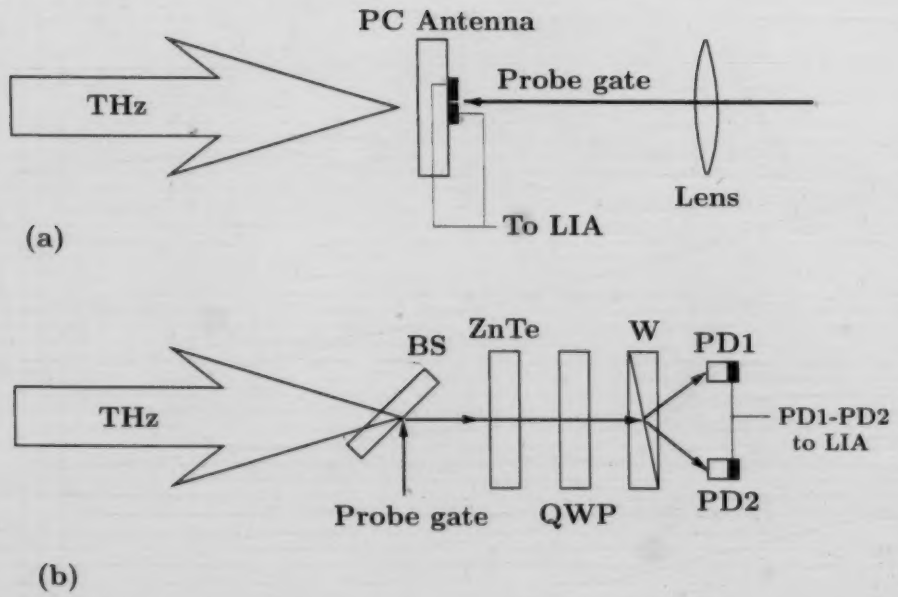

Figure 3.1: Schematic diagram of PCS (a) and FS-EOS (b) methods for detection of THz radiation. LIA is a lock-in amplifier; BS is a beam-splitter; W is a Wollaston prism; PD1 and PD2 are photodiodes; QWP is a quarter-wave plate.

$$g(t) = \int^{t} dt' I(t') \left(1 - e^{-\frac{t-t'}{\tau_C}}\right) e^{-\frac{t-t'}{\tau_R}} \tag{3.3}$$

In general, the antenna response function is frequency-dependent, and depends on the coupling of the THz field into the antenna, as well as the impedance matching conditions of the antenna to the transmission line [52].

For the simple case where proper impedance matching is achieved, no external coupling lens is used for the THz radiation, and $H(\omega) = 1$, the total charge generated by a probe pulse is given by the convolution of the time-dependent substrate conductance, g(t), and the THz field, $E(t)$, with $E(t)$ replacing $v(t)$ in Eq. 3.1. In this case, the detected waveform only recreates a true picture of the THz field when the probe pulsewidth, current rise-time and carrier recombination times are all significantly less than the THz pulsewidth ($\sim 300fs$). For short-pulse lasers, the probe pulse is usually significantly less than this ($\leq 100fs$), so it is the material response function that limits the re-creation of the THz field accurately. Therefore, it is necessary to construct a PCS on a substrate with a fast recombination time, such as low temperature (LT) GaAs [52].

In contrast to this, the linear electro-optic response of a material is virtually instantaneous, so that special preparation of the detector is not required. FS-EOS is achieved by co-propagation of the THz pulse with a time-gated probe pulse, within an electro-optic crystal such as ZnTe [48]. The THz field acts as a bias for the Pockel's effect within the electro-optic crystal, inducing a phase retardance [48]:

$$\Delta\phi(\tau) = \frac{\omega n_o^3 r_{41}}{c} E_{THz}(\tau) dz \tag{3.4}$$

where n_o is the index of refraction, ω is the optical probe frequency, c is the speed of light in vacuum and r_{41} is the linear electro-optic coefficient of ZnTe, all of which are constant for a fixed probe wavelength. The induced phase-retardance, $\Delta\phi(\tau)$, is measured by analyzing the polarization of the probe in a balanced geometry, using a $\lambda/4$ plate to balance the differential photo-diode signal from a Wollaston prism, and monitoring the differential photo-diode signal as a function of the probe delay τ. In the absence of group-velocity dispersion, integrating Eq. 3.4 gives the reconstructed THz field from the measurement of the induced phase retardance as [48]:

$$E_{THz}(\tau) = \frac{\Delta\phi(\tau)}{L \times C_{ZnTe}} \tag{3.5}$$

where L is the length of the electro-optic crystal and C_{ZnTe} is the combination of the constants in Eq. 3.4. Therefore, in the absence of group-velocity dispersion, and for a probe pulsewidth significantly shorter than the THz pulsewidth, the measured signal is directly proportional to the THz field.

It is true that electro-optic detection in ZnTe, in general, will produce a more reliable recreation of the THz field [52] than the PCS, however, if the probe beam is not

modulated at a sufficiently high frequency, the signal-to-noise ratio is superior for the PCS [53]. Moreover, the use of a coupling lens for the PCS can further increase the SNR in the PCS method by an order of magnitude [52]. However, single-shot measurements of the terahertz electric-field have been demonstrated for electro-optic sampling by using a chirped optical probe beam [54] and non-collinear sampling [55].

The bandwidth is limited to about 3THz detection for the PCS, whereas, minimizing the length of the electro-optic crystal, at the expense of signal-to-noise, can achieve bandwidths over 30THz [56]. In fact, it was demonstrated that a bandwidth of detection from 100 GHz to 70 THz could be achieved with electro-optic detection [57].

Therefore, it is a trade-off in terms of signal-to-noise and bandwidth. For the investigations that are carried out in this thesis, only 0.1-2THz is of primary importance, and therefore either of the above methods of detection is suitable.

The choice of implementing FS-EOS was motivated primarily by ease of implementation. No fabrication of antennas or substrates is required for FS-EOS, and it is easier to align the electro-optic detector, as the probe beam does not need to be focused on a small $\sim 5\ \mu m$ spot of the antenna.

The choice of ZnTe as the electro-optic material was motivated by the work of Wu [58], where a comprehensive evaluation of materials for electro-optic sampling was investigated. The conclusion was that for optical probe sources around 800 nm, ZnTe had the largest figure-of-merit.

A more detailed description of some limitations including group-velocity dispersion and sensitivity will be examined later in the thesis.

3.2 Calculation of electro-optic response in ZnTe

This section will examine the electro-optic response of a ZnTe crystal as FS-EOS element in the experimental configuration used in the thesis. Specifically, the electro-optic signal imparted to a probe beam by means of a polarization modulation, is analyzed in a balanced detection geometry. In this section, the effect of the balanced detection set-up will be investigated theoretically. This will be followed by a calculation of the electro-optic effect in ZnTe. Combining these two calculations, it will be shown that the ZnTe FS-EOS can be used as a polarization analyzer in addition to simple detection of THz fields. This will be compared to experimental data, and shown to agree with previous calculations. Finally, in order that the measured electro-optic signals can be converted to real units of the measured THz field, the calibration of the ZnTe crystal was checked by means of comparison to another well-known linear electro-optic crystal.

3.2.1 Balanced detection

We begin the calculation by examining the effect of the balanced detection geometry, where we first define the crystallographic coordinate system, and relevant angles involved

in the calculations. The orientation of the ZnTe crystal with respect to the THz field polarization and the probe polarization is shown in Fig. 3.2. The application of a low frequency (THz), or DC field induces a birefringence in the ZnTe. The orientation of the induced birefringent axes are shown in Fig. 3.3.

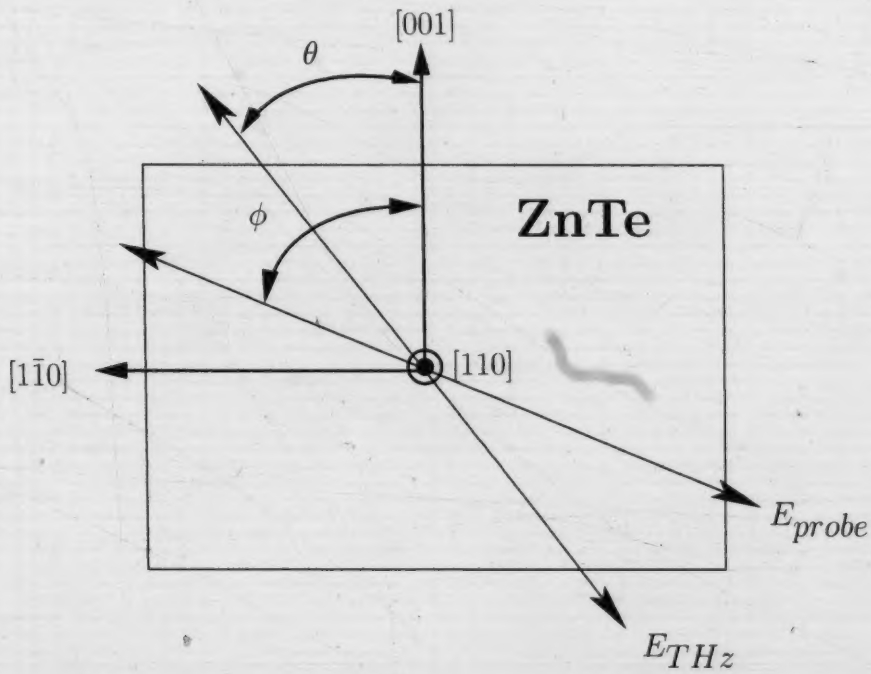

Figure 3.2: Geometry for the calculation of the electro-optic response of ZnTe. The polarization of the probe beam makes an angle ϕ with the [001] axis of the ZnTe, whereas the polarization of the THz beam makes an angle θ with the [001] axis of the ZnTe crystal.

The balanced detection is shown schematically in Fig. 3.4. The input probe beam is polarized linearly, and incident at an angle ϕ with respect to the [0 0 1] axis of the ZnTe crystal. This induces a phase retardance due to the induced birefringent axes, which is at an angle Ψ with respect to the [0 0 1] axis of the ZnTe crystal. The relationship between Ψ and θ will be found later (see Eq. 3.26). This induced phase retardance is analyzed using a quarter-wave plate and Wollaston prism. It is useful to use Jones

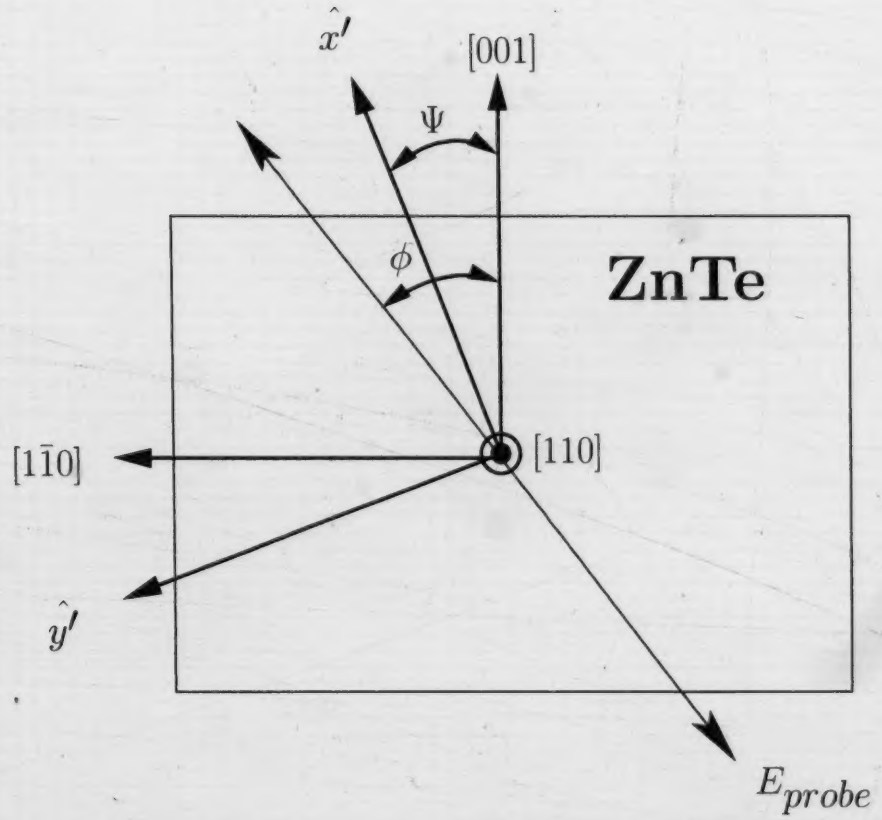

Figure 3.3: The induced birefringence in the ZnTe crystal resulting from the application of a low-frequency electric field (E_{THz}) results in two orthogonal birefringent axes, one of which, $\hat{x}'$ makes an angle Ψ with the [001] crystal axis.

vector analysis [59] to track the polarization state changes and ultimately calculate the differential signal as the difference in the two probe beam powers coming from the Wollaston prism in Fig. 3.4.

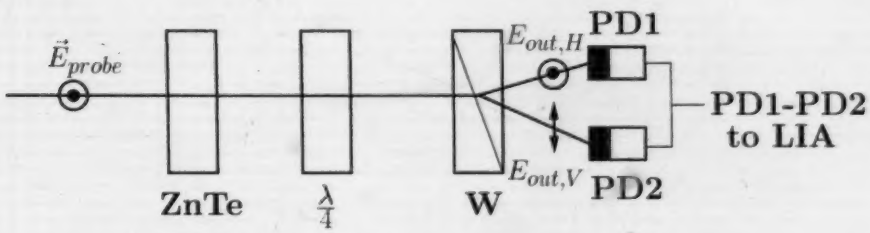

Figure 3.4: Schematic diagram of the balanced detection using ZnTe. PD are photodiodes, W is a Wollaston prism and $E_{out,H}$ and $E_{out,V}$ are the horizontally and vertically polarized components of the input pump field $\boldsymbol{E}_{probe}$ respectively and LIA is a lock-in amplifier.

In order to determine the polarization state changes, we need to define the Jones matrices for rotation, M_{rot}, and phase retardation, M_Γ. These are given by [59]:

$$\begin{aligned} M_{rot} &= \begin{pmatrix} cos(\alpha) & -sin(\alpha) \\ sin(\alpha) & cos(\alpha) \end{pmatrix} \\ M_\Gamma &= \begin{pmatrix} 1 & 0 \\ 0 & e^{i\Gamma} \end{pmatrix} \times e^{\frac{-i\Gamma}{2}} \end{aligned} \tag{3.6}$$

where Γ is the induced phase retardation ($\frac{\pi}{4}$ for a quarter-wave plate), and the rotation matrix rotates a linear polarization by an angle α. It is also important to note that the phase retardance matrix is written for use with the vertical axis parallel to the fast axis of the material. That is, for an input field of:

$$\boldsymbol{E} = \begin{pmatrix} E_x \\ E_y \end{pmatrix} \tag{3.7}$$

x corresponds to the horizontal and y corresponds to the vertical directions, respectively. The retardance matrix is defined with the fast axis parallel to y in the rotated coordinate frame.

Let us examine first the effect of the ZnTe crystal on a probe beam that is linearly polarized horizontally (as in Fig. 3.4). The application of a THz field will induce a birefringence, Γ, which will be calculated later, with the axes at an angle Ψ relative to the [001] crystal axis. Given that the probe beam makes an angle ϕ with respect to the

[001] axis, it makes an angle of $\phi - \Psi$ with respect to the $\hat{x}'$ induced birefringent axis. Therefore, to apply the Jones matrix for phase retardation given above, it is necessary to rotate the frame of reference of the probe beam by an angle $\phi - \Psi \equiv \Lambda$, then apply the Jones matrix for the phase retardation, and finally rotate back to the original coordinate system by rotating by an angle -($\phi - \Psi$). Therefore, the effect of propagation through the ZnTe crystal with a fixed birefringence of Γ is given by Eq. 3.8.

$$M_{tot}^{ZnTe} = e^{-\frac{i\Gamma}{2}} \begin{pmatrix} cos(\Lambda) & sin(\Lambda) \\ -sin(\Lambda) & cos(\Lambda) \end{pmatrix} \times \begin{pmatrix} 1 & 0 \\ 0 & e^{i\Gamma} \end{pmatrix} \times \begin{pmatrix} cos(\Lambda) & -sin(\Lambda) \\ sin(\Lambda) & cos(\Lambda) \end{pmatrix} \quad (3.8)$$

Similarly, for the quarter-wave plate, we orient it such that, in the absence of a THz field ($\Gamma = 0$ in Eq. 3.8), the linearly horizontally polarized pump beam impinges at 45 degrees to the fast axis of the wave plate. Therefore, we apply a 45 degree rotation to the probe beam prior to entering the quarter-wave plate and a -45 degree rotation at the exit. The effect of the quarter-wave plate in the balanced detection system can then be written as:

$$M_{tot}^{QWP} = e^{-\frac{i\pi}{4}} \begin{pmatrix} \frac{1}{\sqrt{2}} & \frac{1}{\sqrt{2}} \\ -\frac{1}{\sqrt{2}} & \frac{1}{\sqrt{2}} \end{pmatrix} \times \begin{pmatrix} 1 & 0 \\ 0 & i \end{pmatrix} \times \begin{pmatrix} \frac{1}{\sqrt{2}} & -\frac{1}{\sqrt{2}} \\ \frac{1}{\sqrt{2}} & \frac{1}{\sqrt{2}} \end{pmatrix} \quad (3.9)$$

Ignoring the phase factors in front of the matrices, as ultimately we will be interested in the absolute square of the electric fields (power measurements), we write the total polarization transfer matrix of the ZnTe and quarter-wave plate as:

$$\begin{aligned} M_{transfer} &= M_{tot}^{QWP} \times M_{tot}^{ZnTe} \\ &= \begin{pmatrix} \frac{1}{2}\left[(A-B)+i(A+B)\right] & \frac{1}{2}\left[(B-C)+i(B+C)\right] \\ \frac{1}{2}\left[(B-A)+i(A+B)\right] & \frac{1}{2}\left[(C-B)+i(C+B)\right] \end{pmatrix} \end{aligned} \quad (3.10)$$

where,

$$\begin{aligned} A &\equiv cos^2(\Lambda) + sin^2(\Lambda)e^{i\Gamma} \\ B &\equiv sin(\Lambda)cos(\Lambda)\left(1 - e^{i\Gamma}\right) \\ C &\equiv sin^2(\Lambda) + cos^2(\Lambda)e^{i\Gamma} \end{aligned} \quad (3.11)$$

Next, we compute the vertical and horizontal polarized components that result from the Wollaston prism. The Wollaston prism separates the vertically and horizontally polarized probe beam components as:

$$M_H^{Wollaston} = \begin{pmatrix} 1 & 0 \\ 0 & 0 \end{pmatrix}$$
$$M_V^{Wollaston} = \begin{pmatrix} 0 & 0 \\ 0 & 1 \end{pmatrix} \quad (3.12)$$

Finally, for a horizontally polarized probe beam, the input is given by:

$$E_{in} = \begin{pmatrix} E_{in} \\ 0 \end{pmatrix} \quad (3.13)$$

Combining equations 3.10 3.12 and 3.13 we obtain:

$$\begin{aligned} E_{out,H} &= M_H^{Wollaston} M_{transfer} E_{in} \\ &= \frac{1}{2}\left((A-B) + i(A+B)\right) \\ E_{out,V} &= M_V^{Wollaston} M_{transfer} E_{in} \\ &= \frac{1}{2}\left((B-A) + i(A+B)\right) \end{aligned} \quad (3.14)$$

where A and B are defined in Eq. 3.11, and $E_{out,H}$ and $E_{out,V}$ are the horizontally and vertically polarized probe beam components for differential detection, respectively.

The differential power monitored in the experimental set-up is given by:

$$\begin{aligned} P_{diff}^{measured} \equiv \frac{\Delta P}{P} &= \frac{P_{out,H} - P_{out,V}}{Pin} \\ &= \frac{|E_{out,H}|^2 - |E_{out,V}|^2}{|E_{in}|^2} \\ &= \frac{1}{4}\left(|(A-B) + i(A+B)|^2 - |(B-A) + i(A+B)|^2\right) \\ &= \frac{1}{4}\left(Re(A-B)^2 + Im(A-B)^2 + Re(A+B)^2\right) \\ &+ \frac{1}{4}\left(Im(A+B)^2 - 2Im\left[(A+B)(\bar{A}-\bar{B})\right]\right) \end{aligned} \quad (3.15)$$

And with a bit of algebra and using the definitions for A,B and C in Eq. 3.11, we finally obtain:

$$\frac{\Delta P}{P} = sin(2\Lambda)sin(\Gamma) \quad (3.16)$$

where $\Lambda \equiv \phi - \Psi$ as before, and Γ was the induced birefringence due to the THz field,

which still needs to be calculated. In addition to the calculation of the birefringence, it is necessary to compute the angle Ψ, which results from the application of the THz field.

3.2.2 Induced birefringence

We must now calculate the magnitude of the field dependent indices of refraction along the induced birefringent axes, or the induced birefringence, Γ, of Eq. 3.16. The geometry of the ZnTe crystal and applied electric field (THz field) is shown in Fig. 3.5. The THz field, as referenced to the crystallographic coordinate system is described as:

$$\boldsymbol{E}_{THz} = E_{THz}cos(\theta)\hat{z} + \frac{E_{THz}sin(\theta)}{\sqrt{2}}\hat{x} - \frac{E_{THz}sin(\theta)}{\sqrt{2}}\hat{y} \tag{3.17}$$

where $\hat{x}$ is parallel to [100], $\hat{y}$ is parallel to [010] and $\hat{z}$ is parallel to [001].

To find the effect of the applied field on the index of refraction of ZnTe, we compute the impermeability tensor $\eta_{ij} = \Delta\left(\frac{1}{n^2}\right) = r_{ij}E_j$ [60], where r_{ij} is the linear electro-optic tensor which is given by Eq. 3.18 for crystals with $\bar{4}3m$ symmetry such as ZnTe.

$$r_{ij} = \begin{bmatrix} 0 & 0 & 0 \\ 0 & 0 & 0 \\ 0 & 0 & 0 \\ r_{41} & 0 & 0 \\ 0 & r_{41} & 0 \\ 0 & 0 & r_{41} \end{bmatrix} \tag{3.18}$$

Using the definition of the impermeability tensor given above, with the THz field given by Eq. 3.17, and the form of the electro-optic tensor in Eq. 3.18, we get the impermeability to be:

$$\begin{bmatrix} \Delta(\frac{1}{n^2})_1 \\ \Delta(\frac{1}{n^2})_2 \\ \Delta(\frac{1}{n^2})_3 \\ \Delta(\frac{1}{n^2})_4 \\ \Delta(\frac{1}{n^2})_5 \\ \Delta(\frac{1}{n^2})_6 \end{bmatrix} = \begin{bmatrix} 0 \\ 0 \\ 0 \\ \frac{2r_{41}E_{THz}sin(\theta)}{\sqrt{2}} \\ -\frac{2r_{41}E_{THz}sin(\theta)}{\sqrt{2}} \\ 2r_{41}E_{THz}cos(\theta) \end{bmatrix} \tag{3.19}$$

Using this, we can write the expression for the index ellipsoid with an applied field as:

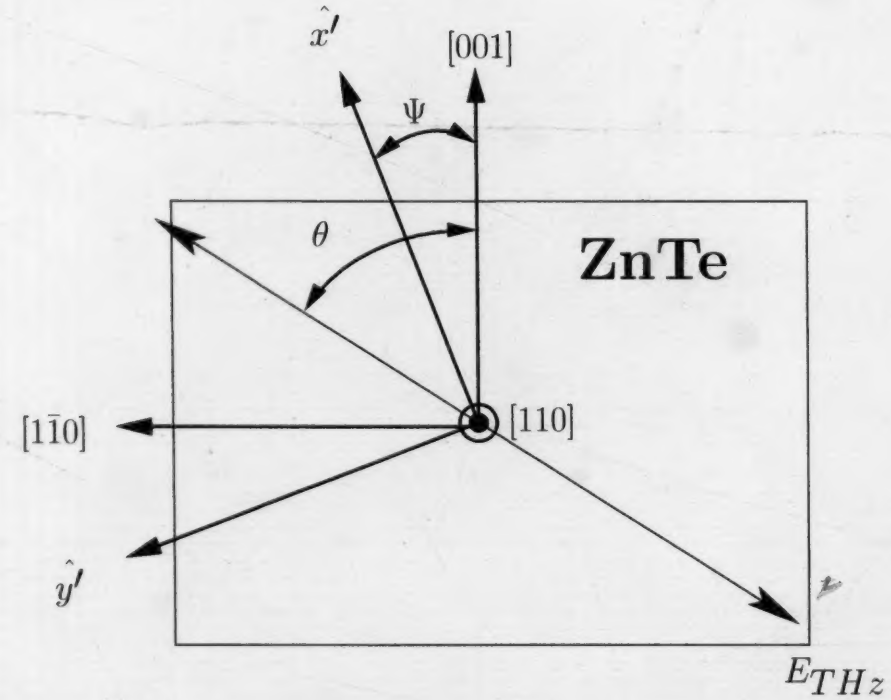

Figure 3.5: Geometry for the calculation of the electro-optic response of ZnTe. The THz field makes an angle θ with respect to the [001] axis of the ZnTe and the induced birefringent axis $\hat{x}'$ makes an angle Ψ with respect to the [001] axis of the ZnTe crystal.

$$
\begin{aligned}
1 &= \frac{x^2}{n_0^2} + \frac{y^2}{n_0^2} + \frac{z^2}{n_0^2} + \frac{2r_{41}E_{THz}sin(\theta)}{\sqrt{2}}yz \\
&- \frac{2r_{41}E_{THz}sin(\theta)}{\sqrt{2}}xz + 2r_{41}E_{THz}cos(\theta)xy
\end{aligned} \tag{3.20}
$$

Which we can write as a matrix, S_{ij}. In matrix form we have:

$$
S_{ij} = \begin{bmatrix} \frac{1}{n_0^2} & r_{41}E_{THz}cos(\theta) & -\frac{r_{41}E_{THz}sin(\theta)}{\sqrt{2}} \\ r_{41}E_{THz}cos(\theta) & \frac{1}{n_0^2} & \frac{r_{41}E_{THz}sin(\theta)}{\sqrt{2}} \\ -\frac{r_{41}E_{THz}sin(\theta)}{\sqrt{2}} & \frac{r_{41}E_{THz}sin(\theta)}{\sqrt{2}} & \frac{1}{n_0^2} \end{bmatrix} \equiv \begin{bmatrix} D & F & -G \\ F & D & G \\ -G & G & D \end{bmatrix} \tag{3.21}
$$

where we have defined:

$$
\begin{aligned}
D &\equiv \frac{1}{n_0^2} \\
F &\equiv r_{41}E_{THz}cos(\theta) \\
G &\equiv \frac{r_{41}E_{THz}sin(\theta)}{\sqrt{2}}
\end{aligned} \tag{3.22}
$$

Now, the problem of finding the new principal axes due to the induced birefringence amounts to diagonalizing the matrix in Eq. 3.21, which in turn is simply the problem of finding the eigenvectors of S_{ij}. Moreover, the indices of refraction corresponding to the principal axes will be given by the eigenvalues of S_{ij}. It is important to note that as the matrix S_{ij} is real and symmetric, the eigenvectors will exist, and be orthogonal (ie. S_{ij} is diagonalizable). A straightforward calculation of the eigenvalues gives:

$$
\begin{aligned}
\lambda_1 &= D + F \\
\lambda_2 &= D - \frac{1}{2}F + \frac{1}{2}\sqrt{F^2 + 8G^2} \\
\lambda_3 &= D - \frac{1}{2}F - \frac{1}{2}\sqrt{F^2 + 8G^2}
\end{aligned} \tag{3.23}
$$

With corresponding eigenvectors:

$$
\begin{aligned}
a_{\lambda_1} &= [110] \\
a_{\lambda_2} &= [1\bar{1}\left(\frac{-F-\sqrt{F^2+8G^2}}{2G}\right)] \\
a_{\lambda_3} &= [1\bar{1}\left(\frac{-F+\sqrt{F^2+8G^2}}{2G}\right)]
\end{aligned} \tag{3.24}
$$

It can be verified that the eigenvectors are orthogonal as expected. The eigenvectors corresponding to the new principal axes in the (110) plane are shown in Fig. 3.6.

From Fig. 3.6, we can relate the angle Ψ to the angle θ of the THz field in Fig. 3.5 by:

$$
\begin{aligned}
tan(\Psi) &= \frac{2\sqrt{2}G}{-F+\sqrt{F^2+8G^2}} \\
&= \frac{2sin(\theta)}{-cos(\theta)+\sqrt{cos^2(\theta)+4sin^2(\theta)}}
\end{aligned} \tag{3.25}
$$

Where we have used the definitions of F and G in Eq. 3.22. This gives the relationship between Ψ and θ that is required to remove the angle Ψ from the calculations. After some trigonometry, Eq. 3.25 reduces to the relation (Eq. A.5 of appendix A.1):

$$
tan(2\Psi) = -2tan(\theta) \tag{3.26}
$$

Given that we now have the orientation of the induced birefringent axes, we can evaluate the magnitude of the index of refraction along the two principal axes in the (110) plane, such that the phase retardance, Γ, can be computed. Noting that the new index of refraction can be written as $n_{\lambda_i} = n_0 + \Delta(n)$, and that we have $\Delta(\frac{1}{n^2}) = \lambda_i$, we can write, in the limit where $\Delta(\frac{1}{n^2}) \ll 1$:

$$
\Delta(n) \simeq -\frac{n^3}{2}\lambda_i \tag{3.27}
$$

So that the index of refraction along $\hat{a}_{\lambda_i}$ is given by:

$$
\begin{aligned}
n_{\lambda_i} &= n_0 + \Delta(n_{\lambda_i}) \\
&= n_0 - \frac{n^3}{2}\lambda_i
\end{aligned} \tag{3.28}
$$

Finally, we note that the total induced phase retardance, Γ, due to propagation along the two birefringent axes λ_2 and λ_3 is given by:

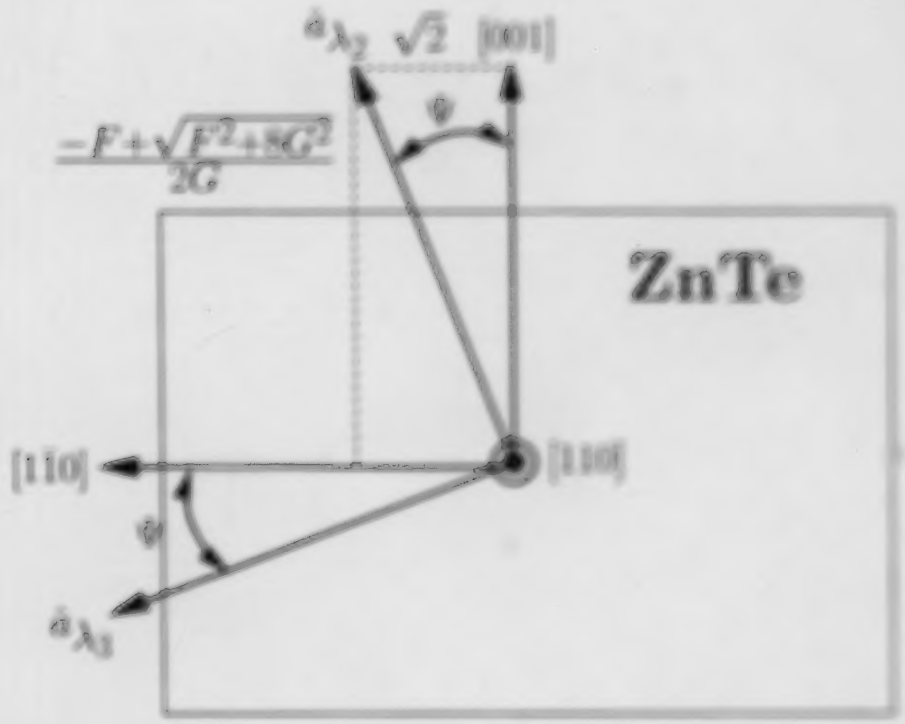

Figure 3.6: Geometry for the induced birefringence. The drop lines indicate the magnitude of the index of refraction along the induced birefringent axis ($\hat{x}_{1'}$) projected along the [001] and [110] crystal axes. The values of D,F and G are given in Eq. 3.20

$$\Gamma = \frac{\omega L}{c}(n_{\lambda_2} - n_{\lambda_3}) \tag{3.29}$$

And from Fig. 3.6 we have the relation:

$$tan(\Psi) = \frac{\sqrt{2}G}{-\frac{1}{2}F + \frac{1}{2}\sqrt{F^2 + 8G^2}} \tag{3.30}$$

Using the relations in Eq. 3.30 in the equation for the eigenvalues in Eq. 3.23 gives:

$$\begin{aligned} n_{\lambda_2} &= D + \frac{\sqrt{2}G}{tan(\Psi)} \\ n_{\lambda_3} &= D - \sqrt{2}Gtan(\Psi) \end{aligned} \tag{3.31}$$

Substitution of Eq. 3.31 into Eq. 3.29 with $G = r_{41}E_{THz}sin(\theta)/\sqrt{2}$ from Eq. 3.22 gives the phase retardance:

$$\Gamma = \frac{-\omega}{2c} r_{41} E_{THz} n^3 sin(\theta) \left(\frac{1 + tan^2(\Psi)}{tan(\Psi)} \right) \tag{3.32}$$

Now that the phase retardance is known, the polarization dependence of the ZnTe electro-optic detection can be completely quantified.

3.2.3 Polarization dependence of ZnTe electro-optic detection

The results of sections 3.2.1 and 3.2.2 can now be used to examine the polarization dependence of the electro-optic detection with ZnTe. Starting with Eq. 3.16 of section 3.2.1, we have:

$$\begin{aligned} \frac{\Delta P}{P} &= sin(2\Lambda)sin(\Gamma) \\ &\simeq \Gamma sin(2\Lambda) \end{aligned} \tag{3.33}$$

where the assumption of a small phase retardance, $\Gamma \ll 1$, has been made. Using the expression for the total phase retardance in Eq. 3.32, with $\Lambda = \phi - \Psi$ we have:

$$\frac{\Delta P}{P} = \frac{-\omega}{2c} r_{41} E_{THz} n^3 sin(\theta) \left(\frac{1 + tan^2(\Psi)}{tan(\Psi)} \right) sin(2(\phi - \Psi)) \tag{3.34}$$

From the appendix (See Eq. A.6 and Eq. A.10) we have the relation:

$$sin(\theta)\left(\frac{1+tan^2(\Psi)}{tan(\Psi)}\right)sin(2(\phi-\Psi)) = -(cos(\theta)sin(2\phi)+2sin(\theta)cos(2\phi)) \tag{3.35}$$

Combining Eq. 3.35 and Eq. 3.34 gives the pump and THz polarization dependence of balanced detection using ZnTe to be:

$$\frac{\Delta P}{P} = \frac{\omega}{2c} r_{41} L E_{THz} n^3 (cos(\theta)sin(2\phi)+2sin(\theta)cos(2\phi)) \tag{3.36}$$

which agrees with the calculation performed by Planken et. al. [49].

3.2.4 ZnTe electro-optic detection as a polarization analyzer

In this section, we will demonstrate that with the appropriate orientation of the ZnTe crystal, and polarization of the probe beam, it is possible to use the ZnTe electro-optic detector as an analyzer.

We begin with a specific orientation of the [001] crystal axis of the ZnTe crystal in the lab reference frame, with fixed polarizations of the THz field and the probe beam. The crystal is then rotated about the surface normal (the [0 0 1] crystal axis is rotated), and the response is examined. We do this for two particular configurations of the probe and THz field polarizations shown in Fig. 3.7.

Using this configuration, we can write the equations for the electro-optic signal response for a horizontally polarized probe and vertically polarized THz field ($S_{H_{probe},V_{THz}}$), as well as for a horizontally polarized probe beam and horizontally polarized THz field ($S_{H_{probe},H_{THz}}$) as follows:

$$S_{H_{probe},H_{THz}} = c_1 (cos(\alpha)sin(2\alpha)+2sin(\alpha)cos(2\alpha)) \tag{3.37}$$

where c_1 is a constant. As well, we have:

$$S_{H_{probe},V_{THz}} = c_1 (-sin(\alpha)sin(2\alpha)+2cos(\alpha)cos(2\alpha)) \tag{3.38}$$

where these equations were obtained by setting $\phi = \alpha$ and $\theta = \alpha$ in Eq. 3.36 for $S_{H_{probe},H_{THz}}$ and $\phi = \alpha$ and $\theta = \alpha + \frac{\pi}{2}$ for $S_{H_{probe},V_{THz}}$.

In order for the ZnTe to behave as a polarization analyzer, we would like to find the angles where there is a maximum sensitivity to horizontally polarized THz fields, while simultaneously having zero response to a vertically polarized THz field and vice versa. In order to examine this question, we tabulate the zeros for the two functions in Table 3.1.

Similarly, the extrema for the electro-optic response are tabulated in Table 3.2.

Obviously, this is not straight-forward given the complicated nature of the zeros and extrema in tables 3.1 and 3.2. To aid in visualizing this, we present analytical plots of the

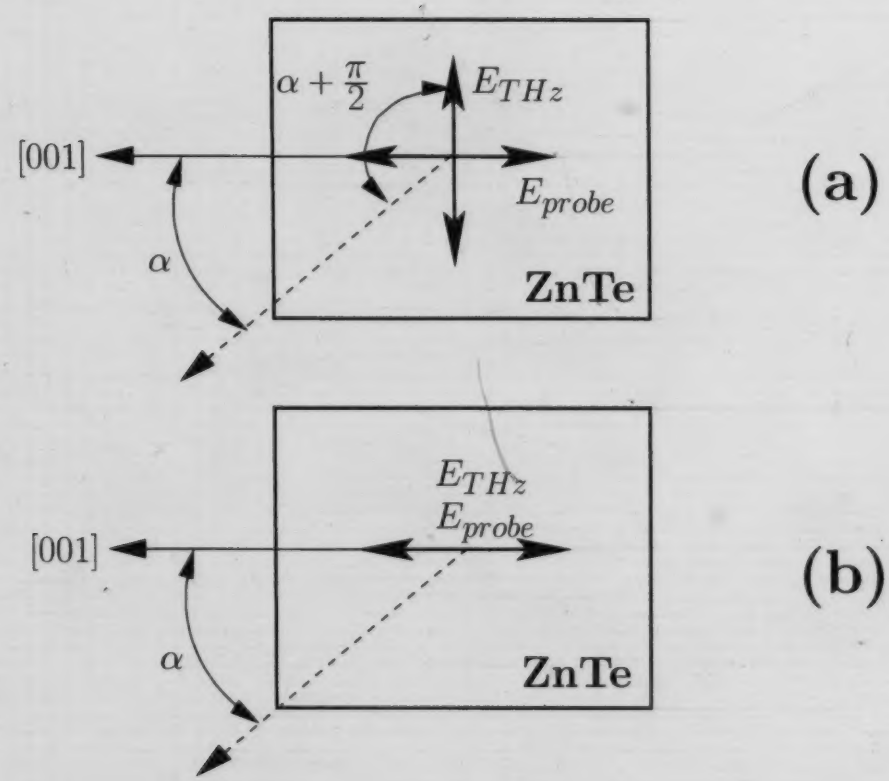

Figure 3.7: Configuration for electro-optic detection of THz radiation with a horizontally polarized probe beam. Detection of vertically (a) and horizontally (b) polarized THz fields as a function of the angle of crystal rotation α.

Table 3.1: Zeros of the polarization response function of the ZnTe electro-optic detector (Equations 3.37 and 3.38).

Zero	$\alpha(S_{H_{probe},H_{THz}})$	$\alpha(S_{H_{probe},V_{THz}})$
1^{st}	0	$cos^{-1}(\sqrt{\frac{2}{3}}) = 35.26^o$
2^{nd}	$cos^{-1}(\frac{1}{\sqrt{3}}) = 54.74^o$	$\frac{\pi}{2} = 90^o$
3^{rd}	$cos^{-1}(-\frac{1}{\sqrt{3}}) = 125.26^o$	$cos^{-1}(-\sqrt{\frac{2}{3}}) = 144.74^o$
4^{th}	$\pi = 180^o$	$\pi + cos^{-1}(\sqrt{\frac{2}{3}}) = 215.26^o$
5^{th}	$\pi + cos^{-1}(\frac{1}{\sqrt{3}}) = 234.74^o$	$\frac{3\pi}{2} = 270^o$

Table 3.2: Extrema of the polarization response function of the ZnTe electro-optic detector (Equations 3.37 and 3.38).

Extrema	$\alpha(S_{H_{probe},H_{THz}})$	$\alpha(S_{H_{probe},V_{THz}})$
1^{st}	$cos^{-1}(\frac{\sqrt{7}}{3}) = 28.13^o$	0
2^{nd}	$\frac{\pi}{2} = 90^o$	$cos^{-1}(\frac{\sqrt{2}}{3}) = 61.87^o$
3^{rd}	$cos^{-1}(-\frac{\sqrt{7}}{3}) = 151.87^o$	$cos^{-1}(-\frac{\sqrt{2}}{3}) = 118.13^o$
4^{th}	$\pi + cos^{-1}(\frac{\sqrt{7}}{3}) = 208.13^o$	$\pi = 180^o$
5^{th}	$\frac{3\pi}{2} = 270^o$	$\pi + cos^{-1}(\frac{\sqrt{2}}{3}) = 241.87^o$

two functions $S_{H_{probe},H_{THz}}$ and $S_{H_{probe},V_{THz}}$ In Fig. 3.8. Experimental measurements have also been made and are plotted in Fig. 3.8 to verify that these results are correct. The experimental data was obtained using a semi-large aperture photoconductive THz emitter, oriented to produce either a horizontally or vertically polarized THz beam at the ZnTe crystal, while the probe beam is horizontally polarized. For a detailed description of the experimental set-up, the reader is referred to Chapter 7. The ZnTe crystal is rotated about the [110] crystal axis, and the angular dependence is monitored.

We first note that the angular dependence is described well by the analysis performed above. In particular, note that the zeros and extremum are as listed in the tables above. It is also clear from the plots and the tabulated zeros and extrema, that there are only four angles of orientation of the ZnTe crystal for which an extrema occurs for one THz polarization, while simultaneously having zero response for the other THz polarization. These angles are, $\alpha = 0, \frac{\pi}{2}, \pi, \frac{3\pi}{2}$. In order for proper relative measurements of the polarizations, the magnitudes at each angle for each polarization of the THz beam must have the same sign. Therefore, there are two ways in which the ZnTe electro-optic response can be used as a polarization analyzer using a fixed horizontally polarized probe beam. These are: (i) ZnTe at $\alpha = 0$ for sensitivity to vertically polarized THz emission

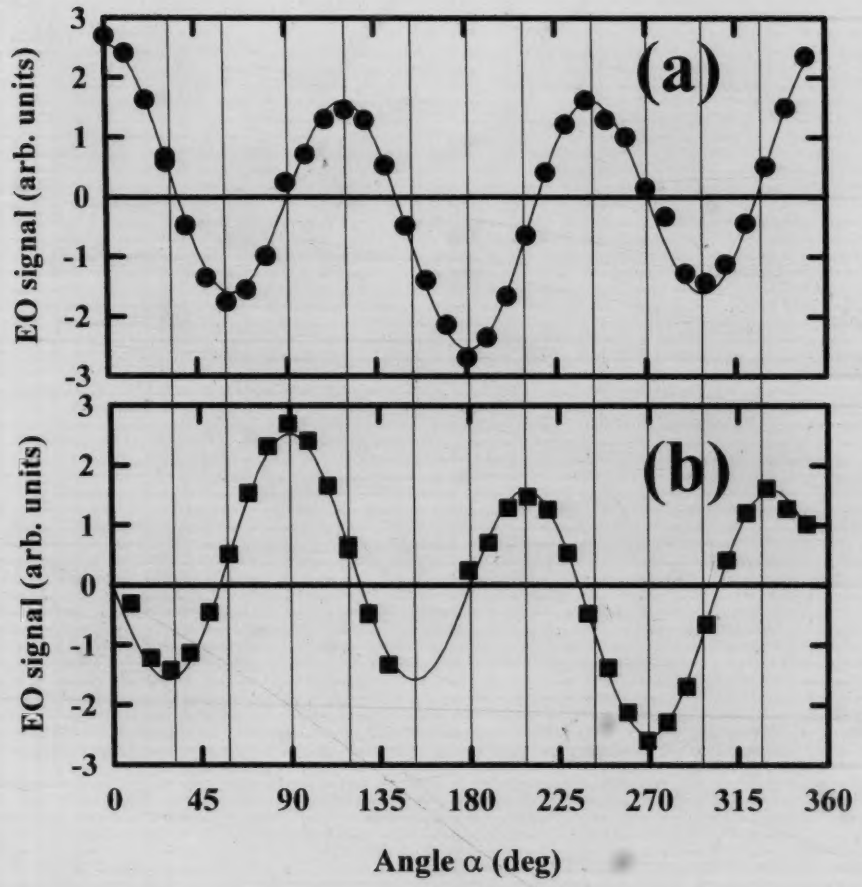

Figure 3.8: Theoretical and experimental angular dependence of ZnTe orientation for a horizontally polarized probe beam, and vertically (top, circles) and horizontally (bottom, squares) polarized THz fields. The experimental data was taken with a semi-large aperture photoconductive switch oriented to produce either horizontally (squares) or vertically (circles) polarized THz emission at the ZnTe crystal.

and ZnTe at $\alpha = \frac{\pi}{2}$ for sensitivity to horizontally polarized THz emission, and (ii) ZnTe at $\alpha = \pi$ for sensitivity to vertically polarized THz emission and ZnTe at $\alpha = \frac{3\pi}{2}$ for sensitivity to horizontally polarized THz emission.

This important result is used to study the polarization dependence of the emitted THz radiation in various configurations throughout the remainder of the thesis. That is, an external polarizer for the THz radiation is not required. By proper selection of the ZnTe orientation, sensitivity to orthogonal THz polarization components can be obtained.

3.3 Examination of the ZnTe electro-optic response

With the qualitative description presented in the previous analysis for the polarization dependence of the electro-optic response of ZnTe, we can analyze our detected fields in real units of $\frac{V}{cm}$, provided that we know the index of refraction and the linear electro-optic coefficient r_{41}. In this section, we will examine the value of r_{41} obtained in a calibration experiment, and compare it to literature values.

The ZnTe crystals used in reporting results here were obtained from eV products Inc. The samples were single crystal, 1mm thick, 1cm square samples. They had very low resistivity (1kΩ-cm), which made the standard calibration of the electro-optic coefficient extremely difficult as large bias fields, required to induce birefringence, were impossible to generate without damaging the crystal.

Without a bolometer for absolute power calibration, and with pyroelectric detectors that are quite noisy, it was found that a cross-calibration with a high-resistivity crystal of Lithium Niobate was one way to check the calibration of the ZnTe crystal. Lithium Niobate is well-characterized, making it a suitable choice for cross-calibration, and it is relatively straight-forward to measure the electro-optic coefficient of Lithium Niobate with DC or low-frequency fields.

In this section, we will first examine the calibration of the DC electro-optic coefficient of the Lithium Niobate crystal, and then proceed to examine the cross-calibration of ZnTe, and finally compare the result to literature values.

3.3.1 Calibration of the electro-optic response of lithium niobate

The lithium niobate crystals used for the calibration measurements were single-crystal $\hat{x}$ cut crystals 0.5 mm thick. Electrodes were formed on the crystal face, parallel to the $\hat{y}$ axis using silver paint, such that the applied electric field was parallel to the $\hat{z}$ crystal axis. $LiNbO_3$ has 3m symmetry, so that the linear electro-optic tensor is given by [60]:

$$r_{ij} = \begin{bmatrix} 0 & -r_{22} & r_{13} \\ 0 & r_{22} & r_{13} \\ 0 & 0 & r_{13} \\ 0 & r_{31} & 0 \\ r_{51} & 0 & 0 \\ -r_{22} & 0 & 0 \end{bmatrix} \tag{3.39}$$

Application of an electric field, $\boldsymbol{E}$, leads to a modification of the indices of refraction, as described in section 3.2.3. For the calibration measurements, the applied field is parallel to the $\hat{z}$ axis (ie. $\boldsymbol{E} = E\hat{z}$), and leads to the index ellipsoid:

$$\left(\frac{1}{n_x^2} + r_{13}E\right)x^2 + \left(\frac{1}{n_y^2} + r_{13}E\right)y^2 + \left(\frac{1}{n_z^2} + r_{33}E\right)z^2 = 1 \tag{3.40}$$

where $n_x = n_y = n_o$ and $n_z = n_e$. Note that the principal axes remain unchanged, however, the magnitude of the index is changed along each principal axis due to the application of an electric field along $\hat{z}$.

For a beam propagating along $\hat{x}$, and polarized in the zy-plane, the phase retardance, Γ is given by:

$$\Gamma = \frac{\omega L}{c}(n_y - n_z) \tag{3.41}$$

where ω is the optical frequency, L is the length of the crystal and c is the speed of light in vacuum. From the index ellipsoid, we have: $n_z \simeq n_e - \frac{1}{2}n_e^3 r_{33}E$ and $n_y \simeq n_o - \frac{1}{2}n_o^3 r_{13}E$. Inserting this into Eq. 3.41 gives:

$$\begin{aligned} \Gamma &= \frac{2\pi L}{\lambda}\left(n_o - n_e - \frac{1}{2}n_o^3 r_{13} + \frac{1}{2}n_e^3 r_{33}E\right) \\ &= \Gamma_o + \Gamma_E \\ \Gamma_o &= \frac{2\pi L}{\lambda}(n_o - n_e) \\ \Gamma_E &= \frac{\pi L E}{\lambda}\left(n_e^3 r_{33} - n_o^3 r_{13}\right) \\ &= \frac{\pi L E}{\lambda} r_{eff} \\ r_{eff} &\equiv \left(n_e^3 r_{33} - n_o^3 r_{13}\right) \end{aligned} \tag{3.42}$$

From Eq. 3.42 it is clear that a measurement of $\Gamma(E)$ will give r_{eff} by evaluating the slope of the curve. The experimental configuration is shown in Fig. 3.9. For the crossed-polarizer geometry of Fig. 3.9, the photodiode signal: $PD1/PD2$ is given by:

$$\frac{P_{out}}{P_{in}} \equiv \frac{PD1}{\alpha PD2} = sin^2(2\theta)sin^2\left(\frac{\Gamma}{2}\right) \tag{3.43}$$

where α is a correction factor taking into account the relative signal produced by the beam splitter (BS) in Fig. 3.9. The value of α is obtained by setting $\alpha PD2 = PD1$ when the input polarization is parallel to $\hat{z}$ (see Fig. 3.9).

The experiments are performed such that the angle θ in Eq. 3.43 is $\pi/4$.

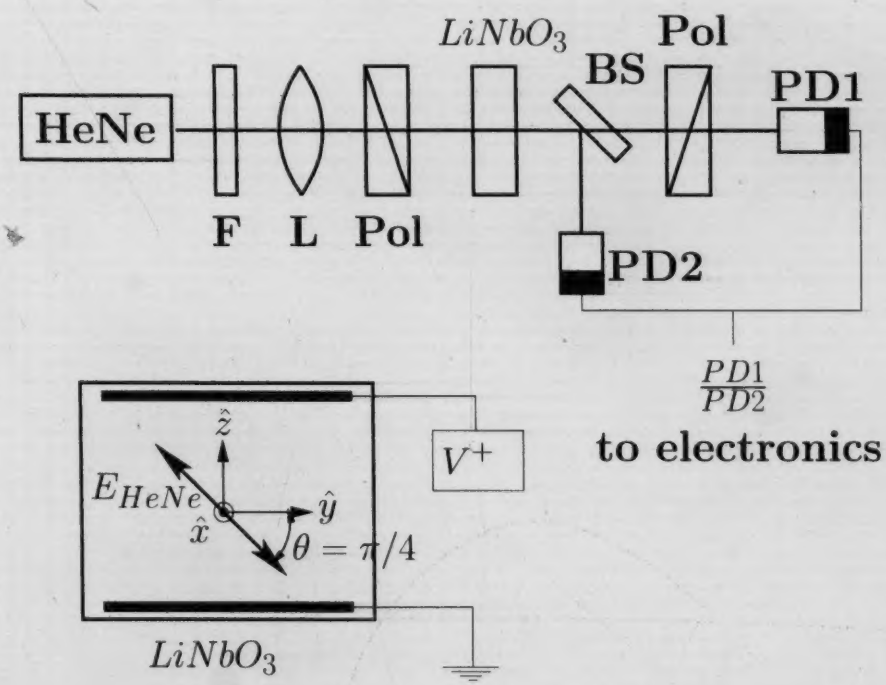

Figure 3.9: Experimental set-up for determining the linear electro-optic coefficient of lithium niobate. F is a filter; L is a lens; Pol is a polarizer; PD are photodiodes; BS is a beam splitter (quartz window). The linearly polarized HeNe beam makes an angle $\theta = \frac{\pi}{4}$ with the $\hat{y}$ crystal axis. The applied field lies along $\hat{z}$. The ratio of input to output powers in a crossed polarizer geometry is measured such that the electro-optic coefficient may be extracted.

Applying the bias field, and extracting the measured phase retardance, Γ_E of Eq. 3.42, we obtain the results in Fig. 3.10. From the slope of the curve, we obtain the

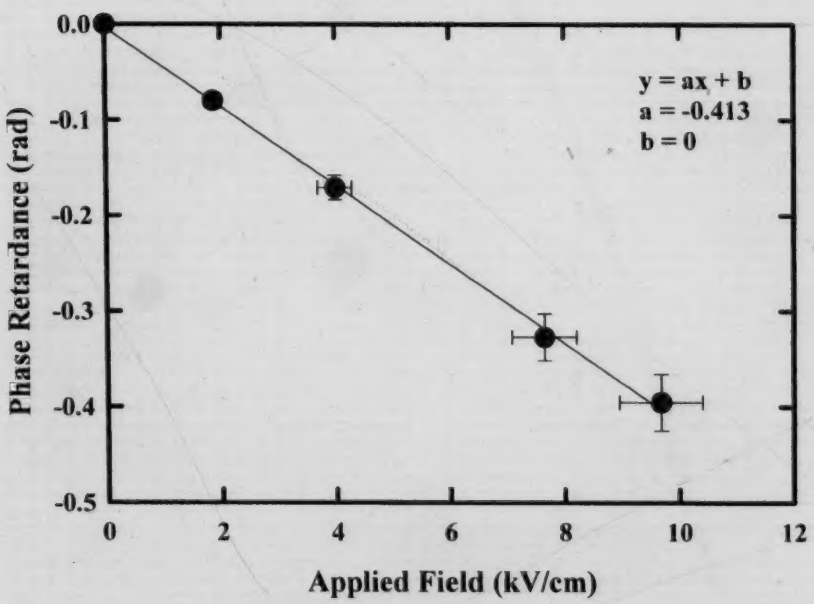

Figure 3.10: Measured phase retardance of a 632.8 nm HeNe laser through a 0.5 mm thick $LiNbO_3$ crystal as a function of the applied bias field. The bias field is applied parallel to the $\hat{z}$ crystal axis and the $\hat{x}$ axis is parallel to the propagation direction of the laser.

effective electro-optic coefficient, $r_{eff} = 166 \pm 5pmV^{-1}$ in Eq. 3.42. An additional correction was required to calculate the exact electric field at the center of the crystal for the layout of the electrodes used. Using FEMLAB [1], it was found that the electric field distribution within the $LiNbO_3$ is expected to be approximately 13% smaller than the simple estimate of $E = V/d_{gap}$. This results primarily from placing the electrodes on opposite sides of the crystal face to avoid breaking down the air between the electrodes upon applying high voltage. Correcting the effective linear electro-optic coefficient for the field distribution gives a value of $r_{eff} = 188 \pm 6pmV^{-1}$. The error is estimated from the experimental data, and does not include systematic errors that may result from deviations in crystal thickness, or variations in the exact electric field distribution obtained from modeling.

Since a DC field was employed; It should be noted at this point that the low frequency value of the linear electro-optic coefficient (unclamped) , r^T_{eff}, was measured. In fact, the linear electro-optic coefficient has acoustic resonances [61], and it is therefore the low frequency value with which we need to compare our result. Examining the reported value of the effective linear electro-optic coefficient for low frequencies at an optical wavelength of 632.8 nm, we find a reported value of $r^T_{eff} = 190pmV^{-1}$ [62], in excellent agreement with our measured value of $r^T_{eff} = 188 \pm 6pmV^{-1}$. Finally, we note that for high frequency measurements, the clamped value of the effective linear electro-optic coefficient, r^S_{eff}, should be used. Therefore, for using lithium niobate in THz experiments, the corresponding high frequency value $r^S_{eff} = 224pmV^{-1}$ should be used [62].

3.3.2 Comparison of ZnTe and $LiNbO_3$ electro-optic responses

With this value for the effective linear electro-optic coefficient for $LiNbO_3$, it is possible to perform a cross-calibration of the ZnTe crystal using the terahertz field as a bias.

Preliminary measurements of radiated THz fields using $LiNbO_3$ demonstrated exceptionally high noise levels. This was a result of not being able to properly balance the detection with a quarter-wave plate due to the intrinsic birefringence of the $LiNbO_3$. To overcome this, measurements with the $LiNbO_3$ were taken with an identical crystal of $LiNbO_3$ in the probe beam path, but oriented orthogonal to the detection crystal, such that the intrinsic birefringence was canceled, allowing proper balancing of the probe beam for differential detection.

A plot of the measured THz field radiated from a large-aperture photoconductive switch, with both $LiNbO_3$ and ZnTe oriented for maximal sensitivity, is shown in Fig. 3.11. The experimental set-up for this measurement is given in detail in chapter 4.

Recall from section 3.2.2, the differential photo-diode signal for optimal detection, $\theta = \frac{\pi}{2}$, which is:

[1] FEMLAB is a commercial finite element numerical computation package created by COSMOL. See their web-site at www.femlab.com for more details.

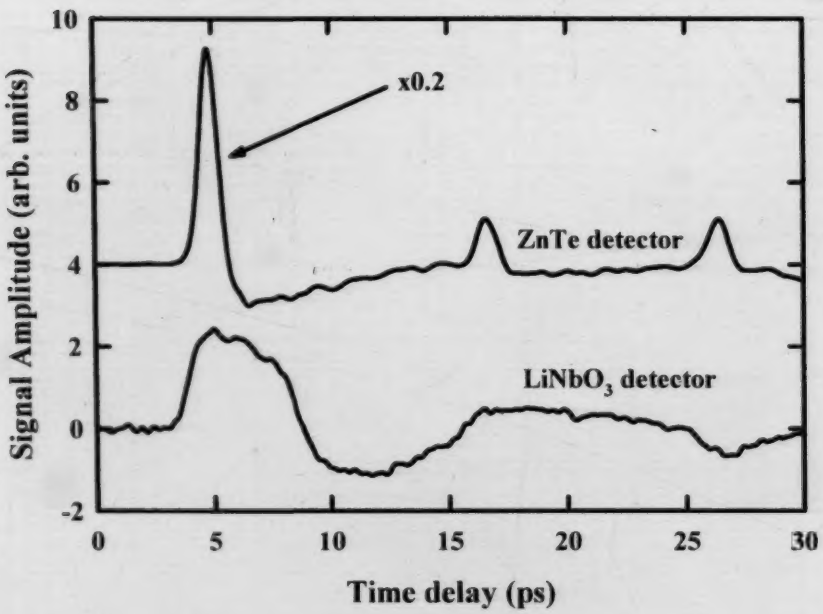

Figure 3.11: Detected THz field radiated from a large-aperture photoconductive switch as function of probe delay using a 1 mm thick ZnTe crystal (top) or a 0.5 mm thick $LiNbO_3$ crystal (bottom). The signal measured from the ZnTe crystal is multiplied by a factor of 0.2 for clarity.

$$\frac{\Delta P}{P} = \frac{\omega}{c} r_{41} E_{THz} L n^3 \tag{3.44}$$

Similarly, for $LiNbO_3$, we expect for small retardance, the differential photodiode signal to be (Using Eq. 3.42 in Eq. 3.16):

$$\begin{aligned} \frac{\Delta P}{P} &= \frac{\pi L E}{2\lambda} r_{eff} \\ r_{eff} &\equiv \left(n_e^3 r_{33} - n_o^3 r_{13}\right) \end{aligned} \tag{3.45}$$

Taking the ratio of equations 3.44 and 3.45 we obtain the expected ratio of responses:

$$\frac{\left(\frac{\Delta P}{P}\right)_{ZnTe}}{\left(\frac{\Delta P}{P}\right)_{LiNbO_3}} = \frac{2 L_{ZnTe} r_{41}}{L_{LiNbO_3} r_{eff}} = 1.65 \tag{3.46}$$

Solving for r_{41}, the linear electro-optic coefficient of ZnTe we obtain:

$$r_{41} = \left(\frac{\left(\frac{\Delta P}{P}\right)_{ZnTe}}{\left(\frac{\Delta P}{P}\right)_{LiNbO_3}} \right) \times \frac{L_{LiNbO_3} r_{eff}}{2 L_{ZnTe}} \tag{3.47}$$

From Fig. 3.11, the measured ratio is 16 ± 2, which is significantly different than 1.65 predicted in Eq. 3.46. This is almost entirely due to the difference in group-velocity mismatch of the THz beam and optical probe beam within the two crystals.

Group-velocity mismatch in $LiNbO_3$ and ZnTe has previously been examined in detail in Refs. [63, 64]. The effect of group-velocity mismatch, in the time domain, on the measured THz signals in Eq. 3.44 and Eq. 3.45 is obtained by setting:

$$E_{THz} \rightarrow \int_0^L \left(E_{THz}\left(\frac{z}{c}\Delta n + T\right) e^{-\alpha z} \right) dz \tag{3.48}$$

where z is the distance of the beam into the crystals, Δn is the index mismatch at optical and far-infrared frequencies, T is the absolute time, and α is the absorption coefficient of the crystals, which is assumed to be frequency independent. In addition, the THz field within the crystals will be different due to Fresnel reflection at the crystal input face. The notation C_{ZnTe} and C_{LiNbO_3} will be used for the Fresnel amplitude reflection coefficient. Taking these both into consideration, we rewrite the ratio of Eq. 3.47 as:

$$r_{41} = \left(\frac{\left(\frac{\Delta I}{I}\right)_{ZnTe}}{\left(\frac{\Delta I}{I}\right)_{LiNbO_3}}\right) \times \frac{L_{LiNbO_3} n_{eff}^3 C_{LiNbO_3}}{2 L_{ZnTe} C_{ZnTe}} \times \left[\frac{\left(\int_0^L \left(E_{THz}\left(\frac{1}{2}\Delta n + T\right) e^{-\alpha z}\right) dz\right)_{LiNbO_3}}{\left(\int_0^L \left(E_{THz}\left(\frac{1}{2}\Delta n + T\right) e^{-\alpha z}\right) dz\right)_{ZnTe}}\right] \tag{3.49}$$

The optical (800 nm) and far-infrared (1 THz) indices of refraction used for ZnTe as given by Ref. [65] were 2.85 and 3.17 respectively. The optical (800 nm) indices of refraction used for the ordinary and extraordinary indices of refraction for $LiNbO_3$ as given by Ref. [66] were 2.26 and 2.17 respectively. The far-infrared (1 THz) indices of refraction used for the ordinary and extraordinary indices of refraction for $LiNbO_3$ as given by Ref. [67] were 6.7 and 5.15 respectively. This gave values for the index mismatch in ZnTe of $\Delta n = n_{fir} - n_{opt} = 0.32$. The index mismatch for the $LiNbO_3$ depends on the geometry; in this case, the THz field is parallel to the extraordinary (z) axis, and the probe beam is at 45° relative to the x and z-axes. Therefore the index mismatch for $LiNbO_3$ is taken as $\Delta n = n_{fir} - n_{opt} = 2.91$. Finally, the values for the power absorption coefficients for the far-infrared radiation in the ZnTe and $LiNbO_3$ crystals are taken as frequency independent with values of 5 cm^{-1} and 10 cm^{-1}, respectively [67]. Numerical evaluation of the correction factor in the square braces of Eq. 3.49, assuming an input Gaussian pulse shape with a pulse-width of 0.5 ps (FWHM), yields 0.10 ± 0.01. This gives a measured value for r_{41} in ZnTe of $r_{41} = 3.9 \pm 0.4 \frac{pm}{V}$, in excellent agreement with reported values for ZnTe between 3.9-4.0 $\frac{pm}{V}$ [63, 64, 68, 69, 70]. Therefore, for the remainder of the thesis a value of $r_{41} = 3.9 \frac{pm}{V}$ will be used.

Chapter 4

Comparison of large-aperture photoconductive switch and InAs surface emission [1]

InAs has previously been reported to be an efficient emitter of Terahertz radiation at low excitation fluences, using femtosecond laser pulses. In an effort to quantify the efficiency of the InAs surface emission, the scaling and saturation of THz emission from a (100) InAs surface as a function of excitation fluence is measured and quantitatively compared to the emission from a GaAs large-aperture photoconductive switch. In this chapter a brief description of the operation of a large-aperture photoconductive switch will be presented, followed by a brief discussion of the current understanding of the emission of THz radiation from InAs. Following this, the experimental results from an experiment where the two emitters were compared will be presented.

4.1 Description of the large-aperture photoconductive switch

The emission of THz radiation from a large-aperture photoconductive switch has been described in detail in Ref. [72]. In this section, the main characteristics associated with the scaling of the emission will be reviewed.

A large-aperture photoconductive switch is what the name implies: a photoconductive switch for which the dimensions are large compared to the wavelength of the emitted radiation. In this case, there exists a current distribution, as a consequence of illumination with an above band-gap wavelength optical pulse, that has a spatial extent larger than the characteristic wavelength of the emitted radiation. Darrow *et. al.* [73] showed that in this case, the theoretical treatment was best approached by use of plane waves.

[1] The results in this chapter have been published in Ref. [71].

The boundary conditions on the radiated THz field can be used in conjunction with Ohm's law, to relate the optically injected current density to the radiated field. The result is that the relation between the time-varying surface conductivity, applied bias field and radiated THz field are given by:

$$E_{rad}(t) = -E_b \frac{\sigma_s(t)\eta_0}{\eta_0\sigma_s(t) + 1 + \sqrt{\epsilon}} \tag{4.1}$$

where $E_{rad}(t)$ is the radiated electric field at the emitter, inside of the substrate, E_b is the applied bias field on the switch, η_0 is the impedance of free space, ϵ is the dielectric constant and the time-dependent surface conductivity, $\sigma_s(t)$, is given by:

$$\sigma_s(t) = \frac{e(1-R)}{h\nu} \int_{-\infty}^{t} dt' \mu(t-t') I_{opt}(t') e^{-\frac{t-t'}{\tau_{car}}} \tag{4.2}$$

where e is the electronic charge, R is the reflectivity (at normal incidence for the above analysis), $h\nu$ is the optical photon energy, μ is the time dependent mobility of the substrate, I_{opt} is the intensity profile of the optical excitation pulse and τ_{car} is the carrier recombination time.

The above model describes the experimentally observed scaling dependence on bias field and optical excitation fluence in a relatively simple way. In Eq. 4.1, the THz field grows as the conductivity increases, however, it eventually saturates. The value to which it saturates is the bias field. That is, the THz field cannot exceed the value of the bias field, and monotonically approaches the bias field (opposite in direction) as the device is pumped harder.

In order to demonstrate the dependence on the optical pump energy, we notice that Eq. 4.1 monotonically increases with increasing conductivity. Therefore, the maximum of the radiated field occurs when the conductivity reaches its respective maximum, and is given by:

$$E_{rad}^{pk} = -E_b \frac{\sigma_{max}\eta_0}{\sigma_{max}\eta_0 + 1 + \sqrt{\epsilon}} \tag{4.3}$$

where σ_{max} is the maximum of the surface conductivity in time. Further, we assume Drude conductivity such that $\sigma(t) = \mu(t)n(t)e$, which assumes that the carrier recombination time is significantly larger than the optical excitation pulse width in Eq. 4.2. Finally, if we assume that the mobility is time-independent and given by the DC mobility, then the conductivity would simply be $\sigma(t) = \mu e n(t)$. This assumes that the injected photon energy is only slightly above the band-gap, which is the case for our experiments with the photon energy of 1.55eV in comparison to the band-gap of 1.5 eV for semi-insulating GaAs.

The time-dependent carrier density, n(t), is given by:

$$n(t) = \frac{(1-R)}{h\nu} \int_{-\infty}^{t} P_{opt}(t')dt' \tag{4.4}$$

where $P_{opt}(t)$ is the incident optical power as a function of time. Using the assumption that the carrier recombination time is much larger than the optical excitation pulse width, the carriers will all be injected before they begin to recombine. Therefore we have that $\sigma_{max} = \mu e n_{max}$, with $n_{max} = F_{opt}(1-R)/h\nu$, which gives the peak radiated field in Eq. 4.3 to be:

$$\begin{aligned} E_{rad}^{pk} &= -E_b \frac{\frac{e(1-R)\mu_{DC}F_{opt}\eta_0}{h\nu}}{\frac{e(1-R)\mu_{DC}F_{opt}\eta_0}{h\nu} + (1+\sqrt{\epsilon})} \\ &= -E_b \frac{F_{opt}}{F_{opt} + F_{sat}} \end{aligned} \tag{4.5}$$

where F_{sat} is the saturation flux, defined by:

$$F_{sat} = \frac{h\nu(1+\sqrt{\epsilon})}{e(1-R)\mu_{DC}\eta_0} \tag{4.6}$$

which is equivalent to the saturation flux expression given in Ref. [68]. From equations 4.5 and 4.6 it is evident that the radiated THz field will scale linearly with the applied bias field and saturate with optical excitation fluence, the saturation fluence given by Eq. 4.6. These scaling behaviours will be discussed in the next section.

4.2 Direct comparison

In this section the efficiency of InAs as a high-power THz emitter under high excitation fluence is examined. The GaAs large-aperture photoconductive switch (LAPCS) has been used in the past to generate the highest reported conversion efficiency from optical to pulsed THz radiation [73], and has been used as a benchmark for efficiency of THz emitters [74]. In this section, such a GaAs LAPCS has been used for comparison to gauge the overall conversion efficiency of InAs. Scaling of emission with excitation fluence and saturation of emission is presented, and a quantitative comparison to a GaAs LAPCS is reported.

The experimental set-up is similar to that of section 2.1 and is shown in Fig. 4.1. A regeneratively amplified Ti:Sapphire laser system (Spectra Physics Hurricane) is used as a source, operating at a center wavelength of 800 nm, at 1 kHz repetition rate, with a maximum pulse energy of 750 μJ and a pulsewidth of 130 fs (Gaussian FWHM). The beam is split into pump (92%) and probe (4%) beams using a wedged window. The probe time is varied with respect to the pump using an optical delay line, allowing time-resolved mapping of the THz field. A variable attenuator ($\lambda/2$ plate and polarizer) is used in the pump beam to vary the fluence. The THz radiation from the emitter is collected and imaged onto the detector using 4 F/2 parabolic mirrors in an f-2f-f geometry to minimize frequency dependent focusing effects [75, 76, 77], and allow a

direct comparison of emitted THz fields between the two emitters. The four parabolic mirrors are employed to attain an intermediate focal plane for testing samples, which is used later in the thesis to study samples of wood. To detect the THz radiation, the probe is co-linearly propagated through a 1mm thick, (110) ZnTe electro-optic crystal, together with the THz pulse. This induces a polarization modulation, which is analyzed using a polarization bridge ($\lambda/4$ plate and Wollaston prism), with the differential photodiode signal detected using a lock-in amplifier at the optical chopping frequency of approximately 330Hz. The orientation of the ZnTe crystal is chosen to maximize the electro-optic signal as in section 3.2.4. The GaAs emitter used is constructed on a high-resistivity GaAs substrate (the carrier concentration and Hall mobility specified by the manufacturer are $n_c = 1.5 \times 10^7 cm^{-3}$ and $\mu_H = 3890 cm^2 V^{-1} s^{-1}$, respectively). Silver paint was used to define electrodes with a gap spacing of 0.19 cm and biased at 300 V (1.6 kV/cm). The GaAs emitter is illuminated at normal incidence and the transmitted THz beam was collected.

The InAs emitter is a (100) oriented, undoped, n-type InAs sample ($n_c = 1.9 \times 10^{16} cm^{-3}$, $\mu_H = 2.5 \times 10^4 cm^2 V^{-1} s^{-1}$) which is illuminated at 45 degrees angle of incidence. The pump beam is telescoped to a $1/e^2$ intensity beam diameter of 2.85 ± 0.05 mm for both emitters using a pair of lenses as shown in Fig. 4.1.

The orientation of the crystal is such that the projection of the p-polarized pump beam on the (100) plane of the InAs crystal is at 45^0 relative to both the [010] and [001] crystallographic axes, and the p-polarized THz beam is collected. Initial measurements of the saturation of the signals from InAs were carried out in the absence of magnetic fields.

In order to determine the efficiency and saturation of the two emitters, the scaling of the THz emission with optical excitation fluence was measured. The fluence is calculated as the full energy of the pump beam before striking the surface of the emitter, divided by the $1/e^2$ (intensity) beam area of $0.064 \pm 0.003 cm^2$. The GaAs-LAPCS is oriented in a transmission geometry, such that the pump beam illuminates the switch at normal incidence, while the InAs sample is unbiased, with the bare (100) surface oriented at 45^0 to the pump beam as shown in Fig. 4.1. The resultant peak measured emitted field as a function of the incident fluence is presented in Fig. 4.2. The peak radiated terahertz field is taken as the maximum of the absolute value of the time-domain waveform. The inset of Fig. 4.3 shows waveforms radiated from the LAPCS and InAs sources. The THz signal from both emitters is observed to saturate as the fluence is increased. The radiated field is well described by the simple saturation formula, $E_{THz}^{pk} = BF/(F + F_{sat})$, where B is a scaling constant, F is the excitation fluence and F_{sat} is the saturation fluence. The solid curves in Fig. 4.2 are the fits of this equation to the data, and the values for B are 300 ± 30 and 220 ± 22 V/cm and F_{sat} are 29 ± 4 and 10 ± 1.3 $\mu J/cm^2$ for InAs and GaAs respectively. The value for the saturation flux of the GaAs obtained is within 30% of the more recently reported results for the saturation flux from GaAs LAPCS [74, 68, 78]. In our case, the GaAs aperture is overfilled, whereas in most reports on saturation behavior of the GaAs LAPCS, the pump beam diameter is comparable to the

aperture dimension.

From Fig. 4.2 it is clear that the peak radiated field from the (100) InAs emitter is larger in the saturated regime, and reaches a saturated field approximately 30% higher than that for the GaAs LAPCS. In addition, the saturation fluence for InAs is almost 3x larger than that for the GaAs LAPCS.

With quantification of the scaling of both emitters with excitation fluence, the question of which emitter most efficiently converts optical to far-infrared energy can be examined. We can estimate the total energy in the THz pulses, and compute an estimate for the overall conversion efficiency. The method is outlined as follows. The conversion efficiency, η, is defined by:

$$\eta = \left(\frac{W_{THz}}{W_{inp}} \right) \tag{4.7}$$

where the estimated THz pulse energy is:

$$W_{THz} \approx \frac{\tau A \left| E_{THz}^{pk} \right|^2}{2\eta_0} \tag{4.8}$$

where W represents energy, τ is the 1/e (electric field) THz pulse width, A is the area of the THz beam at the detector, E_{THz}^{pk} is the peak radiated THz field and η_0 is the impedance of free space. The definition of the 1/e electric-field THz pulse width is shown in Fig. 4.3. The 1/e pulse-width is taken as the time-span between when the absolute value of the field first reaches a value of 1/e of the maximum, and then when it falls to 1/e of the maximum.

Detected fields are corrected for Fresnel reflection at the emitter and detector, T_R, and system transmission losses, T_S as:

$$|E_{THz}^{pk}| \approx \left| E_{THz}^{pk} \right| T_R T_S \tag{4.9}$$

We compute the input optical energy by integrating over the emission aperture:

$$W_{inp} = \iint\limits_{aperture} F_{opt}^{excite}(x,y)\, dxdy \tag{4.10}$$

The experimental values used are given in Table 4.1. The THz beam waist at the detector for the two emitters was measured by scanning the THz beam laterally across the optical probe beam, which is less than 100μm in diameter, and measuring the 1/e THz electric field diameter. The system loss factor was calculated from the transmission spectrum of the optically opaque beam block used to block the laser radiation from hitting the detector, and had a flat frequency response over the bandwidth of both emitters.

Using the values in Table 4.1, and computing the conversion efficiency as outlined

Table 4.1: Parameters used in estimation of optical to far-infrared conversion efficiency

Property	GaAs	InAs	Description
System Loss	1.44	1.44	E-field attenuation factor of beam-block
Fresnel Loss	1.42	1.31	E-field Fresnel reflection losses (emitter and detector)
$\tau(ps)$	1.54	0.79	Average measured 1/e pulse widths
THz spot (cm)	0.342	0.245	Measured 1/e THz field diameters
B (V/cm)	223	294	Measured saturation amplitude
$F_{sat}(\mu J/cm^2)$	9.6	29.3	Measured saturation fluence
$E(\mu J)$	FA	0.82FA	Integral of F(A) over the excitation area
$A(cm^2)$	0.064	0.064	$1/e^2$ Intensity beam area of excitation beam

above, we get the results presented in Fig. 4.4 below.

Note that the conversion efficiency for the GaAs is much larger than for InAs due to a larger THz beam waist at the detector and a longer pulsewidth. The larger THz beam waist at the detector is likely a result of diffraction from the emitting aperture due to the longer emission wavelengths, and the reduced emitting aperture for GaAs compared to the InAs. For our GaAs LAPCS, the maximum conversion efficiency, at a bias field of 1.6 kV/cm was about 1.9×10^{-5}, while for InAs it was 2.1×10^{-6}. The best reported conversion efficiency for a GaAs LAPCS was 1.6×10^{-3} at a bias field of 10.6 kV/cm [73]. Given that the THz pulse energy scales quadratically with the bias field [72], then the maximum conversion efficiency expected from our LAPCS at 10.6 kV/cm would be 0.8×10^{-3}, which is a factor of 2 less than reported by You et. al [73]. This discrepancy is possibly a result of not including group-velocity mismatch in the ZnTe electro-optic detector (thermal detection was used by You et. al [73]) and diffraction losses due to the limited collection angle in our system. The measured frequency spectrum from the two emitters, at an excitation fluence of $1mJ/cm^2$ is presented in Fig. 4.5. From Fig. 4.5 it is also clear that the InAs emitter is better suited to producing higher frequency THz radiation (more efficient above 0.75 THz). Most of the dips in the spectra are due to water absorption lines in air.

Given that the emission aperture for the LAPCS is 0.19 cm in the horizontal direction, and the collection aperture is F/2, the matching frequency is 0.32THz for a diffraction-limited beam diffracting from the aperture and exactly filling the F/2 collection optics (1 e-folding of the peak electric field distribution at the collection aperture), below which we expect the signal will be attenuated. The peak of the measured THz spectra occurs at 0.33 THz (see Fig. 4.5), which also is in agreement with an angularly truncated beam cutting off the lower frequency components. Focusing the THz field from an LAPCS with minimal collection angle losses results in a spectrum with a peak at approximately 0.1THz or less [68]. With larger aperture GaAs-LAPCS emitters measured in our laboratory, we have also observed a peak emission frequency close to

0.1THz. An approximate estimate of the truncation of the spectrum leading to the 0.3THz peak emission frequency observed here indicates that approximately half of the emitted radiation is lost due to diffraction losses of the lower frequencies on the collection optics. Thus our observed peak efficiency is consistent with the peak value reported by You et. al [73]. It is clear that in this regime the large conversion efficiency for GaAs is a result of extracting energy from the electric bias field and not from the energy in the laser pulse itself.

While the conversion efficiency for the GaAs LAPCS in Fig. 4.4 can be scaled to higher bias voltages, the unbiased emission from (100) InAs cannot be scaled further, making it much less efficient at converting optical to far-infrared energy than the GaAs LAPCS. However, the application of a magnetic field at low excitation fluences has been shown to increase the THz emission significantly. In fact, the THz emission power was shown to scale quadratically with the applied magnetic field [34], saturating above approximately 3T [79, 80, 81]. The enhancement in the emission has been ascribed to the deflection of the photo-carrier diffusion current, creating a larger component parallel to the surface which radiates more efficiently and hence increases output radiation [35, 36]. For the case where the THz signal is predominantly a result of surface optical rectification, an applied magnetic field would not have the same dramatic effect. We have measured the effect of a 0.7T magnetic field, which results in no more than a 20% change in the peak radiated field when exciting the InAs at a fluence of approximately 1mJ/cm^2. Assuming quadratic power scaling with magnetic field, that portion of the THz field that is increasing as the square of the magnetic field is estimated to produce at most a 1.7x increase in THz field strength (3x in power) in the present polarization configuration, for a field of 3T at a fluence of 1mJ/cm^2. Since the optimal conversion efficiency is obtained for operation at F_{sat} (see below), the effect of the magnetic field around the saturation fluence is the important parameter. Recent results indicate that above about $0.2\mu J/cm^2$, the effect of the magnetic field is not as dramatic as at lower fluences [82]. In that work, an applied magnetic field of +1.6T resulted in a constant increase in radiated THz power from InAs surfaces of approximately 2x compared to the case of no magnetic field, above excitation fluences of approximately 0.2 μJ/cm^2. Scaling our result observed above, the expected increase at 1.6T, based on our observation of approximately 20% increase in signal at 0.7T, would be 1.45x increase in electric field, or 2x increase in power, consistent with these reports. Thus, the large enhancement for InAs due to the application of a magnetic field only occurs for very weak excitation fluences, well below the saturation fluence. The conclusion is that while the power radiated from the GaAs LAPCS can further be increased by applying higher bias fields, the InAs is not expected to be enhanced by more than a factor of 3, with the application of large magnetic fields.

One can show that the high efficiency reported for the LAPCS is close to the theoretical limit expected for this system. An upper bound on the radiated FIR energy from a LAPCS can be estimated, assuming that the maximum radiated field is given by the bias field. Using the results of Darrow et. al. [72] as summarized above in section 4.1,

we have that in the near-field the peak-radiated THz field is given by (Eq. 4.5):

$$E_{rad,THz}^{near-field} = E_b \left(\frac{F}{F + F_{sat}} \right) \tag{4.11}$$

where F_{sat} is the saturation flux. Using Eq. 4.7, with $W_{inp} = A \times F$, with A being the area of the emitter which is the same as the size of the emitted THz beam we get:

$$\eta = \frac{\tau E_b^2}{2F\eta_0} \left(\frac{F}{F + F_{sat}} \right)^2 \tag{4.12}$$

And noting that the maximum conversion efficiency occurs at Fsat, using $\tau \sim 1ps$ and $F_{sat} = 9.6\ \mu J/cm^2$ gives an upper bound on the conversion efficiency at E_b= 10 kV/cm of:

$$\eta = \frac{\tau E_b^2}{2\eta_0} \left(\frac{1}{4F_{sat}} \right) = 3.2 \times 10^{-3} \tag{4.13}$$

It can be shown that this estimate is consistent with what is calculated using the peak electric-field in Eq. 28 of Ref. [83], if the τ_{eff} in that equation is chosen to be the inverse of the radial frequency. The above estimated value is about 2x larger than reported by You et. al. [73], and 4x larger than the experimental value reported here. Again, possible reasons for observing a lower conversion efficiency in our case are not including the effects of group velocity mismatch in the detection crystal and losing a significant portion of the THz signal outside of the collection angle of the imaging system. It is clear, nonetheless, that the generated THz energies are in the range of the theoretical limit which could be achievable.

In conclusion, the magnitude of the emission from an InAs and a GaAs LAPCS emitter was measured as a function of irradiation fluence. Both emitters saturated and could be fit using a simple saturation equation, with observed saturation fluences in terms of incident laser fluences of 29.3 and 9.6 $\mu J/cm^2$ for the InAs and GaAs emitters respectively. Correcting the detected peak radiated THz fields for Fresnel losses and system losses, the peak conversion efficiencies were estimated to be 2.1×10^{-6} and 1.9×10^{-5} for InAs and GaAs (1.6kV/cm bias) respectively. Using the expected quadratic scaling with the bias field up to the breakdown voltage of GaAs of 10kV/cm, the efficiency of the GaAs LAPCS can be considerably enhanced relative to that of unbiased InAs and approaches the theoretically expected limit based on the bias field and saturation flux.

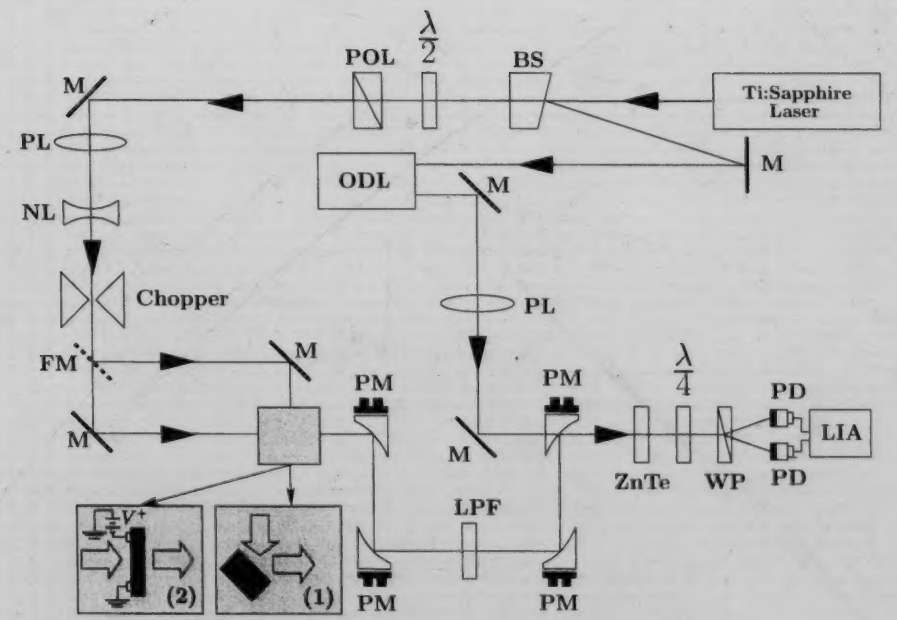

Figure 4.1: Schematic diagram of the THz system used in the experiments. FM is a flip mirror, pol is a polarizer, BS is a wedged beam splitter, PM are parabolic mirrors, QWP and HWP are quarter and half-wave plates respectively, WP is a Wollaston prism, L1 and L2 are +50 and -15cm focal length lenses, and LPF is a visibly opaque low pass filter that blocks the fundamental. The emitter used is either an externally biased GaAs photoconductive switch or a (100) oriented InAs surface. (1) and (2) represent beam paths to InAs and GaAs emitters respectively.

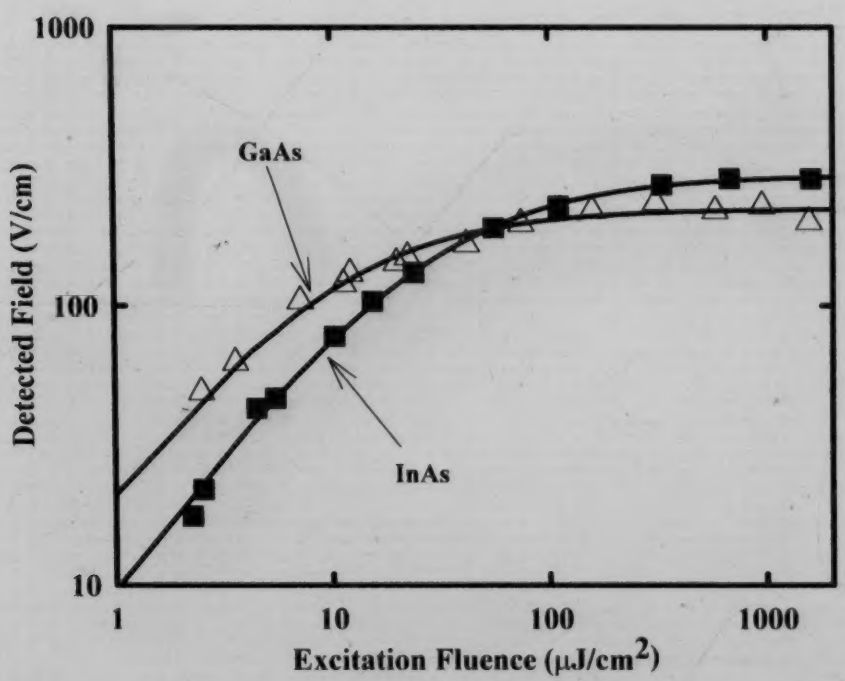

Figure 4.2: Detected peak THz field as a function of excitation fluence for the two emitters used. Open triangles represent signals from GaAs LAPCS biased at 1.6kV/cm, and filled squares represent signals from (100) InAs. The solid lines are least-squares fits of saturation curves to the data.

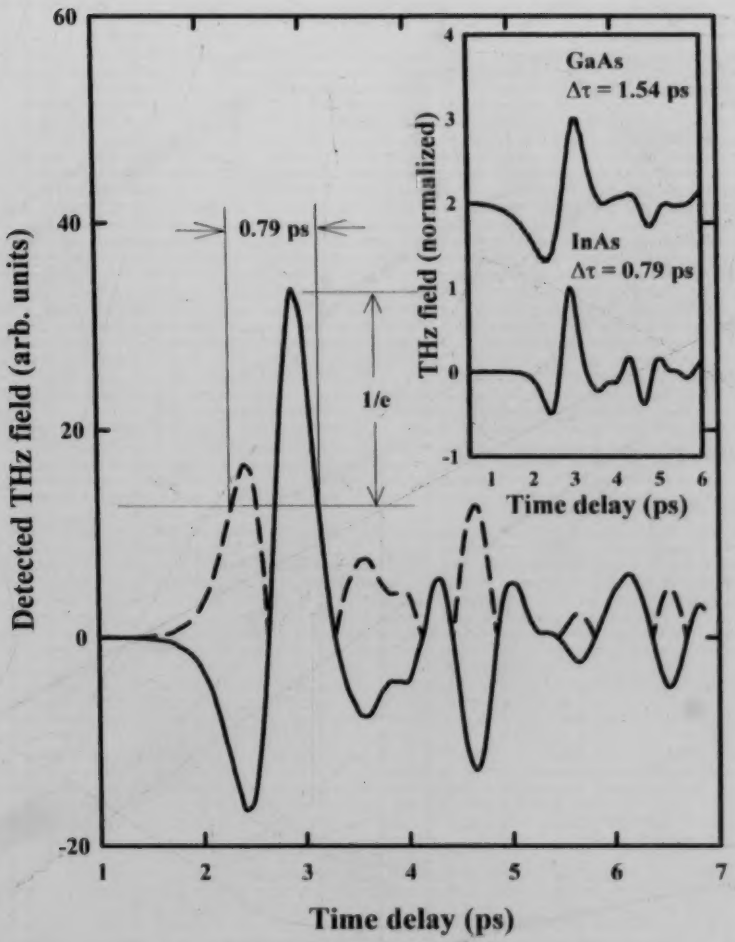

Figure 4.3: Terahertz time-domain signal radiated from the InAs emitter as a function of the time-delay (solid) and the absolute value (long-dashed) of the electric-field pulse with a 1/e pulsewidth of 0.79 ps. This pulse-width is what is used in calculations (see text for details). The inset shows the waveform radiated from the LAPCS (top) and the InAs (bottom), normalized to their peak values.

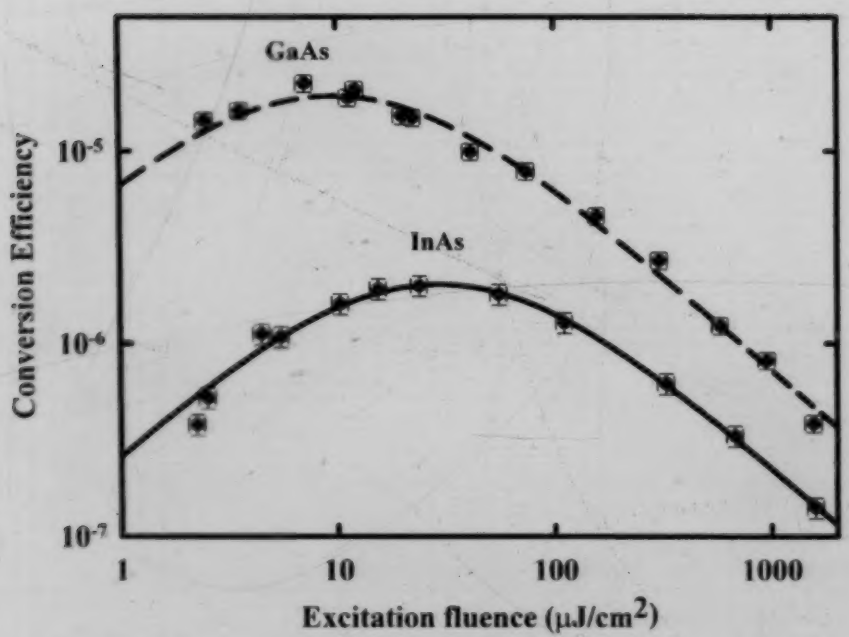

Figure 4.4: Estimated conversion efficiencies based on Equations 1-4 with parameter values as given in table 4.1. Dashed curve is for GaAs LAPCS at 1.6 $kVcm^{-1}$ bias, and solid curve is for (100) InAs.

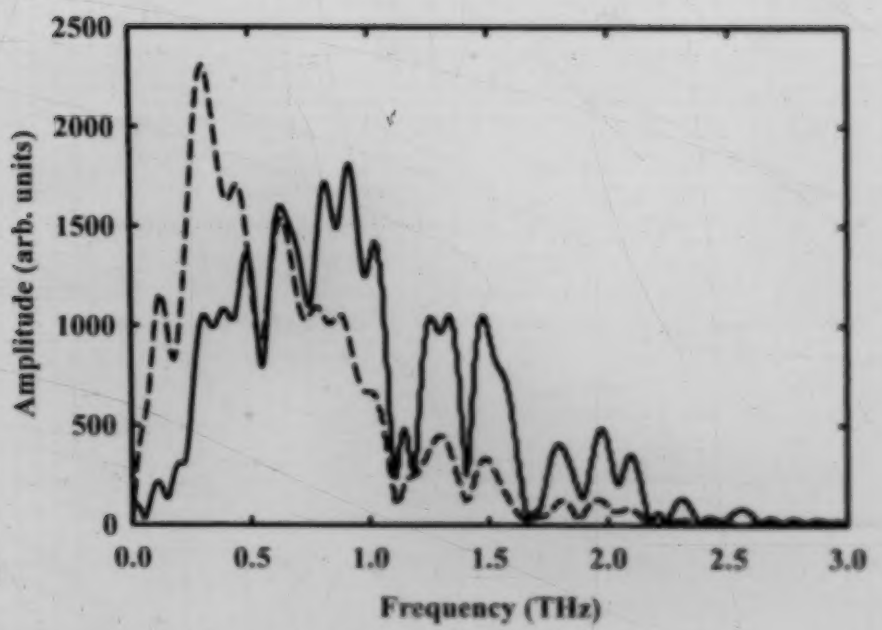

Figure 4.5: Frequency spectrum of THz fields at detector from the GaAs LAPCS biased at 1.6 kV/cm (dashed) and the (100) InAs (solid) at an excitation fluence of $1mJ/cm^2$.

Chapter 5

Terahertz radiation from InAs surfaces at high excitation fluences [1]

As found in chapter 4, the weak dependence of the terahertz emission on an applied magnetic field as the excitation fluence is scaled to higher values suggests that there is a different mechanism contributing to the terahertz emission at high fluences than at low fluences. In this chapter, a detailed analysis of the emission mechanism from InAs at high excitation fluences will be presented.

This chapter is organized as follows. The emission mechanism from InAs (100) surfaces will be introduced, where it is found that emission characteristics are comprised of at least three main mechanisms. The dominant contribution in the end is found to be an effective surface nonlinearity at high fluences, which can arise in at least two distinct forms.

Following this, the bulk dipole response of zinc-blende crystals will be calculated in detail. In order to understand the nonlinear properties better, comparisons are made to second-harmonic generation measurements showing that the emission of second-harmonic radiation from the InAs surfaces predominantly results from bulk second-harmonic generation.

The calculation of the effective second order nonlinear response resulting from surface-electric-field induced nonlinearities will be presented next, and shown to match the observed dependencies of terahertz radiation from InAs surfaces. Comparing the second-harmonic and terahertz emission measurements, the large contribution from surface-electric-field induced optical rectification is then attributed to a large third-order susceptibility.

[1] Parts of this chapter have been published in Refs. [84] and [85], and accepted for publication in Physical Review B (Apr., 2002)

5.1 Emission mechanism of terahertz radiation from InAs (100)

Traditionally, THz emission from InAs is reported to be a result of photo-excited carrier diffusion (photo-Dember effect) [60, 66]. For other wide bandgap materials such as InP and GaAs [67, 68], there is evidence that optical rectification (OR) can contribute significantly to the generation of THz radiation, which has also been reported for narrow bandgap materials such as InSb [69] and (111) InAs [66]. Recently it has been reported that there is a negligible contribution from OR in (100) InAs at low and moderate excitation fluences [66, 70, 83]. The reduced dependence of the THz emission on magnetic field at higher excitation fluences as discussed in chapter 4 strongly supports the occurrence of a workfunction different than photo-carrier effects. In this section, the dependence of the THz radiation on crystallographic orientation and pump polarization will be examined in order to determine the emission mechanism from InAs.

The setup for investigating the emission of terahertz radiation from the InAs (100) surface is the same as the reflection mode emission presented in Fig. 3.1 of section 3.1. A representatively amplified Ti:Sapphire laser system generates 800 nm, 1 kHz, 150 fs, 1.6 W pulses. The variable attenuator (1) in place and polarizer shown in Fig. 3.1 is used in the pump beam to vary the fluence. The polarizer can be removed to allow the linear polarization angle of the pump to be modified. The THz radiation from the emitter surface in a reflection geometry is collected and imaged onto the detector using 4 off-axis parabolic mirrors. The pulse is co-linearly propagated through a 1 mm thick (110) ZnTe electro-optic crystal with the THz field. The setup is polarization modulation which is analyzed using a polarization bridge (λ/4 plate and Wollaston prism) with the differential photodiode signal detected using a lock-in amplifier at the optical chopping frequency of approximately 330 Hz. The orientation of the (001) axis of the (ZnTe) crystal is varied to measure the electro-optic signal from either an n-polarized THz field as discussed in section 3.3.3. The InAs emitter is a (100) oriented undoped n-type InAs crystal illuminated at an incidence angle of 45° (unintentional bulk carrier density and [S] mobility are $1.8 \times 10^{16}\,cm^{-3}$ and $3.4 \times 10^{4}\,cm^{2}V^{-1}s^{-1}$, respectively). The pump beam is attenuated to a 0.7° intensity beam diameter of 1.08 ± 0.08 mm using a pair of lenses and the emitted radiation is collected at an angle of 45° to the surface normal in the specular direction.

The crystallographic orientation of the InAs sample was varied about the surface normal [100], while irradiating the sample with p-linearly p-polarized pump beam at an excitation fluence of approximately $2\,mJ/cm^{2}$. As seen in Fig. 5.1, the p-polarized signal consists of large constant component plus a small component with 2-fold rotational symmetry. The angularly independent component could be attributed to emission from the photo-Dember effect, which should lead to constant p-polarized output, independent of crystal rotation. It could also be attributed to a transient current resulting from the acceleration of photo-generated carriers in the surface electric field. However, the

contribution is small compared to the photo-Dember effect in InAs at low fluence [90]. For the remainder of the thesis, these two processes will be referred to as photo-carrier related effects. It is therefore tempting to attribute the emission to photo-carrier related effects, however, the pump polarization dependence of the terahertz emission will show this to not be the case.

In order to test the idea that the emission results from photo-carrier related effects, the angle of the linearly polarized pump was also varied, while maintaining the InAs crystal fixed with the [011] axis perpendicular to the plane of incidence. Both the s- and p-polarized terahertz emission was measured as the linear polarization angle of the pump beam was rotated, incident at a fluence of 1.7 mJ / cm^2. The result is shown in Fig. 5.2. There is a strong 2-fold rotational symmetry, both in the s- and p-polarized THz signals. A small part of the angular variation in the p-polarized THz signal can be due to variations in Fresnel reflectivity with input polarization since there is a difference in the transmission for p- and s-polarized radiation into the InAs (Tp = 0.81 and Ts = 0.57 for $n = 3.5$ at 800nm and 45° incidence angle). Recall that the p-polarized THz emission from the InAs (100) crystal face saturates at a fluence of 29.3$\mu J/cm^2$ as was found in chapter 4, and explicitly shown in Fig. 4.2. It should also be noted that the crystal orientation was identical in obtaining the results in Fig. 4.2 and Fig. 5.2. Since the angular dependence shown in Fig. 5.2 was measured at an incident fluence of 1.7mJ/cm^2, very little reduction in output would be expected for even a factor of two reduction of pump fluence and thus only a very small part of the rotational anisotropy shown in Fig. 5.2 can be related to Fresnel reflection effects.

Since there can be no s-polarized emission from a dipole radiating normal to a dielectric discontinuity [45], as is the case for the photo-carrier related emission mechanisms, the s-polarized THz signal in Fig. 5.2 indicates that there is a significant nonlinear optical response. Another feature of the results shown in Fig. 5.2 is that the radiated s-polarized THz field is 45° phase shifted from the p-polarized THz signal and exhibits phase reversal under polarization rotation.

The main features that must be explained by any mechanism responsible for the radiated THz field are: (i) large p-polarized isotropic signal under crystal rotation, (ii) large polarization dependence of s- and p-polarized THz signals under pump polarization rotation, (iii) 45° relative phase between the data sets of p- and s-polarized THz signals in Fig. 5.2, and (iv) the change of polarity in the s-polarized THz signal under pump polarization rotation. As will be discussed later, these can be described satisfactorily by the emission mechanism being surface optical rectification.

Both terahertz emission from optical rectification and second harmonic generation are similar second-order nonlinear phenomena described by the same second-order susceptibility terms with different responses given by the frequency dependence of these susceptibilities. However, the angular dependencies which are dependent on crystal symmetries will be the same for both processes. For the similar phenomenon of surface second-harmonic generation from (100) facets of crystals with $\bar{4}2m$ symmetry, the s-polarized emitted field is proportional to $E_x^{pump} E_y^{pump}$, while the p-polarized emitted

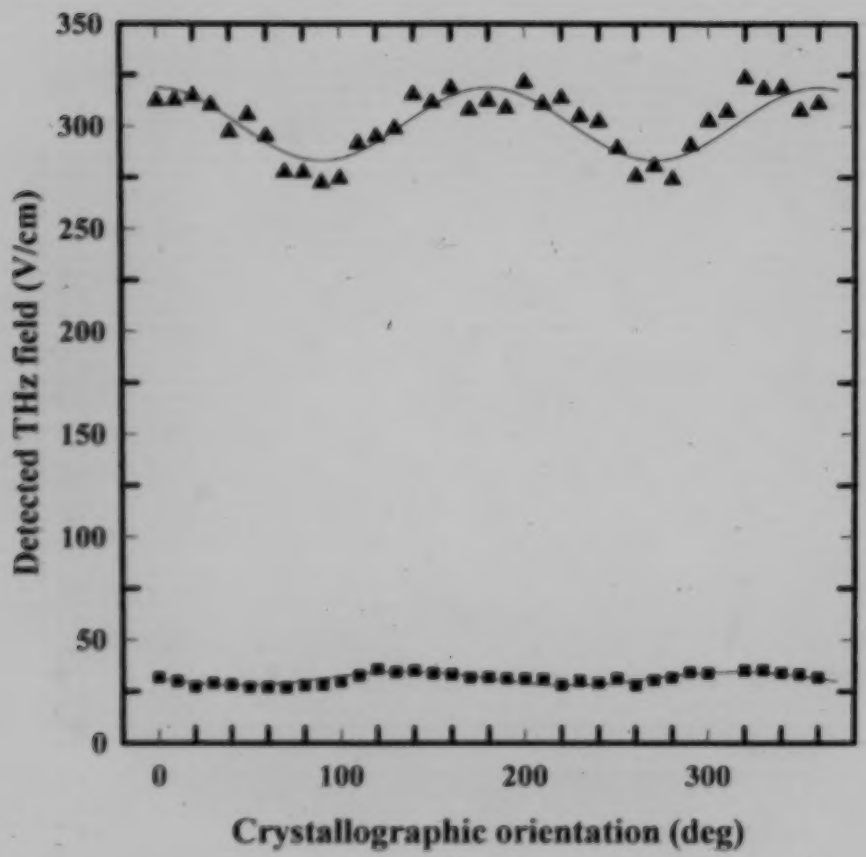

Figure 5.1: Measured p- (triangles) and s-polarized (squares) terahertz emission as a function of the crystallographic orientation for a p-polarized pump beam at a fluence of 2 mJ/cm^2 incident on (100) n-InAs surface. The orientation angle on the figure is defined as the angle that the p-polarized pump beam at the (100) face makes with the $[01\bar{1}]$ crystal direction. The solid curves are fits to the angularly dependent contributions expected from bulk optical rectification.

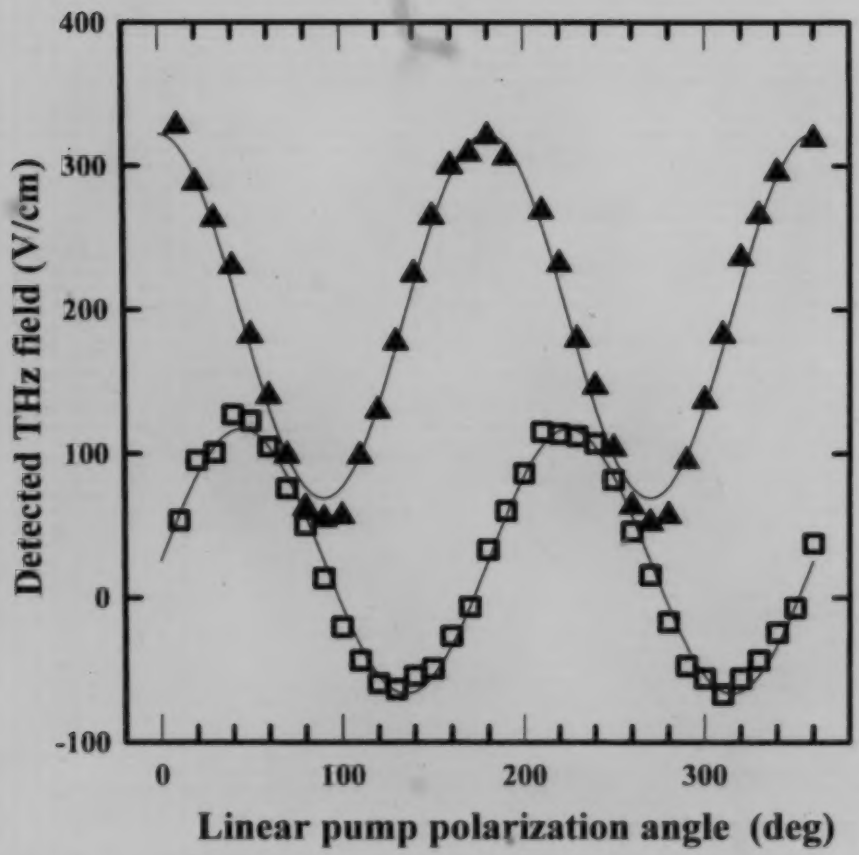

Figure 5.2: Measured p- (triangles) and s-polarized (open squares) THz fields as a function of the angle of the linear pump polarization at an incident fluence of 1.7 mJ / cm^2 incident on a (100) n-InAs surface. On the figure, 0^o corresponds to a p-polarized pump beam while 90^o corresponds to an s-polarized pump beam. The InAs crystal axes are such that the [011] axis is perpendicular to the plane of incidence. The solid curves are fits to the data based on the expected polarization dependencies (see text for details).

field is proportional to a linear combination of $(E_s^{pump})^2$ and $(E_p^{pump})^2$ [equation 30 and Table IV of Ref. [91]]. The constants of proportionality depend on the linear optical properties and the surface nonlinear tensor elements of the InAs, but not the crystallographic orientation. The emission depends only on pump polarization, consistent with observations (i) and (ii) above. The fact that there is a small non-zero s-polarized THz signal in Fig. 5.1 will be discussed later. The large s-polarized THz signal with a change in polarity and 2-fold rotational symmetry 45^0 out of phase with the data set for p-polarized THz radiation is simply described by $E_s^{THz} \sim E_s^{pump} E_p^{pump}$, and E_p^{THz} having a large $(E_p)^2$ and small $(E_s)^2$ contribution [equation 30 and table IV of Ref. [91]], consistent with (iii) and (iv) above.

At this point it is worth noting that there are other possible mechanisms that cannot be ruled out without discussion. These are electric-field induced OR [41] (similar to electric-field induced SHG [47]), bulk OR, and the quadrupolar nonlinear response of InAs.

Calculating the bulk contribution for our configuration, which is done in the following section, we find that there is no angularly independent term for either crystal or pump polarization angle rotation (see Tab. 5.3 of section 5.2.1). However, the small signal modulating the large offset of the p-polarized THz signal of Fig. 5.1 would be consistent with a small contribution from bulk OR.

Electric-field induced second-harmonic generation or optical rectification is a result of the near-surface field mixing with the third-order susceptibility resulting in an effective second order response of the material [41, 47]. It is shown later in this chapter that the symmetry class and (100) orientation of the InAs dictate that the tensor elements describing the process of electric-field induced effective second order nonlinearity are exactly in the same form as described in Ref. [91] for a pure surface response. The description in [91] is phenomenological in nature, and therefore encompasses the related process of the effective second order response due to the surface field. It is therefore impossible to distinguish between surface electric-field induced optical rectification and a pure surface nonlinear optical response with crystallographic orientation and polarization studies alone. We will refer to these two processes as the effective second order surface response of InAs.

Finally, the quadrupolar response of the InAs could lead to a large isotropic contribution under crystal rotation as was observed in Fig. 5.1. We rule out this possibility by noting that there is no 4-fold symmetric contribution observable, and the isotropic and crystallographic angular-dependent contributions from the quadrupolar nonlinearity are expected to be within a factor of 4 of each other in magnitude. This can be shown by calculating the contributions using the index of refraction of InAs and an angle of incidence of 45^o [equation 17 and table II of Ref. [91]].

Therefore, the conclusion is that the dominant emission mechanism at these high fluences is the effective nonlinear surface response of InAs. This may also explain some recent results that report a reduced dependence of THz signal strength on magnetic field as the excitation fluence is increased [82], as we have also observed in the results

presented in chapter 4, since it is expected that the magnetic field predominantly affects the directionality of moving charges in the photo-carrier related mechanisms but has little effect on the nonlinear surface mechanisms.

The residual offset in the s-polarized THz signal seen in Figures 5.1 and 5.2 cannot easily be explained by the above mechanisms, however, it is a small contribution as the s-polarized signal ($\sim 30\mathrm{V/cm}$) is only $1/10$ of the p-polarized signal ($\sim 300\mathrm{V/cm}$), which amounts to a 1 % relative power contribution. The residual effects in the p-polarized signals can also be explained from other generation mechanisms. The 2-fold rotational signal apparent under crystallographic rotation is likely due to bulk optical rectification, as will be shown later in this chapter. The relative contribution is estimated to be approximately 13% of the total signal. The offset observed for p-polarized THz signal in Fig. 5.2 is likely due to photo-carrier related effects. Assuming negligible Fresnel coupling effects (i.e. the emission is saturated), this contribution is approximately 20%. That the emission is reported to be a result of the photo-Dember effect at low excitation fluences [90, 79] may indicate that the saturation fluences for the photo-carrier related effects are substantially less than that for OR at the surface.

5.2 Bulk electric-dipole radiation

In this section, the bulk electric dipole contribution to the radiated field will be calculated. The results will be shown to be consistent with that observed for optical second-harmonic generation in a reflection geometry from InAs surfaces. The second-harmonic radiation is consistent with the expectation that bulk nonlinear optics dominates the radiation process in materials that lack inversion symmetry.

5.2.1 Calculation of bulk electric-dipole radiation

Crystalline InAs has a zinc-blende structure, possessing $\bar{4}3m$ symmetry. The second-order susceptibility tensor therefore has only six non-vanishing tensor elements, all of which are equal: $\chi^{(2)}_{xyz} = \chi^{(2)}_{xzy} = \chi^{(2)}_{yzx} = \chi^{(2)}_{yxz} = \chi^{(2)}_{zxy} = \chi^{(2)}_{zyx} = d_{14}$ [60]. In order to determine the far-infrared polarization at frequency Ω of the InAs lattice that results from an optical field at frequency ω, we compute:

$$\mathbf{P}^{(2)}(\Omega) = \chi^{(2)bulk}(\Omega; -\omega, \omega) : \mathbf{E}_{opt}(-\omega)\mathbf{E}_{opt}(\omega) \tag{5.1}$$

It should be noted that the calculation that follows is also sufficient to describe the process of second-harmonic generation, as the only difference is that the polarization of the lattice occurs at the sum frequency ($\omega + \omega = 2\omega$), whereas the far-infrared generation occurs at the difference frequency ($\omega - \omega = \Omega \sim 0$). In addition, the calculation is performed only for the bulk electric dipole contribution, and higher-order multipoles are not included.

As the second-order polarization depends on the orientation of $\mathbf{E}_{opt}(\omega)$ with respect to the crystal axes, it is useful to transform the coordinate system to the beam coordinate system [91]. Defining the $(\hat{s}, \hat{k}, \hat{z})$ coordinate system, such that the $\hat{s}$ axis is in the surface of the crystal and parallel to an input s-polarized pump beam, $\hat{z}$ is normal to the crystal surface and $\hat{k} = \hat{z} \times \hat{s}$ (see. Fig. 5.3), we can define a rotation matrix, R^{xtal}, from crystallographic coordinates to the beam coordinate system for each of the crystal faces: (111), (110) and (100) studied in the present report. For each of the crystal faces, the crystallographic coordinate system is rotated such that the $\hat{z}$ axis is parallel to the [111], [110] and [100] crystallographic axis, respectively. The rotation matrices used for each of the three crystal faces is given in Tab. 5.1.

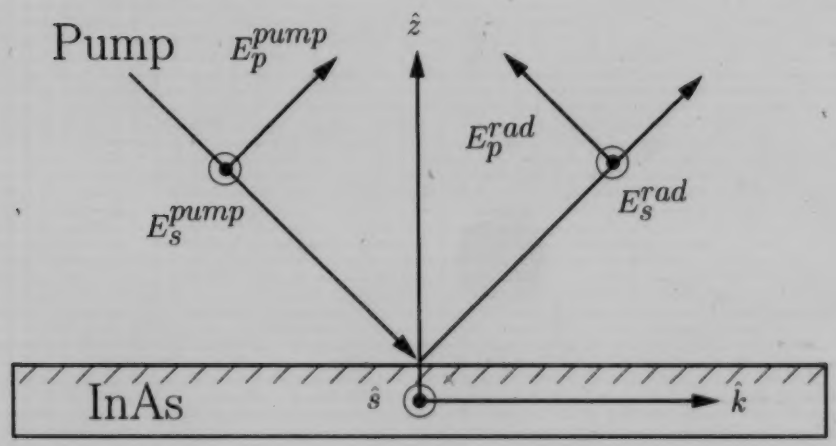

Figure 5.3: Geometry for polarizations and surface orientation of InAs wafers used in the calculations. The pump beam is linearly polarized and the s- and p-polarized radiated fields are examined.

For the bulk contribution to the radiated field, we are interested in the dependence of the THz field amplitude under crystal rotation about the surface normal. We define another rotation matrix, $R^{rot}(\phi)$, that defines the angle of rotation of the crystal about its surface normal, as well as the total transformation, R_{tot} as follows:

Table 5.1: Rotation matrices to bring crystal coordinates to beam coordinate system

Rotation matrices
(100) **crystal face where the** $[01\bar{1}]$ **axis is parallel to** $\hat{s}$
$R_{rot}^{(100)} = \begin{pmatrix} 0 & \frac{1}{\sqrt{2}} & -\frac{1}{\sqrt{2}} \\ 0 & \frac{1}{\sqrt{2}} & \frac{1}{\sqrt{2}} \\ 1 & 0 & 0 \end{pmatrix}$
(110) **crystal face where the** $[\bar{1}10]$ **axis is parallel to** $\hat{s}$
$R_{rot}^{(110)} = \begin{pmatrix} -\frac{1}{\sqrt{2}} & \frac{1}{\sqrt{2}} & 0 \\ 0 & 0 & 1 \\ \frac{1}{\sqrt{2}} & \frac{1}{\sqrt{2}} & 0 \end{pmatrix}$
(111) **crystal face where the** $[2\bar{1}\bar{1}]$ **axis is parallel to** $\hat{s}$
$R_{rot}^{(111)} = \begin{pmatrix} \sqrt{\frac{2}{3}} & -\frac{1}{\sqrt{6}} & -\frac{1}{\sqrt{6}} \\ 0 & \frac{1}{\sqrt{2}} & -\frac{1}{\sqrt{2}} \\ \frac{1}{\sqrt{3}} & \frac{1}{\sqrt{3}} & \frac{1}{\sqrt{3}} \end{pmatrix}$

$$R_{rot}^{\phi} = \begin{pmatrix} sin(\phi) & -cos(\phi) & 0 \\ cos(\phi) & sin(\phi) & 0 \\ 0 & 0 & 1 \end{pmatrix} \tag{5.2}$$

$$R^{tot} = R^{rot} R^{xtal} \tag{5.3}$$

For the (111) crystal face, ϕ is defined as the angle between the $\hat{k}$ axis and the crystal $[211]$ axis. For the (110) face, ϕ is defined as the angle between the $\hat{k}$ axis and the crystal $[1\bar{1}0]$ axis. For the (100) crystal face, ϕ is defined as the angle between $\hat{k}$ and the crystal $[01\bar{1}]$ axis. The positive direction of rotation is taken as counter-clockwise when looking outside from the surface along the direction of the $\hat{z}$ axis. From this, we can compute the susceptibility tensor in the beam coordinate system as a function of ϕ by applying the tensor transformation properties of a third rank tensor, and using the total transformation R^{tot} in Eq. 5.3:

$$\chi^{(2)}_{ijk}(\phi) = \sum_{lmn} \left(R^{tot}_{il} R^{tot}_{jm} R^{tot}_{kn} \chi^{(2)}_{lmn} \right) \tag{5.4}$$

Recall that the susceptibility tensor, in contracted notation, is given by [60]:

$$\chi^{(2)}_{ijk} = \begin{pmatrix} \chi_{xxx} & \chi_{xyy} & \chi_{xzz} & \chi_{xyz} = \chi_{xzy} & \chi_{xxz} = \chi_{xzx} & \chi_{xxy} = \chi_{xyx} \\ \chi_{yxx} & \chi_{yyy} & \chi_{yzz} & \chi_{yyz} = \chi_{yzy} & \chi_{yxz} = \chi_{yzx} & \chi_{yxy} = \chi_{yyx} \\ \chi_{zxx} & \chi_{zyy} & \chi_{zzz} & \chi_{zyz} = \chi_{zzy} & \chi_{zxz} = \chi_{zzx} & \chi_{zxy} = \chi_{zyx} \end{pmatrix} \tag{5.5}$$

and that the second order susceptibility tensor for the $\bar{4}3m$ symmetry group before transformation is given by:

$$\chi^{(2)}_{ijk} = \begin{pmatrix} 0 & 0 & 0 & d_{14} & 0 & 0 \\ 0 & 0 & 0 & 0 & d_{14} & 0 \\ 0 & 0 & 0 & 0 & 0 & d_{14} \end{pmatrix} \tag{5.6}$$

For each element of the contracted susceptibility given in Eq. 5.5, the transformation of Eq. 5.6 is computed based on Eq. 5.4. For example, after simplification, the element χ_{xxx} is given by:

$$\frac{\chi_{xxx}(\phi)}{d_{14}} = 6 R^{tot}_{xx} R^{tot}_{xy} R^{tot}_{xz} \tag{5.7}$$

The list of all tensor elements under transformation is given in the appendix A.2, Eq. A.11.For each of the crystal faces, each of the 18 elements in Eq. 5.5 is computed using Eq. 5.4, and the transformed tensors are given in Table 5.2.

Now that the proper transformations have been derived, the lattice polarization can be obtained. That is, Eq. 5.1 can be evaluated with the expressions for the susceptibilities in Table. 5.2 for each of the three crystal faces. However, before the calculation can proceed, the optical fields within the medium must be known. Referring to Fig. 5.4, the pump fields are given by:

$$\begin{aligned} E^{in}_{s,pump} &= t_s E^{out}_{s,pump} \equiv t_s E_s \\ E^{in}_{k,pump} &= t_p f_c E^{out}_{p,pump} \equiv t_p f_c E_p \\ E^{in}_{z,pump} &= t_p f_s E^{out}_{p,pump} \equiv t_p f_s E_p \end{aligned} \tag{5.8}$$

where,

Table 5.2: Electric dipole susceptibility tensor, $\chi^{(2)}(\phi)$, in the transformed coordinate systems

Transformed susceptibilities

(100) **crystal face**

$$\begin{pmatrix} 0 & 0 & 0 & -2d_{14}sin(2\phi) & d_{14}cos(2\phi) & 0 \\ 0 & 0 & 0 & -d_{14}cos(2\phi) & -2d_{14}sin(2\phi) & 0 \\ d_{14}cos(2\phi) & -d_{14}cos(2\phi) & 0 & 0 & 0 & -d_{14}sin(2\phi) \end{pmatrix}$$

(110) **crystal face**

$$\left(\begin{array}{ccc|ccc} 3d_{14}cos(\phi)sin(\phi)^2 & \frac{d_{14}}{4}(cos(\phi)+3cos(3\phi)) & -d_{14}cos(\phi) & 0 & 0 & -\frac{d_{14}}{4}(sin(\phi)-3sin(3\phi)) \\ -d_{14}(sin(\phi)-3sin(3\phi)) & -3d_{14}cos^2(\phi)sin(\phi) & d_{14}sin(\phi) & 0 & 0 & \frac{d_{14}}{4}(cos(\phi)+3cos(3\phi)) \\ 0 & 0 & 0 & d_{14}sin(\phi) & -d_{14}sin(\phi) & 0 \end{array}\right)$$

(111) **crystal face**

$$\begin{pmatrix} -\sqrt{\frac{2}{3}}d_{14}sin(3\phi) & \sqrt{\frac{2}{3}}d_{14}sin(3\phi) & 0 & 0 & \frac{d_{14}}{\sqrt{3}} & -\sqrt{\frac{2}{3}}d_{14}cos(3\phi) \\ -\sqrt{\frac{2}{3}}d_{14}cos(3\phi) & \sqrt{\frac{2}{3}}d_{14}cos(3\phi) & 0 & \frac{d_{14}}{\sqrt{3}} & 0 & \sqrt{\frac{2}{3}}d_{14}sin(3\phi) \\ -\frac{d_{14}}{\sqrt{3}} & -\frac{d_{14}}{\sqrt{3}} & 2\frac{d_{14}}{\sqrt{3}} & 0 & 0 & 0 \end{pmatrix}$$

$$\begin{aligned} f_s &= \frac{\sin(\Phi)}{n} \\ f_c &= \sqrt{1-f_s^2} \\ t_p &= \frac{2\cos(\Phi)}{n\cos(\Phi)+f_c} \\ t_s &= \frac{2\cos(\Phi)}{\cos(\Phi)+nf_c} \end{aligned} \tag{5.9}$$

where t_s and t_p are the Fresnel transmission coefficients and f_s and f_c would be the sine and cosine of the angle inside of the medium (Φ' of Fig. 5.4) if n were real. Using these definitions, we may therefore write the total polarization of the medium due to

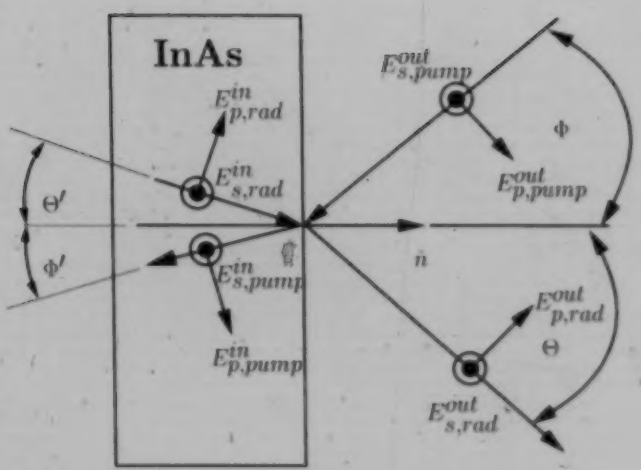

Figure 5.4: Geometry for the calculation involving the transmitted pump fields into and the radiated fields out of the nonlinear medium. The angle Φ is the angle of incidence with respect to the surface normal, $\hat{n}$, and the angle Θ is the generated radiation propagation direction taken to be the specular direction.

the incident optical field as:

$$\mathbf{P}_{NL}^{(2)} \equiv \begin{pmatrix} P_s \\ P_k \\ P_z \end{pmatrix} = \chi^{(2)}(\phi) : \begin{pmatrix} t_s^2 E_s^2 \\ t_p^2 f_c^2 E_p^2 \\ t_p^2 f_s^2 E_p^2 \\ 2t_p^2 f_s f_c E_p^2 \\ 2t_s t_p f_s E_s E_p \\ 2t_s t_p f_c E_p E_s \end{pmatrix} \tag{5.10}$$

Using table 5.2 combined with equation 5.10, we obtain explicit expressions for each independent component of the lattice polarization in the beam coordinate system, i.e. P_s, P_k and P_z, for each of the three crystallographic faces. This requires some algebra, resulting in relatively long expressions. These are given in appendix A.2, in Eq. A.12.

With the expressions for the three independent lattice polarizations, for each of the crystal faces, we may now derive expressions for the radiated field, either second-harmonic or far-infrared emission. To do this, we introduce the notation from Hübner [92] and write:

$$E_{s,rad}(\Omega) = A_s \Omega L_{eff} P_s^{bulk} \tag{5.11}$$

and

$$E_{p,rad}(\Omega) = A_p \Omega L_{eff} (F_s P_z - F_c P_k) \tag{5.12}$$

where we have written the expressions for far-infrared radiation, Ω, however, they hold equally well for second-harmonic generation at frequency 2ω. In this case F_s and F_c would be the sine and cosine of the angle of the generated radiation within the medium (Θ' of Fig. 5.4), and A_p and A_s are as defined in Hübners paper [92], which are all given by:

$$\begin{aligned} F_s &= \frac{\sin(\Theta)}{N} \\ F_c &= \sqrt{1 - F_s^2} \\ A_S &= \frac{2\pi T_s}{\cos(\Theta)} \\ A_p &= \frac{2\pi T_p}{\cos(\Theta)} \\ T_p &= \frac{2\cos(\Theta)}{N\cos(\Theta) + F_c} \\ T_s &= \frac{2\cos(\Theta)}{\cos(\Theta) + NF_c} \end{aligned} \tag{5.13}$$

where N is the index of refraction for the generated radiation within the nonlinear

medium.

Taking the appropriate expressions for each crystal face from Table 5.2, and using Eq. 5.1 together with equations 5.12 and 5.11 we may obtain the results for the different polarization combinations. For example, substituting in $E_s = 0$ in the polarization expressions and computing Eq. 5.12 yields the results for the p-in p-out polarization geometry, whereas substituting $E_s = 0$ in Eq. 5.11 yields the p-in s-out geometry and so on. The results are tabulated in table 5.3, where Ω is either the far-infrared or second-harmonic frequency, depending on the situation of interest.

Table 5.3: THz or SH field strengths for different polarization combinations. Combinations are listed as $E_{in,out}$.

Bulk dipole nonlinear response
(111) crystal face
$E^{THz}_{p,p} = \frac{1}{\sqrt{2}} A_p L_{xyz} \Omega d_{14} t_p^2 E_p^2 \times$
$\left[(2F_x f_x^2 - F_x f_z^2 + 2F_z f_x f_z) - (\sqrt{2} F_z f_z^2) \cos(3\phi) \right]$
$E^{THz}_{p,s} = \sqrt{\frac{2}{3}} A_s L_{xyz} \Omega d_{14} t_p^2 f_z^2 E_p^2 \sin(3\phi)$
(100) crystal face
$E^{THz}_{p,p} = A_p L_{xyz} \Omega d_{14} t_p^2 E_p^2 \left[2F_z f_x f_z - F_x f_z^2 \right] \cos(2\phi)$
$E^{THz}_{p,s} = -2 A_s L_{xyz} \Omega d_{14} t_p^2 E_p^2 f_x f_z \sin(2\phi)$
(110) crystal face
$E^{THz}_{p,p} = A_p L_{xyz} \Omega d_{14} t_p^2 E_p^2 \times$
$\left[(2F_z f_x f_z - F_x f_z^2 - \frac{1}{2} F_x f_y^2) \sin(\phi) + \frac{3}{2} F_x f_y^2 \sin(3\phi) \right]$
$E^{THz}_{p,s} = A_s L_{xyz} \Omega d_{14} t_p^2 E_p^2 \left[(\frac{1}{2} f_y^2 - f_z^2) \cos(\phi) + \frac{3}{2} f_y^2 \cos(3\phi) \right]$

5.2.2 Measurements of optical second-harmonic generation from InAs

Optical second-harmonic generation (SHG) from the InAs samples was investigated as a function of crystallographic orientation and for three crystal faces: (100), (110) and (111). The optical pump source used was identical to the experiments involving THz radiation (Spectra-physics Hurricane), and the set-up is shown schematically in Fig. 5.5. The Ti:Sapphire pump laser beam was passed through a polarizer to select p-polarized

pump and was incident at 45° on the InAs sample. The pump fluence was adjusted to approximately $1mJ/cm^2$ incident on the sample surface. A low-pass filter was used to block the second harmonic leakage from the laser system prior to striking the sample surface. The reflected SH radiation at 400 nm wavelength was collected using a 7.5 cm focal length lens and passed through a high-pass filter to block the fundamental beam. A UV polarizer was used to pass only the p-polarized or s-polarized second harmonic radiation at 400 nm to a Hamamatsu R7518 photo-multiplier tube, which was in turn blocked by a 400 nm interference filter to remove any further leakage of the 800 nm fundamental beam.

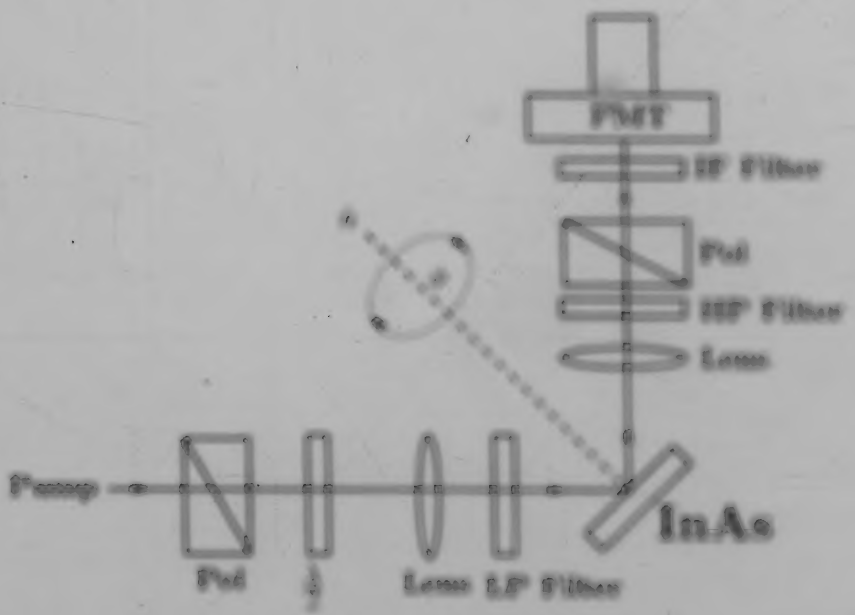

Figure 3.5: Experimental set up for SHG measurements. Pol are polarizers, LP Filter is a low-pass filter, HP Filter is a high-pass filter, IF Filter is an interference filter, PMT is a photo-multiplier, $\frac{\lambda}{2}$ is a half-wave plate. The InAs sample are rotated about their surface normal ($\hat{n}$) by an azimuthal angle ϕ.

The samples are rotated about their surface normal, and the SH intensities are measured as a function of the azimuthal angle ϕ. The results are shown in Fig. 3.6.

Note that the SH intensity as a function of the azimuthal angle ϕ is described very well by the solid curves in Fig. 3.6, which are fits to the data based on the

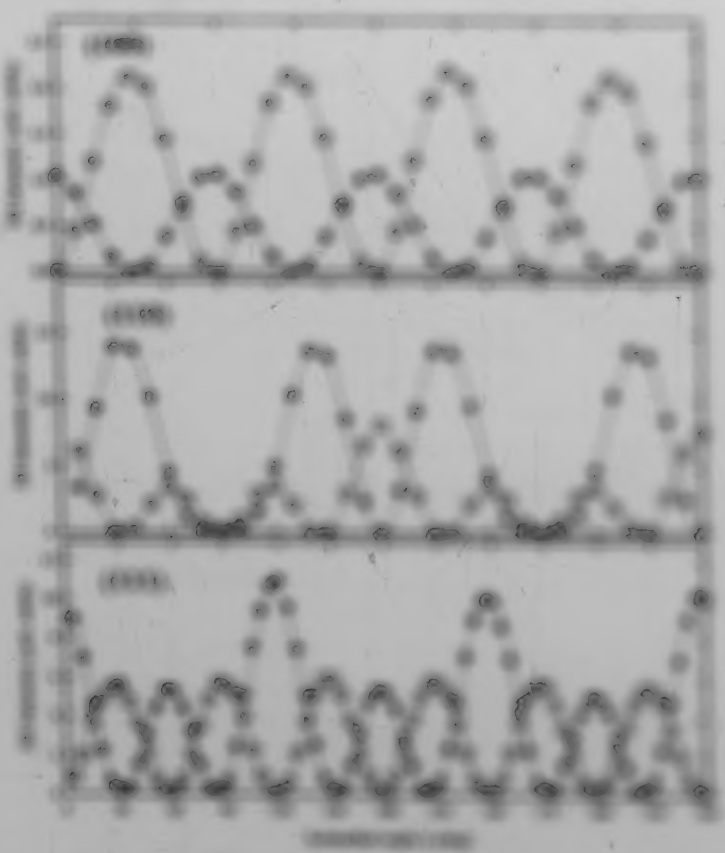

Figure 5.6 Rutherford backscattering of GaN (1um) (100), (110) and (111) faces of cubic crystals at approximately 1×10^{15} ions/cm^2 exposure fluence for a particular group reference. The solid curves represent the best fitted computed for the multi-electric dipole oscillation using the results in Table 5.2. While circles represent experimental RBS channeling and open circles represent computed RBS channeling. The horizontal axis is defined as the angle that the projection of the ions beam in the surface plane of the crystal (i.e. [1g. 5.5] makes with the [01]. [100] and [11] crystal axis for the (100), (110) and (111) crystal faces respectively. The plots are shown in the same scale.

appropriate azimuthal dependencies listed in Table 5.3, expected for a bulk electric dipole contribution to the SH radiation. In general, for crystals that lack inversion symmetry, it is expected that the bulk electric dipole contribution to the SH radiation dominates any contribution from the surface terms [93, 94, 95, 96].

We can verify that the azimuthal dependencies are as expected from Table 5.3, by least squares fitting the derived angular functions to the data. For the (111) and (110) crystal faces these are (with the notation $I_{input,output}$): $I_{pp}^{SH,111} = (a_1 + b_1 cos(3\phi))^2, I_{ps}^{SH,111} = (a_2 sin(3\phi))^2, I_{pp}^{SH,110} = (a_3 sin(\phi) + b_3 sin(3\phi))^2$, and $I_{ps}^{SH,110} = (a_4 cos(\phi) + b_4 cos(3\phi))^2$. The coefficients that were obtained by fitting were: $a_1 = 1.5 \pm 0.1, b_1 = 8.8 \pm 0.2, a_2 = 7.6 \pm 0.2, a_3 = 8.0 \pm 0.2, b_3 = 7.7 \pm 0.2, a_4 = 2.0 \pm 0.1$, and $b_4 = 6.9 \pm 0.2$. The error in the measured values is taken as the 3 σ fitting error obtained by fitting the data using SigmaPlot[2]. Tabulating some of the coefficient ratios in Table 5.4 together with the expected theoretical values, we find good agreement between experiment and theory. The values for the index of refraction used in the calculations for the optical pump and second-harmonic wavelengths were: $n_{opt} = 3.108 + i1.957$ and $n_{2\omega} = 3.714 + i0.432$, respectively [97].

Table 5.4: Measured and calculated values for ratios of the coefficients in the fitting functions. The ratios are obtained by using the fitting functions and the functional dependence of the radiation on the angle ϕ from Table. 5.3. Error bars on the measured values are 3 σ errors in this case.

Expected	Calculated	Measured
$\frac{a_3}{a_4} = \frac{T_p}{T_s} \frac{2F_s f_c f_s - F_c f_s^2 - \frac{3}{4} F_c f_c^2}{\frac{1}{4} f_c^2 - f_s^2}$	4.1	4.0 ± 0.2
$\frac{b_3}{b_4} = \frac{T_p F_c}{T_s}$	1.20	1.12 ± 0.04
$\frac{a_3}{b_3} = \frac{2F_s f_c f_s - F_c f_s^2 - \frac{3}{4} F_c f_c^2}{\frac{3}{4} F_c f_c^2}$	0.97	1.04 ± 0.04
$\frac{a_4}{b_4} = \frac{\frac{1}{4} f_c^2 - f_s^2}{\frac{3}{4} f_c^2}$	0.29	0.29 ± 0.02
$\frac{b_1}{b_4} = -\sqrt{\frac{2}{3}} \frac{4T_p F_c}{3T_s}$	1.32	1.28 ± 0.05
$\frac{a_2}{b_3} = -\sqrt{\frac{2}{3}} \frac{4T_s}{3T_p F_c}$	0.90	0.99 ± 0.04
$\frac{b_1}{a_4} = -\sqrt{\frac{2}{3}} \frac{T_p}{T_s} \frac{F_c f_c^2}{1/4 f_c^2 - f_s^2}$	4.6	4.3 ± 0.2
$\frac{a_2}{a_3} = -\sqrt{\frac{2}{3}} \frac{T_s}{T_p} \frac{f_c^2}{2F_s f_s f_c - F_c f_s^2 - 3/4 F_c f_c^2}$	0.92	0.95 ± 0.03

The quantities T_s and T_p in Table 5.4 are as defined in Eq. 5.13 of section 5.2.1 and are simply the SH Fresnel transmission coefficients from the InAs into air for the s- and p-polarized SH respectively. Similar results are obtained for the (100) crystal face, however a larger deviation from the calculated values was found (20%). This deviation

[2]SigmaPlot is a commercial data-analysis software package

was a result of changing the photo-multiplier bias voltage to increase the measured SH signals for the InAs (100) leading to some variations in the photomultiplier gain coefficient.

The conclusion here is that, as expected for crystals that lack inversion symmetry, the optical second-harmonic radiation is a result of the bulk nonlinear optical response of the InAs.

5.3 Electric-field induced nonlinearity

In this section, the effective second-order nonlinearity of InAs that results from a DC electric-field through the third-order nonlinear susceptibility is examined in detail. The results are calculated in the context of surface electric-field induced optical rectification. The calculations demonstrate that surface-electric field induced optical rectification have exactly the same dependence on pump polarization and crystallographic orientation as a pure surface response in cubic materials. The emission of terahertz radiation from various crystal faces of InAs is shown to be consistent with surface electric-field induced optical rectification at high optical excitation fluences.

5.3.1 Calculation of surface electric-field induced optical rectification

The third order susceptibility tensor for zinc-blende crystals with $\bar{4}3m$ symmetry, $\chi^{(3)}_{ijkl}$, has only 21 nonzero elements, 4 of which are unique: $\chi^{(3)}_{iijj}, \chi^{(3)}_{ijij}, \chi^{(3)}_{ijji}$ and $\chi^{(3)}_{iiii}$ [98]. This can lead to an effective second order nonlinearity, $\chi^{(2)eff}_{ijk}$, if a DC field is involved. In the present case, we consider a surface field in the $\hat{z}$ direction normal to the surface, resulting from the space-charge layer at the InAs / air interface. Following Germer et al. [47], the effective nonlinear susceptibility, $\chi^{(2)eff}_{ijk}$, in the electric dipole approximation, can be expanded in terms of the surface electric field, E_z^{surf}, as:

$$\begin{aligned} \chi^{(2)eff}_{ijk} &= \chi^{(2)}_{ijk}(\Omega;-\omega,\omega) + 3\chi^{(3)}_{ijkz}(\Omega;-\omega,\omega,0)(E_z^{surf}) \\ &+ 6\chi^{(4)}_{ijkzz}(\Omega;-\omega,\omega,0,0)(E_z^{surf})^2 + O((E_z^{surf})^3) \end{aligned} \tag{5.14}$$

Considering only the term of first-order in the surface field (i.e. the second term on the LHS of Eq. 5.14), we can write the effective surface electric field (SEF) induced second-order response of the system, $\chi^{(2)SEF}_{ijk}$ as:

$$\chi^{(2)SEF}_{ijk} = 3\chi^{(3)}_{ijkz}(\Omega;-\omega,\omega,0)E_z^{surf} \tag{5.15}$$

To properly examine the effective second-order surface response, we transform the susceptibility tensor to beam coordinates (as done in sec. 5.2.1), so that the surface

field lies along the $\hat{z}$ axis (see Fig. 5.3). The rotation matrices for the three crystal faces considered here are listed in section 5.2.1 in Tab. 5.1.

Using the transformation properties of a fourth rank tensor:

$$\chi^{rot}_{\alpha\beta\gamma\delta} = \sum_{lmno} R^{rot}_{\alpha l} R^{rot}_{\beta m} R^{rot}_{\gamma n} R^{rot}_{\delta o} \chi^{(3)}_{lmno}, \tag{5.16}$$

contracted with the surface field, we expect the form of the effective SEF induced second-order tensor to be:

$$\chi^{(2)SEF}_{\alpha\beta\gamma} = 3E^{surf}_{z} \sum_{lmno} R^{rot}_{\alpha l} R^{rot}_{\beta m} R^{rot}_{\gamma n} R^{rot}_{zo} \chi^{(3)}_{lmno} \tag{5.17}$$

Applying the appropriate rotation matrix, from Tab. 5.1, and evaluating each independent tensor element of Eq. 5.5 (18 in total), the transformed susceptibilities can be found. For example, the $\chi^{(2)SEF}_{xxx}$ component of the electric field induced nonlinear tensor is given by:

$$\begin{aligned}
\chi_{xxx} &= \chi^{(3)}_{iijj}(R_{xx}R_{xx}R_{xy}R_{zy} + R_{xx}R_{xx}R_{xz}R_{zz} + R_{xy}R_{xy}R_{xx}R_{zx}) \\
&+ \chi^{(3)}_{iijj}(R_{xy}R_{xy}R_{xz}R_{zz} + R_{xz}R_{xz}R_{xx}R_{zx} + R_{xz}R_{xz}R_{xy}R_{zy}) \\
&+ \chi^{(3)}_{ijij}(R_{xx}R_{xy}R_{xx}R_{zy} + R_{xx}R_{xz}R_{xx}R_{zz} + R_{xy}R_{xx}R_{xy}R_{zx}) \\
&+ \chi^{(3)}_{ijij}(R_{xy}R_{xz}R_{xy}R_{zz} + R_{xz}R_{xx}R_{xz}R_{zx} + R_{xz}R_{xy}R_{xz}R_{zy}) \\
&+ \chi^{(3)}_{ijji}(R_{xx}R_{xy}R_{xy}R_{zx} + R_{xx}R_{xz}R_{xz}R_{zx} + R_{xy}R_{xx}R_{xx}R_{zy}) \\
&+ \chi^{(3)}_{ijji}(R_{xy}R_{xz}R_{xz}R_{zy} + R_{xz}R_{xx}R_{xx}R_{zz} + R_{xz}R_{xy}R_{xy}R_{zz}) \\
&+ \chi^{(3)}_{iiii}(R_{xx}R_{xx}R_{xx}R_{zx} + R_{xy}R_{xy}R_{xy}R_{zy} + R_{xz}R_{xz}R_{xz}R_{zz})
\end{aligned} \tag{5.18}$$

All 18 elements of the susceptibility tensor are found in the same way, for each of the crystallographic faces studied here. The results are listed in appendix A.3 in equations A.13 to A.30.

Looking at each of the crystallographic faces separately, the transformed effective second order susceptibilities are found. The tensor for the (111) crystal face is given by:

$$\left(\chi^{(2)SEF}_{xyz}\right)_{(111)} = \begin{pmatrix} \partial_{11} & -\partial_{11} & 0 & 0 & \partial_{15} & 0 \\ 0 & 0 & 0 & \partial_{15} & 0 & -\partial_{11} \\ \partial_{31} & \partial_{31} & \partial_{33} & 0 & 0 & 0 \end{pmatrix} \tag{5.19}$$

where we have:

$$
\begin{aligned}
\partial_{11} &= \frac{E_z^{surf}}{\sqrt{2}}\left(-\chi^{(3)}_{iijj} - \chi^{(3)}_{ijij} - \chi^{(3)}_{ijji} + \chi^{(3)}_{iiii}\right) \\
\partial_{15} &= E_z^{surf}\left(2\chi^{(3)}_{iijj} - \chi^{(3)}_{ijij} - \chi^{(3)}_{ijji} + \chi^{(3)}_{iiii}\right) \\
\partial_{31} &= E_z^{surf}\left(-\chi^{(3)}_{iijj} - \chi^{(3)}_{ijij} + 2\chi^{(3)}_{ijji} + \chi^{(3)}_{iiii}\right) \\
\partial_{33} &= E_z^{surf}\left(2\chi^{(3)}_{iijj} + 2\chi^{(3)}_{ijij} + 2\chi^{(3)}_{ijji} + \chi^{(3)}_{iiii}\right)
\end{aligned} \tag{5.20}
$$

It should be noted that, in general, the only symmetry conditions that can be applied in the present case, due to above-band-gap excitation, and without knowing all the system resonances, is that of intrinsic permutation symmetry [60]. Given that we have optical frequency ω, far-infrared frequency Ω, and the SEF at zero frequency ($\chi^{(3)}_{ijkl}(\Omega;\omega,-\omega,0)$), the intrinsic permutation symmetry allows interchanging the second and third indices, which will reduce the independent susceptibility elements to 3: $\chi^{(3)}_{iiii}$, $\chi^{(3)}_{ijij}(=\chi^{(3)}_{iijj})$ and $\chi^{(3)}_{ijji}$. If the far-infrared frequency, $\Omega \sim 0$, is approximated as a DC field, and overall permutation symmetry holds, the number of independent susceptibility elements will be 2: $\chi^{(3)}_{iiii}$ and $\chi^{(3)}_{ijij}(=\chi^{(3)}_{iijj}=\chi^{(3)}_{ijji})$.

Similarly, applying the appropriate transformation matrices to the (110) and (100) crystal faces, we obtain the effective SEF induced second order susceptibility as:

$$
\left(\chi^{(2)SEF}_{xyz}\right)_{(110)} = \begin{pmatrix} 0 & 0 & 0 & 0 & \partial_{15} & 0 \\ 0 & 0 & 0 & \partial_{24} & 0 & 0 \\ \partial_{31} & \partial_{32} & \partial_{33} & 0 & 0 & 0 \end{pmatrix} \tag{5.21}
$$

where we have:

$$
\begin{aligned}
\partial_{15} &= \frac{3E_z^{surf}}{2}\left(\chi^{(3)}_{iijj} - \chi^{(3)}_{ijij} - \chi^{(3)}_{ijji} + \chi^{(3)}_{iiii}\right) \\
\partial_{24} &= 3E_z^{surf}\chi^{(3)}_{iijj} \\
\partial_{31} &= \frac{3E_z^{surf}}{2}\left(-\chi^{(3)}_{iijj} - \chi^{(3)}_{ijij} + \chi^{(3)}_{ijji} + \chi^{(3)}_{iiii}\right) \\
\partial_{32} &= 3E_z^{surf}\chi^{(3)}_{ijji} \\
\partial_{33} &= \frac{3E_z^{surf}}{2}\left(\chi^{(3)}_{iijj} + \chi^{(3)}_{ijij} + \chi^{(3)}_{ijji} + \chi^{(3)}_{iiii}\right)
\end{aligned} \tag{5.22}
$$

And finally for the (100) crystal face:

$$\left(\chi^{(2)SEF}_{xyz}\right)_{(100)} = \begin{pmatrix} 0 & 0 & 0 & 0 & \partial_{15} & 0 \\ 0 & 0 & 0 & \partial_{15} & 0 & 0 \\ \partial_{31} & \partial_{31} & \partial_{33} & 0 & 0 & 0 \end{pmatrix} \tag{5.23}$$

where we have:

$$\begin{aligned} \partial_{15} &= 3E_z^{surf}\chi^{(3)}_{iijj} \\ \partial_{31} &= 3E_z^{surf}\chi^{(3)}_{ijji} \\ \partial_{33} &= 3E_z^{surf}\chi^{(3)}_{iiii} \end{aligned} \tag{5.24}$$

At this point we note that the tensors in Eq.'s 5.19,5.21 and 5.23 are identical in form to the tensors representing a pure surface nonlinear optical response for cubic materials [91]. In addition, it should be noted that the tensor elements are not the same for different crystal faces; that is, $\partial_{31}^{(100)} \neq \partial_{31}^{(110)}$, for example. The expected dependence of SH or THz radiation on azimuthal angle is thus found to be functionally identical to that listed in the paper by Sipe et al. [91]. Following the above derivation for the bulk fields, the effective susceptibility is used to evaluate the nonlinear polarization. With this, the radiated fields are found in exactly the same way as for the bulk. The results are listed in Table 5.5.

The coefficients $f_s, f_c, t_s, t_p, A_s, A_p, F_s$, and F_c in Table 5.5 are as defined previously in section 5.2.1 in equations 5.13 and 5.9, and L_{eff} is the effective depth of the medium from which the medium polarization contributes to harmonic radiation. Note that ∂_{ij} of the different crystal orientations are not equivalent and are given by equations 5.20, 5.22 or 5.24 according to the crystal orientation. The angle ϕ is defined in the same way as in section 5.2.

One finds that the form of the susceptibility tensor for the SEF induced effective second-order nonlinear response is identical to that of an intrinsic surface response [91], but clearly differs from the bulk optical nonlinear response given in Table 5.3. Therefore, in general, crystal rotation measurements alone will not be able to distinguish between these two responses.

5.3.2 Terahertz emission from InAs

The experimental set-up for investigating the THz emission from the InAs samples is shown in Fig. 5.7. A regeneratively amplified Ti:Sapphire laser system (Spectra Physics Hurricane) is used as a pump source, operating at a center wavelength of 800 nm, at 1 kHz repetition rate, with a maximum pulse energy of 750 μJ and a pulse width of 120 fs (Gaussian full width at half maximum). The variable attenuator ($\lambda/2$ plate and polarizer) is used in the pump beam to vary the fluence. The THz radiation from the surface of the sample oriented at 45^o angle of incidence is collected in the specular

Table 5.5: THz field strengths for different polarization combinations. Combinations are listed as $E_{in,out}$.

Surface electric field induced nonlinear response
(111) **crystal face**
$E^{THz}_{p,p} = A_p L_{eff} \Omega E_p^2 t_p^2 \left[F_s f_c^2 \partial_{31} + F_s f_s^2 \partial_{33} - 2F_c f_s f_c \partial_{15}\right] - A_p L_{eff} \Omega E_p^2 t_p^2 \left[F_c f_s^2 \partial_{11}\right] cos(3\phi)$
$E^{THz}_{p,s} = A_s L_{eff} \Omega E_p^2 t_p^2 f_c^2 \partial_{11} sin(3\phi)$
(100) **crystal face**
$E^{THz}_{p,p} = A_p L_{eff} \Omega E_p^2 t_p^2 \left[-2\partial_{15} F_c f_s f_c + F_s f_c^2 \partial_{31} + F_s f_s^2 \partial_{33}\right]$
$E^{THz}_{p,s} = 0$
(110) **crystal face**
$E^{THz}_{p,p} = A_p L_{eff} \Omega E_p^2 t_p^2 \left[F_s f_s^2 \partial_{33} + F_s f_c^2 \partial_{32} - 2F_s f_c f_s \partial_{24}\right] + A_p L_{eff} \Omega E_p^2 t_p^2 \left[\frac{1}{2} F_s f_c^2 \left(\partial_{31} - \partial_{32}\right) - F_s f_s f_c \left(\partial_{15} - \partial_{24}\right)\right] + A_p L_{eff} \Omega E_p^2 t_p^2 \left[\frac{1}{2} F_s f_c^2 \left(\partial_{31} - \partial_{32}\right) - F_s f_c f_s \left(\partial_{15} - \partial_{24}\right)\right] cos(2\phi)$
$E^{THz}_{p,s} = A_s L_{eff} \Omega E_p^2 t_p^2 f_s f_c \left(\partial_{15} - \partial_{24}\right) sin(2\phi)$

direction and imaged onto the ZnTe detector using four F/2 parabolic mirrors. A 1 mm thick ZnTe (110) electro-optic crystal is used as detector/analyzer, which can be oriented either for sensitivity to p-polarized THz emission, or to the s-polarized THz emission as described in section 3.2.4.

The InAs samples were mechanically polished, nominally undoped, n-type single crystals of 0.5 mm thickness. The InAs (111), (110) and (100) samples had intrinsic carrier concentrations of approximately $3 \times 10^{16}\mathrm{cm}^{-3}$, $1.9 \times 10^{16}\mathrm{cm}^{-3}$ and $2.8 \times 10^{16}\mathrm{cm}^{-3}$, respectively. The carrier mobilities for the InAs (111), (110) and (100) samples were approximately 20 000 $\mathrm{cm}^2/\mathrm{Vs}$, 22 000 $\mathrm{cm}^2/\mathrm{Vs}$ and 19 000 $\mathrm{cm}^2/\mathrm{Vs}$, respectively. All values are those specified by the manufacturer.

The InAs samples were rotated about their surface normals, and the measured THz signals recorded as a function of the azimuthal orientation. The results are presented in Fig. 5.8.

The emission characteristics from each of the crystallographic faces will be discussed individually. First, the emission from the InAs (100) crystal face is re-plotted from

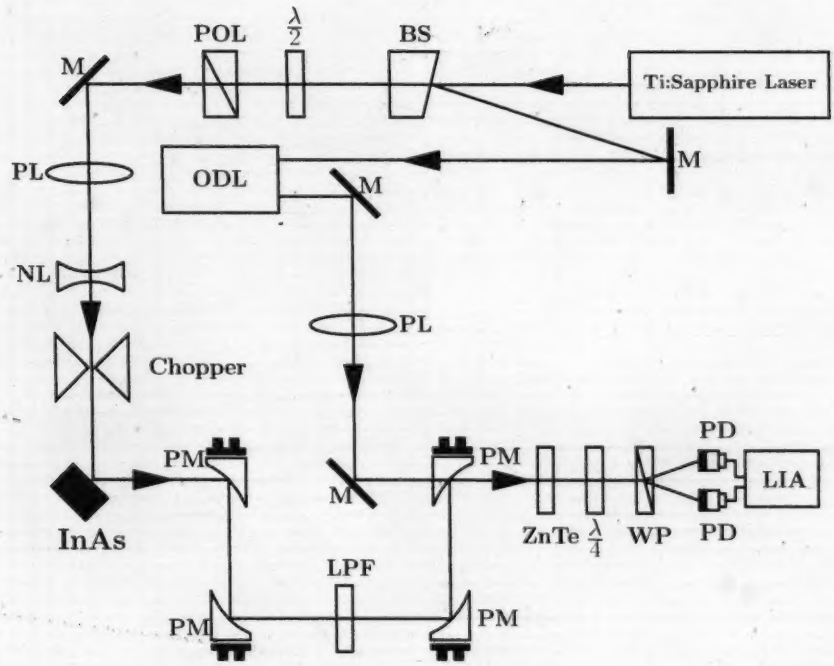

Figure 5.7: Experimental set-up for THz experiments. M are mirrors; BS is a beam splitter; $\frac{\lambda}{2}$ is a half-wave plate; PL are positive lenses; NL is a negative lens; PM are parabolic mirrors; $\frac{\lambda}{4}$ is a quarter-wave plate; LPF is a low-pass filter; PD are photodiodes; LIA is a lock-in-amplifier; WP is a Wollaston prism; ODL is an optical delay line. The arrows represent the beam propagation directions.

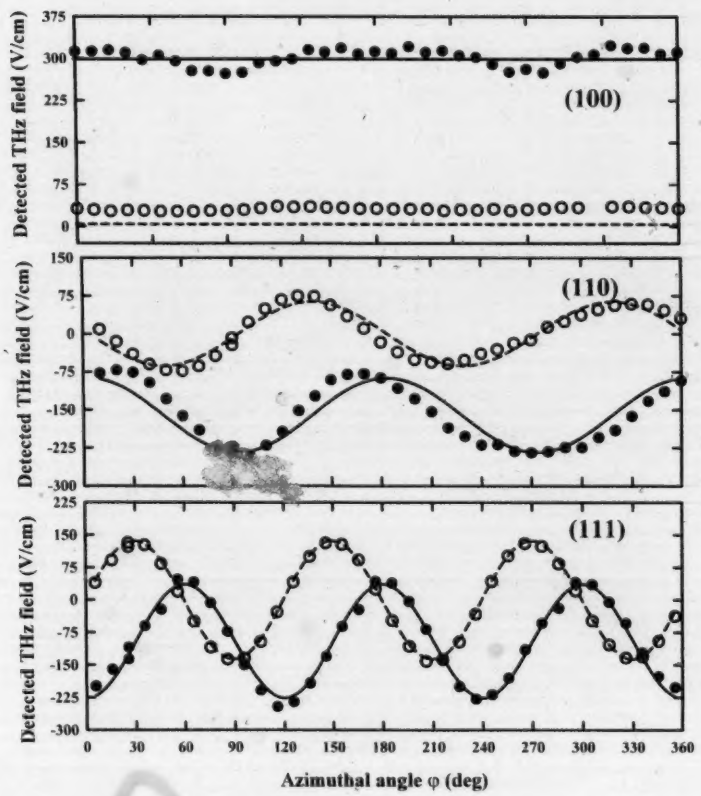

Figure 5.8: Azimuthal dependencies of THz generation from (100), (110) and (111) faces of n-InAs crystals at approximately 1 $\mathrm{mJ/cm^2}$ excitation fluence for p-polarized pump radiation. Filled circles represent detected p-polarized THz fields, and open circles represent s-polarized THz fields. The azimuthal angle is defined as the angle that the projection of the pump beam in the surface plane of the crystal ($\hat{k}$ in Fig. 5.3) makes with the $[01\bar{1}]$, $[1\bar{1}0]$ and $[\bar{2}11]$ crystal axes for the (100), (110) and (111) crystal faces respectively. The solid curves are fits to the data for p-polarized THz emission, while dashed curves are the fits to the data for s-polarized THz emission expected for surface-field induced optical rectification as listed in Tab. 5.5.

section 5.1 for comparison to the other crystal faces. In section 5.1, it was concluded that, while the emission characteristics may indicate that photo-carrier related effects dominate the emission, polarization dependencies (ie. Fig. 5.2) discount this possibility, and demonstrate that the dominant emission mechanism of THz radiation from the (100) crystal face is consistent with surface electric-field induced optical rectification.

Next we discuss the case of the (110) crystal face. Possibly the most clear evidence for the dominant contribution to THz radiation from surface optical rectification from InAs is the crystallographic dependence of the THz radiation from the (110) crystal face in Fig. 5.8. There are three observations that can be made from the results presented in Fig. 5.8 for the (110) crystal face. First, the existence of a significant angularly independent contribution to the radiated terahertz field exists. Second, the angular dependence is not what should be expected for bulk optical rectification as outlined in table 5.3. Finally, the angular dependence matches that expected for surface electric-field induced optical rectification as outlined in table 5.5 shown as solid and dashed curves for the p- and s-polarized THz emission in Fig. 5.8, respectively. However, a clear systematic deviation from the theoretical curve is obvious in the measured data for the (110) crystal face of Fig. 5.8. Each of these points will be examined next individually.

The angularly independent contribution to the radiated terahertz field may result from photo-carrier contributions to the radiated terahertz field as discussed previously in section 5.1. Given that the magnitudes of the radiated terahertz field from the (110) and (100) crystal faces are similar, and that the contribution from photo-carrier related effects radiated from the (100) crystal face was estimated to be only approximately 20% as revealed by pump polarization studies in section 5.1, the majority of the angularly independent contribution to the terahertz field for the (110) crystal face is attributed to the angularly independent contribution from surface electric-field induced optical rectification. From table 5.5, the p-polarized radiated terahertz field is expected to be of the form: $E_p^{THz} \propto c_1 + c_2 cos(2\phi)$. Therefore an angularly independent contribution is expected for the p-polarized terahertz emission from the (110) crystal face due to surface electric-field induced optical rectification. A small contribution to this angularly independent contribution from photo-carrier effects may be present as was observed for the (100) crystal face in section 5.1.

The bulk optical rectification contribution to the radiated terahertz field is predicted to be of the form: $E_p^{THz} \propto c_1 sin(\phi) + c_2 sin(3\phi)$ from table 5.3. Clearly, this dependence on orientation is qualitatively not observed. In fact, the solid curve for the (110) crystal face in Fig. 5.8 is a least squares fit to the data based on a dependence of the form: $E_p^{THz} \propto c_1 + c_2 cos(2\phi)$ expected for surface electric-field induced optical rectification from table 5.5. What can be concluded here is that the functional form expected for bulk optical rectification is not present at a significant level, and therefore, the dominant emission mechanism is consistent with surface electric-field induced optical rectification. These arguments also hold for the s-polarized terahertz emission.

Finally, the systematic deviation from the data of the theoretical angular dependence

predicted in table 5.5, shown as solid and dashed curves for the p- and s-polarized terahertz emission from the (110) crystal face in Fig. 5.8 can be explained by a contribution to the radiated terahertz field from bulk optical rectification on the order of 10%.

To demonstrate explicitly that the deviation of the data from the expected curves for the (110) crystal face presented in Fig. 5.8 may result from a smaller contribution due to bulk optical rectification, consider Fig. 5.9 for the s-polarized THz data from the (110) crystal face. The solid curve is what might be expected from a 20% contribution from bulk optical rectification: $E^{THz}_{s,detected} = c_1 cos(\phi) + c_2 cos(3\phi)$, whereas the dotted curve represents what might be expected for surface optical rectification: $E^{THz}_{s,detected} = c_1 sin(2\phi)$. If we take the sum of the solid curve and the dotted curve, we obtain the long dashed curve in Fig. 5.9. From this, it is evident that a contribution from bulk optical rectification may lead to the distortion in the data from the expected behavior for surface optical rectification. Similar results are obtained for the p-polarized THz emission, and shown in Fig. 5.10. The observation that there is a contribution to the radiated field from bulk optical rectification is consistent with the small contribution from bulk optical rectification observed as the angular modulation for the (100) crystal face in Fig. 5.8.

To summarize, there is clear evidence that the dominant terahertz emission mechanism from the (110) InAs face is surface optical rectification, with a contribution from bulk optical rectification and possible small contributions from photo-carrier related effects. The possible contribution from photo-carrier related effects would appear in the angularly independent contribution to the p-polarized terahertz field from the (110) crystal face. The existence of a partial contribution from bulk optical rectification is observed as a systematic deviation of the measured data from the expected theoretical behaviour for surface optical rectification shown as solid and dashed curves for the p- and s-polarized terahertz fields from the (110) crystal face of Fig. 5.8, respectively.

Next, we discuss the terahertz radiation from the (111) InAs crystal face. From Fig. 5.8, it is clear that a large contribution to the radiated THz field with 3-fold rotationally symmetry exists. This would be consistent with bulk optical rectification; however, the three-fold rotational symmetry is also consistent with surface electric-field induced optical rectification as is discussed next. The solid and dashed curves in Fig. 5.8 for the (111) crystal face are fits to the data of the form: $E^{THz}_{p,pk} = c_1 + c_2 cos(\phi)$ and $E^{THz}_{s,pk} = c_1 sin(\phi)$ for the p- and s-polarized THz emission respectively, obtained from table 5.3, which are also expected for surface electric-field induced optical rectification from table 5.5. Therefore, the Terahertz emission from n-InAs is consistent with emission resulting from bulk optical rectification as reported elsewhere for n-InAs and InSb at high excitation fluence [90, 88] in which only (111) crystal faces were studied. However, it is also consistent with surface electric-field induced optical rectification. Therefore, the experiments done here cannot distinguish between surface and bulk optical rectification for the (111) InAs face. However, since the emission from the (100) and (110) InAs crystal faces is dominated by surface electric-field induced optical rectification, and the

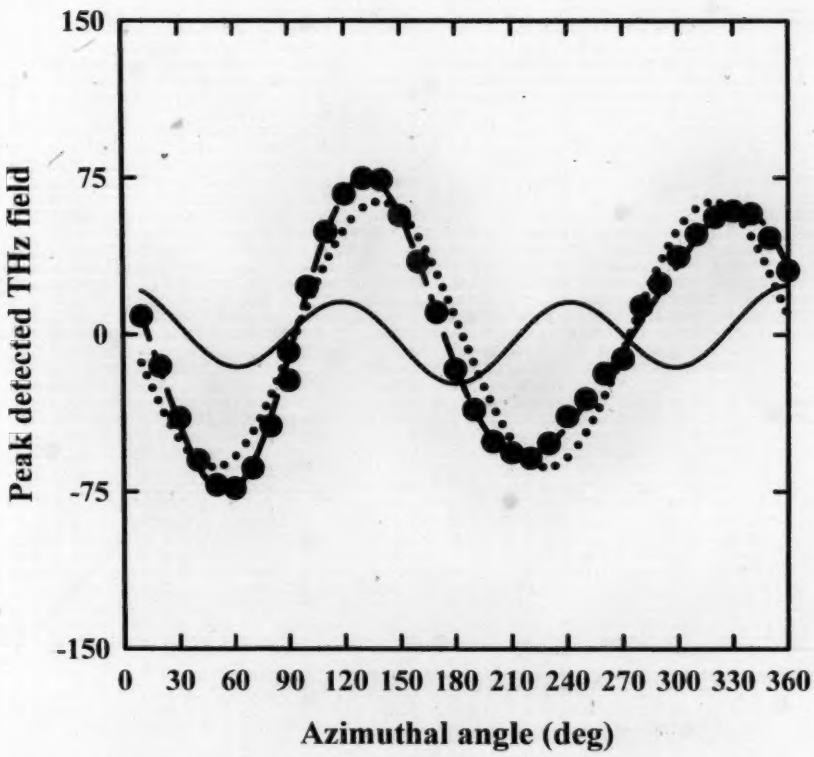

Figure 5.9: Peak detected s-polarized THz field radiated from n-InAs (110) as a function of the azimuthal angle ϕ, defined as the angle the projection of the linearly p-polarized pump beam in the (110) plane makes with the $[\bar{1}10]$ crystal axis. The data is taken at an incident fluence of approximately 1 $\mathrm{mJ/cm^2}$. The dotted line is a best-fit to the data based on the expected functional form for surface electric-field induced optical rectification. The solid curve is what might be expected for a 20% contribution from bulk optical rectification. The dashed curve is the sum of the the solid and dotted curves. The THz field scale is in units of V/cm

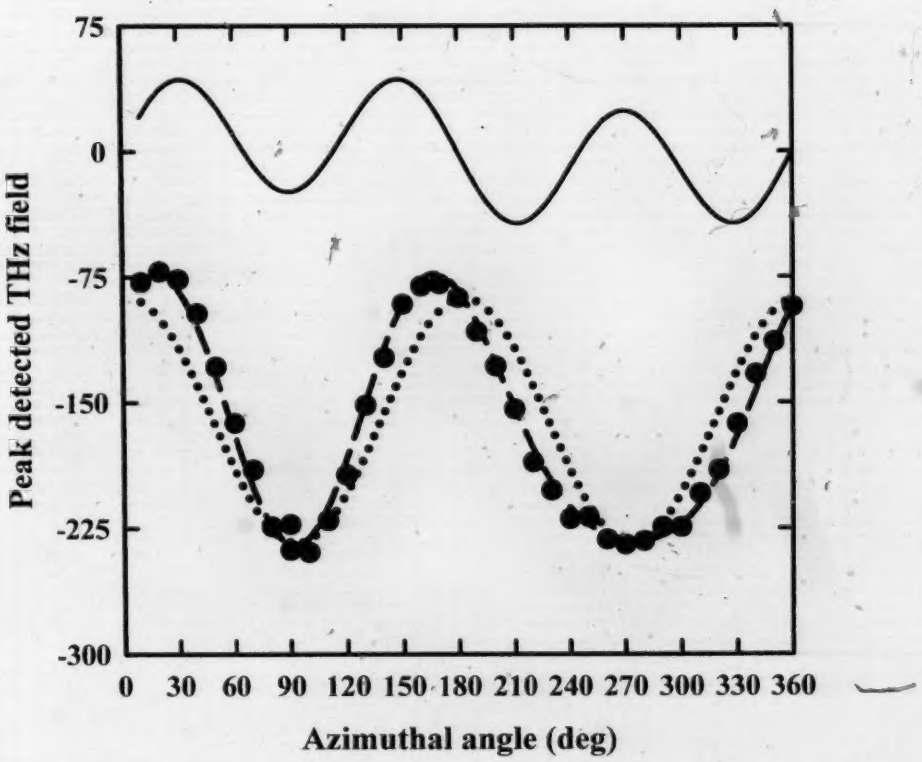

Figure 5.10: Peak detected p-polarized THz field radiated from n-InAs (110) as a function of the azimuthal angle ϕ, defined as the angle the projection of the linearly p-polarized pump beam in the (110) plane makes with the $[\bar{1}10]$ crystal axis. The data is taken at an incident fluence of approximately 1 $\mathrm{mJ/cm^2}$. The dotted line is a best-fit to the data based on the expected functional form for surface electric-field induced optical rectification. The solid curve is what might be expected for a 20% contribution from bulk optical rectification. The dashed curve is the sum of the the solid and dotted curves.

peak radiated fields are comparable from all three crystal faces, it seems likely that the emission from the (111) InAs crystal face is also a result of surface optical rectification.

The conclusion is that the terahertz emission from InAs surfaces at high excitation fluence is consistent with a pure surface nonlinear mechanism such as surface electric-field induced optical rectification. Any emission mechanism responsible for the terahertz emission from InAs at high excitation fluences must be consistent with the following observations (see figures 5.8 and 5.2):

(i) Large p-polarized angularly independent terahertz signal under crystal rotation for the (100) crystal face.

(ii) Large polarization dependence of s- and p-polarized radiated terahertz fields under pump polarization rotation for the (100) crystal face.

(iii) 45^o relative phase between data sets for s- and p-polarized terahertz fields under pump polarization rotation for the (100) crystal face.

(iv) Change in polarity of the s-polarized terahertz fields from all crystal faces.

(v) Two-fold rotational symmetry in the s- and p-polarized terahertz emission from the (110) crystal face.

(vi) Three-fold rotational symmetry in the s- and p-polarized terahertz fields for the (111) crystal face.

Photo-carrier related terahertz emission would be consistent with (i) above, however, inconsistent with (ii)-(vi) above. Bulk optical rectification would be consistent with (vi) above, however inconsistent with (i) and (v) above. A pure surface nonlinearity or surface electric-field induced optical rectification, however, is consistent with all of the observations (i)-(vi) above. Small contributions from bulk optical rectification and photo-carrier related contributions were shown to be present, but are not the dominant emission mechanisms.

5.4 Comparison of second-harmonic generation and terahertz emission from InAs

The measured azimuthal dependencies of the radiated THz field are compared to the respective SH measurements next. In Fig. 5.11, the THz emission measurements from InAs presented in section 5.3.2 are plotted with the SH measurements of Sec. 5.2. Note that as the detection for the terahertz radiation is coherent, the electric field is plotted directly (containing amplitude and phase information), whereas only the intensity of SH is plotted for the SHG data.

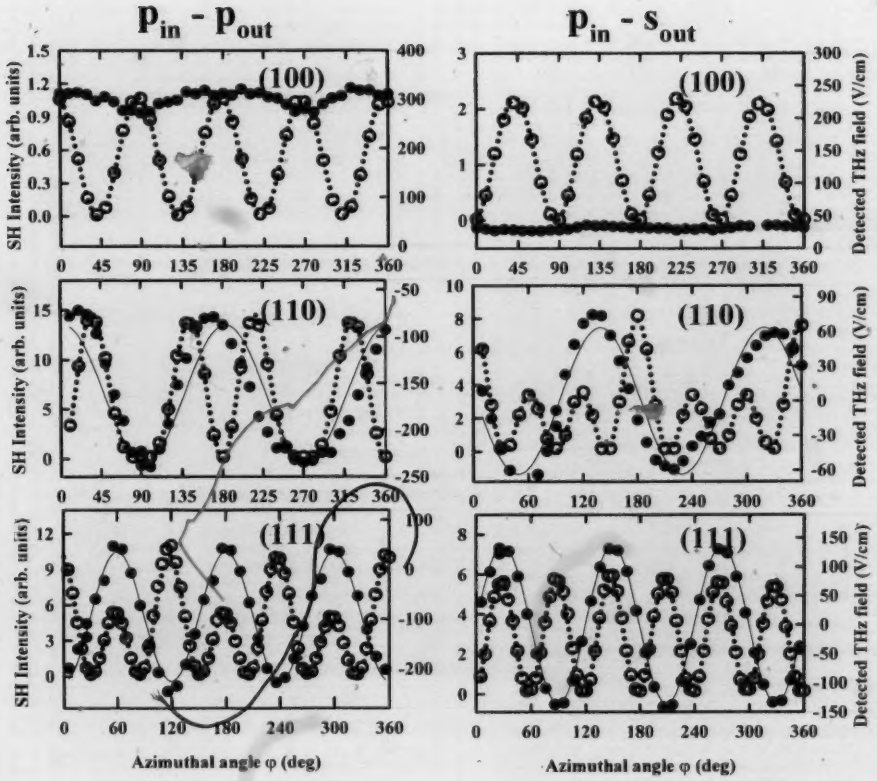

Figure 5.11: Comparison of terahertz to SH emission for p-p and p-s polarization combinations, respectively. Filled circles represent THz emission (scale on right axis), and open circles represent SH intensity (scale on left axis). The solid curves are fits to the THz data based on the expectation of surface electric field induced optical rectification (Table 5.5), and the dotted curves are fits to the SH intensity based on the expectation of bulk dipole second order response (Table 5.3). In both measurements, the data is taken at a fluence of $\sim 1mJ/cm^2$. The azimuthal angle is defined as the angle that the projection of the pump beam in the surface plane of the crystal ($\hat{k}$ in Fig. 5.3) makes with the $[01\bar{1}]$, $[1\bar{1}0]$ and $[\bar{2}11]$ crystal axes for the (100), (110) and (111) crystal faces, respectively.

It was found that for the case of terahertz emission from the InAs samples, the dominant emission mechanism is consistent with pure surface or surface electric-field induced optical rectification, whereas the optical second-harmonic generation is dominated by bulk optical rectification, as found in sections 5.2.1 and 5.3.2. This is most evident on the plots shown in Fig. 5.11.

Since optical rectification and second-harmonic generation are complementary processes, it may seem strange that they are not governed by the same process. Based on recent work [99], where varying the doping concentration in (111) InAs supported their conclusion that surface electric-field induced optical rectification is the dominant emission mechanism, it seems likely that the THz emission results from surface-field induced optical rectification rather than a pure surface response. This seems likely as a pure surface response with the symmetry demonstrated in the present report, would result from at most a few monolayers near the surface [91]. In the present case the surface is covered with a native oxide layer, and the samples are single-crystal wafers that were mechanically polished, such that a high quality surface is likely not present. Thus it is expected that the effective second-order nonlinear effect due to the surface electric-field could be the dominant contributing mechanism. Nonetheless, the azimuthal dependence of the radiation in the far-infrared due to optical rectification agrees with an effective surface response due to either or a combination of these mechanisms.

There are two important points that should be discussed. First, the fact that the second-harmonic emission from the InAs surfaces is dominated by bulk optical rectification, whereas the terahertz emission results primarily from surface electric-field induced optical rectification. Secondly, it has been reported in the literature that the terahertz emission from other semiconductor surfaces, such as InP, shows a strong contribution from bulk optical rectification to the radiated terahertz fields at high excitation fluences [43]. This raises the question as to why the dominant emission mechanism appears to differ for InAs in comparison to InP.

We begin by noting that it is expected that there is a surface-field at the mechanically polished, oxidized n-InAs surfaces used in the present study as found by Raman scattering in Ref [100], where surface-electric field induced Raman scattering was used to identify the polarity of the surface field in various orientations of InAs with varying doping concentrations. Given the narrow band-gap of InAs, it seems unlikely that there is a several order of magnitude larger surface electric field within InAs as compared to InP, which would be required to explain such a dominant contribution from surface electric field induced optical rectification observed here.

The difference in surface fields that would be required to explain the results can be estimated as follows. We assume that the susceptibilities for InAs and InP are the same ($\chi^{(3)}_{InAs} = \chi^{(3)}_{InP}$). We take the peak radiated THz field to be approximately 200 V / cm from InAs (see Fig. 5.8), and the peak radiated field from InP to be 2 V / cm (see Fig. 6.7 of chapter 6) from the (100) crystal faces respectively. Taking the angularly independent contribution to the radiated THz field from the (100) face of InP in Fig. 6.7

as completely due to surface-electric field induced optical rectification, then at most, the surface electric field induced optical rectification component from (100) InP is 50% of the bulk optical rectification contribution. Further, we assume a maximum contribution to the terahertz emission from (100) InAs due to surface electric-field induced optical rectification of 80%. Noting that the radiated terahertz fields from surface electric-field induced optical rectification are proportional to: $E_{THz} \propto \chi^{(3)} E_{surf}$, we can write:

$$\begin{aligned} E_{THz}^{InAs} &= c_1 \chi^{(3)} E_{surf}^{InAs} \\ E_{THz}^{InP} &= c_2 \chi^{(3)} E_{surf}^{InP} \end{aligned} \tag{5.25}$$

where c_1 and c_2 are constants of proportionality that depend on the linear optical properties of the material which are similar. Here, we assume that $c_1 \sim c_2$. Using the above factors, we would estimate the ratio of the required electric field to be:

$$\begin{aligned} \frac{E_{surf}^{InAs}}{E_{surf}^{InP}} &= \frac{c_2}{c_1} \times \frac{E_{THz}^{InAs}}{E_{THz}^{InP}} \\ &\simeq 1 \times \frac{0.8 \times 200 V/cm}{0.5 \times 2 V/cm} \\ &= 160 \end{aligned} \tag{5.26}$$

which seems rather unlikely. Therefore, the strong emission due to surface electric field induced optical rectification is more likely a result of a much stronger third-order susceptibility coefficient. However, if there exists a strong third-order susceptibility, there must also exist a strong frequency dependence in it as well since electric-field induced second harmonic generation is not observed to be dominant from InAs.

A strong third-order susceptibility in the narrow band-gap III-V semiconductors (InAs and InSb) is expected relative to the larger band-gap semiconductors (InP, GaAs etc), based on the theoretical calculations by Ching and Huang [101]. Third-order susceptibilities in the narrow band-gap III-V semiconductors are predicted to be several orders of magnitude larger than in the larger band-gap semiconductors [101]. Moreover, free-carrier contributions to $\chi^{(3)}$ dominate in InAs, whereas the valence-electron contribution tends to dominate in GaAs, for example [102]. Jha and Bloembergen [103] showed that the free carrier-contribution is expected to scale as :

$$\chi^{(3)}(\omega_4; \omega_1, \omega_2, \omega_3) \propto \frac{1}{\omega_1 \omega_2 \omega_3 \omega_4} \tag{5.27}$$

where ω_4 is the generated radiation frequency.

Since ω_4 is much smaller for THz generation than for second harmonic generation, this is sufficient to explain the results obtained here. That is, the far-infrared response

of the third-order susceptibility is significantly larger than the response at the second-harmonic frequency. Therefore, one would expect a much weaker surface electric field induced SH intensity in comparison to the electric-field induced optical rectification signals due to the large increase in the free-carrier contribution to the susceptibility for lower frequencies. Moreover, the third-order susceptibility in InAs is expected to exhibit resonances in the far-infrared due to longitudinal optical phonon scattering at room temperatures [104].

Assuming the THz emission is mostly a result of surface electric-field induced optical rectification, we have sufficient information with the fitting functions and the results in Table 5.5, that we can calculate the ratio of the tensor elements: $\chi^{(3)}_{ijij}/\chi^{(3)}_{iiii}$ for the (110) and (111) crystal faces. This cannot be done for the (100) crystal face as there is only 1 equation in three unknowns (surface-field, two independent tensor elements). An exact determination of the tensor elements, while possible, is complicated by lack of knowledge of the magnitude of the surface field and the fact that the emission is saturated at these high fluences. It should also be noted that the ratio $\chi^{(3)}_{ijij}/\chi^{(3)}_{iiii}$ is the measured ratio in saturation. Using the fitting functions to the data for the (110) and (111) crystal faces: $E_{pp}^{THz,111} = a_1 + b_1 cos(3\phi), E_{ps}^{THz,111} = b_2 sin(3\phi), E_{pp}^{THz,110} = a_3 + b_3 cos(2\phi)$ and $E_{ps}^{THz,110} = b_4 sin(2\phi)$. The measured values were: $a_1 = -95 \pm 7, b_1 = -130 \pm 11, b_2 = 137 \pm 8, a_3 = -160 \pm 14, b_3 = -73 \pm 18$ and $b_4 = -63 \pm 13$ in V / cm. Given the calculated values for the coefficients a_i and b_i listed in Table 5.5, the extracted ratio $\chi^{(3)}_{ijij}/\chi^{(3)}_{iiii}$ is found to be 0.30 ± 0.03 for the (111) crystal face and 0.26 ± 0.06 for the (110) crystal face. Note that the ratio b_1/b_2 is independent of the surface-field and the magnitude of the susceptibility tensor elements. It is calculated to be -1.0 in comparison to the measured value of -1.0 ± 0.1, which agrees very well. The indices of refraction used for this calculation are $n_{opt} = 3.714 + i0.432$ and $n_{FIR} = 3.868 + i0.0039$ at 1.5eV and 0.01 eV respectively [97].

The value of $\chi^{(3)}_{ijij}/\chi^{(3)}_{iiii} \sim 0.3$ is in the correct range for III-V semiconductors, but about a factor of three larger than calculated by Ching [101]. This is possibly due to the fact that the data is taken in a saturated regime.

In conclusion, while it is possible that the terahertz emission from InAs surfaces is a result of pure surface optical rectification, there is much evidence that supports the emission mechanism being surface electric-field induced optical rectification. However, it certainly has not yet been proven that surface optical rectification does not play a role in the present measurements.

Chapter 6

Terahertz emission from porous and unstructured InP [1]

In chapter 5, it was found that the terahertz emission from InAs surfaces at high fluences was primarily a result of surface electric-field induced optical rectification. Moreover, in chapter 4, it was found that the conversion efficiency from optical to far-infrared energy from the InAs surface emission was considerably less than from the large-aperture photoconductive switch. In this chapter, the possibility of increasing the conversion efficiency from optical to far-infrared energy radiated by means of enhancing the nonlinear optical processes is examined on porous surfaces. High quality porous surfaces could be obtained for InP samples from I. M. Tiginyanu and L. Sirbu at the Technical University of Moldova and thus the emission from these samples was studied and compared to emission from solid surfaces. Terahertz emission from InP (111) surfaces is examined first, where a large enhancement in the radiated energy from a porous, relative to a bulk sample is observed. The enhancement factor in this case exists primarily at lower excitation fluences, where the exact source of the radiation can be due to a number of mechanisms. By using a comparison of optical second-harmonic generation and terahertz emission by optical rectification from InP (100) at high excitation fluences, it is found that a significant enhancement of both second-harmonic and terahertz emission is observed from the InP (100) surfaces. The results indicate that the enhancement is primarily on that component of the radiated THz field that results from bulk optical rectification. The mechanism leading to the enhancement is believed to be local electric-field enhancement within the porous network.

[1] **Portions of this chapter have been published in references [105],[106] and [107]**

6.1 InP (111)

Bulk n-InP wafers and porous membranes with (111) crystallographic orientation were irradiated with 120 fs pulses of 800 nm radiation from a Ti:Sapphire amplified laser system. The terahertz emission from samples was measured as a function of excitation fluence in the reflection geometry. It was established that the terahertz emission from both bulk and porous InP (111) saturates at high excitation fluence, emitting comparable levels of far-infrared radiation. Below saturation, however, the emission from the porous InP (111) membrane was found to be approximately an order of magnitude greater in radiated electric field or approximately two orders of magnitude in power relative to the bulk sample. The observed increase in efficiency from the porous, relative to the bulk samples, can be attributed to either the local field enhancement in the porous network for the nonlinear contribution to the radiated THz fields, or to modifications of the transient currents resulting in enhanced THz radiation.

6.1.1 Experimental

As already discussed, emission from semiconductor surfaces arises from transient photocurrents radiating terahertz fields [31], as well as from nonlinear optical rectification [41, 87, 42]. For InP, at high excitation fluence, there is a strong contribution to the radiated THz field from optical rectification in the surface region within the optical penetration depth of the pump beam [87]. The conversion efficiency from optical to far-infrared energy radiated by optical pumping is lower for InP as compared to InAs. However, the emission of terahertz radiation from both InP and InAs at high excitation fluence appear to have large contributions from their nonlinear optical responses. As such, it is worth investigating methods for increasing the efficiency of these nonlinear optical interactions, in order to determine if the emission from InAs could be improved and made competitive in relation to the large-aperture photoconductive switch. Unfortunately, good quality porous InAs samples are not available to date for such studies.

It has been recently reported that electrochemical etching of GaP can introduce a large birefringence into the semiconductor, allowing phase matching for optical second-harmonic generation [108]. In addition to directly modifying nonlinear optical processes, changes in the sample surface architecture can alter the transient currents generated in semiconductors that may also modify the terahertz emission.

The porous samples were provided by I. M. Tiginyanu and L. Sirbu at the Technical Institute of Moldova. (111)-oriented substrates of n-InP single crystals with 500 μm thickness and free electron concentration of $1.3 \times 10^{18} cm^{-3}$ were used. The electrochemical etching was carried out in 5 % HCl aqueous solution in potentiostatic regime [109], the area of the samples exposed to the electrolyte was 1 cm^{-2}. A scanning electron microscope (Tescan SEM) equipped with an energy dispersive X-ray (Oxford Instruments INCA EDX) system was used to analyze the morphology and chemical composition of the porous samples. Fig. 6.1 shows an SEM image taken from a porous

InP membrane in cross-section. Note that the pores stretch perpendicular to the initial surface ($\pm 5^o$ tolerance), leaving InP walls with an average thickness of about 50 nm (see insert in Fig. 6.1), and extend 65 μm into the sample, which is deeper than the optical penetration depth of the pump beam used in the experiments ($\sim$ 300 nm for InP at $\lambda = 800$ nm). The EDX microanalysis confirmed the stoichiometric composition of the InP skeleton.

Figure 6.1: SEM micrograph of the porous InP (111) membrane. The inset shows the top view of the membrane

The experimental set-up for investigating the terahertz emission from bulk and porous InP (111) is identical to that used to study InAs in chapter 5, and is shown in Fig. 6.2. The regeneratively amplified Ti:Sapphire laser system (Spectra Physics Hurricane) is used as a source, operating at a center wavelength of 800 nm, at 1 kHz repetition rate, with a maximum pulse energy of 750 μJ and a pulsewidth of 120 fs (Gaussian FWHM). The probe pulse is delayed with respect to the pump using an optical delay line. A variable attenuator ($\lambda/2$ plate and polarizer) is used in the pump

beam to vary the fluence. The THz radiation from the surface of the sample oriented at 45^o angle of incidence is collected in the specular direction and imaged onto the ZnTe detector using four F/2 parabolic mirrors. The 1 mm thick ZnTe (110) electro-optic crystal is used as detector, oriented for sensitivity to p-polarized Terahertz emission as discussed in section 3.2.4 of chapter 3.

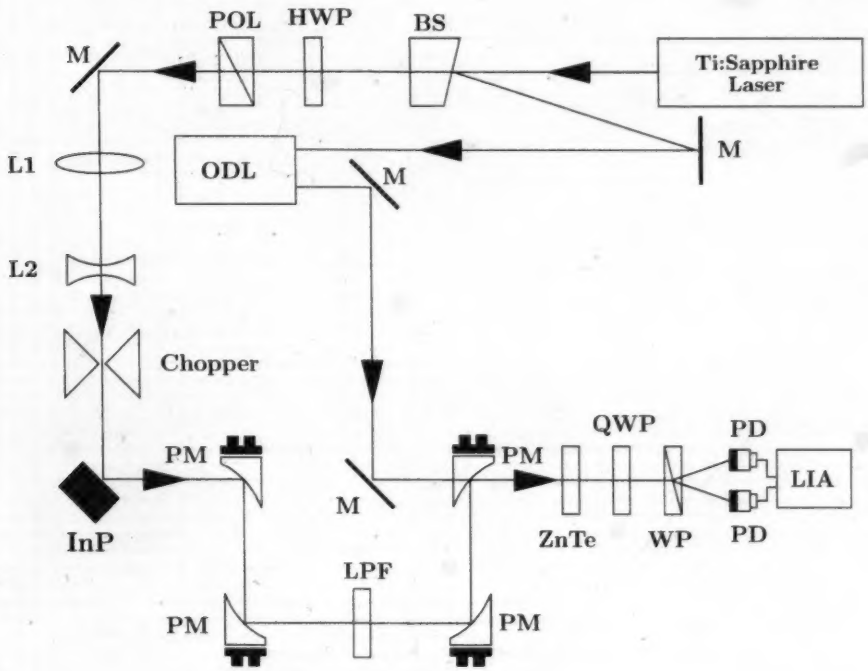

Figure 6.2: Experimental set-up for investigating THz emission from InP. The InP samples are oriented at an angle of incidence of 45 degrees. BS is a beam splitter, HWP is a half-wave plate, P is a polarizer, M are mirrors, ODL is an optical delay line, L1 and L2 are lenses, LPF is a filter used to remove the fundamental, PM are parabolic mirrors, QWP is a quarter wave plate, WP is a Wollaston prism, PD are photodiodes and LIA is a lock-in amplifier.

As previously discussed, the terahertz generation mechanism from semiconductor surfaces can be classified into two distinct categories: (i) nonlinear-optical response of the material (optical rectification), and (ii) transient photo-carrier related effects as discussed in chapter 5. Nonlinear contributions may come from bulk [87] or surface second

order nonlinearity of the semiconductor [41], or through higher order nonlinear effects [42]. Photo-carrier related effects arise as a consequence of transient photocurrents, resulting from either acceleration of carriers in the surface field [31] or from diffusion of carriers into the sample away from the surface [40] (photo-Dember effect). At high excitation fluence, there is typically a large contribution in InP from the nonlinear response of the material [87].

A typical waveform and spectrum from bulk and porous InP (111) is presented in Fig. 6.3. As can be seen, the waveforms are similar in both frequency and time, with the bulk semiconductor exhibiting slightly higher field amplitudes at frequencies above 1.75 THz than the porous membrane. The THz signals reported here are not corrected for Fresnel reflection at the detector, and suffer attenuation in the opaque beam block used to remove the fundamental beam. The beam block has a flat frequency response over the bandwidth of the detected THz signals.

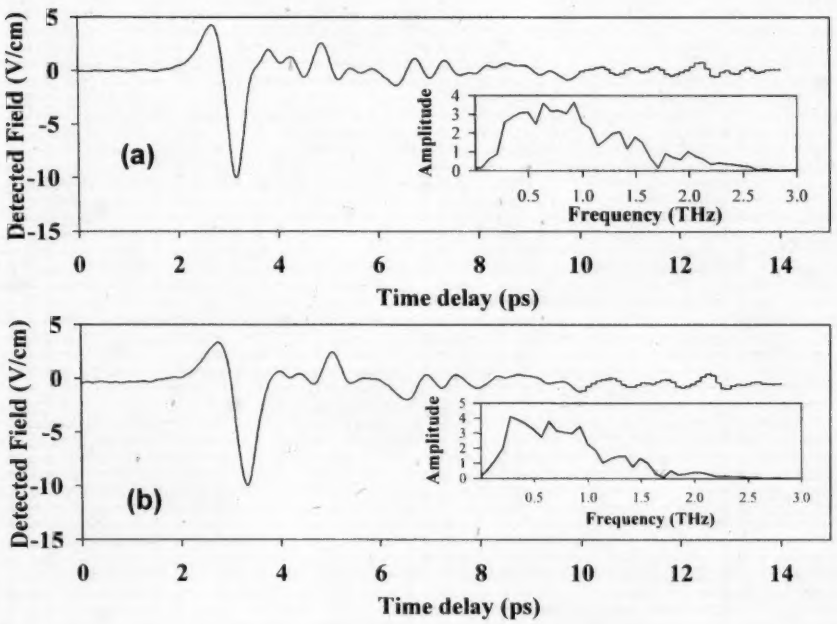

Figure 6.3: Measured terahertz waveforms in the time domain from bulk (a) and porous (b) InP (111) samples. Insets show the frequency spectrum, taken as the Fourier transform of the time-domain signals.

In order to determine if there is a measurable difference between the radiated THz fields from the bulk and porous InP (111) samples, the fluence was varied using a variable attenuator. Fig. 6.4 shows the peak detected THz field as a function of pump fluence for both bulk and porous InP samples. The measurements were made with the p-polarized pump beam parallel to the $[11\bar{2}]$ crystal axis in the (111) plane for both samples,as there is a 3-fold rotational symmetry in the measured terahertz waveforms from both porous and bulk InP (111) at high excitation fluence as shown in Fig. 6.5. The angular dependence of the terahertz field on crystallographic orientation is measured at an excitation fluence of approximately 1 mJ/cm^2 and demonstrates a contribution to the radiated terahertz field from optical rectification. In turn, the optical rectification component reflects the high crystallinity of the porous sample.

The peak THz field is seen to saturate for both bulk and porous InP (see Fig. 6.4). At lower excitation fluences, however, the peak radiated field from the porous sample proves to be substantially larger than that of the to bulk InP. At the excitation fluence of $2\mu J/cm^2$, the peak radiated THz field from the porous membrane is approximately 10 times as large as that from the bulk InP. The increased radiated field amounts to a relative power increase of approximately two orders of magnitude. Note that for an index of refraction of 3.46 at 800 nm the transmission of the pump beam into the bulk InP is T_p =0.82 (45^o incident angle, p-polarized pump and THz). The reduced Fresnel reflectivity of the porous InP due to the reduced effective refractive index could lead to enhancements of emission from porous InP on the order of 10 % relative to bulk, far smaller than the differences observed here. It is difficult to determine the origin of the increase in conversion efficiency from optical to far-infrared between porous and bulk InP (111) without knowing the exact contributions from the various processes to the radiated THz field. If one assumes that the nonlinear response is the dominant THz emission mechanism for the range of excitation fluences considered here, then the increase in conversion efficiency could result from the local field enhancement in the porous network of the membrane, as was proposed for the increase in second harmonic generation from nanostructured GaP reported in Ref. [108].

In contrast to this, if the emission were predominantly a result of photo-carrier related effects, then the observed increase of the THz radiation from porous membrane relative to the bulk can be explained by the fact that due to high density of pores most of the volume of the porous InP skeleton is subjected to the surface surface field which may contribute to the acceleration of carriers and, as a consequence, to the intensification of transient photocurrent. However, for the surface field within the walls, the lateral photo-currents from both sides of the side wall would be expected to be equal and opposite under uniform illumination, and therefore, cancel. However, asymmetry may arise as a consequence of the angled illumination of the pores from a single direction. The resultant net lateral photocurrent in the surface plane of the substrate could radiate more efficiently than the transient current generated normal to the surface for the bulk sample. One could estimate the magnitude of this effect for a given geometry, however it is expected to be small for the following reasons. The pump radiation has an absorption

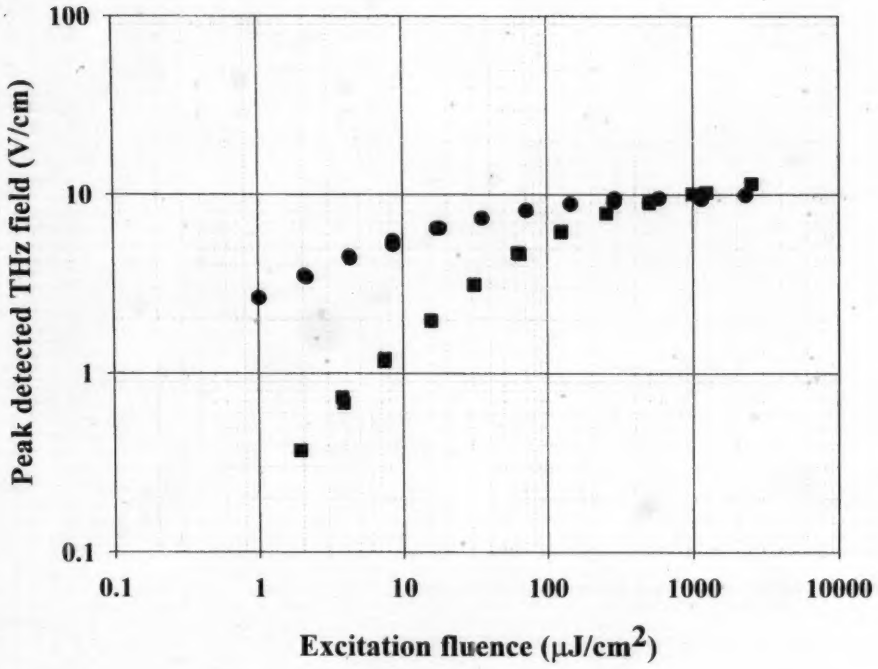

Figure 6.4: Peak detected THz field as a function of fluence for porous (filled circles) and bulk (filled squares) InP (111) samples.

depth of approximately 300 nm in the bulk material, and the wall thickness is only 50 nm. Therefore in the presence of an isotropic surface field, the optical beam will generate surge currents at both sides of the wall. The magnitudes of the radiation near each side wall, and therefore injected carrier densities, will only be slightly different as the the absorption depth is longer than the wall thickness. In this way, one would expect only a very minimal asymmetry in the net lateral photocurrents due to injected carries within the lateral surface fields. In addition, the portion of the transient current resulting from the diffusion of photo-generated carriers will predominantly flow down the pore walls. In this case, because the side-walls are open to free-space the dipole would couple efficiently out through the membrane walls. Similar arguments for enhanced emission by redirection of photo-carrier generated currents along the surface plane have been used to explain enhanced emission when an external magnetic field is applied to

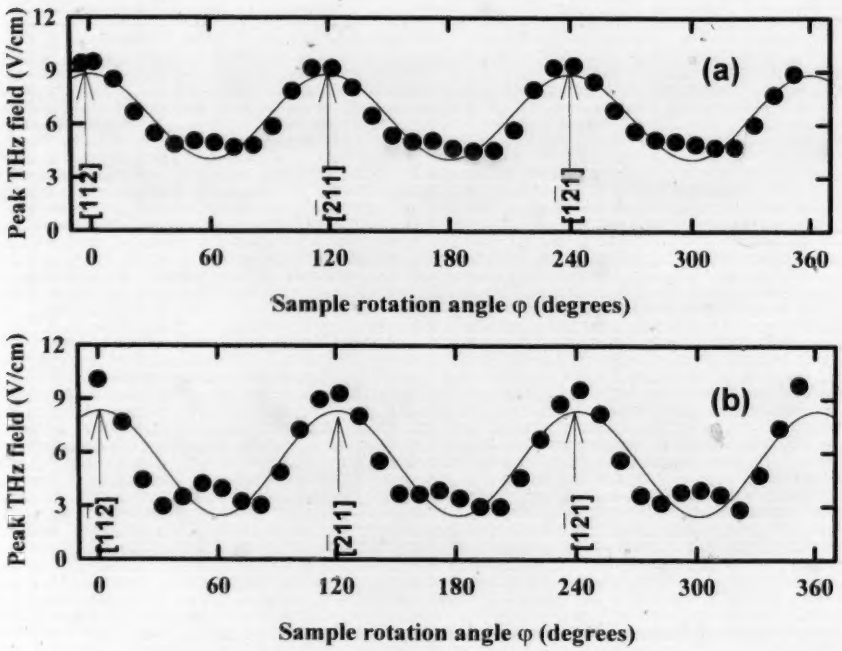

Figure 6.5: Rotational dependencies of the peak THz field radiated from bulk (top) and porous (bottom) InP (111) in the p-p polarization geometry used in the experiment. The solid curves are fits to E = A + Bcos(3ϕ).

the system [35, 36, 86].

At very low excitation fluences (1-100 nJ/cm^2) [39], the emission from InP is due to transient photocurrents, either diffusion of carriers at low temperatures or acceleration of carriers in the surface surface field at room temperature [39]. At higher fluences ($\sim$ 10 - 100 $\mu J/cm^2$), optical rectification contributes significantly to the emission [41, 87, 42]. For fluences of $1 - 1000 \mu J/cm^2$ as studied here, it is expected that there is a transition in the dominant emission mechanism. The clarification of the detailed balance of emission mechanisms in this fluence range will require further study.

6.2 InP (100)

The study of InP was extended to that of a second crystal orientation, (100), where an enhancement in the terahertz emission was observed even at high driving fields, where the nonlinear optical component is expected to dominate. By comparing the emission of THz radiation and optical second-harmonic generation from the same samples, the enhancement of both processes can be attributed to local field enhancement within the porous network. Such porous III-V semiconductors have exhibited a strongly enhanced nonlinear optical response in previous studies [108, 110, 111]. It was demonstrated experimentally that a 100-fold increase of the second-harmonic power could be achieved in porous, relative to bulk III-V semiconductors [108, 110]. The observed enhancement factor is currently the subject of investigation, and has been attributed to such processes as local field enhancement within the porous network [108], and an increased interaction of the radiation within the porous network due to scattering [110, 111].

In order to explore the effect of local field enhancement, we carried out investigations of the second-harmonic generation (SHG) and optical rectification (OR) from bulk and porous InP (100) in a reflection geometry, using pump radiation with photon energies greater than the band-gap.

It is expected that the enhancement would also exist for the related phenomenon of optical rectification (OR) which would, in turn, lead to enhanced emission of pulsed terahertz radiation from InP surfaces. However, the comparison of SHG and OR has to be done carefully as there are multiple mechanisms leading to the emission of THz radiation, the relative magnitudes of which are strongly dependent upon pump fluence [44]. To address this point, high excitation fluences are used ($1mJ/cm^2$), where optical rectification is expected to dominate the THz emission. This is confirmed by measuring the polarization characteristics of the THz radiation.

Crystalline (100)-oriented substrates of n-InP with 500 μm thickness and free electron concentration of $1.3 \times 10^{18} cm^{-3}$ were used. The electrochemical etching was carried out as described in the previous section. Fig. 6.6 shows a SEM image taken from a porous InP membrane. Note that pores with an average diameter of about 100 nm stretch perpendicular to the initial surface ($\pm 5^o$ tolerance), leaving InP walls with an average thickness of about 50 nm, which extend up to 100 μm into the sample, deeper than the optical penetration depth of the pump beam used in the experiments (300 nm for InP at $\lambda = 800$ nm). The EDX microanalysis confirmed the stoichiometric composition of the InP skeleton.

The experimental set-up for investigating the THz emission from bulk and porous InP is identical to that shown in Fig. 6.2. The InP (100) samples were rotated about the surface normal, and the detected THz fields were measured as a function of the azimuthal angle ϕ, defined as the angle that the linearly p-polarized pump beam makes with the $[01\bar{1}]$ crystal axis in the (100) crystal plane. The samples were irradiated with an incident flux of approximately $1mJ/cm^2$ in a p-pol-in p-pol-out polarization geometry. The azimuthal dependencies of the THz field are shown in Fig. 6.7. Qualitative fits to the

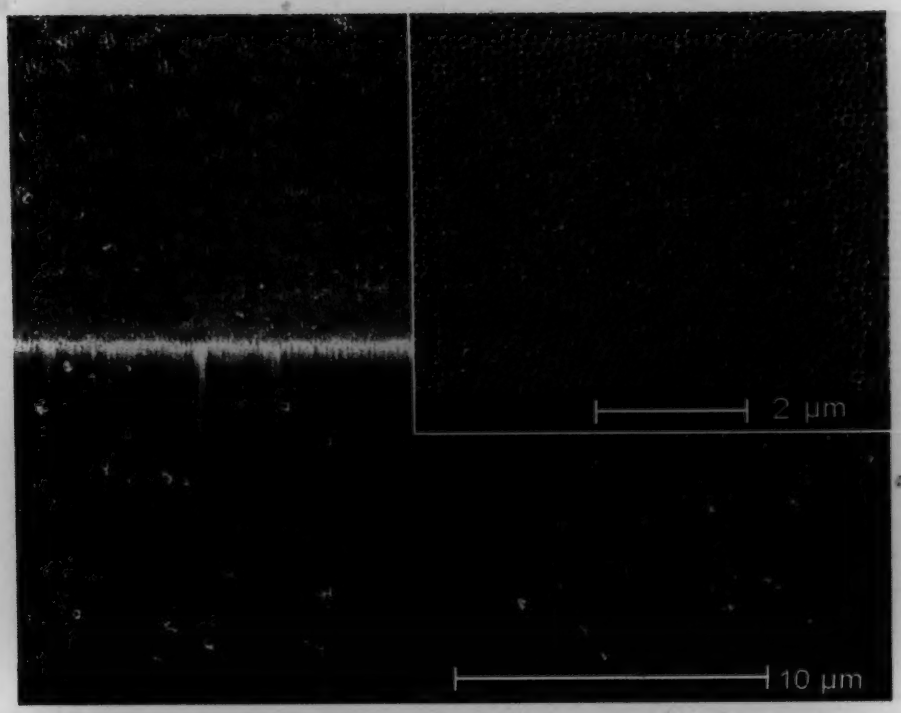

Figure 6.6: SEM image of porous InP(100) membrane.

data of the form, $E_{THZ} = a\cos(2\phi)+b$, are plotted together with the measured electric field. A change in polarity in the emitted electric field is observed from both samples as a function of the azimuthal angle. The observed angularly independent contribution to the radiated THz field may result from, e.g., photo-carrier effects [41, 42]; however, it is inconsistent with bulk OR [47]. This issue will be discussed below. What is most apparent in Fig. 6.7 is that the peak magnitude of the detected field from the bulk sample is approximately $1.6 \pm 0.25V/cm$, while the peak magnitude of detected field from the porous InP (100) membrane is in excess of $7.0 \pm 0.25V/cm$. Taking into account that the total emitted THz power scales as the square of the radiated field, this amounts to a relative power enhancement of 20 ± 4.

For InP, at low excitation fluence it has been shown that photo-carrier acceleration in the surface surface field dominates (at room temperature) [39], whereas bulk OR and photo-carrier diffusion dominate at higher fluences, with the crossover in mechanisms occurring at fluences between $0.1 - 10\mu J/cm^2$ [44].

To address the question of which process is being enhanced here, the s-polarized

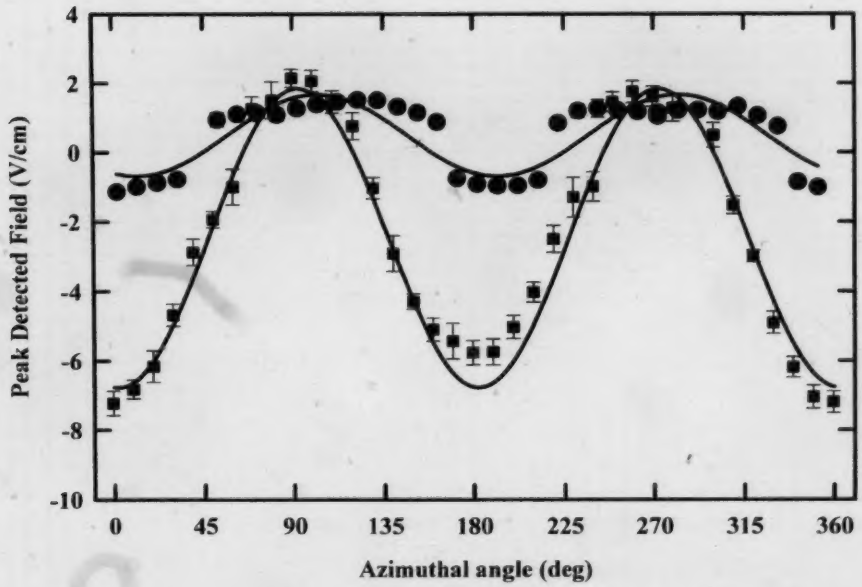

Figure 6.7: Azimuthal dependence of the p-polarized THz field amplitude in reflection from the porous (squares) and bulk (circles) InP (100) samples under p-polarized excitation. Solid lines are qualitative fits to the data reflecting azimuthal dependence.

THz emission from the porous sample was also examined as a function of the azimuthal angle. For emission from bulk samples resulting from photo-carrier effects, the generated transient current is oriented perpendicular to the surface, and cannot radiate an s-polarized wave [45], and will therefore not contribute to the THz radiation for a p-s geometry. In the porous sample, where there is the possibility of lateral photo-currents due to the more complex surface geometry, s-polarized THz radiation may be generated. Though for a perfectly symmetric system there can be no s-polarized radiation since there is no preference in which direction the s-polarized radiated field should point. Also, the emission would be expected to be angularly independent. The result for the porous sample is plotted, along with the data for the p-polarized THz emission from Fig. 6.7, in Fig. 6.8. Clearly, the s-polarized THz field is non-zero, and has the expected two-fold rotational symmetry associated with a second-order nonlinear response from (100)-oriented InP. Moreover, the angularly-independent contribution to the s-polarized THz field is less than 10 %, indicating the s-polarized THz emission is primarily due to optical rectification.

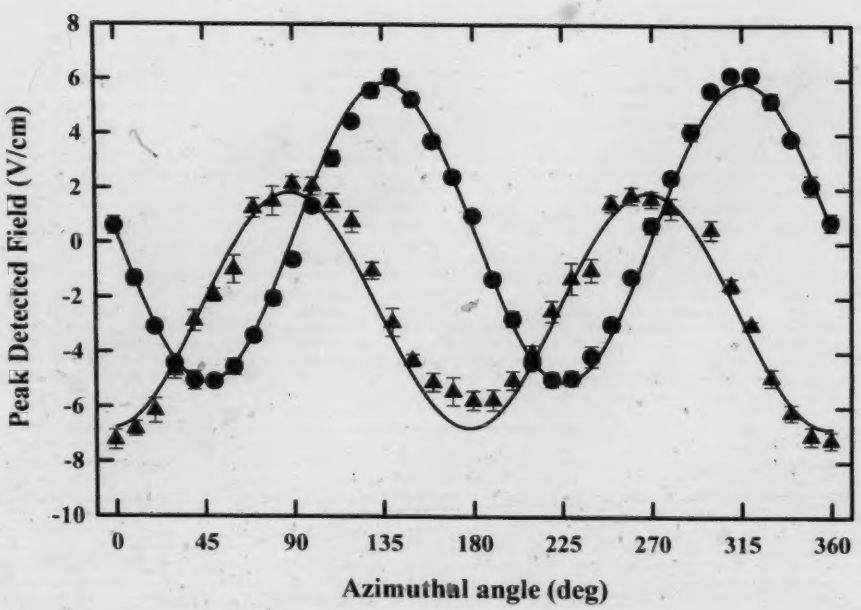

Figure 6.8: Azimuthal dependence of the p-polarized (triangles) and s-polarized (circles) THz field amplitude in reflection from the porous InP (100) sample under p-polarized excitation. Solid lines are qualitative fits to the data reflecting azimuthal dependence.

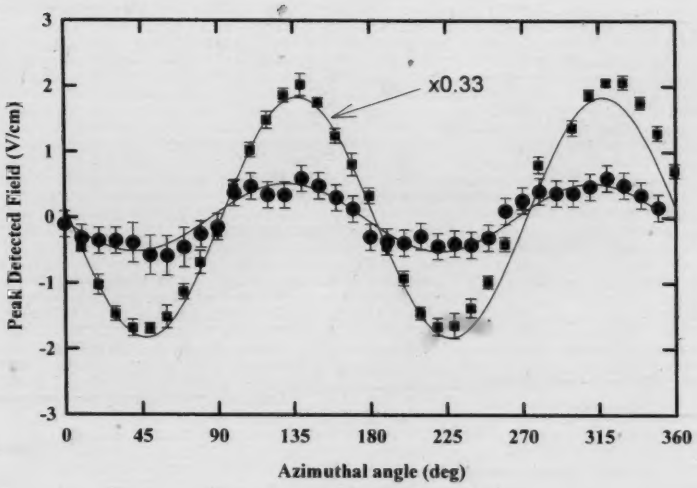

Figure 6.9: Azimuthal dependence of the s-polarized THz field amplitude in reflection from the porous (squares) and bulk (circles) InP (100) sample under p-polarized excitation. Solid lines are qualitative fits to the data reflecting azimuthal dependence.

Measurements of the s-polarized emission from the bulk InP (100) show a peak detected field of approximately $0.6 \pm 0.25 V/cm$ (maximum of the signal as a function of angle), however, the signals were close to the noise floor of our detection system. The measured data is shown in Fig. 6.9. Taking the ratio of the square of the peak detected s-polarized THz signals from porous relative to bulk InP gives a power ratio of 100 ± 40. The power enhancement factor is therefore attributed to the portion of the THz wave radiated by the process of optical rectification.

Optical second-harmonic generation (SHG) from bulk and porous InP (100) was also investigated. The same optical pump source was used. The Ti:Sapphire pump laser beam was passed through a polarizer to select p-polarized pump and incident at 45^o on the InP samples. The pump fluence was adjusted to approximately $1 mJ/cm^2$ incident on the sample surfaces. A low pass filter was used to block the second harmonic leakage from the laser cavity prior to striking the sample surfaces. The reflected SH radiation at 400 nm wavelength was collected using a 7.5 cm focal length lens and passed through a short-pass filter to block the fundamental beam. A UV-polarizer was used to pass only the p-polarized second harmonic to a Hamamatsu R7518 photomultiplier tube, which was in turn blocked by a 400 nm interference filter to remove any further leakage of the 800 nm fundamental beam. The InP samples were rotated about their surface normal. The measured azimuthal dependence of the SH intensity is shown in Fig. 6.10. The solid curve is a fit to the function: $I_{SH} = a cos^2(2\phi)$, which is expected for (100)-oriented InP. It is seen from Fig. 6.10 that the SH intensity measured from the porous sample is approximately three times smaller than measured from the bulk InP sample. Given the fact that the skeleton feature size in the porous network is comparable with the generated SH wavelength, significant scattering of the SH radiation in the porous network is expected. It is therefore expected that only a fraction of the total SH radiation generated in the specular direction from the porous sample, is detected by the photomultiplier detector system.

To test this assertion, in a separate experiment using 400 nm radiation the reflection from the porous membrane was compared to that from the bulk. For the porous sample it was determined that only 10 % of the reflected portion of the radiation was specularly reflected within a cone angle of 5.9×10^{-3} sr, whereas 90 % of the reflected radiation was diffusely reflected. If we assume that the diffusely reflected 400 nm radiation from the porous InP surface acts as a Lambertian surface and that generated SH radiation will be completely scattered into 2 π sr in the reflection (backward) direction, we may correct for the limited collection angle of the SH detection system. In our case, the effective solid angle for collecting diffusely reflected SH radiation is 0.038 sr due to the limiting aperture of the UV-polarizer in the beam path. Taking this into account, it was estimated that approximately 0.86 % of the total reflected SH radiation has been collected and detected in the present experiment. Correcting the measurement for this scattering fraction gives a measured power ratio of SH radiation from the porous membrane relative to the bulk sample of 33 ± 7.

Measurements were also made on the s-polarized SH emission and presented in Fig.

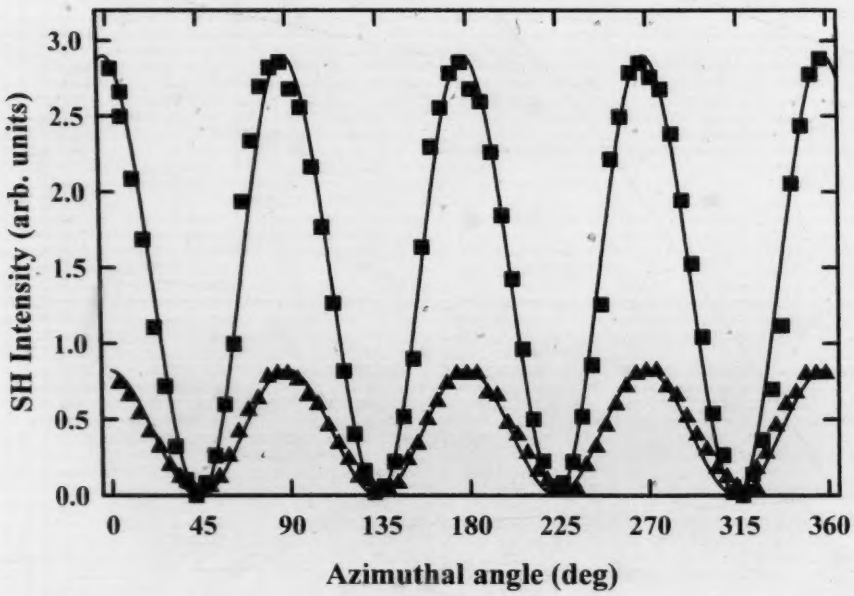

Figure 6.10: Azimuthal dependence of the p-polarized second-harmonic intensity measured in reflection from bulk (squares) and porous (triangles) InP (100) under p-polarized excitation. Solid lines are qualitative fits to the data reflecting azimuthal dependence.

6.11. In this case, the solid lines are least-squares fits of the data to the function: $I_{SH} = asin^2(2\phi)$, expected for the s-polarized SH emission. The ratio of the detected power in the SH beam from porous, relative to bulk was measured to be 0.48 ± 0.08. Again, correcting for the scattering losses, an estimated enhancement factor for the p-s geometry of 56 ± 9 was deduced. This qualitatively agrees with the observation from the terahertz emission that a higher conversion efficiency results from the porous network in the p-s as compared to the p-p geometry.

This enhancement is believed to be a result of local field enhancement within the porous network. It is well known that fields near sharp edges can be very large. The power in the SH or THz radiation scales as the input pump intensity squared, such that the output scales as the input electric field strength to the fourth power. Therefore a volumetric averaged field strength in the porous network would only have to be approximately $30^{1/4} = 2.3$ times larger than in the bulk in order to explain the results presented here.

At this point it is worth noting that an increased effective interaction length of the

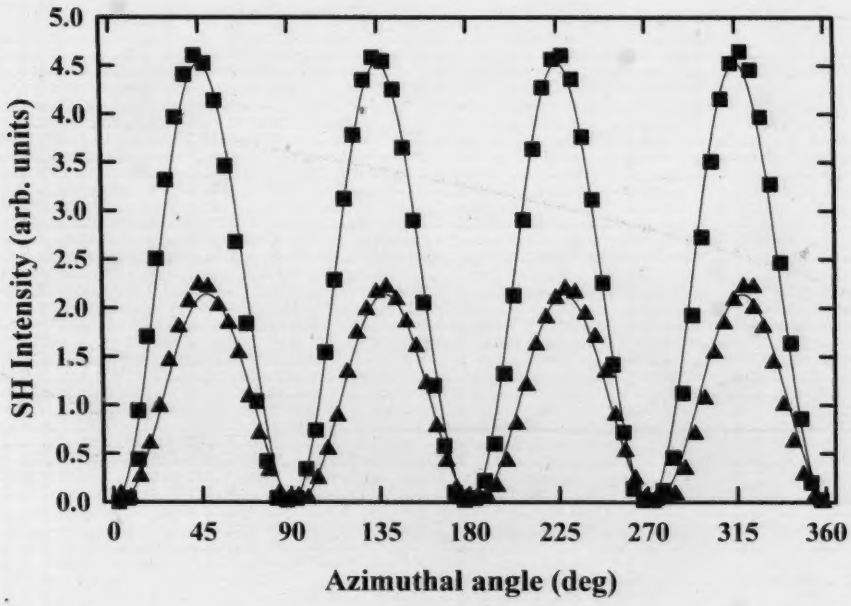

Figure 6.11: Azimuthal dependence of the s-polarized second-harmonic intensity measured in reflection from bulk (squares) and porous (triangles) InP (100) under p-polarized excitation. Solid lines are qualitative fits to the data reflecting azimuthal dependence.

fundamental and SH or THz radiation may exist due to scattering, which has also been proposed to explain the enhancement [110, 111]. We expect this effect to be minor in comparison to local field enhancement for the following reasons. First, the absorption in InP of the second harmonic beam is strong enough that the escape depth of the SH radiation limits the probed volume to a small depth. This implies that even if there were substantial scattering of the pump beam, the effective interaction length with the SH radiation is limited by the escape depth of the 400 nm light, which is much less than the optical absorption depth of the fundamental beam. For the case of THz emission, there is virtually no scattering of the THz radiation as the wavelength in this case is much larger than the characteristic sizes of the porous membrane entities. Given that the enhancement factors are qualitatively similar for THz and SHG, it seems likely that the same process governs both emissions. However, more work is required to demonstrate the exact contributions from scattering and local field enhancement to enhanced second harmonic and terahertz radiation from these porous samples.

In conclusion, it was found that a porous InP (100) membrane radiates approxi-

mately 20 times more power to the far-infrared by optical rectification of a femtosecond Ti:Sapphire laser in comparison to bulk InP(100), at an excitation fluence of $1mJ/cm^2$. Measurements made in a p-s geometry indicate that the primary enhancement comes from the optical rectification component to the radiated THz field. Measurements of the related process of second harmonic generation were made on the same samples and at the same excitation fluence. As a result, approximately 30 times more power was radiated in the second harmonic beam from the porous samples. The enhancement factor is tentatively attributed to enhancements of the local field within the porous network.

Chapter 7

Semi-large aperture photoconductive switch

In this chapter, the photoconductive switch will be examined further as an emitter of terahertz radiation in a semi-large aperture configuration. This is developed into an operational source which is based on a lower energy oscillator source of femtosecond radiation which can be used in application studies. The construction and electronics required to use this device are outlined, followed by the performance characteristics.

7.1 Description of the SLAPCS

In section 4.1 the operation of a large-aperture photoconductive switch was outlined. The idea of a semi-large aperture photoconductive switch comes from the idea of scaling the aperture down in size to accommodate a more reasonable source of optical energy in, for example, a femtosecond oscillator beam.

The use of photoconductive switches to efficiently generate far-infrared radiation from femtosecond switching using an optical beam [2] has been used for a long time, and described in detail by van Exter and Grischkowsky [3]. The use of a photoconductive switch to generate free-space terahertz radiation typically uses a co-planar transmission line with a small gap ($\sim 5\ \mu$m), which is illuminated by femtosecond optical pulses [48].

The fundamental difference in operation between the large-aperture photoconductive switch and the small-gap photoconductive switch is the limitation on the radiated field. That is, for the large-aperture photoconductive switch, the limitation on the radiated field is the terahertz field screening of the bias field within the switch [72], as described in section 4.1. In contrast to this, the limitation on the radiated field in a small photoconductive switch is the space-charge field screening of the bias field limiting the transient current. As the optical excitation pulse energy grows, the number of injected carriers grows. As the injected carrier density becomes sufficient to screen out the bias field, on the time scale of the terahertz pulse, there is a subsequent deceleration of the

carriers, leading to a bipolar waveform [112, 78].

An important note to make is that the time it takes light to propagate across the 5μm gap in GaAs (with a far-infrared index of refraction of 3.6 [25]) is approximately 60 fs, which is significantly smaller than the pulsewidth of the terahertz radiation. This implies that any space-charge accumulation in the plane of the emitter can screen out the applied bias field on the time-scale of the radiated terahertz pulse. Therefore, in addition to terahertz field screening [72], such devices suffer limitations due to space-charge screening. In fact, the space charge screening is significant, as observed directly by Uhd Jepsen et al. [112]. The question of where the cross-over from space-charge screening to terahertz-field screening occurs is difficult to answer exactly, however, one can estimate it to be roughly at the size scale where the speed of light in the substrate gives a propagation time across the gap less than the radiated THz pulse width ($\sim$ 1 ps). In such a configuration, even if there were a substantial build-up of charge carriers in the emitter surface on the time-scale of the terahertz pulse, the terahertz radiation would not respond to a screened bias field. This amounts to a gap spacing of approximately 85 μm in GaAs. For gap sizes significantly larger than this, the space-charge field will not be able to screen the internal fields on the time-scale of the terahertz radiation, and will therefore not affect the transient currents that lead to the radiation. For this case, one might expect that terahertz-field screening will limit the radiation. This would appear to be the case in the modeling calculations by Rodriguez and Taylor [78].

Having said this, it seems reasonable to want to keep the dimensions of the switch in the range where terahertz-field screening limits the radiated power, as this is the geometry that has led to the maximum reported conversion efficiency from optical to pulsed terahertz radiation [73].

The femtosecond oscillator source available in the laboratory is an 82 MHz source, operating at 800 nm, with a pulse width of approximately 80 fs, with an average power of up to 1W. Assuming the average power of 1 W can be used at the emitter (for generating terahertz radiation), then the optical pulse energy of the source is approximately 12.5 nJ. Recalling from section 4.2 that the saturation flux for GaAs photoconductive switches is approximately 12 $\mu J/cm^2$, this amounts to focusing the beam to a diameter of approximately 0.36 mm. Based on the simple estimate above, this is well within the terahertz field screening regime (ie. 0.36 mm $\gg$ 0.085 mm), such that optimal conversion efficiency might be expected. However, as the small dimension of the aperture will violate the conditions of validity ($\lambda \ll$ aperture dimension for all λ) in the theoretical analysis of the large-aperture photoconductive switch [72], differences might be expected.

This is the idea of the semi-large aperture photoconductive switch. That is, by scaling down the aperture size of the large-aperture photoconductive switch, so that optimal conversion efficiency might be expected from an oscillator source of much lower pulse energy, however not scaling down to the point where the device is limited by space-charge screening, we obtain a *semi-large aperture photoconductive switch* . Indeed, such a device has been quantified in the literature, and found to be an exceptionally efficient

source of terahertz radiation from an oscillator optical source [4, 113].

7.2 Construction of the SLAPCS

Part of the motivation for using a semi-large aperture photoconductive switch for the generation of pulsed terahertz radiation is the simplicity of construction. Specifically, as outlined above, there is no need for micro fabrication techniques or special substrate preparation. The GaAs used is a high-resistivity GaAs substrate (the carrier concentration and Hall mobility specified by the manufacturer are $n_c = 1.5 \times 10^7 cm^{-3}$ and $\mu_H = 3890 cm^2 V^{-1} s^{-1}$, respectively). Silver paint was used on the GaAs to create two elliptically shaped electrodes with a minimum separation distance of $470 \pm 12 \mu m$. Sheet copper was used to contact the silver paint, with approximate dimensions of 5 cm × 8 cm. The copper served two purposes, as an electrical contact to the electrodes, allowing connection to external bias circuitry, as well as to help keep the switch cool [4, 113]. A schematic diagram of the semi-large aperture photoconductive switch used for this chapter is shown in Fig. 7.1 (a).

In order to modulate the signal, an alternating voltage bias supply was employed capable of operation at different modulation frequencies. Bias fields up to approximately 400 V peak (800 V peak-to-peak) were required for optimal performance. Under illumination with the optical laser source, the resistivity drops dramatically, and several watts of power are dissipated in the switch. Given that the lock-in-amplifier works up to 250 kHz, it was also of interest to produce the bias fields at frequencies up to 250 kHz. Therefore the general design characteristics for the bias field driver were to operate at frequencies from DC to 250 kHz, achieve voltages as high as 800 V peak-to-peak and deliver 5W of electrical power to the semi-large aperture photoconductive switch . In addition, as the lock-in-amplifier measures the first Fourier coefficient of the signal at the reference frequency, a sine wave is desired for the driving signal. In order to achieve this, it was found that a simple (yet hard to find) operational power amplifier is available [1], capable of delivering up to 30 W of electrical power at voltages up to 900 V under the constraints listed above. This is made possible by the exceptional slew-rate of the op-amp (500 $V/\mu s$). The driver construction is relatively simple with the op-amp, and shown schematically in Fig. 7.1 (b).

7.3 Performance of the SLAPCS

In this section, the performance characteristics of the semi-large aperture photoconductive switch are described. The main characteristics of interest in the present report are the scaling of the emission with the applied bias field, the scaling with optical pump

[1] The operation amplifier was model PA94 obtained from APEX Microtechnologies (www.apexmicrotech.com).

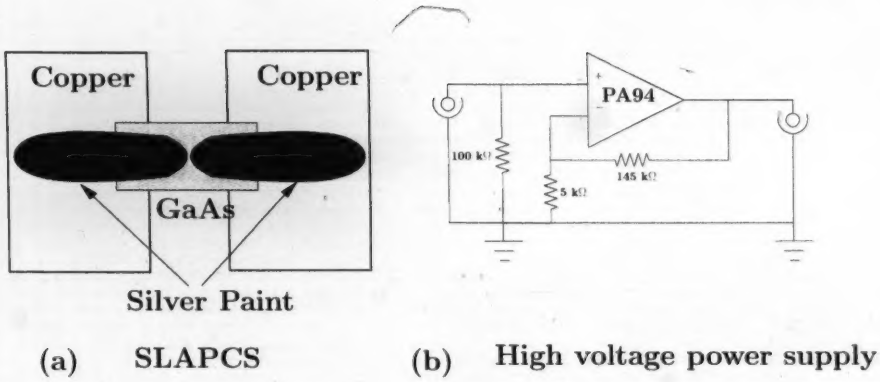

Figure 7.1: Schematic representation of semi-large aperture photoconductive switch (a) and high-voltage, high-power, high-frequency bias driver schematic diagram (b).

energy, and the scaling of the signal-to-noise with frequency of operation. Each of these will be examined individually.

7.3.1 Terahertz emission scaling with applied bias field

The experimental set-up for investigating the properties of terahertz radiation from the SLAPCS is similar to that used for the majority of the experimental work in the thesis, and is shown in Fig. 7.2.

The peak radiated terahertz field is monitored as the bias field is changed. The result is plotted in Fig. 7.3. The terahertz radiation is seen to scale nonlinearly at low bias fields, and linearly with the applied bias field at higher applied bias fields. It is expected that an emitter that behaves as a large-aperture photoconductive switch, will radiated a terahertz field that depends linearly on the applied bias field as seen in section 4.1. This appears to be the case for high applied bias fields, however, the deviation from the linear dependence at low bias fields is likely a result of the fabrication method for the switch. In this case, silver paint was applied to a semi-insulating wafer of GaAs, forming a metal-semiconductor contact. The contact may be non-ohmic, resulting in the observed dependence of the terahertz radiation on applied voltage [114].

Therefore, operation at the highest possible bias field is desired. In our case this is approximately $5.5kV/cm$, limited by the current limit in the operational-amplifier. To get higher bias fields, a higher driving current (delivering more than 5 W of power) is required. A current limit is set for the operational-amplifier, such that the operation is kept in the safe operating range, and therefore in the present configuration, the operational-amplifier cannot deliver its maximum 30W power.

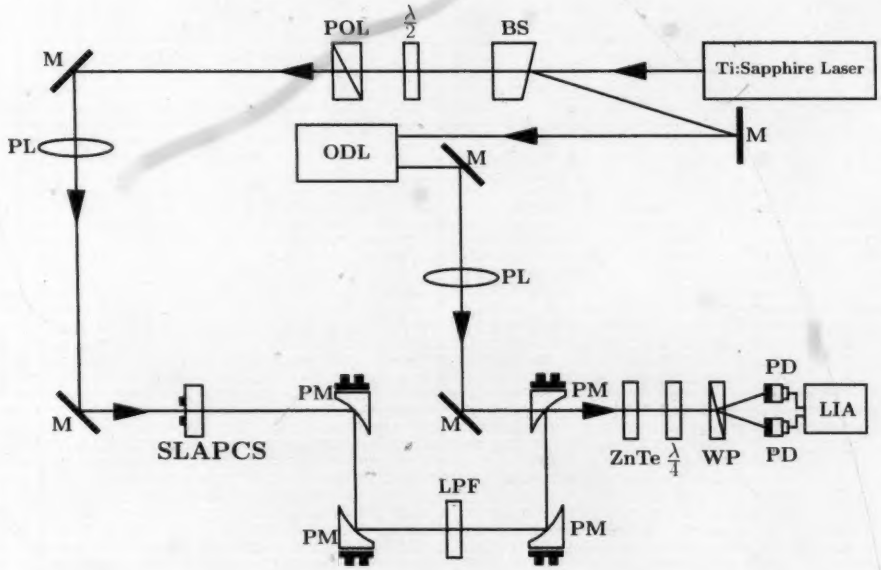

Figure 7.2: Schematic diagram of the set-up used in testing the semi-large aperture photoconductive switch . BS is a beam splitter; $\lambda/2$ is a half-wave plate; POL is a polarizer; M is a mirror; ODL is an optical delay line; PL is a positive lens, PM is a parabolic mirror; LPF is a low-pass filter blocking the optical leakage and passing the far-infrared radiation; $\lambda/4$ is a quarter-wave plate; WP is Wollaston prism; PD are photo-diodes; LIA is a lock-in-amplifier.

7.3.2 Terahertz emission scaling with optical pump energy

The set-up used for investigating the terahertz emission characteristics as the optical pump energy is varied is identical to that shown in Fig. 7.2. The polarizer and half-wave plate combination is used as a variable attenuator in the pump beam path to vary the optical excitation fluence at the emitter.

Knife edge scans of the optical beam indicate that the $1/e^2$ optical beam power diameter is 272 $\pm$ 30 μm. A photodiode is placed directly behind the last mirror before the semi-large aperture photoconductive switch to calibrate the optical energy. Calibration of the photodiode and knowledge of the optical beam spot size on the semi-large aperture photoconductive switch allows the extraction of the optical flux falling on the switch as shown in Fig. 7.4. The peak of the radiated terahertz waveform is monitored as the optical fluence is varied, and the result is shown in Fig. 7.4. The

inset shows the result on a log-log scale, demonstrating the power-law dependence of the emission.

It is interesting to note that the radiated THz field is not linear in the optical excitation energy. Also, we were not able to apply optical pump energies as large as those in Ref. [114], where thermal runaway was observed at higher driving energies.

A power law fit to the data gave an exponent of 0.72. This power law is likely a result of the start of optical saturation together with a contribution from the high temperatures in the crystal. Liquid cooled heat-sinks were used to reduce the heat in the crystal in Refs. [4, 113].

In this case, we simply operate at the highest possible optical flux, to give the largest signal possible, for the largest signal-to-noise ratio.

7.3.3 Noise scaling with operation frequency

Again, the set-up of section 7.3.1 shown in Fig. 7.2 is used to examine the noise characteristics of the of the semi-large aperture photoconductive switch. Terahertz waveforms are acquired at various modulation frequencies, while operating the semi-large aperture photoconductive switch at the highest possible bias field (5.5 kV / cm) and highest possible optical driving flux (8 μJ / cm^2). The noise is taken to be 1 standard deviation of the measured signal prior to the main terahertz signal as shown in Fig. 7.5. Note that this is acquired with the system in full operation.

Scans are taken over the modulation frequency range of 10 - 100 000 Hz. The 1 standard deviation noise is then converted to the standard measurement unit of $VHz^{-1/2}$ by using the equivalent noise bandwidth of the lock-in-amplifier. The scans were taken with a lock-in amplifier time constant of 50 msec, using an output filter of 24 dB / octave, and therefore having an equivalent noise bandwidth of 2.395 Hz. Taking this bandwidth into account, the measured noise was converted, and the result plotted in Fig. 7.6 as a function of the semi-large aperture photoconductive switch frequency of operation.

The solid horizontal line in Fig. 7.6 is the calculated quantum shot-noise limit of the differential photo-diode detection system. This is calculated as follows.

The rms shot-noise current fluctuations in the current from each photo-diode is given by [4]:

$$I_{rms}^{SN} = \sqrt{2qI_o} \tag{7.1}$$

where q is the charge of an electron and I_o is the average current flowing from each diode. This gives an rms noise in units of $AHz^{-1/2}$, that is, for a detection bandwidth of 1 Hz. In our detectors, the current flowing from each diode crosses a 12 $k\Omega$ resistor to ground to limit the current from the photo-diode so as not to damage it, and also forms a 12 $k\Omega$ termination for the voltage signal. Therefore the voltage noise generated by the shot-noise across the 12 $k\Omega$ termination is $12k\Omega \times I_{rms}^{SN}$, which gives a value of V_{rms}^{SN}

$= 0.19\ \mu V Hz^{-1/2}$, where the value of I_o is approximately 0.775 mA, corresponding to an average power on the photodiodes of approximately 1.58 mW. This is the noise per photo-diode. The differential signal from two photo-diodes is the actual signal that is measured, so that the noise in the differential signal is $\sqrt{2}$ times larger than this as the noise adds in quadrature. So the total shot-noise expected for this set-up is:

$$V_{rms}^{SN} = 0.27 \frac{\mu V}{\sqrt{Hz}} \tag{7.2}$$

The detected noise is larger than the shot-noise limit (by 2x or so) as seen in Fig. 7.6. This is possibly due to the rather small photo-diode currents used here of 0.775 mA, in comparison to the 2 mA used in Ref. [4]. Since the signal scales linearly with the driving current, and the noise scales as the root of the driving current, it is possible that photo-diode currents on the order of 2 mA are required to reach the shot-noise limit. In addition, if the noise source is independent of driving current, which may arise, for example, in Johnson noise (or thermal noise in the 12 $k\Omega$ resistor) as it is independent of the driving current, I_o, further increasing the driving current would allow one to reach the shot-noise limit. However, an estimate of the thermal noise, at 300 K, in a 1 Hz bandwidth (B) is approximately $\sqrt{4kTR_sB} = 0.014 \frac{\mu V}{\sqrt{Hz}}$, or 1 order of magnitude lower than the shot noise. This is shown as the dashed line in Fig. 7.6. Therefore it is not expected that thermal noise dominates this detector. Higher photo-diode driving currents are not used so as to stay in the linear current range of the photo-diodes, which is 1mA. Higher performance photo-diodes could be used in the future to improve the noise performance.

What is important here is the minimum detectable THz field. In our case, the minimum detectable field is calculated from the noise floor of the detection system. From Fig. 7.6, the noise floor is $V_{rms}^{noise} = 0.6\ \mu V Hz^{-1/2}$. Using the calculation of Ref. [4], we define the noise-equivalent differential power, ΔP_{NEPD}, that can be measured to be:

$$\frac{\Delta P_{NEPD}}{(P_{probe}\sqrt{B})} = \frac{\sqrt{2} I_{N,meas}^{rms}}{(2 I_o \sqrt{B})} \tag{7.3}$$

where B is the bandwidth of the measurement, P_{probe} is the sum of the probe powers on the two photo-diodes, and where $I_{rms}^{noise} = V_{rms}^{noise}/12k\Omega$ is used instead of the shot-noise limit used in Ref. [4]. The values $I_o = 1.58mA$, $P_{probe} = 2I_o\ R = 3.2mA$, with R = 0.5 A / W, and $\sqrt{2} I_{N,meas}^{rms}/\sqrt{B} = 5 \times 10^{-11} AHz^{-1/2}$ are used to obtain:

$$\frac{\Delta P_{NEPD}}{(P_{probe}\sqrt{B})} = 1.6 \times 10^{-8} \frac{1}{\sqrt{Hz}} \tag{7.4}$$

Finally, the calculations of section 3.2.3 (ie. Eq. 3.36 with $\theta = \pi/2$ and $\phi = 0$) can be used to convert the value of Eq. 7.4 to a noise equivalent terahertz electric field (NETEF), which gives:

$$\frac{\Delta P_{NEPD}}{(P_{probe}\sqrt{B})} = \frac{\omega}{c} r_{41} L E_{NETEF} n^3$$
$$E_{NETEF} = \frac{\Delta P_{NEPD}}{(P_{probe}\sqrt{B})} \frac{c}{\omega} r_{41} L n^3 \quad (7.5)$$

using the values of $r_{41} = 3.9pm/V$, $L = 1mm$, $n = 2.85$, $c = 3 \times 10^8 m/s$, $\omega = 2\pi c/\lambda$ and $\lambda = 800nm$ we obtain:

$$E_{NETEF} = 220 \frac{\mu V}{cm\sqrt{Hz}} \quad (7.6)$$

Finally, we note that even though the present system is not shot-noise limited, it is only approximately a factor of 2 less sensitive than that reported in Refs. [4, 113] (130 $\mu V cm^{-1} Hz^{-1/2}$), which comes exactly from the factor of 2 difference between our noise floor and the shot-noise limit. In future designs of such a system, photodiodes should be obtained that are capable of being driven at several mA in the linear range of operation.

7.3.4 Estimate of source efficiency

In this section, an estimate of the conversion efficiency from the semi-large aperture photoconductive switch will be presented and compared to that reported in Ref. [4].

The results from section 7.3.1 can be used to estimate the conversion efficiency from optical to far-infrared energy that is obtained with the semi-large aperture photoconductive switch . The time-domain waveform for an applied bias field of approximately 5 kV /cm (from Fig. 7.3) is converted to real units of V / cm.

The lock-in amplifier signal is divided by the sum of the two photo-diode voltages (8 V each in this case) to generate the signal modulation $\Delta P/P$. This modulation is then converted directly to a measured THz field using Eq. 3.36, with $L = 1mm$, $r_{41} = 3.9pm/V$ from chapter 3, and n = 2.85 from Ref. [70].

As can be seen in Fig. 7.7, the peak detected field from the semi-large aperture photoconductive switch is approximately 5 V / cm. The pulse energy in the terahertz beam can then be estimated using:

$$W_{THz} = \frac{\tau A |E_{THz}^{pk}|^2}{2\eta_0} \quad (7.7)$$

where W_{THz} is the terahertz pulse energy, τ is the terahertz pulsewidth, A is the terahertz beam area at the detector, E_{THz}^{pk} is the peak terahertz field and η_0 is the impedance of free-space. From Fig. 7.7, the 1/e terahertz pulsewidth is approximately $\tau = 1ps$. The 1/e terahertz electric-field diameter was measured to be 1.4 mm at the ZnTe crystal, giving a terahertz beam area of $A = 1.54 \times 10^{-6} m^2$ at the detector.

Using a value of 530 V / m for the peak radiated terahertz field in Eq. 7.7 yields an estimated pulse energy of 0.57 fJ. An optical excitation power of 250 mW was used on the semi-large aperture photoconductive switch , giving an optical excitation pulse energy of approximately 3 nJ. The conversion efficiency in this case is estimated to be:

$$\eta = \frac{W_{THz}}{W_{opt}} \approx 2 \times 10^{-7} \tag{7.8}$$

where W_{opt} is the optical excitation pulse energy. This is significantly lower than reported in Ref. [4], where using a 450 mW optical beam, a measured power of 40 μ W was observed, for an approximate conversion efficiency of 10^{-4}. This higher conversion efficiency is consistent with their reported peak detected terahertz field of 95 V / cm, in comparison to our 5 V / cm.

Even though the conversion efficiency of our semi-large aperture photoconductive switch is relatively poor, it is more than sufficient for the spectroscopy applications of interest in the present thesis, due to a large signal-to-noise ratio. The peak signal relative to the rms noise floor before the main pulse is over 6000 in Fig. 7.7 obtained in a time of less than 10 seconds.

Nonetheless, this raises the question as to what is the cause of the significantly lower conversion efficiency reported here. There are three main contributions which lead to this result.

First, a hemispherical silicon lens is used in Ref. [4] to collimate the initially strongly divergent radiation that emerges from the semi-large aperture photoconductive switch as a consequence of the physical size of the switch. The peak of the terahertz spectrum for the time-domain signal shown above is below 1 THz (300 μm wavelength), which indicates that most of the radiation generated will be scattered in the forward direction as a consequence of the electrodes, with a spacing of $470\mu m$. The parabolic mirrors used to collect and re-focus the terahertz radiation are F/2, which subtend a solid angle of 0.2 srad with respect to the source. If it is assumed that most of the radiation is diffracted into 2 π srad, then only 1 / 30 of the total terahertz power is being collected with the parabolic mirrors.

Second, a bias field of 10 kV / cm was used in Ref. [4], while only 5 kV / cm was applied here (due to the limitation in current of the power supply). In this case, we expect a factor of 4 more power in scaling to the results of Ref. [4]. Combining these last two effects, at least two orders of magnitude improvement could, in principle, be achieved.

Finally, it was noted in Ref. [4] that the semi-large aperture photoconductive switch radiated significantly less radiation when the switch was hot, as opposed to at room temperature. To overcome this, liquid water cooling was added to the semi-large aperture photoconductive switch in Ref. [4], where no such consideration was given for the semi-large aperture photoconductive switch in this thesis.

Combining all of these factors, it is possible that the large difference in observed

conversion efficiency can be explained by collection angle losses, higher applied bias fields and not cooling the semi-large aperture photoconductive switch .

In future designs of such a device, these points should be considered for improved efficiency. However, as will be seen in the next chapter, the current set-up works sufficiently well for the purposes of this thesis.

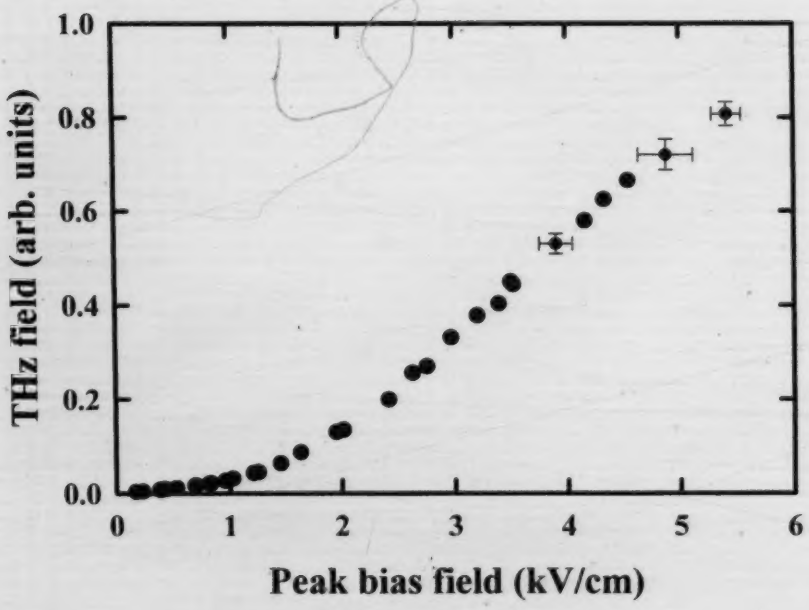

Figure 7.3: Peak measured terahertz signal as a function of the peak applied bias field from the GaAs SLAPCS. The peak applied bias field is obtained by dividing the applied voltage by the minimum gap separation of the semi-large aperture photoconductive switch ($470 \pm 12\ \mu m$). The error bars are 1 standard deviation of random triplicate data measurements, reflecting the likely error in the measurements.

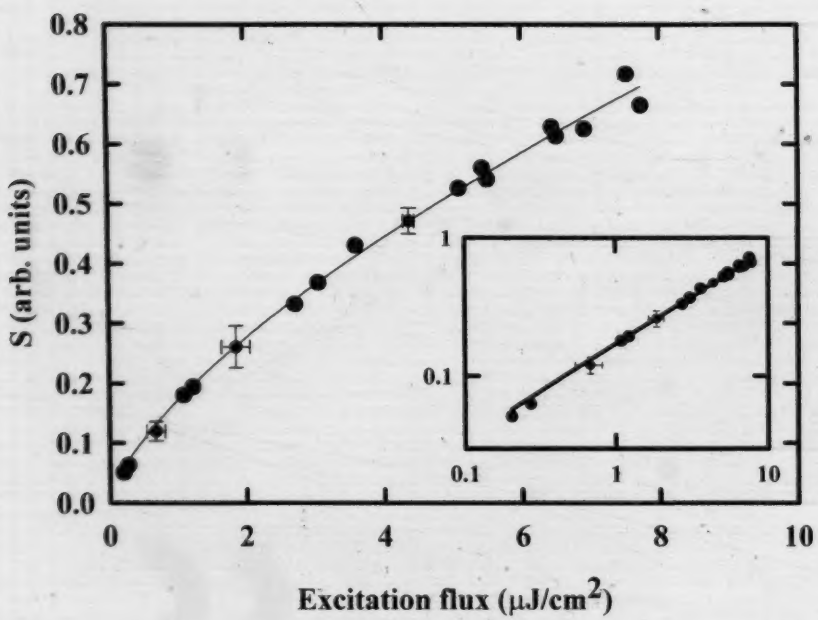

Figure 7.4: Peak radiated terahertz field as a function of the average optical excitation fluence from the GaAs SLAPCS. The error bars reflect 1 standard deviation of measurements made in random triplicate, and reflect the error associated with the measurement. The inset shows the data on a log-log scale, reflecting the power-law dependence of the peak terahertz field on the optical excitation fluence. The measured exponent from the fit was 0.72.

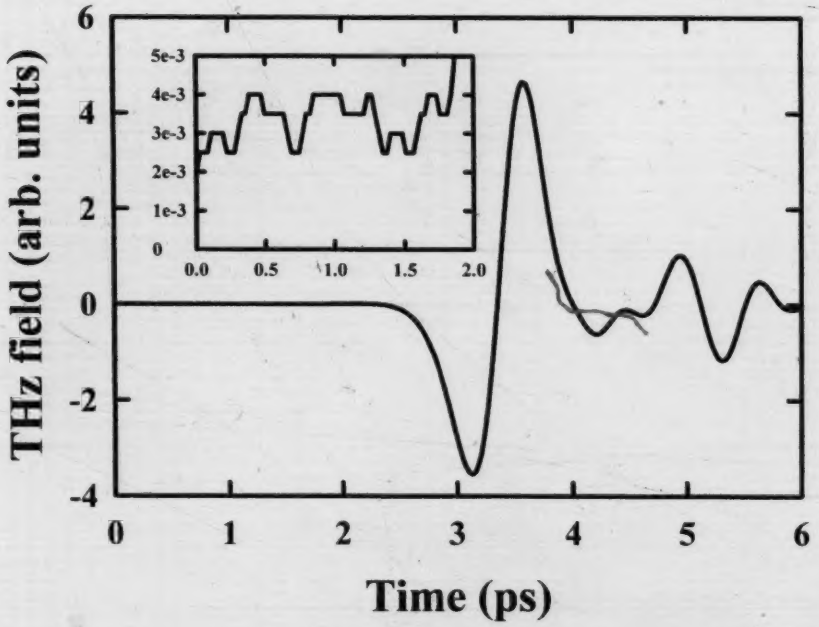

Figure 7.5: Typical time-domain terahertz waveform from the semi-large aperture photoconductive switch for a modulation frequency of 40 kHz and a scan rate of 2.3 ps / second. The peak detected field is plotted against the gating time delay. The inset shows an expanded scale of the noise floor in the time-region prior to the main terahertz pulse. The noise in the measurement is taken as 1 standard deviation of the data in the inset. The vertical scale is in units of mV, measured at the lock-in-amplifier.

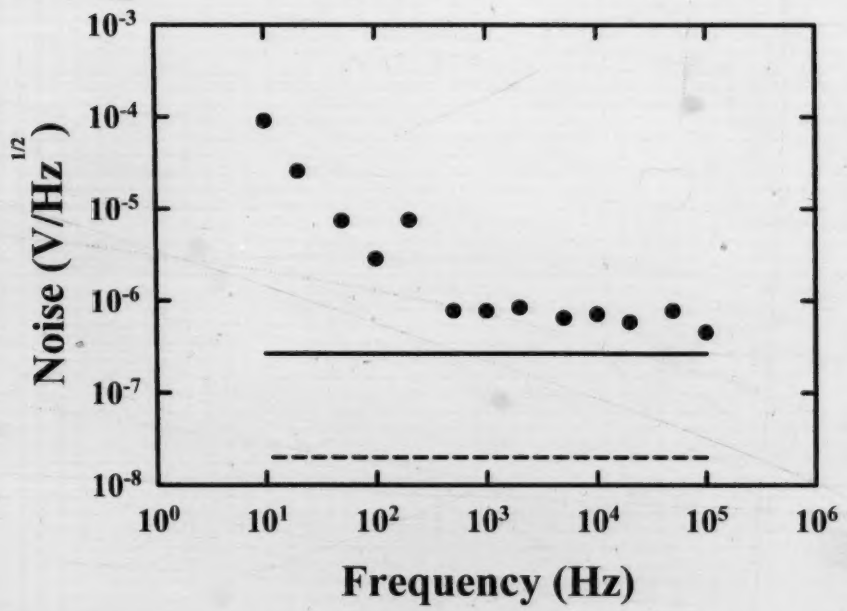

Figure 7.6: Frequency resolved noise measurements. The 1 standard deviation of noise in the time-domain data prior to the main pulse is plotted as the frequency is varied. The solid curve represents the quantum (or shot-noise) limit in the electrical system, and the dashed curve shows the thermal limit for the electrical system.

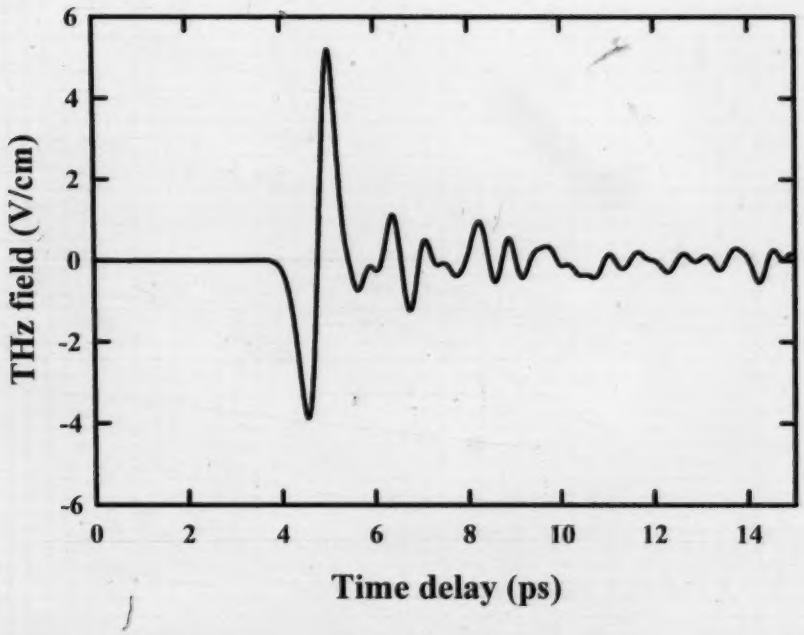

Figure 7.7: Terahertz time-domain scan from the semi-large aperture switch biased at 215V peak, modulated at 32kHz with a lock-in time constant of 20 msec and a total scan time of 10 seconds. The detected field is plotted in V / cm, and the result is not corrected for Fresnel loss at the GaAs or ZnTe crystals, or the loss due to the opaque low pass filter used to block the 800 nm radiation.

Chapter 8

Applications

In this chapter the semi-large aperture photoconductive switch outlined in chapter 7 is used to examine a potential industrial application for pulsed terahertz radiation which involves the birefringence of wood and wood products in the far-infrared. The far-infrared properties of wood, including birefringence and diattenuation, are outlined first. This is followed by an example that exploits the birefringence of wood, and demonstrates quarter and half-wave plates constructed from wood in the far-infrared . The system sensitivity is demonstrated next, by examining the birefringence of a single piece of lens paper. Finally, the difference in transmission through wood is exploited to generate a two dimensional map of a piece of wood in a transmission geometry in the far-infrared.

8.1 Birefringence of wood

Surprisingly little work has been done with pulsed terahertz radiation in terms of applications with wood and wood products. In fact, the only studies related to wood, aside from moisture content in leaves [115], is using the far infrared radiation to image the density of wood [116, 117].

The reason that this is so surprising is that there essentially is a window of about 0-2 THz over which wood is transparent (below x-ray frequencies). Therefore, pulsed terahertz radiation is capable of transmission through wood, but more importantly, with frequencies spanning the upper range of the transparent frequency range of wood (below x-ray frequencies) in a single pulse! In addition, terahertz frequencies are non-ionizing and much safer than x-rays [118].

What is found in this unique frequency window is that wood exhibits both birefringence and diattenuation. To demonstrate this explicitly, we consider first an example of the birefringence of wood in the far-infrared.

We begin with a discussion of the birefringence of oak. A standard piece of oak was obtained from a hardware store, where a small piece was cut with smooth surfaces to a thickness of 3.27 mm in the machine shop. The set-up used was identical to that in

Fig. 7.2 and the sample was placed at the intermediate focus between the second and third parabolic mirrors. The transmission spectrum through the sample was obtained at various orientations of the applied THz field with respect to the visible grain of the wood. The applied THz field is oriented horizontally and the ZnTe analyzer is oriented for maximum sensitivity to horizontal polarization. Terahertz waveforms are collected as the wood is rotated about the surface normal, with the terahertz field incident normally on the wood surface. Waveforms obtained with terahertz polarizations parallel and perpendicular to the grain, along with the reference scan, are shown in Fig. 8.1.

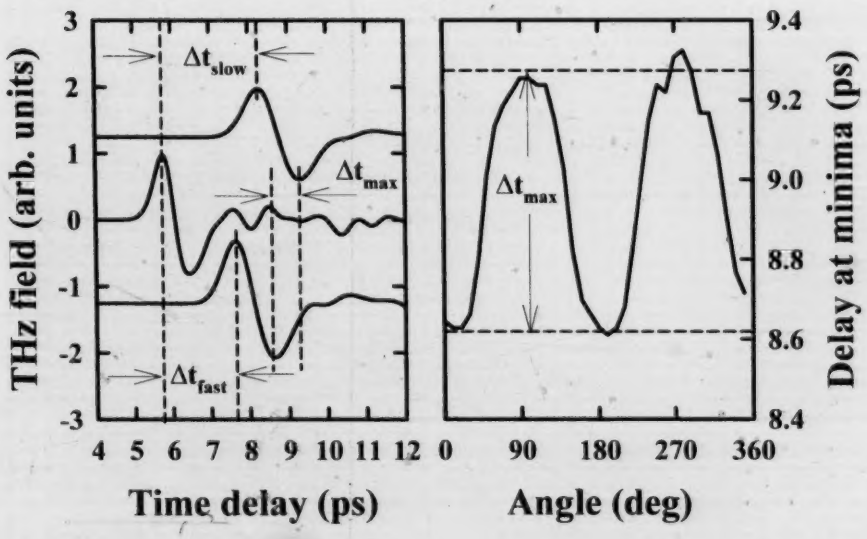

Figure 8.1: Time domain scans (a) of terahertz fields propagating through 3.27 mm oak with terahertz field parallel (top) to the grain, perpendicular (bottom) to the grain and the reference (center). The absolute time delay of the minima in the waveforms (b), as the angle is rotated 360 degrees. The angle is defined as the angle that the polarization of the terahertz field makes with the perpendicular to the grain in the plane of the wood.

From Fig. 8.1, the birefringence of the wood shows up as a time delay between the arrival of the terahertz fields at the detector, as measured with the terahertz field polarized perpendicular and parallel to the grain structure of the wood. This is shown explicitly in the figure 8.1 (b), which shows the absolute time delay of the minima of the terahertz field as measured at various orientations of the wood. Clearly, there exist

a fast and slow axis. The birefringence can be estimated from the time-domain data of Fig. 8.1 as follows. The absolute time delay between fast and slow axes can be written as:

$$\Delta t_{max} = \frac{n_{slow} L_{wood}}{c} - \frac{n_{fast} L_{wood}}{c} = \Delta n \frac{L_{wood}}{c} \tag{8.1}$$

where $\Delta n = n_{slow} - n_{fast}$, L_{wood} is the thickness of the wood sample and c is the speed of light in vacuum. Solving Eq. 8.1 for Δn, we obtain for the birefringence:

$$\Delta n = \Delta t_{max} \frac{c}{L_{wood}} \tag{8.2}$$

Using $L_{wood} = 3.27mm$, $c = 3 \times 10^8 m/s$ and using $\Delta t_{max} = 0.66ps$ from Fig. 8.1, we obtain as an estimate of the frequency averaged birefringence, $\Delta n = 0.061$. One would likely expect this estimate to be relatively accurate for the center frequency of the terahertz pulse, and represent the average birefringence over the entire frequency spectrum of the transmitted terahertz pulse.

As the terahertz radiation is pulsed, and composed of a broad frequency spectrum, the proper way to analyze the birefringence of the oak is to examine the index of refraction, which can be obtained from the transmission spectrum of the oak. In fact, as the detection is coherent, we can extract the frequency-resolved complex index of refraction directly from the measured data. To do this, we use the thick sample approximation of Ref. [119], truncating the time-domain spectrum before multiple reflections occur, and write the ratio of the measured transmission spectrum to the reference spectrum as:

$$\frac{\boldsymbol{E}_{wood}(\nu)}{\boldsymbol{E}_{ref}(\nu)} = \hat{t}_{AW} \hat{t}_{WA} e^{-\frac{i 2\pi \nu L}{c}(\hat{n}_W - \hat{n}_A)} \tag{8.3}$$

Where $\boldsymbol{E}_{wood}$ and $\boldsymbol{E}_{ref}$ are the measured terahertz fields in the frequency domain with 3.27 mm of oak and nothing in the beam paths respectively, ν is the frequency, c is the speed of light in vacuum, L is the length of the wood sample, and $\hat{t}_{WA}$ and $\hat{t}_{AW}$ are the complex Fresnel transmission coefficients of wood-to-air and air-to-wood respectively. The Fresnel transmission coefficients are given by:

$$\hat{t}_{ij} = \frac{2\hat{n}_i}{\hat{n}_i + \hat{n}_j} \tag{8.4}$$

for normal incidence [120]. Writing the ratio of Eq. 8.3 in Euler form: $Re^{i\theta}$, we may make use of the measured data to extract the complex index $\hat{n}_W$. We take $\hat{n}_A = 1$, and:

$$\hat{n}_W = n_W - i k_W \tag{8.5}$$

with the approximation in the Fresnel coefficients that $k \ll n$, to obtain:

$$Re^{i\theta} = \frac{\boldsymbol{E}_{wood}(\nu)}{\boldsymbol{E}_{ref}(\nu)} \approx \frac{4n_W}{(n_W+1)} e^{-\frac{2\pi\nu L}{c}k_w} e^{-\frac{i2\pi\nu L}{c}(n_w-1)} \tag{8.6}$$

Solving for n_W and k_W in Eq. 8.6, and using the relation $\alpha_W = 4\pi\nu k_W/c$ we obtain:

$$n_W = -\frac{\theta c}{2\pi\nu L} + 1 \tag{8.7}$$

$$\alpha_W = -\frac{2}{L} ln\left(R\frac{(n_W+1)^2}{4n_W}\right) \tag{8.8}$$

where α_W is the absorption coefficient. Using the results measured and shown in Fig. 8.1 for 3.27 mm of oak, in combination with Eq. 8.7, the index of refraction and absorption coefficient for the fast and slow axes (0^o and 90^o in the right-hand plot of Fig. 8.1 respectively) is shown in Fig. 8.2.

Two very interesting characteristics of wood in general are highlighted by the data for oak shown in Fig. 8.2. First, the fact that the absorption coefficient depends on the orientation of the wood with respect to the grain orientation demonstrates that the wood exhibits diattenuation. This has been used to, for example, identify the orientation of wood for industrial applications [121]. In addition, there is a large difference in the index of refraction when the terahertz radiation is polarized parallel and perpendicular to the grain structure of the wood, demonstrating that the wood exhibits birefringence. From the data in Fig. 8.2, the average difference in the index of refraction between the fast and slow axes is approximately 0.06, with a standard deviation of approximately 0.008 in the frequency range 0.2-1.2 THz. This is quite large, given that the index of refraction is in the range 1.3-1.4. This is not a unique property of oak, but rather a property of wood in general, as will be discussed next.

Before proceeding to examine other types of wood, it is important to note how well the time-domain method is able to extract the value for the birefringence. This is, in part, due to the fact that there is very little dispersion in the birefringence over the bandwidth of the transmitted terahertz pulse, as observed in Fig. 8.2. For some of the wood samples used, the thickness is very large, and hence the time-domain signals are very noisy. Therefore, some of the birefringence measurements are taken directly from the time-domain data.

Birefringence is a very interesting phenomenon in general, however, it is additionally interesting when viewed directly on a short time-scale with pulsed radiation in the time domain. If the birefringent material can be made sufficiently long, and the pulse-width of the electromagnetic radiation sufficiently short, then the effect of the birefringence will be more than the introduction of a phase relation between orthogonal polarization components. Specifically, if the phase difference corresponds to a time-scale longer than the pulsewidth of the radiation, two orthogonally polarized pulses of electromagnetic radiation will result, the magnitude of which will depend on the orientation of the input

polarization and the birefringent axes.

In fact, this was observed for the terahertz transmission through spruce, one of the more strongly birefringent woods that was investigated. Using 8.5 mm thick spruce, the transmission of the terahertz radiation was as shown in Fig. 8.3. The birefringence is estimated to be $\Delta n = 0.07 \pm 0.015$ which is significant enough to separate the main transmitted THz pulse in time between the fast and slow axes of the poplar.

To demonstrate explicitly that the birefringence is enough to generate two orthogonally polarized pulses in the time domain, the time-domain waveforms of transmitted terahertz radiation are examined as a function of the orientation of the grain with respect to the terahertz polarization. The angular dependence of the transmitted THz field is shown in Fig. 8.4 with the detection set to detect horizontally polarized transmitted terahertz radiation.

When the angle between the input terahertz polarization and the visible grain is approximately 22^o, as seen in Fig. 8.4, the output radiation is comprised of two pulses, roughly equal in amplitude, and separated by approximately 2 ps in time with orthogonal polarizations. From the measurement shown in Fig. 8.4 we can estimate $\Delta\tau = 2.23ps$, which gives a measure of the frequency averaged birefringence of 0.08 ± 0.01.

This value is in reasonable agreement with the value calculated using the frequency dependent indices of refraction, calculating in the same way as for oak above. This method gives a value of $\Delta n = 0.07 \pm 0.015$.

The other types of wood that were investigated were poplar and maple. The values for the fast and slow indices of refraction, and birefringence are given in Table 8.1, where the slow axis is parallel to the grain for all measured samples.

Wood	n_{fast}	n_{slow}	Δn	$1\sigma error$	freq range (THz)
$Poplar(1)$	1.33	1.46	0.13	0.02	0.1 - 0.6
$Poplar^*(2)$	1.22	1.33	0.11	0.03	0.1 - 0.25
$Maple^*$	1.32	1.44	0.12	0.03	0.1 - 0.25
$Spruce$	1.25	1.33	0.07	0.015	0.1 - 1
Oak	1.18	1.24	0.06	0.008	0.1 - 1.2

Table 8.1: Table of birefringence measurements. Those listed with a (*) superscript reflect data that was taken only in the time domain due to poor signal-to-noise ratios.

8.2 Waveplates constructed from solid wood

The large birefringence of wood allows the possibility of fabricating birefringent optical elements from wood for terahertz applications. In this section we consider the use of wood for constructing waveplates for the far-infrared. As discussed in section 8.1, wood demonstrates both birefringence and diattenuation. Those results were presented only

in the time-domain. The frequency resolved measurements are shown in Fig. 8.5 for spruce wood which will be used to fabricate birefringent waveplates.

We will demonstrate the operation of a 3.025 mm thick piece of spruce as both a quarter- and half-waveplate for specific frequencies, however, we must first compute what is expected for such a device when diattenuation is present. To do this, we calculate the angular dependence of the vertically and horizontally polarized terahertz fields after propagation through a 3.025 mm thick piece of spruce. Consider the geometry shown in Fig. 8.6.

The field at the output of the wood, parallel ($E_{\parallel}$) and perpendicular to the grain ($E_{\perp}$) structure is given by:

$$\begin{aligned} E_{\perp}^{out} &= E_{in}\cos(\theta)e^{i\Gamma_{\perp}}e^{-\frac{1}{2}\alpha_{\perp}d} \\ E_{\parallel}^{out} &= E_{in}\sin(\theta)e^{i\Gamma_{\parallel}}e^{-\frac{1}{2}\alpha_{\parallel}d} \end{aligned} \tag{8.9}$$

where E_{in} is the incident electric field amplitude, θ is as defined in Fig. 8.6, $\Gamma_{\parallel}$ and $\Gamma_{\perp}$ are the incurred phase retardances along the grain and perpendicular to the grain, respectively, d is the thickness of the wood sample, and $\alpha_{\parallel}$ and $\alpha_{\perp}$ are the power absorption coefficients parallel and perpendicular to the grain, respectively.

Again considering Fig. 8.6, the output fields along the two grain axes will recombine to form horizontally and vertically polarized THz fields at the output, to which our analyzer is sensitive. The vertical and horizontal components are given by:

$$\begin{aligned} E_{vert}^{out} &= E_{\parallel}^{out}\cos(\theta) - E_{\perp}^{out}\sin(\theta) \\ E_{horiz}^{out} &= E_{\perp}^{out}\cos(\theta) + E_{\parallel}^{out}\sin(\theta) \end{aligned} \tag{8.10}$$

Using Eq. 8.9 in Eq. 8.10 we obtain the angular dependence of the horizontal and vertical components of the output field along the analyzer axes:

$$\begin{aligned} |E_{vert}^{out}| &= |E_{in}|e^{-\frac{1}{2}\alpha_{\parallel}d}|\sin(\theta)\cos(\theta)||1 - e^{i\Delta\Gamma}e^{-\Delta\alpha d}| \\ |E_{horiz}^{out}| &= |E_{in}|e^{-\frac{1}{2}\alpha_{\parallel}d}|\cos^2(\theta)e^{-\Delta\alpha d}e^{i\Delta\Gamma} + \sin^2(\theta)| \end{aligned} \tag{8.11}$$

where $\Delta\alpha = \frac{1}{2}\left(\alpha_{\perp} - \alpha_{\parallel}\right)$ and $\Delta\Gamma = \Gamma_{\perp} - \Gamma_{\parallel}$ are the differences in absorption and induced phase for propagation perpendicular to the grain and along to the grain, respectively.

Finally, taking Eq. 8.11 with $\Delta\Gamma = \frac{\pi}{2}$ and $\Delta\Gamma = \pi$, the expressions for the terahertz field as a function of the angular orientation of the wood for quarter- and half-waveplate behaviour are obtained:

$$
\begin{aligned}
E_{vert}^{out,QWP} &= E_{in}e^{-\frac{1}{2}\alpha_{\parallel}d}|\sin(\theta)\cos(\theta)|\sqrt{1+e^{-2\Delta\alpha}} \\
E_{vert}^{out,HWP} &= E_{in}e^{-\frac{1}{2}\alpha_{\parallel}d}|\sin(\theta)\cos(\theta)|\left(1+e^{-\Delta\alpha d}\right) \\
E_{horiz}^{out,QWP} &= E_{in}e^{-\frac{1}{2}\alpha_{\parallel}d}\sqrt{\sin^4(\theta)+\cos^4(\theta)e^{-2\Delta\alpha d}} \\
E_{horiz}^{out,HWP} &= E_{in}e^{-\frac{1}{2}\alpha_{\parallel}d}\sqrt{\left(\sin^2(\theta)\left(1+e^{-\Delta\alpha d}\right)-e^{-\Delta\alpha d}\right)^2}
\end{aligned}
\tag{8.12}
$$

Note that only specific frequencies will meet the criteria for $\Delta\Gamma = \frac{\pi}{2}$ and $\Delta\Gamma = \pi$. We can use Eq. 3.41 to relate the matching wavelength to the desired phase retardance and birefringence (Δn) as:

$$\lambda_{match} = \frac{2\pi L}{\Delta\Gamma}\Delta n \tag{8.13}$$

where λ_{match} is the matching wavelength, Δn is the birefringence and $\Delta\Gamma$ is the desired phase retardance. From Fig. 8.5, we have an approximately frequency independent birefringence of $\Delta n = 0.07$, which gives a matching wavelength of 847 μm (or 0.35 THz) and 424 μm (or 0.71 THz) for quarter-wave ($\Delta\Gamma = \pi/2$) and half-wave ($\Delta\Gamma = \pi$) phase retardance, respectively, for a 3.025 mm thick piece of spruce.

Taking terahertz time-domain scans as a function of the angle θ in Fig. 8.6, and Fourier transforming to the frequency domain, a set of frequency spectra is obtained. The amplitudes in specific frequency bins are computed to form an angularly resolved measurement for each frequency bin. Both horizontally polarized and vertically polarized transmitted terahertz fields are measured in this way. The result is plotted for frequency bins at 0.32, 0.36, and 0.39 THz in figures 8.7, 8.8 and 8.9. The solid lines are the expectation for perfect birefringent operation as given by Eq. 8.12. Clearly, the data matches quarter-wave plate behavior most closely at 0.36THz which is very close to the calculated value of 0.35 THz. Given that each of these plots is taken at one frequency bin spacing, the limitation here is the frequency bin resolution. Nonetheless, it appears that the 3.025 mm thick piece of spruce wood behaves as a quarter-waveplate at 0.36THz.

A similar result is obtained for the half-wave plate. In this case, the best fit to the data is for the 0.71 THz frequency bin, as expected based on the matching wavelength calculated above. The angularly resolved s- and p-polarized transmitted fields at 0.71 THz are plotted in Fig. 8.10.

These results clearly demonstrate the ability of spruce to be used as a waveplate for frequencies in the far infrared. While likely not a practical device due to significant attenuation within the wood, the possibility for constructing birefringent elements from wood is clearly demonstrated.

8.3 Birefringence of lens paper

Paper products are a derivative of wood, and therefore contain wood fiber. The fiber of the wood is what leads to the birefringence that was demonstrated in section 8.1. Therefore, depending on whether or not there exists a preferential orientation of the fibers within a paper product, one might expect paper to also exhibit birefringence. For the case of lens paper that one might find in any standard laboratory containing optical components, it is easily verified that lens paper has a preferential fiber orientation. This is most easily observed by tearing the paper. One will find that the paper preferentially tears along one fixed direction, while it is difficult to tear the paper in any other direction.

The observation of the existence of a preferential tearing direction in the lens paper was used to predict that lens paper is birefringent. This hypothesis is easily verified. A collection of 27 pieces of identically oriented lens paper was put in the terahertz spectrometer set-up. It was immediately observed that the position of the maxima of the terahertz pulse in the time domain changed as a function of the orientation of the lens paper with respect to the polarization of the terahertz beam. This is the time-domain manifestation of birefringence outlined previously in section 8.1.

In fact, the orientation of the fibers with respect to the polarization of the terahertz beam is easily mapped out using the change in time-delay as a function of the orientation of the lens paper. Consider that the index of refraction is $n_\perp$ and $n_\parallel$ when the polarization of the terahertz radiation is perpendicular and parallel to the preferential fiber orientation, respectively, and the 27 pieces of lens paper form a sample of thickness d_{lens}. Then the time delay, $\Delta\tau$, as a function of the orientation of the lens paper with respect to the terahertz polarization is given by:

$$\Delta\tau = \frac{d_{lens}}{c}\left[n_\perp \cos(\theta) + n\| \sin(\theta)\right] \tag{8.14}$$

where c is the speed of light in vacuum, θ is the angle that the linear polarization of the terahertz radiation makes with the vector perpendicular to the preferential fiber orientation, and the quantity in braces is the effective index of refraction for propagation through the lens paper at normal incidence for this polarization state.

This time delay is most easily measured on a portion of the terahertz time-domain waveform that is rapidly changing in time. Therefore, we choose a rapidly varying linear portion of the terahertz time-domain waveform as the operating point as shown in Fig. 8.11.

Once the optical delay-line is fixed at the operating point shown in Fig. 8.11, the signal on the lock-in amplifier is zeroed. The resultant change in signal as the orientation of the lens paper is changed is a direct measure of $\Delta\tau$. The result is plotted in Fig. 8.12.

The lock-in amplifier signal (time-delay) is negative in Fig. 8.12 as the angle is defined as the angle that the linearly polarized terahertz beam makes with the fiber orientation. Since the fiber axis is the slow-axis, as the angle is rotated by 90 degrees

($E_{THz} \parallel n_{\perp}$), it falls along the fast-axis and therefore arrives earlier leading to negative time-delays and a decrease in signal due to the operating point chosen. Once the data is taken over an angular range of 90 degrees, it is then possible to determine the orientation of the polarization with respect to the preferential fiber alignment at an arbitrary position.

The important point for a practical application is that the full terahertz time-domain waveform is unnecessary. A simple measurement of a relative lock-in amplifier signal (time-delay) is sufficient once the indices of refraction are known and the operating point chosen.

Another important point for practical applications is that the time required to obtain data over a 90 degree span is essentially limited by the lock-in time constant. In this case a lock-in amplifier time constant of 100 ms was used, however, the data was taken before the semi-large aperture photoconductive switch was optimized. A more realistic value of 5 ms for the time constant would be easily attainable with the semi-large aperture photoconductive switch outlined in chapter 7. In either case, a 90 degree scan would take a fraction of a second.

As one final example of the power of the semi-large aperture photoconductive switch developed in chapter 7, the frequency-dependent index of refraction of a single piece of lens paper which is $21\mu m$ thick is measured using a terahertz time-domain waveform acquired in 3 seconds, limited by the speed of the optical delay line, for each polarization orientation. A reference scan is taken, and then a transmission scan with the terahertz polarization parallel and perpendicular to the grain. A clear difference in the time-delay of the transmitted terahertz pulses is apparent, indicative of the birefringence of the single piece of lens paper. The results in the time-domain are shown in Fig. 8.13.

In fact, the complete frequency-resolved measurement of the indices of refraction for propagation of the terahertz radiation polarized parallel and perpendicular to the fiber orientation are possible from the data presented in the inset of Fig. 8.13. The index of refraction is computed based on the procedure outlined in section 8.1, and the results are presented in Fig. 8.14.

The frequency-resolved index measurements of the single piece of lens paper demonstrate the birefringence is quite large in the lens paper, with a frequency-averaged value of $\Delta n = 0.10 \pm 0.03$ in the frequency range of 0.2 - 1.4 THz. The data is fairly noisy as a consequence of the short time scan for the transmission measurements (less than 1 second for each), and the fact that the reference and transmitted signals are only very slightly different.

Given that both the frequency resolved index of refraction and the preferential fiber orientation are obtainable on a sub 1 second time-scale, in a transmission mode, through a 21 μm thick piece of lens paper, it seems likely that there will be applications for this in industry.

8.4 A method to image wood in transmission

In this section the method of Koch et al [116] will be used to demonstrate rudimentary imaging capability in Douglas Fir. First the imaging method will be presented, followed by preliminary imaging results.

In the work of Koch et. al. [116], transmission imaging of beech and balsa wood was demonstrated for the first time in the far-infrared. As mentioned previously, pulsed terahertz technology provides a unique spectroscopic tool for studying wood in transmission as it offers access to the upper end of the frequency range over which wood is transparent (below X-rays), is non-destructive and avoids potential health hazards that can be associated with X-rays. In the work of Koch et. al. [116] a linear relationship between density of the wood and the terahertz extinction coefficient was found. This relationship was calibrated against a gravitometric-volumetric method. Using the spectral range between 0.75 and 1.2 THz, the calibration was used to map the density of the wood in units of g/cm^3 with a sub-annular ring spatial resolution.

In this section we will simply consider the transmission of terahertz radiation through Douglas Fir, where the early and latewood (the "rings" of the tree) have a clear and observable difference in color. This color difference is a result of a much larger density of smaller sized pores in the latewood in comparison to the early wood. Wood with a structure like this is termed ring-porous [122] and Douglas Fir demonstrates this structure [123].

As dry wood makes a relatively good insulator, and is therefore a poor conductor [122], the majority of the large extinction observed in the transmission of terahertz radiation through wood is likely a result of scattering. The size scale of the pores in the wood is typically on the order of several hundred microns [122], and therefore comparable to the terahertz radiation wavelength. As such, the dominant extinction mechanism is likely scattering. Therefore, one expects that the extinction coefficient will be strongly dependent on the size and density of the pores.

To observe the dependence of the terahertz transmission on the presence of early or latewood, consider first the optical picture of a sample of Douglas Fir that is 2.2 mm thick presented in Fig. 8.15.

The two dots roughly near the center of the piece of wood and to the right of center show the start and end points for a linear transmission scan. The terahertz beam clearly traverses regions of both earlywood (light) and latewood (dark).

The terahertz transmission scan as a function of lateral position is presented in Fig. 8.16. The top of the figure shows the portion of the optical image that is being scanned with the terahertz beam in the main figure. Clearly, the regions of early and latewood are resolved in the linear scan. In fact, a significant difference in the terahertz transmission between the two regions is observed.

Having demonstrated that the early and latewood suffer from substantially different extinction coefficients, a full 2D transmission map of Douglas Fir can be generated. In Fig. 8.17, a two dimensional plot of the terahertz transmission through a 2 mm thick

piece of Douglas Fir is presented. For the THz scan a grid of 14 by 5 points was taken with spacings of 1 mm and 2mm between points, respectively, and an acquisition time of 10 seconds per point. A contour plot was then generated from the data as shown in Fig. 8.17. The contrast between earlywood and latewood is very good. The annular rings are clearly resolved. Comparing the THz image (right) with the optical image (left) it is seen that the dark regions in the THz map correspond to smaller transmission or higher attenuation in the latewood which is dark in the optical image.

The spatial resolution of the imaging of the Douglas Fir is not particularly good in these examples as the beam spot at the samples, which limits the spatial resolution, is estimated to be no smaller than 3 mm. Nonetheless, these examples illustrate the potential for far-infrared radiation to be used in transmission imaging of wood and wood-related products.

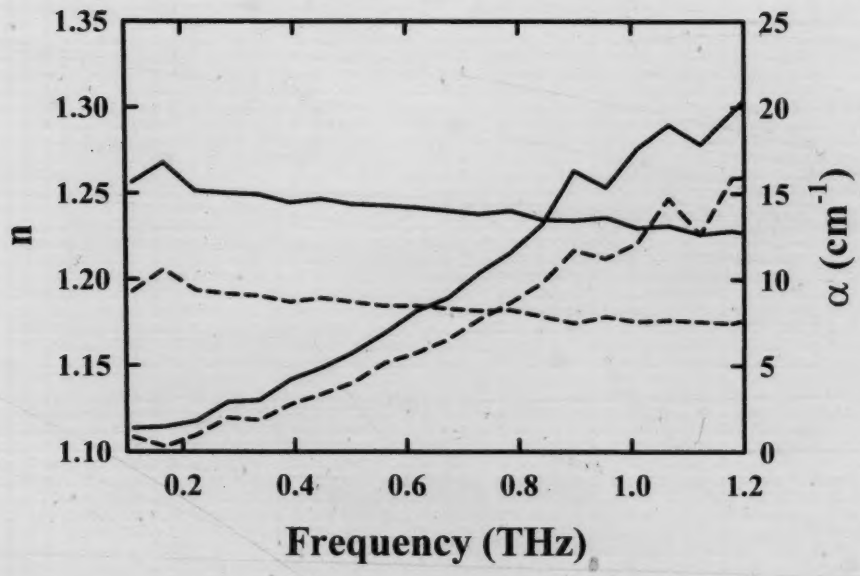

Figure 8.2: Measured frequency dependence of the index of refraction (left axis) and absorption coefficient (right axis) as measured using a semi-large aperture photoconductive switch to generate terahertz radiation and transmission spectrum of 3.27 mm of oak wood in THz beam path. Dashed curves are for terahertz radiation polarized perpendicular to the wood grain, while solid curves are data taken with terahertz polarization parallel to the grain of the wood.

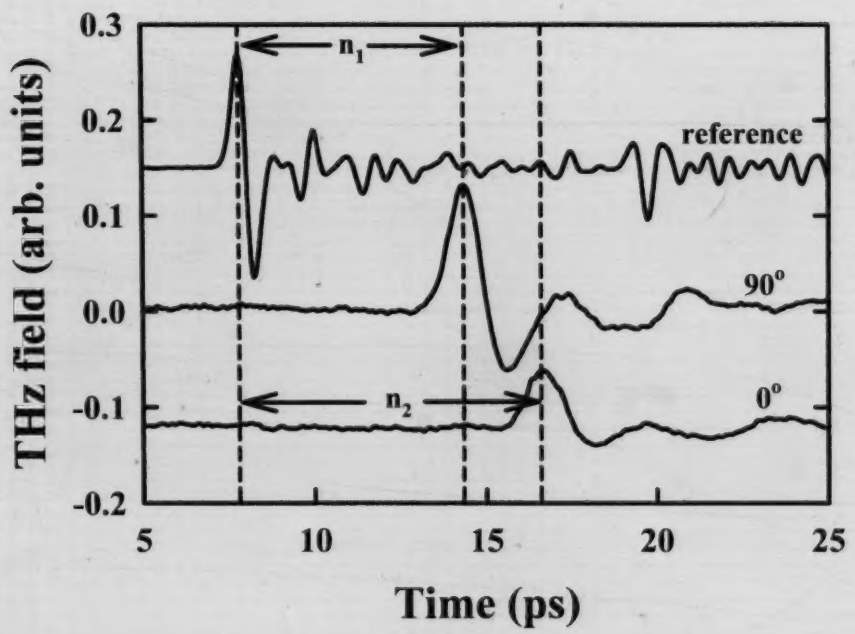

Figure 8.3: Reference (top) terahertz scan, transmission through 8.5 mm spruce with terahertz field polarized perpendicular to grain (90^o center) and transmission through 8.5 mm spruce with terahertz field polarization parallel to grain (0^o bottom). n_1 and n_2 show the effect of the difference in index of refraction in the time domain as a time-delay.

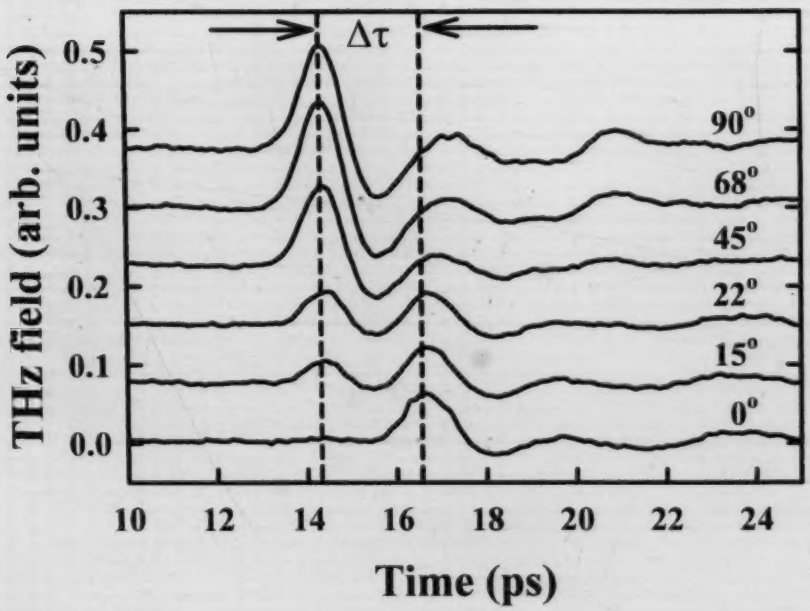

Figure 8.4: Terahertz time-domain waveforms obtained by transmission through 8.5 mm thick spruce wood, with terahertz polarization making an angle θ with respect to the visible grain of the wood. The angle θ is marked above each scan on the right hand side of the figure. The total time delay between fast and slow axes is marked as $\Delta\tau$ on the plot, which can be used to estimate the birefringence of the wood.

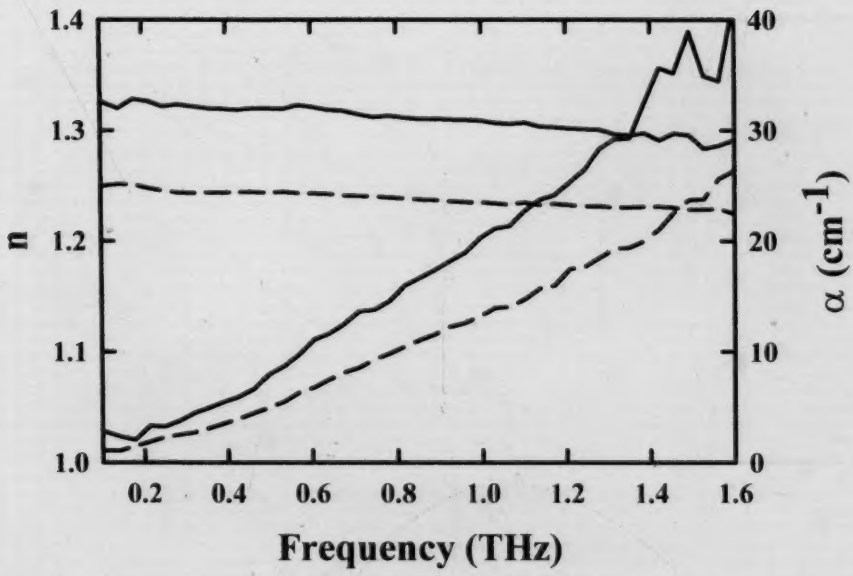

Figure 8.5: Frequency resolved index of refraction (n) and absorption coefficient (α) obtained in transmission spectroscopy of a 3.025 mm thick piece of spruce wood. Measurements are taken with the terahertz polarization parallel to the grain (solid curves) and perpendicular to the grain (dashed curves).

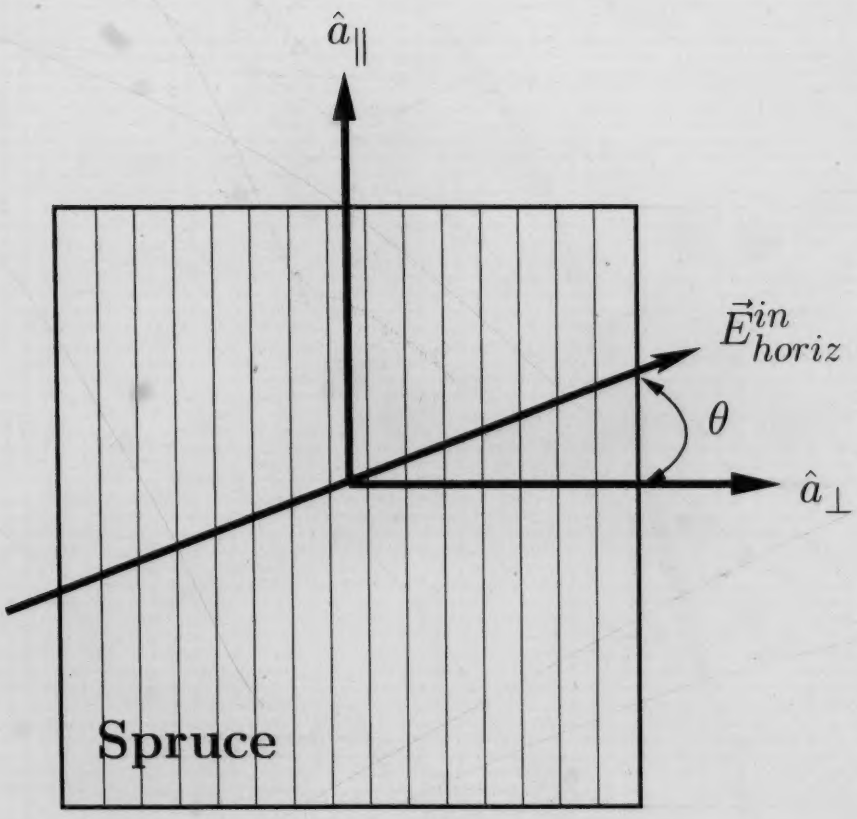

Figure 8.6: Schematic diagram of the orientation of the wood with respect to analyzer axes (vertical and horizontal) for the input terahertz fields. The directions $\hat{a}_{\parallel}$ and $\hat{a}_{\perp}$ are parallel and perpendicular to the wood grain, respectively.

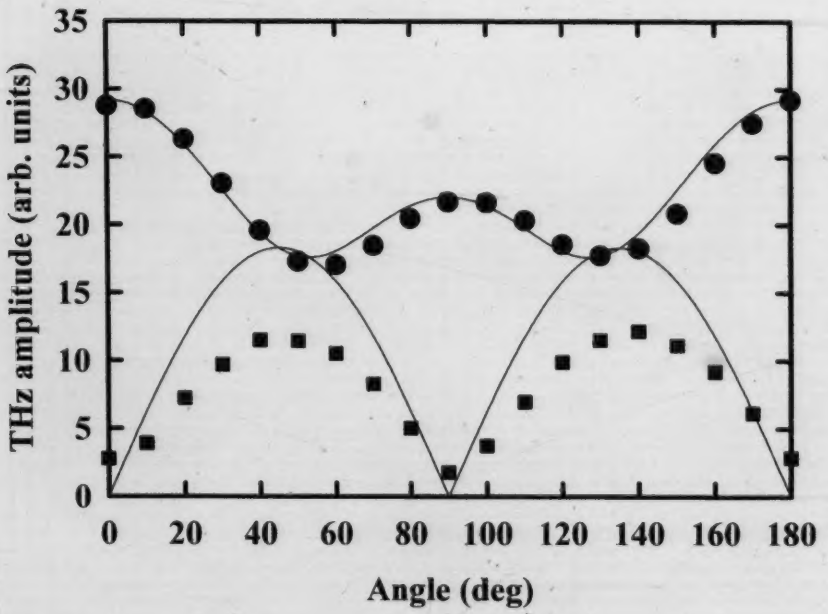

Figure 8.7: Frequency bin data as a function of wood orientation at a center frequency of 320 GHz. The data for vertically (squares) and horizontally (circles) polarized terahertz fields are shown for transmission through 3.025mm thick spruce, along with the expected angular dependence for behavior as a quarter-wave plate (Eq. 8.12). The angle is defined as the angle that the grain direction makes with the vertical axis.

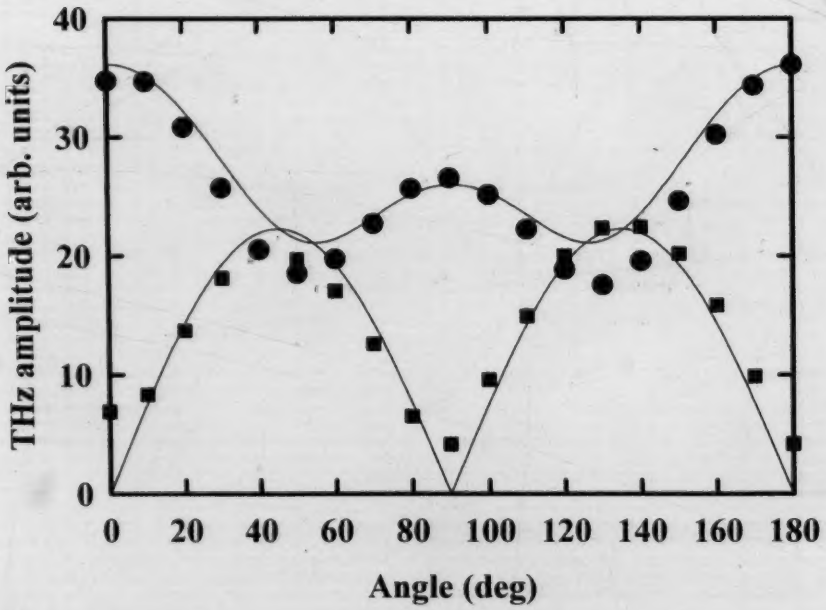

Figure 8.8: Frequency bin data as a function of wood orientation at a center frequency of 356 GHz. The data for vertically (squares) and horizontally (circles) polarized terahertz fields are shown for transmission through 3.025mm thick spruce, along with the expected angular dependence for behavior as a quarter-wave plate (Eq. 8.12). The angle is defined as the angle that the grain direction makes with the vertical axis.

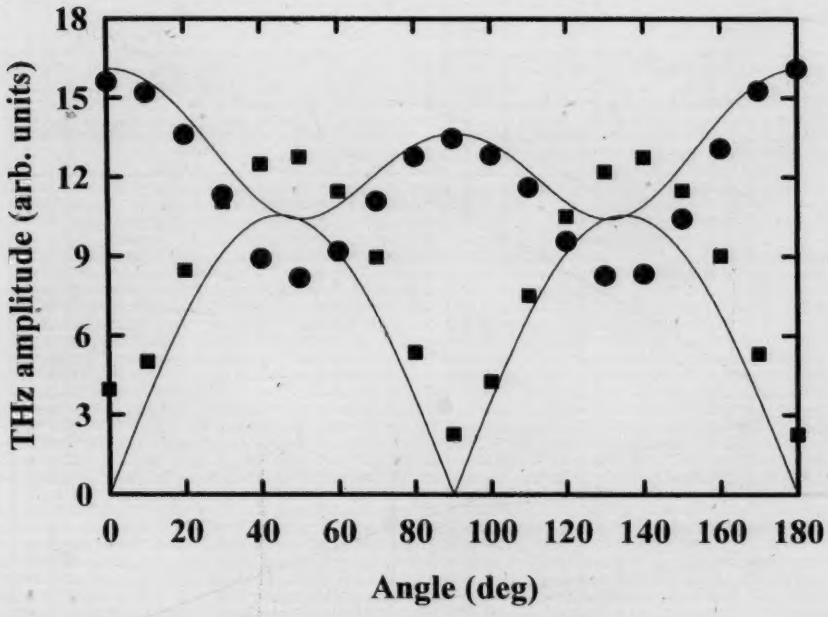

Figure 8.9: Frequency bin data as a function of wood orientation at a center frequency of 391 GHz. The data for vertically (squares) and horizontally (circles) polarized terahertz fields are shown for transmission through 3.025mm thick spruce, along with the expected angular dependence for behavior as a quarter-wave plate (Eq. 8.12). The angle is defined as the angle that the grain direction makes with the vertical axis.

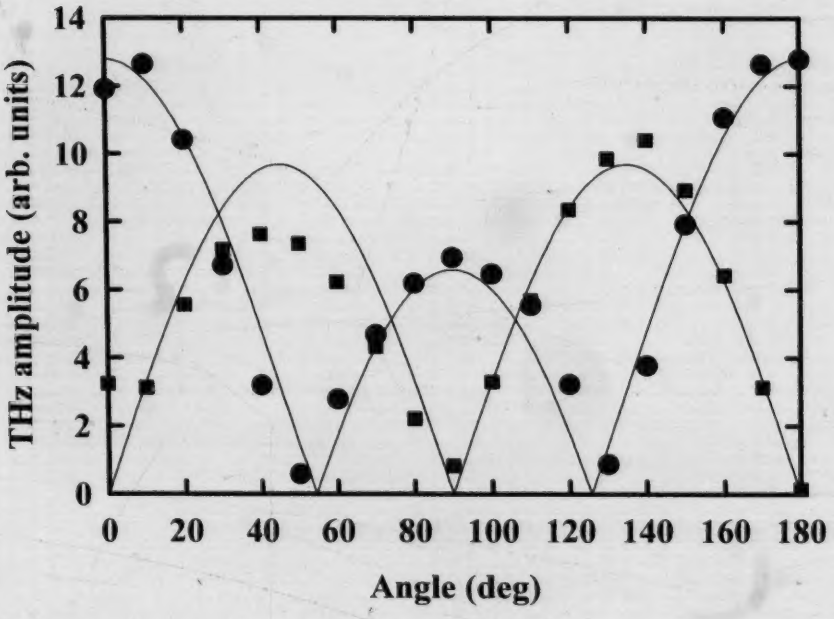

Figure 8.10: Frequency bin data as a function of wood orientation at a center frequency of 711 GHz. The data for vertically (squares) and horizontally (circles) polarized terahertz fields are shown for transmission through 3.025mm thick spruce, along with the expected angular dependence for behavior as a half-wave plate (Eq. 8.12). The angle is defined as the angle that the grain direction makes with the vertical axis.

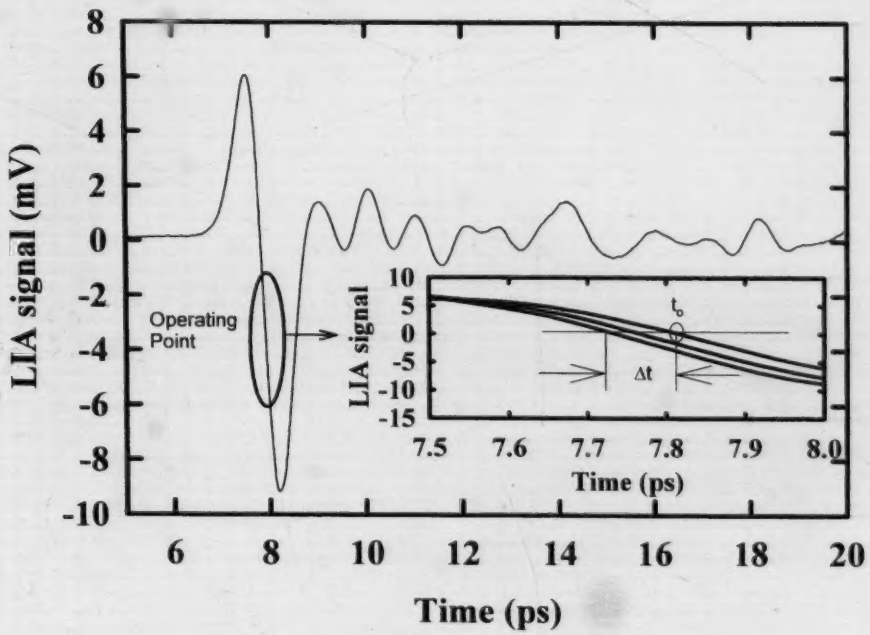

Figure 8.11: Operating point for mapping time delay of terahertz radiation to birefringence data. The figure shows a typical terahertz time-domain waveform, and the location of the operating point is shown in the inset. The lock-in amplifier signal is zeroed at the operating point, and the lens paper sample is rotated about its surface normal to map time-delay to amplitude information.

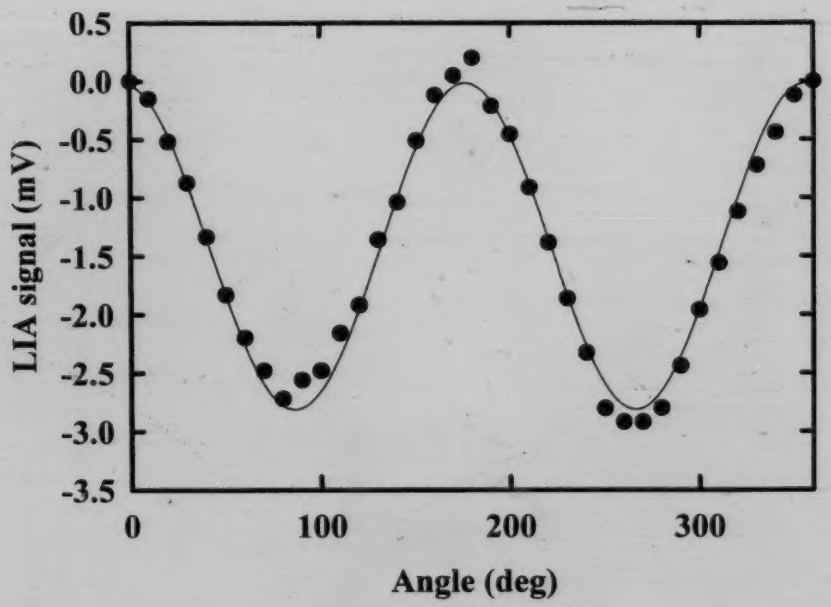

Figure 8.12: Lock-in amplifier signal as a function of orientation for transmission of terahertz radiation through 27 pieces of aligned lens paper. The lens paper oriented with fiber alignment vertical corresponds to zero degrees in the figure. The input terahertz field is polarized horizontally. The measured signal corresponds to mapping time delay to birefringence (see text for details).

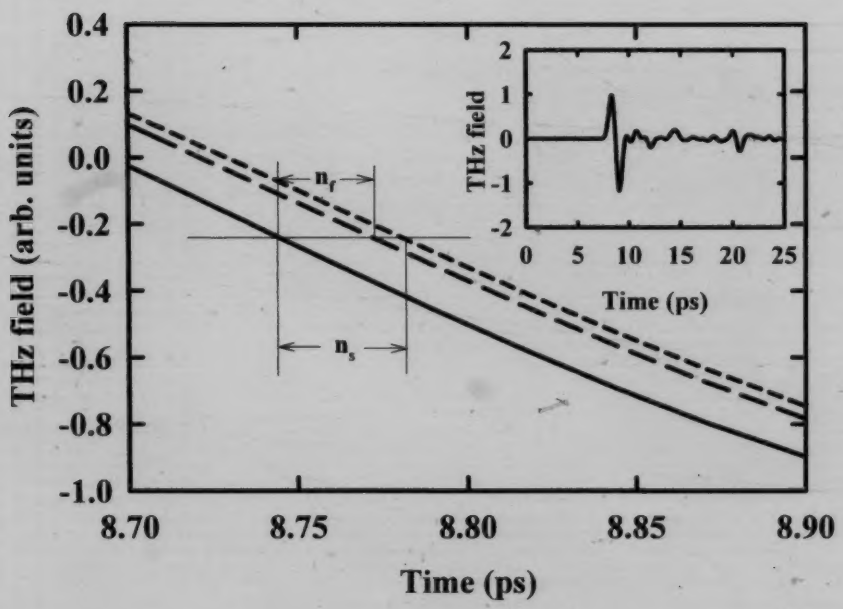

Figure 8.13: Terahertz signal as function of time delay for reference (solid), transmission through 21 μm thick single piece of lens paper with terahertz polarization perpendicular (long dashed) and parallel (short dashed) to the fiber orientation on an expanded scale. All three time-domain scans are shown in the inset, and are virtually indistinguishable on that scale. n_f and n_s represent the fast and slow axes, respectively.

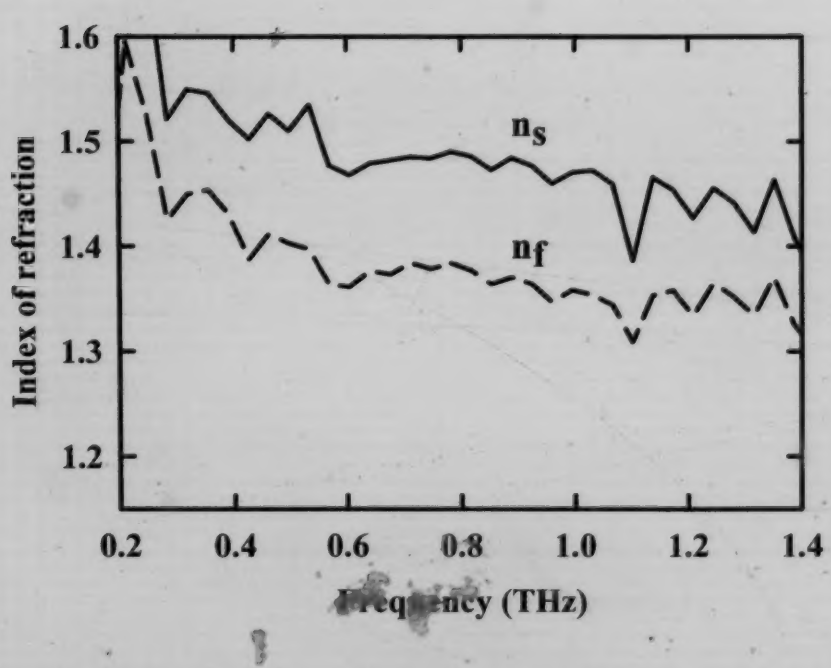

Figure 8.14: Index of refraction of a 21 μm thick piece of lens paper obtained with terahertz polarization perpendicular (long dashed) and parallel (solid) to the fiber orientation. n_f and n_s represent the fast and slow axes, respectively.

Figure 8.15: Optical image of the 2 mm thick piece of fir wood used for a linear transmission terahertz map (see text for details).

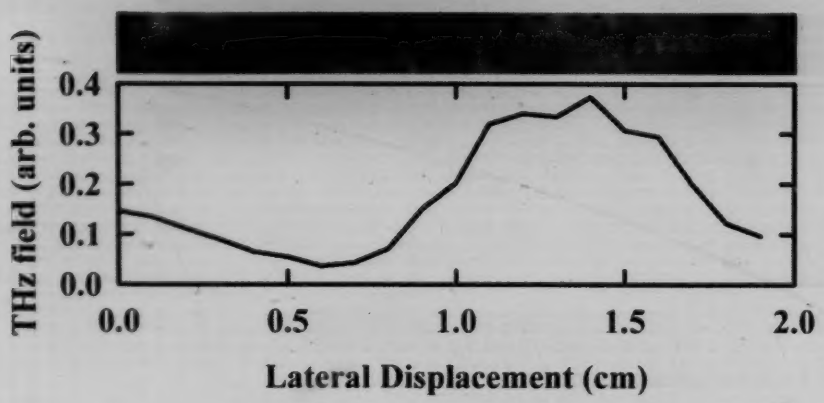

Figure 8.16: Terahertz transmission measurements as function of linear distance along a piece of fir. The top picture shows an optical image of the lateral scan, while the bottom figure plots the peak transmitted terahertz field amplitude as a function of displacement.

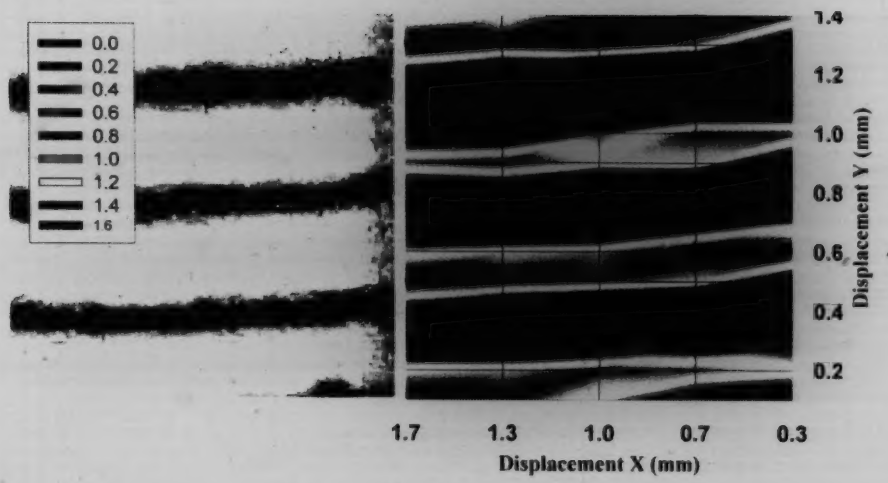

Figure 8.17: Optical picture of 2.2 mm thick fir (left) and terahertz transmission image of the same sample (right). Note that dark rings on left appear as dark rings on the figure in the right, as the higher porosity and larger density maps to higher terahertz attenuation. The scale on the upper left corresponds to the signal strength scale for the THz image.

Chapter 9

Conclusion and future work

9.1 Conclusions

Terahertz emission has been studied at high excitation fluences from GaAs, InAs and InP emitters in order to optimize their performance as sources of far-infrared radiation for industrial applications.

The emission of terahertz radiation from InAs surfaces was examined as a function of excitation fluence, and directly compared to the emission from a large-aperture photoconductive switch. It was found that the large aperture-photoconductive switch demonstrated a larger conversion efficiency. At an applied bias field of 1.6 kV / cm, the maximum conversion efficiency obtained with the large-aperture photoconductive switch was 1.9×10^{-5} in comparison to an unbiased (100) InAs surface, for which a measured maximum conversion efficiency of 2.1×10^{-6} was obtained. A reduced dependence of the radiated terahertz field on an applied magnetic field at high excitation fluences was observed, which indicates at most an enhancement of 3 times in performance of the InAs emitter could be expected with the application of a large 2 T magnetic field.

The emission mechanism from InAs surfaces at high excitation fluences was examined in detail. Pump polarization dependencies of terahertz radiation from the (100) crystal face of InAs demonstrated that the emission was dominated by a process other than bulk optical rectification or photo-carrier-related emission, which only contribute at levels of 13 % and 20 %, respectively. Complete calculations of bulk optical rectification and surface electric-field induced optical rectification were presented and compared to experimental results for terahertz emission and optical second harmonic generation from (100), (110) and (111) crystal faces of InAs. It was determined that the dominant emission mechanism for terahertz radiation from InAs surfaces is consistent with surface electric-field induced optical rectification, while the second-harmonic emission is consistent with bulk second-harmonic generation. Comparison of terahertz emission and optical second-harmonic emission from the InAs crystal faces revealed that a likely explanation for the dominant contribution to the terahertz radiation from surface electric-field

induced optical rectification is the large free-carrier contribution to the third-order susceptibility in InAs which scales with the inverse of the output frequency.

In order to try to enhance the conversion efficiency from semiconductor surface emitters, structuring of the surfaces was investigated. It was demonstrated that optical nonlinear interactions at semiconductor surfaces could be enhanced with the introduction of porosity. Porous samples of InP were shown to exhibit increased optical rectification, as well as second-harmonic generation, in comparison to bulk samples of InP, with output intensities on the order of 20 to 100 times those from unstructured surfaces, depending on the radiation process and polarization geometry used.

A system was constructed for spectroscopy measurements, employing a semi-large aperture photoconductive switch and characterized in detail. It was found that the overall conversion efficiency was approximately 2×10^{-7}, limited by the magnitude of the applied bias field and collection angle losses within the system, which could potentially be improved with the addition of a silicon collimating lens and an improved amplifier design for the bias field. The large signal-to-noise ratios and short acquisition times that are obtained using this set-up are a substantial improvement over the other sources studied in this thesis.

The application of pulsed terahertz radiation to wood and wood products was investigated. The terahertz properties of wood were first studied in detail. It was demonstrated that several wood species measured exhibit both diattenuation and birefringence. The magnitude of the birefringence was in the range of 0.06 to 0.13 depending on the wood species measured. This birefringence could also be used to determine fiber alignment in wood products and the sensitivity of this system was demonstrated by measuring the birefringence of a single piece of lens paper (20 μm thick) in less than a second. The dependence of terahertz transmission on the presence of early and latewood was also demonstrated and used to map out the grain pattern in a piece of wood.

9.2 Future Work

There are several questions that have been raised throughout this thesis, which require substantially more work to answer. These questions will be highlighted here.

In the data presented, the two processes of surface electric-field induced optical rectification and surface optical rectification cannot be distinguished from the measurements made in this thesis. One possible way to proceed with separating these two contributions would be to perform a systematic investigation of the terahertz emission from clean oxide-free InAs surfaces, and from samples with different doping concentrations. The doping concentration would affect the surface electric field, while having little effect on the pure surface nonlinear optical response.

It has been demonstrated that the introduction of porosity could enhance the bulk nonlinear optical response to the radiated terahertz field from InP surfaces. The tentative mechanism responsible for the increase was attributed to local-field enhancement within

the porous network. However, further measurements will be required to clarify this dependence and resolve whether other enhancement mechanisms are also involved.

As surface electric-field induced optical rectification is also a nonlinear optical process, it stands to reason that local-field enhancement would work to improve the conversion efficiency for terahertz radiation from InAs surfaces at high excitation fluence. In order to demonstrate whether or not this is a fact, high quality porous InAs samples are required which are not currently available. With such high-quality samples, it may be possible to generate terahertz fields from InAs surfaces with conversion efficiencies 30 to 100 times higher than the present solid surfaces making a large-aperture geometry competitive with large-aperture photoconductive switches. The benefit that this would have is that external bias fields and extensive cooling would not be required. Further work on both the enhancement mechanism for nonlinear optical interactions within the porous network as well as manufacturing of high-quality porous InAs would be required for this.

It was found that wood exhibits both birefringence and diattenuation in the terahertz frequency range. These properties are intrinsically related to the structural properties of wood. For example, the cell diameter and wall thickness likely contribute to the diattenuation. However, absorption within the wood due to water is expected to be significant due to the large absorption coefficient of water in the far-infrared. Therefore, it would be desirable to quantify the absorption of terahertz radiation by water within wood products. This may also be useful, for example, as a tool for measuring the water content for wood. A further refinement could be to investigate THz probing in a reflection geometry from wood such that thin samples would not be required and such a system could easily be adapted for use in industry.

Bibliography

[1] P. D. Coleman, "Reminiscences on selected millennium highlights in the quest for tunable terahertz-submillimeter wave oscillators," *IEEE J. Sel. Top. Quant. Electron.*, vol. 6, pp. 1000–1007, 2000.

[2] D. H. Auston, K. P. Cheung, and P. R. Smith, "Picosecond photoconducting hertzian dipoles," *Appl. Phys. Lett.*, vol. 45, pp. 284–286, 1984.

[3] M. van Exter and D. Grischkowsky, "Characterization of an optoelectronic terahertz beam system," *IEEE Trans. Microwave Theory Tech.*, vol. 38, pp. 1684–1691, 1990.

[4] G. Zhao, R. N. Schouten, N. van der Valk, W. T. Wenckebach, and P. C. M. Planken, "Design and performance of THz emission and detection setup based on a semi-insulating GaAs emitter," *Rev. Sci. Inst.*, vol. 73, pp. 1715–1719, 2002.

[5] B. B. Hu and M. C. Nuss, "Imaging with terahertz waves," *Opt. Lett.*, vol. 20, pp. 1716–1718, 1995.

[6] D. Mittleman, R. Jacobsen, and M. Nuss, "T-ray imaging," *IEEE J. Sel. Top. Quant. Electron.*, vol. 2, pp. 679–692, 1996.

[7] B. Ferguson, S. Wang, D. Gray, D. Abbot, and X. C. Zhang, "T-ray computed tomography," *Opt. Lett.*, vol. 27, pp. 1312–1314, 2002.

[8] K. McClatchey, M. T. Reiten, and R. A. Cheville, "Time-resolved synthetic aperture terahertz impulse imaging," *Appl. Phys. Lett.*, vol. 79, pp. 4485–4487, 2001.

[9] T. D. Dorney, W. W. Symes, R. G. Baraniuk, and D. M. Mittleman, "Terahertz multistatic reflection imaging," *J. Opt. Soc. Am. A*, vol. 19, pp. 1432–1442, 2002.

[10] Z. Jiang and X. C. Zhang, "Terahertz imaging via electrooptic effect," *IEEE Trans. Microwave Theory Tech.*, vol. 47, pp. 2644–2650, 1999.

[11] A. Nahata, J. T. Yardley, and T. F. Heinz, "Two-dimensional imaging of continuous-wave terahertz radiation using electro-optic detection," *Appl. Phys. Lett.*, vol. 81, pp. 963–965, 2002.

[12] J. E. Bjarnason, T. L. J. Chan, A. W. M. Lee, M. A. Celis, and E. R. Brown, "Millimeter-wave, terahertz and mid-infrared transmission through common clothing," *Appl. Phys. Lett.*, vol. 85, pp. 519–521, 2004.

[13] H. Zhong, N. Karpowicz, J. Partridge, X. Xie, J. Xu, and X. C. Zhang, "Terahertz wave imaging for landmine detection," in *Proc. SPIE*, vol. 5411, pp. 33–44, 2004.

[14] V. P. Wallace, R. M. Woodward, A. J. Fitzgerald, E. Pickwell, R. J. Pye, and D. A. Arnone, "Terahertz pulsed imaging of cancers," in *Proc. SPIE*, vol. 4949, pp. 353–359, 2003.

[15] D. Crawley, C. Longbottom, V. P. Wallace, B. Cole, D. Arnone, and M. Pepper, "Three-dimensional teraherz pulse imagaging of dental tissue," in *Proc. SPIE*, vol. 4633, pp. 84–89, 2002.

[16] M. van Exter, C. Fattinger, and D. Grischkowsky, "Terahertz time-domain spectroscopy of water vapor," *Opt. Lett.*, vol. 14, pp. 1128–1130, 1989.

[17] L. Thrane, R. H. Jacobsen, P. U. Hepsen, and S. R. Keiding, "THz reflection spectroscopy of liquid water," *Chem. Phys. Lett.*, vol. 240, pp. 330–333, 1995.

[18] R. A. Cheville and D. Grischkowsky, "Observation of pure rotational absorption spectra in the ν_2 band of hot H_2O in flames," *Opt. Lett.*, vol. 23, pp. 531–533, 1996.

[19] J. Zhang and D. Grischkowsky, "Waveguide terahertz time-domain spectroscopy of nanometer water layers," *Opt. Lett.*, vol. 29, pp. 1617–1619, 2004.

[20] J. Zhang and D. Grischkowsky, "Terahertz time-domain spectroscopy of submonolayer water adsorption in hydrophilic silica aerogel," *Opt. Lett.*, vol. 29, pp. 1031–1033, 2004.

[21] D. M. Mittleman, R. H. Jacobsen, R. Neelamani, R. G. Baraniuk, and M. C. Nuss, "Gas sensing using terahertz time-domain spectroscopy," *Appl. Phys. B*, vol. 67, pp. 379–390, 1998.

[22] M. Walther, S. Fischer, M. Shcall, H. Helm, and P. U. Jepsen, "Far-infrared vibrational spectra *all trans*, 9-cis and 13-cis retinal measured by THz time-domain spectroscopy," *Chem. Phys. Lett.*, vol. 332, pp. 389–396, 2000.

[23] A. G. Markelz, A. Roitberg, and E. J. Heilweil, "Pulsed terahertz spectroscopy of DNA, bovine serum albumin and collagen between 0.1 and 2.0 THz," *Chem. Phys. Lett.*, vol. 320, pp. 42–48, 2000.

[24] K. Kawase, Y. Ogawa, Y. Watanabe, and H. Inoue, "Non-destructive terahertz imaging of illicit drugs using spectral fingerprints," *Opt. Express*, vol. 11, pp. 2549–2554, 2003.

[25] D. Grischkowsky, S. Keiding, M. van Exter, and C. Fattinger, "Far-infrared time-domain spectroscopy with terahertz beams of dielectrics and semiconductors," *J. Opt. Soc. Am. B*, vol. 7, pp. 2006–2015, 1990.

[26] M. C. Beard, G. M. Turner, and C. A. Schmuttenmaer, "Subpicosecond carrier dynamics in low-temperature grown GaAs as measured by time-resolved terahertz spectroscopy," *Phys. Rev. Lett.*, vol. 86, pp. 340–343, 2001.

[27] F. A. Hegmann, R. R. Tywinski, K. P. H. Lui, J. E. Bullock, and J. E. Anthony, "Picosecond transient photoconductivity in functionalized pentacene molecular crystals probed by terahertz spectroscopy," *Phys. Rev. Lett.*, vol. 89, pp. 2274031–2274034, 2002.

[28] E. Knoesel, M. Bonn, J. Shan, and T. F. Heinz, "Charge transport and carrier dynamics in liquids probed by THz time-domain spectroscopy," *Phys. Rev. Lett.*, vol. 86, pp. 340–343, 2001.

[29] M. C. Kemp, P. F. Taday, B. E. Cole, J. A. Cluff, A. J. Fitzgerald, and W. R. Tribe, "Security applications of terahertz imaging," in *Proc. SPIE*, vol. 5070, pp. 44–52, 2003.

[30] G. C. Walker, E. Berry, N. N. Zinov'ev, A. J. Fitzgerald, R. E. Miles, M. Chamberlain, and M. A. Smith, "Teraherz imaging and international safety guidelines," in *Proc. SPIE*, vol. 4682, pp. 683–690, 2002.

[31] X.-C. Zhang and D. H. Auston, "Optoelectronic measurement of semiconductor surfaces and interfaces with femtosecond optics," *J. Appl. Phys.*, vol. 71, pp. 326–338, 1992.

[32] B. B. Hu, X.-C. Zhang, D. H. Auston, and P. R. Smith, "Free-space radiation from electro-optic crystals," *Appl. Phys. Lett.*, vol. 56, pp. 506–508, 1990.

[33] L. Xu, X.-C. Zhang, and D. H. Auston, "Terahertz beam generation by femtosecond optical pulses in electro-optic materials," *Appl. Phys. Lett.*, vol. 61, pp. 1784–1786, 1992.

[34] N. Sarukura, H. Ohtake, S. Izumida, and Z. Liu, "High average-power THz radiation from femtosecond laser-irradiated InAs in a magnetic field and its elliptical polarization characteristics," *J. Appl. Phys.*, vol. 84, pp. 654–656, 1998.

[35] C. Weiss, R. Wallenstein, and R. Beigang, "Magnetic-field-enhanced generation of terahertz radiation in semiconductor surfaces," *Appl. Phys. Lett.*, vol. 77, pp. 4160–4162, 2000.

[36] J. Shan, C. Weiss, R. Wallenstein, R. Beigang, and T. F. Heinz, "Origin of magnetic field enhancement in the generation of terahertz radiation from semiconductor surfaces," *Opt. Lett.*, vol. 26, pp. 849–851, 2001.

[37] R. McLaughlin, A. Corchia, M. B. Johnston, Q. Chen, C. M. Ciesla, D. D. Arnone, G. A. C. Jones, E. H. linfield, A. G. Davies, and M. Pepper, "Enhanced coherent terahertz emission from indium arsenide in the presence of a magnetic field," *Appl. Phys. Lett.*, vol. 76, pp. 2038–2040, 2000.

[38] J. N. Heyman, P. Neocleous, D. Hebert, P. A. Crowell, T. Mueller, and K. Unterrainer, "Terahertz emission from GaAs and InAs in a magnetic field," *Phys. Rev. B.*, vol. 64, pp. 0852021–0852027, 2001.

[39] M. Nakajima, M. Hangyo, M. Ohta, and H. Miyazaki, "Polarity reversal of terahertz waves radiated from semi-insulating InP surfaces induced by temperature," *Phys. Rev. B.*, vol. 67, pp. 195308–7, 2003.

[40] T. Dekorsy, H. Auer, H. J. Baker, H. G. Roskos, and H. Kurz, "THz electromagnetic emission by coherent infrared-active phonons," *Phys. Rev. B.*, vol. 53, pp. 4005–4014, 1996.

[41] S. Chuang, S. Schmitt-Ring, B. Greene, P. Saeta, and A. Levi, "Optical rectification at semiconductor surfaces," *Phys. Rev. Lett.*, vol. 68, pp. 102–105, 1992.

[42] D. You, R. R. Jones, P. H. Bucksbaum, and D. R. Dykaar, "Coherent generation of far-infrared radiation from InP," *J. Opt. Soc. Am. B.*, vol. 11, pp. 486–491, 1994.

[43] P. Saeta, B. Greene, and S. Chuang, "Short terahertz pulses from semiconductor surfaces: The importance of bulk difference-frequency mixing," *Appl. Phys. Lett.*, vol. 63, pp. 3482–3484, 1993.

[44] M. Nakajima, Y. Oda, and T. Suemoto, "Competing terahertz radiation mechanisms in semi-insulating InP at high-density excitation," *Appl. Phys. Lett.*, vol. 85, pp. 2694–2696, 2004.

[45] W. Lukosz, "Light emission by magnetic and electric dipoles close to a plane dielectric interface. iii. radiation patterns of dipoles with arbitrary orientation," *J. Opt. Soc. Am.*, vol. 69, pp. 1495–1503, 1979.

[46] H. K. Yang, P. L. Richards, and Y. R. Shen, "A wideband coherent terahertz spectroscopy system using optical rectification and electro-optic sampling," *Appl. Phys. Lett.*, vol. 19, pp. 320–323, 1971.

[47] T. A. Germer, K. W. Kolasinski, J. C. Stephenson, and L. J. Richter, "Depletion-electric-field-induced second-harmonic generation near oxidized GaAs (001) surfaces," *Phys. Rev. B*, vol. 55, pp. 10694–10706, 1997.

[48] D. Dragoman and M. Dragoman, "Terahertz fields and applications," *Progr. Quant. Electr.*, vol. 28, pp. 1–66, 2004.

[49] P. C. M. Planken, H.-K. Nienhuys, H. J. Bakker, and T. Wenckebach, "Measurement and calculation of the orientation dependence of terahertz pulse detection in ZnTe," *J. Opt. Soc. Am. B.*, vol. 18, pp. 313–317, 2001.

[50] E. Gerecht, C. F. Musante, Y. Zhuang, K. S. Yngvesson, T. Goyette, J. C. Dickinson, J. Waldman, P. A. Yagoubov, G. N. Goltsman, B. M. Voronav, and E. M. Gershenzon, "NbN hot electron bolometric mixers - a new technology for low-noise THz recievers," *IEEE Trans. Microwave Theory Tech.*, vol. 47, pp. 2519–2527, 1999.

[51] P. Y. Han, M. Tani, M. Usami, S. Kono, R. Kersting, and X. C. Zhang, "A direct comparison between terahertz time-domain spectroscopy and far-infrared fourier transform spectroscopy," *J. Appl. Phys.*, vol. 89, pp. 2357–2359, 2001.

[52] S.-G. Park, M. R. Melloch, and A. M. Weiner, "Comparison of terahertz waveforms measured by electro-optic and photoconductive sampling," *Appl. Phys. Lett.*, vol. 73, pp. 3184–3186, 1998.

[53] Y. Cai, I. Brener, J. Lopata, J. Wynn, L. Pfeiffer, J. B. Stark, Q. Wu, X. C. Zhang, and J. F. Federici, "Coherent terahertz radiation detection: Direct comparison between free-space electro-optic sampling and antenna detection," *Appl. Phys. Lett.*, vol. 73, pp. 444–446, 1998.

[54] Z. Jiang and X. C. Zhang, "Electro-optic measurement of THz field pulses with a chirped optical beam," *Appl. Phys. Lett.*, vol. 72, pp. 1945–1947, 1998.

[55] J. Shan, A. S. Weling, E. Knoesel, L. Bartels, M. Bonn, A. Nahata, G. A. Reider, and T. F. Heinz, "Single-shot measurement of terahertz electromagnetic pulses by use of electro-optic sampling," *Opt. Lett.*, vol. 25, pp. 426–428, 2000.

[56] Q. Wu and X. C. Zhang, "Free-space electro-optics sampling of mid-infrared pulses," *Appl. Phys. Lett.*, vol. 71, pp. 1285–1287, 1997.

[57] A. Leitenstorfer, S. Hunsche, J. Shah, M. C. Nuss, and W. H. Knox, "Detectors and sources for ultrabroadband electro-optic sampling: Experiment and theory," *Appl. Phys. Lett.*, vol. 74, pp. 1516–1518, 1999.

[58] Q. Wu and X. C. Zhang, "Design and characterization of traveling-wave electrooptic terahertz sensors," *IEEE J. Sel. Top. Quantum Electron.*, vol. 2, pp. 693–700, 1996.

[59] F. L. Pedrotti and L. S. Pedrotti, *Introduction to Optics.* New Jersey: Prentice Hall, 2nd ed., 1993.

[60] R. W. Boyd, *Nonlinear Optics.* San Diego: Academic Press, 2nd ed., 2003.

[61] M. Abarkan, J. P. Salvestrini, M. D. Fontana, and M. Aillerie, "Frequency and wavelength dependences of electro-optic coefficients in inorganic crystals," *Appl. Phys. B*, vol. 76, pp. 765–769, 2003.

[62] E. H. Turner, "High-frequency electro-optic coefficients of lithium niobate," *Appl. Phys. Lett.*, vol. 8, pp. 303–304, 1966.

[63] P. U. Jepsen, C. Winnewisser, M. Schall, V. Schyja, S. R. Keiding, and H. Helm, "Detection of THz pulses by phase retardation in lithium tantalate," *Phys. Rev. B*, vol. 53, pp. R3052–R3054, 1996.

[64] C. Winnewisser, P. U. Jepsen, M. Schall, V. Schyja, and H. Helm, "Electro-optic detection of THz radiation in $LiTaO_3$, $LiNbO_3$ and ZnTe," *Appl. Phys. Lett.*, vol. 70, pp. 3069–3071, 1997.

[65] A. Nahata, A. S. Weling, and T. F. Heinz, "A wideband coherent terahertz spectroscopy system using optical rectification and electro-optic sampling," *Appl. Phys. Lett.*, vol. 69, pp. 2321–2323, 1996.

[66] G. D. Boyd, W. L. Bond, and H. L. Carter, "Refractive index as a function of temperature in $LiNbO_3$," *J. Appl. Phys.*, vol. 38, pp. 1941–1943, 1967.

[67] M. Schall, H. Helm, and S. R. Keiding, "Far infrared properties of electro-optic crystals measured by THz time-domain spectroscopy," *Int. J. of Infrared and Millimeter Waves*, vol. 20, pp. 595–604, 1999.

[68] T. Hattori, K. Tukamoto, and H. Nakatsuka, "Time-resolved study of intense terahertz pulses generated by a large-aperture photoconductive antenna," *Jpn. J. Appl. Phys.*, vol. 40, pp. 4907–4912, 2001.

[69] Q. Wu and X. C. Zhang, "7 terahertz broadband GaP electro-optic sensor," *Appl. Phys. Lett.*, vol. 70, pp. 1784–1786, 1997.

[70] A. Nahata, J. T. Yardley, and T. F. Heinz, "Free-space electro-optic detection of continuous-wave terahertz radiation," *Appl. Phys. Lett.*, vol. 75, pp. 2524–2526, 1999.

[71] M. Reid and R. Fedosejevs, "Quantitative comparison of THz emission from (100) InAs surfaces and GaAs large-aperture photoconductive switch at high fluences," *Appl. Opt.*, vol. 44, pp. 149–153, 2004.

[72] J. T. Darrow, X.-C. Zhang, and D. H. Auston, "Saturation properties of large-aperture photoconducting antennas," *IEEE J. Quantum Electron.*, vol. 28, pp. 1607–1616, 1992.

[73] D. You, R. R. Jones, P. H. Bucksbaum, and D. R. Dykaar, ""generation of high-power sub-single-cycle 500-fs electromagnetic pulses"," *Opt. Lett.*, vol. 18, pp. 290–292, 1993.

[74] T. Loffler and H. G. Roskos, "Gas-pressure dependence of terahertz-pulse generation in a laser-generated nitrogen plasma," *J. Appl. Phys.*, vol. 91, pp. 2611–2614, 2002.

[75] A. Gurtler, C. Winnewisser, H. Helm, and P. U. Jepsen, "Terahertz propagation in the near field and far field," *J. Opt. Soc. Am. A.*, vol. 17, pp. 74–83, 2000.

[76] D. You and P. H. Bucksbaum, "Propagation of half-cycle far infrared pulses," *J. Opt. Soc. Am. B.*, vol. 14, pp. 1651–1655, 1997.

[77] E. Budiarto, N.-W. Pu, S. Jeong, and J. Bokor, "Near-field propagation of terahertz pulses from a large-aperture antenna," *Opt. Lett.*, vol. 23, pp. 213–215, 1998.

[78] G. Rodriguez and A. J. Taylor, "Screening of the bias field in terahertz generation from photoconductors," *Opt. Lett.*, vol. 21, pp. 1046–1048, 1996.

[79] H. Takahashi, Y. Suzuki, A. Quema, M. Sakai, T. Yano, S. Ono, N. Sarukura, M. Hosomizu, T. Tsukamoto, G. Nishijima, and K. Watanabe, "Magnetic-field-induced enhancement of THz-radiation power from femtosecond-laser-irradiated InAs up to 27T," *Jpn. J. Appl. Phys.*, vol. 42, pp. L532–L534, 2003.

[80] H. Takahashi, Y. Suzuki, M. Sakai, S. Ono, N. Sarukura, T. Sugiura, T. Hirosumi, and M. Yoshida, "Significant enhancement of terahertz radiation from InSb by use of a compact fiber laser and an external magnetic field," *Appl. Phys. Lett.*, vol. 82, pp. 2005–2007, 2003.

[81] M. Hangyo, M. Migita, and K. Nakayama, "Magnetic field and temperature dependence of terahertz radiation from InAs surfaces excited by femtosecond laser pulses," *J. Appl. Phys.*, vol. 90, pp. 3409–3412, 2001.

[82] H. Takahashi, A. Quema, R. Yoshioka, S. Ono, and N. Sarukura, "Excitation fluence dependence of terahertz radiation mechanism from femtosecond-laser-irradiated InAs under magnetic field," *Appl. Phys. Lett.*, vol. 82, pp. 1068–1070, 2003.

[83] T. Hattori, R. Rungsawang, K. Ohta, and K. Tukamoto, "Gaussian beam analysis of temporal waveform of focused terahertz pulses," *Jpn. J. Appl. Phys.*, vol. 41, pp. 5198–5204, 2002.

[84] M. Reid and R. Fedosejevs, "Terahertz emission from (100) InAs surfaces at high excitation fluence," *Appl. Phys. Lett.*, vol. 86, pp. 011904–011906, 2005.

[85] M. Reid and R. Fedosejevs, "Terahertz emission from surface optical rectification in n-InAs," in *Proc. SPIE*, vol. 5577, pp. 659–669, 2004.

[86] M. B. Johnston, D. M. Whittaker, A. Corchia, A. G. Davies, and E. H. Linfield, "Simulation of terahertz generation at semiconductor surfaces," *Phys. Rev. B.*, vol. 65, pp. 1653011–1653018, 2002.

[87] B. I. Greene, P. N. Saeta, D. R. Dykaar, S. Schmitt-Rink, and S. L. Chuang, "Far-infrared light generation at semiconductor surfaces and its spectroscopic applications," *IEEE J. Quantum. Electron.*, vol. 28, pp. 2302–2311, 1992.

[88] S. Howells and L. Schlie, "Temperature dependence of terahertz pulses produced by difference-frequency mixing in InSb," *Appl. Phys. Lett.*, vol. 67, pp. 3688–3690, 1995.

[89] S. Kono, P. Gu, M. Tani, and K. Sakai, "Temperature dependence of terahertz radiation from n-type InSb and n-type InAs surfaces," *Appl. Phys. B*, vol. 71, pp. 901–904, 2000.

[90] P. Gu, M. Tani, S. Kono, K. Sakai, and X.-C. Zhang, "Study of terahertz radiation from InAs and InSb," *J. Appl. Phys.*, vol. 91, pp. 5533–5537, 2002.

[91] J. Sipe, D. Moss, and H. van Driel, "Phenomenological theory of optical second- and third-harmonic generation from cubic centrosymmetric crystals," *Phys. Rev. B.*, vol. 35, pp. 1129–1140, 1987.

[92] W. Hübner, K. Bennemann, and K. Böhmer, "Theory for the nonlinear optical response of transition metals: Polarization dependence as a fingerprint of the electronic structure at suraces and interfaces," *Phys. Rev. B*, vol. 50, pp. 17597–17605, 1994.

[93] T. Stehlin, M. Feller, P. Guyot-Sionnest, and Y. Shen, "Optical second-harmonic generation as a surface probe for noncentrosymmetric media," *Opt. Lett.*, vol. 13, pp. 389–391, 1988.

[94] N. Bloembergen, "Surface nonlinear optics: a historical overview," *Appl. Phys. B*, vol. 68, pp. 289–293, 1999.

[95] J. F. McGilp, "A review of optical second-harmonic and sum-frequency generation at surfaces and interfaces," *J. Phys. D*, vol. 29, pp. 1812–1821, 1996.

[96] Y. R. Shen, "Surface contribution versus bulk contribution in surface nonlinear optical spectroscopy," *Appl. Phys. B*, vol. 68, pp. 295–300, 1999.

[97] S. Adachi, *Optical Constants of Crystalline and Amorphous Semiconductors*. Boston: Kluwer Academic Publishers, 1st ed., 1999.

[98] P. N. Butcher and D. Cotter, *The elements of Nonlinear Optics*. Cambridge: Cambridge University Press, 1st ed., 1990.

[99] R. Adomavicius, A. Urbanowicz, G. Molis, A. Krotkus, and E. Satkovskis, "Terahertz emission from p-InAs due to the instantaneous polarization," *Appl. Phys. Lett.*, vol. 85, pp. 2463–2465, 2004.

[100] S, Buchner, L. Y. Ching, and E. Burstein, "Raman scattering at the (111) and $(\bar{1}\bar{1}\bar{1})$ surfaces of n- and p-InAs," *Phys. Rev. B*, vol. 14, pp. 4459–4462, 1976.

[101] W. Y. Ching and M. Z. Huang, "Calculation of optical excitations in cubic semiconductors. III. third-harmonic generation," *Phys. Rev. B*, vol. 47, pp. 9479–9491, 1993.

[102] J. J. Wynne, "Optical third-order mixing in GaAs, Ge, Si, and InAs," *Phys. Rev.*, vol. 178, pp. 1295–1303, 1969.

[103] S. S. Jha and N. Bloembergen, "Nonlinear optical susceptibilities in group-IV and III-V semiconductors," *Phys. Rev.*, vol. 171, pp. 891–898, 1968.

[104] A. Mayer and F. Keilmann, "Far-infrared nonlinear optics II. $\chi^{(3)}$ contributions from the dynamics of free cariers in semiconductors," *Phys. Rev. B*, vol. 33, pp. 6962–6968, 1986.

[105] M. Reid, I. V. Cravetchi, R. Fedosejevs, I. M. Tiginyanu, and L. Sirbu, "Enhanced terahertz emission from porous InP (111) membranes," *Appl. Phys. Lett.*, vol. 86, pp. 021904–1–021904–3, 2005.

[106] M. Reid, I. V. Cravetchi, R. Fedosejevs, I. M. Tiginyanu, L. Sirbu, and R. W. Boyd, "Enhanced nonlinear optical response of InP (100) membranes," *Phys. Rev. B*, vol. 71, pp. 081306R–1–081306R–4, 2005.

[107] M. Reid, I. V. Cravetchi, R. Fedosejevs, I. M. Tiginyanu, L. Sirbu, and R. W. Boyd, "Enhanced terahertz emission from porous InP," in *Optical Terahertz Science and Technology Topical Meeting on CD-ROM*, p. WA4, 2005.

[108] I. M. Tiginyanu, I. V. Kravetsky, S. Langa, G. Marowsky, J. Monecke, and H. Föll, "Porous III-V compounds as nonlinear optical materials," *Phys. Stat. Sol. A*, vol. 197, pp. 549–555, 2003.

[109] S. Langa, J. Carstensen, M. Christophersen, H. Föll, and I. Tiginyanu, "Observation of crossing pores in anodically etched n-GaAs," *Appl. Phys. Lett.*, vol. 78, pp. 1074–1076, 2001.

[110] V. A. Mel'nikov, L. A. Golovan, S. O. Konorov, D. A. Muzychenko, A. B. Fedotov, A. M. Zheltikov, V. Y. Timoshenko, and P. K. Kashkarov, "Second-harmonic generation in strongly scattering porous gallium phosphide," *Appl. Phys. B*, vol. 79, pp. 225–228, 2004.

[111] L. A. Golovan, V. A. Mel'nikov, S. O. Konorov, A. B. Fedotov, S. A. Gavrilov, A. M. Zheltikov, P. K. Kashkarov, V. Y. Timoshenko, G. I. Petrov, L. Li, and V. V. Yakovlev, "Efficient second-harmonic generation by scattering from porous galllium phosphide," *JETP Lett.*, vol. 78, pp. 193–197, 2003.

[112] P. U. Jepsen, R. H. Jacobsen, and S. R. Keiding, "Generation and detection of terahertz pulses from biased semiconductor antennas," *J. Opts. Soc. Am. B*, vol. 13, pp. 2424–2436, 1996.

[113] G. Zhao, R. N. Schouten, N. van der Valk, W. T. Wenckebach, and P. C. M. Planken, "A terahertz system using semi-large emitters: noise and performance characteristics," *Phys. Med. Biol.*, vol. 47, pp. 3609–3704, 2002.

[114] M. R. Stone, M. Naftaly, R. E. Miles, J. R. Fletcher, and D. P. Steenson, "Electrical and radiation characteristics of semilarge photoconductive terahertz emitters," *IEEE Trans. Microwave Theory Tech.*, vol. 52, pp. 2420–2429, 2004.

[115] S. Hadjiloucas, L. S. Karatzas, and J. W. Bowen, "Measurements of leaf water content using terahertz radiation," *IEEE Trans. Microwave Theory Tech.*, vol. 47, pp. 142–149, 1999.

[116] M. Koch, S. Hunsche, P. Schaucher, M. C. Nuss, J. Feldmann, and J. Fromm, "THz-imaging: a new method for density mapping of wood," *Wood Sci. Technol.*, vol. 32, pp. 421–427, 1998.

[117] S. Hunsche and M. C. Nuss, "Terahertz "T-ray" tomography," in *Proc. SPIE*, vol. 3465, pp. 426–433, 1998.

[118] S. W. Smye, J. M. Chamberlain, A. J. Fitzgerald, and E. Berry, "The interaction between terahertz radiation and biological tissue," *Phys. Med. Biol.*, vol. 46, pp. R101–R112, 2001.

[119] L. Duvillaret, F. Garet, and J.-L. Coutaz, "A reliable method for extraction of material parameters in terahertz time-domain spectroscopy," *IEEE J. Sel. Top. Quant. Electron.*, vol. 2, pp. 739–746, 1996.

[120] J. D. Jackson, *Classical Electrodynamics*. New York: John Wiley and Sons, Inc., 3rd ed., 1999.

[121] R. Boulay, B. Drouin, and R. Gagnon, "Method for measuring the fibre orientation anisotropy in a fibrous structure," 1987.

[122] F. P. Kollmann and W. A. Côté, *Principles of Wood Science and Technology I Solid Wood*. New York: Springer-Verlag, 1st ed., 1968.

[123] A. J. Stamm, *Wood and Cellulose Science*. New York: The Ronald Press Company, 1st ed., 1964.

Appendix A

Appendix

A.1 Electro-optic detection in ZnTe

A.1.1 Derivation of relation 3.26

From Fig. 3.5 we can write:

$$tan(\Psi) = \frac{\sqrt{2}C}{-\frac{1}{2}B + \frac{1}{2}\sqrt{B^2 + 8C^2}} \tag{A.1}$$

where

$$\begin{aligned} B &= r_{41}E_{THz}cos(\theta) \\ C &= \frac{r_{41}E_{THz}sin(\theta)}{\sqrt{2}} \end{aligned} \tag{A.2}$$

Inserting the definitions in Eq. A.2 into Eq. A.1, we obtain:

$$\begin{aligned} tan(\Psi) &= \frac{2sin(\theta)}{-cos(\theta) + \sqrt{cos^2(\theta) + 4sin^2(\theta)}} \\ &= \frac{2tan(\theta)}{-1 + \sqrt{1 + 4tan^2(\theta)}} \\ &\Rightarrow tan(\Psi)\sqrt{1 + 4tan^2(\theta)} = 2tan(\theta) + tan(\Psi) \\ &\Rightarrow tan^2(\Psi)(1 + 4tan^2(\theta)) = 4tan^2(\theta) + tan^2(\Psi) + 4tan(\theta)tan(\Psi) \\ &\Rightarrow 0 = 4tan^2(\theta)(1 - tan^2(\Psi)) + 4tan(\theta)tan(\Psi) \\ &\Rightarrow -\frac{tan(\Psi)}{1 - tan^2(\Psi)} = tan(\theta) \end{aligned} \tag{A.3}$$

Using the trigonometric identity:

$$tan(2x) = \frac{2tan(x)}{1 - tan^2(x)} \tag{A.4}$$

in Eq. A.3 we obtain the desired result:

$$tan(2\Psi) = -2tan(\theta) \tag{A.5}$$

A.1.2 Derivation of Eq. 3.35

The first derivation is as follows:

$$\begin{aligned}
sin(2\left[\phi - \Psi\right]) &= 2sin(\phi - \Psi)cos(\phi - \Psi) \\
&= 2\left(sin(\phi)cos(\Psi) - cos(\phi)sin(\Psi)\right)\left(cos(\phi)cos(\Psi) + sin(\phi)sin(\Psi)\right) \\
&= 2sin(\phi)cos(\phi)cos^2(\Psi) - 2cos^2(\phi)cos(\Psi)sin(\Psi) \\
&+ \; 2sin^2(\phi)cos(\Psi)sin(\Psi) - 2sin(\phi)cos(\phi)sin^2(\Psi) \\
&= 2\left(\left[cos^2(\Psi) - sin^2(\Psi)\right]sin(\phi)cos(\phi) + sin(\Psi)cos(\Psi)\left[sin^2(\phi) - cos^2(\phi)\right]\right) \\
&= 2\left(cos(2\Psi)\frac{1}{2}sin(2\phi) - \frac{1}{2}cos(2\phi)sin(2\Psi)\right) \\
&= cos(2\Psi)sin(2\phi) - cos(2\phi)sin(2\Psi) \\
&= cos(2\Psi)\left(sin(2\phi) - tan(2\Psi)cos(2\phi)\right) \\
&= \left(cos^2(\Psi) - sin^2(\Psi)\right)\left(sin(2\phi) - tan(2\Psi)cos(2\phi)\right)
\end{aligned} \tag{A.6}$$

The second identity is derived as follows:
let

$$lhs \equiv sin(\theta)\left(\frac{1 + tan^2(\Psi)}{tan(\Psi)}\right)sin(2(\phi - \Psi)) \tag{A.7}$$

then

$$lhs = sin(\theta)\left(\frac{1 + tan^2(\Psi)}{tan(\Psi)}\right)\left(cos^2(\Psi) - sin^2(\Psi)\right)\left(sin(2\phi) - tan(2\Psi)cos(2\phi)\right) \tag{A.8}$$

where the identity derived in Eq. A.6 has been used. We can then reduce as follows:

$$
\begin{aligned}
lhs &= sin(\theta)\left(\frac{1+tan^2(\Psi)}{tan(\Psi)}\right)\left(cos^2(\Psi)-sin^2(\Psi)\right)\left(sin(2\phi)-tan(2\Psi)cos(2\phi)\right) \\
&= sin(\theta)\left(\frac{cos^4(\Psi)-sin^4(\Psi)}{cos(\Psi)sin(\Psi)}\right)\left(sin(2\phi)-tan(2\Psi)cos(2\phi)\right) \\
&= 2sin(\theta)\left(\frac{cos(2\Psi)}{sin(2\Psi)}\right)\left(sin(2\phi)+2tan(\theta)cos(2\phi)\right) \qquad \text{(A.9)}
\end{aligned}
$$

where the relation in Eq. A.5 has been used. Continuing with Eq. A.9 we have:

$$
\begin{aligned}
lhs &= \left(\frac{2sin(\theta)}{tan(2\Psi)}\right)\left(sin(2\phi)+2tan(\theta)cos(2\phi)\right) \\
&= -cos(\theta)\left(sin(2\phi)+2tan(\theta)cos(2\phi)\right) \\
&= -\left(cos(\theta)sin(2\phi)+2sin(\theta)cos(2\phi)\right) \qquad \text{(A.10)}
\end{aligned}
$$

This is the end of the derivation.

A.2 Calculation of the bulk electric-dipole contribution to nonlinear susceptibility

In section 5.2.1, the independent elements of the susceptibility tensor were computed under the application of a transformation. In this case, the transformation was a combination of a rotation to orient the $\hat{z}$ axis perpendicular to the crystal faces for each of the (100), (110) and (111) crystal faces, with a subsequent rotation about the surface normal by an amount ϕ. The total transformation matrix as given by Eq. 5.2 is written as: R_{ij}, here, which is a 3 × 3 matrix. The new susceptibility elements in contracted notation are given by:

$$
\begin{aligned}
\frac{\chi_{xxx}(\phi)}{d_{14}} &= 6R_{xx}R_{xy}R_{xz} \\
\frac{\chi_{yyy}(\phi)}{d_{14}} &= 6R_{yx}R_{yy}R_{yz} \\
\frac{\chi_{zzz}(\phi)}{d_{14}} &= 6R_{zx}R_{zy}R_{zz} \\
\frac{\chi_{xyy}(\phi)}{d_{14}} &= 2R_{xx}R_{yy}R_{yz} + 2R_{xy}R_{yx}R_{yz} + 2R_{xz}R_{yx}R_{yy} \\
\frac{\chi_{yxx}(\phi)}{d_{14}} &= 2R_{yx}R_{xy}R_{xz} + 2R_{yy}R_{xx}R_{xz} + 2R_{yz}R_{xy}R_{xx} \\
\frac{\chi_{xzz}(\phi)}{d_{14}} &= 2R_{xx}R_{zy}R_{zz} + 2R_{xy}R_{zx}R_{zz} + 2R_{xz}R_{zy}R_{zx} \\
\frac{\chi_{zxx}(\phi)}{d_{14}} &= 2R_{zx}R_{xy}R_{xz} + 2R_{zy}R_{xx}R_{xz} + 2R_{zz}R_{xy}R_{xx} \\
\frac{\chi_{yzz}(\phi)}{d_{14}} &= 2R_{yx}R_{zy}R_{zz} + 2R_{yy}R_{zx}R_{zz} + 2R_{yz}R_{zy}R_{zx} \\
\frac{\chi_{zyy}(\phi)}{d_{14}} &= 2R_{zx}R_{yy}R_{yz} + 2R_{zy}R_{yz}R_{yx} + 2R_{zz}R_{yy}R_{yx} \\
\frac{\chi_{xyz}(\phi)}{d_{14}} &= R_{xx}R_{yy}R_{zz} + R_{xx}R_{yz}R_{zy} + R_{xy}R_{yz}R_{zx} \\
&+ R_{xy}R_{yx}R_{zz} + R_{xz}R_{yx}R_{yy} + R_{xz}R_{yy}R_{zx} \\
\frac{\chi_{yxz}(\phi)}{d_{14}} &= R_{yx}R_{xy}R_{zz} + R_{yx}R_{xz}R_{zy} + R_{yy}R_{xz}R_{zx} \\
&+ R_{yy}R_{xx}R_{zz} + R_{yz}R_{xx}R_{zy} + R_{yz}R_{xy}R_{zx} \\
\frac{\chi_{zxy}(\phi)}{d_{14}} &= R_{zx}R_{xy}R_{yz} + R_{zx}R_{xz}R_{yy} + R_{zy}R_{xz}R_{yx} \\
&+ R_{zy}R_{xx}R_{yz} + R_{zz}R_{xx}R_{yy} + R_{zz}R_{xy}R_{yx} \\
\frac{\chi_{xxz}(\phi)}{d_{14}} &= 2R_{xx}R_{xy}R_{zz} + 2R_{xx}R_{xz}R_{zy} + 2R_{xy}R_{xz}R_{zx} \\
\frac{\chi_{xxy}(\phi)}{d_{14}} &= 2R_{xx}R_{xy}R_{yz} + 2R_{xx}R_{xz}R_{yy} + 2R_{xy}R_{xz}R_{yx} \\
\frac{\chi_{yyz}(\phi)}{d_{14}} &= 2R_{yx}R_{yy}R_{zz} + 2R_{yx}R_{yz}R_{zy} + 2R_{yy}R_{yz}R_{zx} \\
\frac{\chi_{zxz}(\phi)}{d_{14}} &= 2R_{zx}R_{xy}R_{zz} + 2R_{zx}R_{xz}R_{zy} + 2R_{zy}R_{xx}R_{zz} \\
\frac{\chi_{zyz}(\phi)}{d_{14}} &= 2R_{zx}R_{yy}R_{zz} + 2R_{zx}R_{yz}R_{zy} + 2R_{zy}R_{yx}R_{zz} \\
\frac{\chi_{yxy}(\phi)}{d_{14}} &= 2R_{yx}R_{xy}R_{yz} + 2R_{yx}R_{xz}R_{yy} + 2R_{yy}R_{xx}R_{yz} \qquad \text{(A.11)}
\end{aligned}
$$

It is important to note that this is for crystals of symmetry class $\bar{4}3m$. However, this holds for an arbitrary rotation matrix, R_{ij}.

Once the susceptibilites are found, the lattice polarization can be obtained. For the geometry outlined in section 5.2.1, the lattice polarizations were calculated to be:

$$
\begin{aligned}
P_s^{(100)} &= -4d_{14}sin(2\phi)t_p^2 f_s f_c E_p^2 + 2d_{14}cos(2\phi)t_s t_p f_s E_p E_s \\
P_k^{(100)} &= -2d_{14}cos(2\phi)t_p^2 f_s f_c E_p^2 - 4d_{14}sin(2\phi)t_s t_p f_s E_p E_s \\
P_z^{(100)} &= d_{14}cos(2\phi)t_s^2 E_s^2 - d_{14}cos(2\phi)t_p^2 f_c^2 E_p^2 - 2d_{14}sin(2\phi)t_s t_p f_c E_p E_s \\
P_s^{(110)} &= 3d_{14}cos(\phi)sin^2(\phi)t_s^2 E_s^2 + \frac{d_{14}}{4}(cos(\phi) + 3cos(3\phi))t_p^2 f_c^2 E_p^2 \\
&- d_{14}cos(\phi)t_p^2 f_s^2 E_p^2 - 2\frac{d_{14}}{4}(sin(\phi) - 3sin(3\phi))t_s t_p f_c E_p E_s \\
P_k^{(110)} &= -d_{14}(sin(\phi) - 3sin(3\phi))t_s^2 E_s^2 - 3d_{14}cos^2(\phi)sin(\phi)t_p^2 f_c^2 E_p^2 \\
&+ d_{14}sin(\phi)t_p^2 f_s^2 E_p^2 + 2\frac{d_{14}}{4}(cos(\phi) + 3cos(3\phi))t_s t_p f_c E_p E_s \\
P_z^{(110)} &= 2d_{14}sin(\phi)t_p^2 f_s f_c E_p^2 - 2d_{14}cos(\phi)t_s t_p f_s E_p E_s \\
P_s^{(111)} &= \sqrt{\frac{2}{3}}d_{14}(t_p^2 f_c^2 E_p^2 - t_s^2 E_s^2)sin(3\phi) - \frac{2d_{14}}{\sqrt{3}}t_s t_p f_s E_p E_s \\
&- 2\sqrt{\frac{2}{3}}d_{14}t_s t_p f_c E_p E_s cos(3\phi) \\
P_k^{(111)} &= \sqrt{\frac{2}{3}}d_{14}(t_p^2 f_c^2 E_p^2 - t_s^2 E_s^2)cos(3\phi) - \frac{2d_{14}}{\sqrt{3}}tp^2 f_s f_c E_p^2 \\
&+ 2\sqrt{\frac{2}{3}}d_{14}t_s t_p f_c E_p E_s sin(3\phi) \\
P_z^{(111)} &= \frac{d_{14}}{\sqrt{3}}\left(2t_p^2 f_s^2 E_p^2 - t_p^2 f_c^2 E_p^2 - t_s^2 E_s^2\right)
\end{aligned}
\tag{A.12}
$$

A.3 Calculation of surface electric-field induced nonlinearity

Below, each independent element of the effective second order susceptibility tensor used for the calculation in section 5.3 is listed. The rotation matrix can be arbitrary, however, the elements are calculated only for a crystal with $\bar{4}3m$ symmetry.

$$
\begin{aligned}
\chi_{xxx} &= \chi^{(3)}_{iijj}(R_{xx}R_{xx}R_{xy}R_{zy} + R_{xx}R_{xx}R_{xz}R_{zz} + R_{xy}R_{xy}R_{xx}R_{zx}) \\
&+ \chi^{(3)}_{iijj}(R_{xy}R_{xy}R_{xz}R_{zz} + R_{xz}R_{xz}R_{xx}R_{zx} + R_{xz}R_{xz}R_{xy}R_{zy}) \\
&+ \chi^{(3)}_{ijij}(R_{xx}R_{xy}R_{xx}R_{zy} + R_{xx}R_{xz}R_{xx}R_{zz} + R_{xy}R_{xx}R_{xy}R_{zx}) \\
&+ \chi^{(3)}_{ijij}(R_{xy}R_{xz}R_{xy}R_{zz} + R_{xz}R_{xx}R_{xz}R_{zx} + R_{xz}R_{xy}R_{xz}R_{zy}) \\
&+ \chi^{(3)}_{ijji}(R_{xx}R_{xy}R_{xy}R_{zx} + R_{xx}R_{xz}R_{xz}R_{zx} + R_{xy}R_{xx}R_{xx}R_{zy}) \\
&+ \chi^{(3)}_{ijji}(R_{xy}R_{xz}R_{xz}R_{zy} + R_{xz}R_{xx}R_{xx}R_{zz} + R_{xz}R_{xy}R_{xy}R_{zz}) \\
&+ \chi^{(3)}_{iiii}(R_{xx}R_{xx}R_{xx}R_{zx} + R_{xy}R_{xy}R_{xy}R_{zy} + R_{xz}R_{xz}R_{xz}R_{zz}) \qquad \text{(A.13)}
\end{aligned}
$$

$$
\begin{aligned}
\chi_{yyy} &= \chi^{(3)}_{iijj}(R_{yx}R_{yx}R_{yy}R_{zy} + R_{yx}R_{yx}R_{yz}R_{zz} + R_{yy}R_{yy}R_{yx}R_{zx}) \\
&+ \chi^{(3)}_{iijj}(R_{yy}R_{yy}R_{yz}R_{zz} + R_{yz}R_{yz}R_{yx}R_{zx} + R_{yz}R_{yz}R_{yy}R_{zy}) \\
&+ \chi^{(3)}_{ijij}(R_{yx}R_{yy}R_{yx}R_{zy} + R_{yx}R_{yz}R_{yx}R_{zz} + R_{yy}R_{yx}R_{yy}R_{zx}) \\
&+ \chi^{(3)}_{ijij}(R_{yy}R_{yz}R_{yy}R_{zz} + R_{yz}R_{yx}R_{yz}R_{zx} + R_{yz}R_{yy}R_{yz}R_{zy}) \\
&+ \chi^{(3)}_{ijji}(R_{yx}R_{yy}R_{yy}R_{zx} + R_{yx}R_{yz}R_{yz}R_{zx} + R_{yy}R_{yx}R_{yx}R_{zy}) \\
&+ \chi^{(3)}_{ijji}(R_{yy}R_{yz}R_{yz}R_{zy} + R_{yz}R_{yx}R_{yx}R_{zz} + R_{yz}R_{yy}R_{yy}R_{zz}) \\
&+ \chi^{(3)}_{iiii}(R_{yx}R_{yx}R_{yx}R_{zx} + R_{yy}R_{yy}R_{yy}R_{zy} + R_{yz}R_{yz}R_{yz}R_{zz}) \qquad \text{(A.14)}
\end{aligned}
$$

$$
\begin{aligned}
\chi_{zzz} &= \chi^{(3)}_{iijj}(R_{zx}R_{zx}R_{zy}R_{zy} + R_{zx}R_{zx}R_{zz}R_{zz} + R_{zy}R_{zy}R_{zx}R_{zx}) \\
&+ \chi^{(3)}_{iijj}(R_{zy}R_{zy}R_{zz}R_{zz} + R_{zz}R_{zz}R_{zx}R_{zx} + R_{zz}R_{zz}R_{zy}R_{zy}) \\
&+ \chi^{(3)}_{ijij}(R_{zx}R_{zy}R_{zx}R_{zy} + R_{zx}R_{zz}R_{zx}R_{zz} + R_{zy}R_{zx}R_{zy}R_{zx}) \\
&+ \chi^{(3)}_{ijij}(R_{zy}R_{zz}R_{zy}R_{zz} + R_{zz}R_{zx}R_{zz}R_{zx} + R_{zz}R_{zy}R_{zz}R_{zy}) \\
&+ \chi^{(3)}_{ijji}(R_{zx}R_{zy}R_{zy}R_{zx} + R_{zx}R_{zz}R_{zz}R_{zx} + R_{zy}R_{zx}R_{zx}R_{zy}) \\
&+ \chi^{(3)}_{ijji}(R_{zy}R_{zz}R_{zz}R_{zy} + R_{zz}R_{zx}R_{zx}R_{zz} + R_{zz}R_{zy}R_{zy}R_{zz}) \\
&+ \chi^{(3)}_{iiii}(R_{zx}R_{zx}R_{zx}R_{zx} + R_{zy}R_{zy}R_{zy}R_{zy} + R_{zz}R_{zz}R_{zz}R_{zz}) \qquad \text{(A.15)}
\end{aligned}
$$

$$
\begin{aligned}
\chi_{xyy} &= \chi^{(3)}_{iijj}(R_{xx}R_{yx}R_{yy}R_{zy} + R_{xx}R_{yx}R_{yz}R_{zz} + R_{xy}R_{yy}R_{yx}R_{zx}) \\
&+ \chi^{(3)}_{iijj}(R_{xy}R_{yy}R_{yz}R_{zz} + R_{xz}R_{yz}R_{yx}R_{zx} + R_{xz}R_{yz}R_{yy}R_{zy}) \\
&+ \chi^{(3)}_{ijij}(R_{xx}R_{yy}R_{yx}R_{zy} + R_{xx}R_{yz}R_{yx}R_{zz} + R_{xy}R_{yz}R_{yy}R_{zx}) \\
&+ \chi^{(3)}_{ijij}(R_{xy}R_{yz}R_{yy}R_{zz} + R_{xz}R_{yx}R_{yz}R_{zx} + R_{xz}R_{yy}R_{yz}R_{zy}) \\
&+ \chi^{(3)}_{ijji}(R_{xx}R_{yy}R_{yy}R_{zx} + R_{xx}R_{yz}R_{yz}R_{zx} + R_{xy}R_{yx}R_{yx}R_{zy}) \\
&+ \chi^{(3)}_{ijji}(R_{xy}R_{yz}R_{yz}R_{zy} + R_{xz}R_{yx}R_{yx}R_{zz} + R_{xz}R_{yy}R_{yy}R_{zz}) \\
&+ \chi^{(3)}_{iiii}(R_{xx}R_{yx}R_{yx}R_{zx} + R_{xy}R_{yy}R_{yy}R_{zy} + R_{xz}R_{yz}R_{yz}R_{zz}) \quad \text{(A.16)}
\end{aligned}
$$

$$
\begin{aligned}
\chi_{yxx} &= \chi^{(3)}_{iijj}(R_{yx}R_{xx}R_{xy}R_{zy} + R_{yx}R_{xx}R_{xz}R_{zz} + R_{yy}R_{xy}R_{xx}R_{zx}) \\
&+ \chi^{(3)}_{iijj}(R_{yy}R_{xy}R_{xz}R_{zz} + R_{yz}R_{xz}R_{xx}R_{zx} + R_{yz}R_{xz}R_{xy}R_{zy}) \\
&+ \chi^{(3)}_{ijij}(R_{yx}R_{xy}R_{xx}R_{zy} + R_{yx}R_{xz}R_{xx}R_{zz} + R_{yy}R_{xx}R_{xy}R_{zx}) \\
&+ \chi^{(3)}_{ijij}(R_{yy}R_{xz}R_{xy}R_{zz} + R_{yz}R_{xx}R_{xz}R_{zx} + R_{yz}R_{xy}R_{xz}R_{zy}) \\
&+ \chi^{(3)}_{ijji}(R_{yx}R_{xy}R_{xy}R_{zx} + R_{yx}R_{xz}R_{xz}R_{zx} + R_{yy}R_{xx}R_{xx}R_{zy}) \\
&+ \chi^{(3)}_{ijji}(R_{yy}R_{xz}R_{xz}R_{zy} + R_{yz}R_{xx}R_{xx}R_{zz} + R_{yz}R_{xy}R_{xy}R_{zz}) \\
&+ \chi^{(3)}_{iiii}(R_{yx}R_{xx}R_{xx}R_{zx} + R_{yy}R_{xy}R_{xy}R_{zy} + R_{yz}R_{xz}R_{xz}R_{zz}) \quad \text{(A.17)}
\end{aligned}
$$

$$
\begin{aligned}
\chi_{xzz} &= \chi^{(3)}_{iijj}(R_{xx}R_{zx}R_{zy}R_{zy} + R_{xx}R_{zx}R_{zz}R_{zz} + R_{xy}R_{zy}R_{zx}R_{zx}) \\
&+ \chi^{(3)}_{iijj}(R_{xy}R_{zy}R_{zz}R_{zz} + R_{xz}R_{zz}R_{zx}R_{zx} + R_{xz}R_{zz}R_{zy}R_{zy}) \\
&+ \chi^{(3)}_{ijij}(R_{xx}R_{zy}R_{zx}R_{zy} + R_{xx}R_{zz}R_{zx}R_{zz} + R_{xy}R_{zx}R_{zy}R_{zx}) \\
&+ \chi^{(3)}_{ijij}(R_{xy}R_{zz}R_{zy}R_{zz} + R_{xz}R_{zx}R_{zz}R_{zx} + R_{xz}R_{zy}R_{zz}R_{zy}) \\
&+ \chi^{(3)}_{ijji}(R_{xx}R_{zy}R_{zy}R_{zx} + R_{xx}R_{zz}R_{zz}R_{zx} + R_{xy}R_{zx}R_{zx}R_{zy}) \\
&+ \chi^{(3)}_{ijji}(R_{xy}R_{zz}R_{zz}R_{zy} + R_{xz}R_{zx}R_{zx}R_{zz} + R_{xz}R_{zy}R_{zy}R_{zz}) \\
&+ \chi^{(3)}_{iiii}(R_{xx}R_{zx}R_{zx}R_{zx} + R_{xy}R_{zy}R_{zy}R_{zy} + R_{xz}R_{zz}R_{zz}R_{zz}) \quad \text{(A.18)}
\end{aligned}
$$

$$
\begin{aligned}
\chi_{zxx} &= \chi^{(3)}_{iijj}(R_{zx}R_{xx}R_{xy}R_{zy} + R_{zx}R_{xx}R_{xz}R_{zz} + R_{zy}R_{xy}R_{xx}R_{zx}) \\
&+ \chi^{(3)}_{iijj}(R_{zy}R_{xy}R_{xz}R_{zz} + R_{zz}R_{xz}R_{xx}R_{zx} + R_{zz}R_{xz}R_{xy}R_{zy}) \\
&+ \chi^{(3)}_{ijij}(R_{zx}R_{xy}R_{xx}R_{zy} + R_{zx}R_{xz}R_{xx}R_{zz} + R_{zy}R_{xx}R_{xy}R_{zx}) \\
&+ \chi^{(3)}_{ijij}(R_{zy}R_{xz}R_{xy}R_{zz} + R_{zz}R_{xx}R_{xz}R_{zx} + R_{zz}R_{xy}R_{xz}R_{zy}) \\
&+ \chi^{(3)}_{ijji}(R_{zx}R_{xy}R_{xy}R_{zx} + R_{zx}R_{xz}R_{xz}R_{zx} + R_{zy}R_{xx}R_{xx}R_{zy}) \\
&+ \chi^{(3)}_{ijji}(R_{zy}R_{xz}R_{xz}R_{zy} + R_{zz}R_{xx}R_{xx}R_{zz} + R_{zz}R_{xy}R_{xy}R_{zz}) \\
&+ \chi^{(3)}_{iiii}(R_{zx}R_{xx}R_{xx}R_{zx} + R_{zy}R_{xy}R_{xy}R_{zy} + R_{zz}R_{xz}R_{xz}R_{zz}) \qquad \text{(A.19)}
\end{aligned}
$$

$$
\begin{aligned}
\chi_{yzz} &= \chi^{(3)}_{iijj}(R_{yx}R_{zx}R_{zy}R_{zy} + R_{yx}R_{zx}R_{zz}R_{zz} + R_{yy}R_{zy}R_{zx}R_{zx}) \\
&+ \chi^{(3)}_{iijj}(R_{yy}R_{zy}R_{zz}R_{zz} + R_{yz}R_{zz}R_{zx}R_{zx} + R_{yz}R_{zz}R_{zy}R_{zy}) \\
&+ \chi^{(3)}_{ijij}(R_{yx}R_{zy}R_{zx}R_{zy} + R_{yx}R_{zz}R_{zx}R_{zz} + R_{yy}R_{zx}R_{zy}R_{zx}) \\
&+ \chi^{(3)}_{ijij}(R_{yy}R_{zz}R_{zy}R_{zz} + R_{yz}R_{zx}R_{zz}R_{zx} + R_{yz}R_{zy}R_{zz}R_{zy}) \\
&+ \chi^{(3)}_{ijji}(R_{yx}R_{zy}R_{zy}R_{zx} + R_{yx}R_{zz}R_{zz}R_{zx} + R_{yy}R_{zx}R_{zx}R_{zy}) \\
&+ \chi^{(3)}_{ijji}(R_{yy}R_{zz}R_{zz}R_{zy} + R_{yz}R_{zx}R_{zx}R_{zz} + R_{yz}R_{zy}R_{zy}R_{zz}) \\
&+ \chi^{(3)}_{iiii}(R_{yx}R_{zx}R_{zx}R_{zx} + R_{yy}R_{zy}R_{zy}R_{zy} + R_{yz}R_{zz}R_{zz}R_{zz}) \qquad \text{(A.20)}
\end{aligned}
$$

$$
\begin{aligned}
\chi_{zyy} &= \chi^{(3)}_{iijj}(R_{zx}R_{yx}R_{yy}R_{zy} + R_{zx}R_{yx}R_{yz}R_{zz} + R_{zy}R_{yy}R_{yx}R_{zx}) \\
&+ \chi^{(3)}_{iijj}(R_{zy}R_{yy}R_{yz}R_{zz} + R_{zz}R_{yz}R_{yx}R_{zx} + R_{zz}R_{yz}R_{yy}R_{zy}) \\
&+ \chi^{(3)}_{ijij}(R_{zx}R_{yy}R_{yx}R_{zy} + R_{zx}R_{yz}R_{yx}R_{zz} + R_{zy}R_{yx}R_{yy}R_{zx}) \\
&+ \chi^{(3)}_{ijij}(R_{zy}R_{yz}R_{yy}R_{zz} + R_{zz}R_{yx}R_{yz}R_{zx} + R_{zz}R_{yy}R_{yz}R_{zy}) \\
&+ \chi^{(3)}_{ijji}(R_{zx}R_{yy}R_{yy}R_{zx} + R_{zx}R_{yz}R_{yz}R_{zx} + R_{zy}R_{yx}R_{yx}R_{zy}) \\
&+ chi^{(3)}_{ijji}(R_{zy}R_{yz}R_{yz}R_{zy} + R_{zz}R_{yx}R_{yx}R_{zz} + R_{zz}R_{yy}R_{yy}R_{zz}) \\
&+ \chi^{(3)}_{iiii}(R_{zx}R_{yx}R_{yx}R_{zx} + R_{zy}R_{yy}R_{yy}R_{zy} + R_{zz}R_{yz}R_{yz}R_{zz}) \qquad \text{(A.21)}
\end{aligned}
$$

$$
\begin{aligned}
\chi_{xyz} &= \chi^{(3)}_{iijj}(R_{xx}R_{yx}R_{zy}R_{zy} + R_{xx}R_{yx}R_{zz}R_{zz} + R_{xy}R_{yy}R_{zx}R_{zx}) \\
&+ \chi^{(3)}_{iijj}(R_{xy}R_{yy}R_{zz}R_{zz} + R_{xz}R_{yz}R_{zx}R_{zx} + R_{xz}R_{yz}R_{zy}R_{zy}) \\
&+ \chi^{(3)}_{ijij}(R_{xx}R_{yy}R_{zx}R_{zy} + R_{xx}R_{yz}R_{zx}R_{zz} + R_{xy}R_{yx}R_{zy}R_{zx}) \\
&+ \chi^{(3)}_{ijij}(R_{xy}R_{yz}R_{zy}R_{zz} + R_{xz}R_{yx}R_{zz}R_{zx} + R_{xz}R_{yy}R_{zz}R_{zy}) \\
&+ \chi^{(3)}_{ijji}(R_{xx}R_{yy}R_{zy}R_{zx} + R_{xx}R_{yz}R_{zz}R_{zx} + R_{xy}R_{yx}R_{zx}R_{zy}) \\
&+ \chi^{(3)}_{ijji}(R_{xy}R_{yz}R_{zx}R_{zy} + R_{xz}R_{yx}R_{zx}R_{zz} + R_{xz}R_{yy}R_{zy}R_{zz}) \\
&+ \chi^{(3)}_{iiii}(R_{xx}R_{yx}R_{zx}R_{zx} + R_{xy}R_{yy}R_{zy}R_{zy} + R_{xz}R_{yz}R_{zz}R_{zz}) \quad \text{(A.22)}
\end{aligned}
$$

$$
\begin{aligned}
\chi_{yxz} &= \chi^{(3)}_{iijj}(R_{yx}R_{xx}R_{zy}R_{zy} + R_{yx}R_{xx}R_{zz}R_{zz} + R_{yy}R_{xy}R_{zx}R_{zx}) \\
&+ \chi^{(3)}_{iijj}(R_{yy}R_{xy}R_{zz}R_{zz} + R_{yz}R_{xz}R_{zx}R_{zx} + R_{yz}R_{xz}R_{zy}R_{zy}) \\
&+ \chi^{(3)}_{ijij}(R_{yx}R_{xy}R_{zx}R_{zy} + R_{yx}R_{xz}R_{zx}R_{zz} + R_{yy}R_{xx}R_{zy}R_{zx}) \\
&+ \chi^{(3)}_{ijij}(R_{yy}R_{xz}R_{zy}R_{zz} + R_{yz}R_{xx}R_{zz}R_{zx} + R_{yz}R_{xy}R_{zz}R_{zy}) \\
&+ \chi^{(3)}_{ijji}(R_{yx}R_{xy}R_{zy}R_{zx} + R_{yx}R_{xz}R_{zz}R_{zx} + R_{yy}R_{xx}R_{zx}R_{zy}) \\
&+ \chi^{(3)}_{ijji}(R_{yy}R_{xz}R_{zz}R_{zy} + R_{yz}R_{xx}R_{zx}R_{zz} + R_{yz}R_{xy}R_{zy}R_{zz}) \\
&+ \chi^{(3)}_{iiii}(R_{yx}R_{xx}R_{zx}R_{zx} + R_{yy}R_{xy}R_{zy}R_{zy} + R_{yz}R_{xz}R_{zz}R_{zz}) \quad \text{(A.23)}
\end{aligned}
$$

$$
\begin{aligned}
\chi_{zxy} &= \chi^{(3)}_{iijj}(R_{zx}R_{xx}R_{yy}R_{zy} + R_{zx}R_{xx}R_{yz}R_{zz} + R_{zy}R_{xy}R_{yx}R_{zx}) \\
&+ \chi^{(3)}_{iijj}(R_{zy}R_{xy}R_{yz}R_{zz} + R_{zz}R_{xz}R_{yx}R_{zx} + R_{zz}R_{xz}R_{yy}R_{zy}) \\
&+ \chi^{(3)}_{ijij}(R_{zx}R_{xy}R_{yx}R_{zy} + R_{zx}R_{xz}R_{yx}R_{zz} + R_{zy}R_{xx}R_{yy}R_{zx}) \\
&+ \chi^{(3)}_{ijij}(R_{zy}R_{xz}R_{yy}R_{zz} + R_{zz}R_{xx}R_{yz}R_{zx} + R_{zz}R_{xy}R_{yz}R_{zy}) \\
&+ \chi^{(3)}_{ijji}(R_{zx}R_{xy}R_{yy}R_{zx} + R_{zx}R_{xz}R_{yz}R_{zx} + R_{zy}R_{xx}R_{yx}R_{zy}) \\
&+ \chi^{(3)}_{ijji}(R_{zy}R_{xz}R_{yz}R_{zy} + R_{zz}R_{xx}R_{yx}R_{zz} + R_{zz}R_{xy}R_{yy}R_{zz}) \\
&+ \chi^{(3)}_{iiii}(R_{zx}R_{xx}R_{yx}R_{zx} + R_{zy}R_{xy}R_{yy}R_{zy} + R_{zz}R_{xz}R_{yz}R_{zz}) \quad \text{(A.24)}
\end{aligned}
$$

$$
\begin{aligned}
\chi_{xxy} &= \chi^{(3)}_{iijj}(R_{xx}R_{xx}R_{yy}R_{zy} + R_{xx}R_{xx}R_{yz}R_{zz} + R_{xy}R_{xy}R_{yx}R_{zx}) \\
&+ \chi^{(3)}_{iijj}(R_{xy}R_{xy}R_{yz}R_{zz} + R_{xz}R_{xz}R_{yx}R_{zx} + R_{xz}R_{xz}R_{yy}R_{zy}) \\
&+ \chi^{(3)}_{ijij}(R_{xx}R_{xy}R_{yx}R_{zy} + R_{xx}R_{xz}R_{yx}R_{zz} + R_{xy}R_{xx}R_{yy}R_{zx}) \\
&+ \chi^{(3)}_{ijij}(R_{xy}R_{xz}R_{yy}R_{zz} + R_{xz}R_{xx}R_{yz}R_{zx} + R_{xz}R_{xy}R_{yz}R_{zy}) \\
&+ \chi^{(3)}_{ijji}(R_{xx}R_{xy}R_{yy}R_{zx} + R_{xx}R_{xz}R_{yz}R_{zx} + R_{xy}R_{xx}R_{yx}R_{zy}) \\
&+ \chi^{(3)}_{ijji}(R_{xy}R_{xz}R_{yz}R_{zy} + R_{xz}R_{xx}R_{yx}R_{zz} + R_{xz}R_{xy}R_{yy}R_{zz}) \\
&+ \chi^{(3)}_{iiii}(R_{xx}R_{xx}R_{yx}R_{zx} + R_{xy}R_{xy}R_{yy}R_{zy} + R_{xz}R_{xz}R_{yz}R_{zz}) \quad \text{(A.25)}
\end{aligned}
$$

$$
\begin{aligned}
\chi_{xxz} &= \chi^{(3)}_{iijj}(R_{xx}R_{xx}R_{zy}R_{zy} + R_{xx}R_{xx}R_{zz}R_{zz} + R_{xy}R_{xy}R_{zx}R_{zx}) \\
&+ \chi^{(3)}_{iijj}(R_{xy}R_{xy}R_{zz}R_{zz} + R_{xz}R_{xz}R_{zx}R_{zx} + R_{xz}R_{xz}R_{zy}R_{zy}) \\
&+ \chi^{(3)}_{ijij}(R_{xx}R_{xy}R_{zx}R_{zy} + R_{xx}R_{xz}R_{zx}R_{zz} + R_{xy}R_{xx}R_{zy}R_{zx}) \\
&+ \chi^{(3)}_{ijij}(R_{xy}R_{xz}R_{zy}R_{zz} + R_{xz}R_{xx}R_{zz}R_{zx} + R_{xz}R_{xy}R_{zz}R_{zy}) \\
&+ \chi^{(3)}_{ijji}(R_{xx}R_{xy}R_{zy}R_{zx} + R_{xx}R_{xz}R_{zz}R_{zx} + R_{xy}R_{xx}R_{zx}R_{zy}) \\
&+ \chi^{(3)}_{ijji}(R_{xy}R_{xz}R_{zz}R_{zy} + R_{xz}R_{xx}R_{zx}R_{zz} + R_{xz}R_{xy}R_{zy}R_{zz}) \\
&+ \chi^{(3)}_{iiii}(R_{xx}R_{xx}R_{zx}R_{zx} + R_{xy}R_{xy}R_{zy}R_{zy} + R_{xz}R_{xz}R_{zz}R_{zz}) \quad \text{(A.26)}
\end{aligned}
$$

$$
\begin{aligned}
\chi_{yyz} &= \chi^{(3)}_{iijj}(R_{yx}R_{yx}R_{zy}R_{zy} + R_{yx}R_{yx}R_{zz}R_{zz} + R_{yy}R_{yy}R_{zx}R_{zx}) \\
&+ \chi^{(3)}_{iijj}(R_{yy}R_{yy}R_{zz}R_{zz} + R_{yz}R_{yz}R_{zx}R_{zx} + R_{yz}R_{yz}R_{zy}R_{zy}) \\
&+ \chi^{(3)}_{ijij}(R_{yx}R_{yy}R_{zx}R_{zy} + R_{yx}R_{yz}R_{zx}R_{zz} + R_{yy}R_{yx}R_{zy}R_{zx}) \\
&+ \chi^{(3)}_{ijij}(R_{yy}R_{yz}R_{zy}R_{zz} + R_{yz}R_{yx}R_{zz}R_{zx} + R_{yz}R_{yy}R_{zz}R_{zy}) \\
&+ \chi^{(3)}_{ijji}(R_{yx}R_{yy}R_{zy}R_{zx} + R_{yx}R_{yz}R_{zz}R_{zx} + R_{yy}R_{yx}R_{zx}R_{zy}) \\
&+ \chi^{(3)}_{ijji}(R_{yy}R_{yz}R_{zz}R_{zy} + R_{yz}R_{yx}R_{zx}R_{zz} + R_{yz}R_{yy}R_{zy}R_{zz}) \\
&+ \chi^{(3)}_{iiii}(R_{yx}R_{yx}R_{zx}R_{zx} + R_{yy}R_{yy}R_{zy}R_{zy} + R_{yz}R_{yz}R_{zz}R_{zz}) \quad \text{(A.27)}
\end{aligned}
$$

$$
\begin{aligned}
\chi_{zxz} &= \chi^{(3)}_{iijj}(R_{zx}R_{xx}R_{zy}R_{zy} + R_{zx}R_{xx}R_{zz}R_{zz} + R_{zy}R_{xy}R_{zx}R_{zx}) \\
&+ \chi^{(3)}_{iijj}(R_{zy}R_{xy}R_{zz}R_{zz} + R_{zz}R_{xz}R_{zx}R_{zx} + R_{zz}R_{xz}R_{zy}R_{zy}) \\
&+ \chi^{(3)}_{ijij}(R_{zx}R_{xy}R_{zx}R_{zy} + R_{zx}R_{xz}R_{zx}R_{zz} + R_{zy}R_{xx}R_{zy}R_{zx}) \\
&+ \chi^{(3)}_{ijij}(R_{zy}R_{xz}R_{zy}R_{zz} + R_{zz}R_{xx}R_{zz}R_{zx} + R_{zz}R_{xy}R_{zz}R_{zy}) \\
&+ \chi^{(3)}_{ijji}(R_{zx}R_{xy}R_{zy}R_{zx} + R_{zx}R_{xz}R_{zz}R_{zx} + R_{zy}R_{xx}R_{zx}R_{zy}) \\
&+ \chi^{(3)}_{ijji}(R_{zy}R_{xz}R_{zz}R_{zy} + R_{zz}R_{xx}R_{zx}R_{zz} + R_{zz}R_{xy}R_{zy}R_{zz}) \\
&+ \chi^{(3)}_{iiii}(R_{zx}R_{xx}R_{zx}R_{zx} + R_{zy}R_{xy}R_{zy}R_{zy} + R_{zz}R_{xz}R_{zz}R_{zz}) \qquad \text{(A.28)}
\end{aligned}
$$

$$
\begin{aligned}
\chi_{zyz} &= \chi^{(3)}_{iijj}(R_{zx}R_{yx}R_{zy}R_{zy} + R_{zx}R_{yx}R_{zz}R_{zz} + R_{zy}R_{yy}R_{zx}R_{zx}) \\
&+ \chi^{(3)}_{iijj}(R_{zy}R_{yy}R_{zz}R_{zz} + R_{zz}R_{yz}R_{zx}R_{zx} + R_{zz}R_{yz}R_{zy}R_{zy}) \\
&+ \chi^{(3)}_{ijij}(R_{zx}R_{yy}R_{zx}R_{zy} + R_{zx}R_{yz}R_{zx}R_{zz} + R_{zy}R_{yx}R_{zy}R_{zx}) \\
&+ \chi^{(3)}_{ijij}(R_{zy}R_{yz}R_{zy}R_{zz} + R_{zz}R_{yx}R_{zz}R_{zx} + R_{zz}R_{yy}R_{zz}R_{zy}) \\
&+ \chi^{(3)}_{ijji}(R_{zx}R_{yy}R_{zy}R_{zx} + R_{zx}R_{yz}R_{zz}R_{zx} + R_{zy}R_{yx}R_{zx}R_{zy}) \\
&+ \chi^{(3)}_{ijji}(R_{zy}R_{yz}R_{zz}R_{zy} + R_{zz}R_{yx}R_{zx}R_{zz} + R_{zz}R_{yy}R_{zy}R_{zz}) \\
&+ \chi^{(3)}_{iiii}(R_{zx}R_{yx}R_{zx}R_{zx} + R_{zy}R_{yy}R_{zy}R_{zy} + R_{zz}R_{yz}R_{zz}R_{zz}) \qquad \text{(A.29)}
\end{aligned}
$$

$$
\begin{aligned}
\chi_{yxy} &= \chi^{(3)}_{iijj}(R_{yx}R_{xx}R_{yy}R_{zy} + R_{yx}R_{xx}R_{yz}R_{zz} + R_{yy}R_{xy}R_{yx}R_{zx}) \\
&+ \chi^{(3)}_{iijj}(R_{yy}R_{xy}R_{yz}R_{zz} + R_{yz}R_{xz}R_{yx}R_{zx} + R_{yz}R_{xz}R_{yy}R_{zy}) \\
&+ \chi^{(3)}_{ijij}(R_{yx}R_{xy}R_{yx}R_{zy} + R_{yx}R_{xz}R_{yx}R_{zz} + R_{yy}R_{xx}R_{yy}R_{zx}) \\
&+ \chi^{(3)}_{ijij}(R_{yy}R_{xz}R_{yy}R_{zz} + R_{yz}R_{xx}R_{yz}R_{zx} + R_{yz}R_{xy}R_{yz}R_{zy}) \\
&+ \chi^{(3)}_{ijji}(R_{yx}R_{xy}R_{yy}R_{zx} + R_{yx}R_{xz}R_{yz}R_{zx} + R_{yy}R_{xx}R_{yx}R_{zy}) \\
&+ \chi^{(3)}_{ijji}(R_{yy}R_{xz}R_{yz}R_{zy} + R_{yz}R_{xx}R_{yx}R_{zz} + R_{yz}R_{xy}R_{yy}R_{zz}) \\
&+ \chi^{(3)}_{iiii}(R_{yx}R_{xx}R_{yx}R_{zx} + R_{yy}R_{xy}R_{yy}R_{zy} + R_{yz}R_{xz}R_{yz}R_{zz}) \qquad \text{(A.30)}
\end{aligned}
$$